AN ABSTRACT OF THE THESIS OF

Erik S. Edgar for the degree of Master of Science in Chemical Engineering presented on September 26, 2008.

Title: Computational and Experimental Investigation of Steady Flow Fields, Turbulence, and Hemodynamic Wall Stresses in Patient-specific Abdominal Aortic Aneurysm Models.

Abstract approved:

Robert A. Peattie

Steady flow fields and flow-induced wall stresses have been evaluated by experimental measurements and computational fluid dynamics (CFD) analysis in a series of patient-specific abdominal aortic aneurysm (AAA) models, over a range of Reynolds numbers (Re) from 125 to 3000 (500 to 3000 for CFD). Experimental methods used particle image velocimetry (PIV) to evaluate velocity flow fields, wall shear stress, flow fields and pressure were predicted in corresponding AAA models. Both laminar and turbulent solutions were obtained at each *Re*, using k-ω techniques for turbulence simulation.

Qualitatively the measurements and predictions were in good agreement, especially with respect to velocity. AAA lumen shape was found to significantly alter flow structure, producing large recirculating vortices in the sacs of bulged lumens, but little to no vortical structure in nearly isodiametric lumens from patients with substantial

intraluminal thrombus. Recirculating vortices were associated with adverse wall pressure gradients and retrograde, reduced wall shear stress. For example, CFD predicted at *Re* = 3000, wall shear stress to be near 8.0 dynes/cm^2 in non-dilated aortas but only 2.2 dynes/cm^2 within dilations. Quantitative agreement was limited between the measured and predicted wall shear stress and turbulence. Wall shear stress was in reasonable agreement between measurements and predictions at Re = 500, showing global wall shear stress mean values of 0.41 dyne/cm^2 for experimental results versus 0.63 dyne/cm^2 for computational results. However, at Re = 3000, the difference was much greater as the global wall shear stress mean value was 2.75 dyne/cm^2 for experimental results versus 5.78 dyne/cm^2 for computational results. Computational results associated separated flows with adverse wall pressure gradients, though experimental measurements did not confirm this. Experimental pressure measurements indicated that under these conditions, wall height was the greatest determinant of wall pressure. The complex flows formed within patient specific lumens seemed to promote turbulence, even in non-dilated sections. Turbulence was measured at all flow rates including Re = 125. At Re = 3000, fluctuating velocities of up to 0.7 times the overall mean velocity were found in the saccular dilation. Computational simulation produced lower turbulence than was found experimentally, with fluctuating velocities generally remaining below 0.1 times the overall mean velocity.

This investigation shows the importance of patient-specific analysis, and provides some description of the hemodynamic forces experienced at rest and exercise conditions. The quantitative disagreements between measured and predicted results also suggest that current computational techniques are not yet sufficiently accurate for reliable clinical predictions.

©Copyright by Erik S. Edgar

September 26, 2008

All Rights Reserved

Computational and Experimental Investigation of Steady Flow Fields, Turbulence, and Hemodynamic Wall Stresses in Patient-specific Abdominal Aortic Aneurysm Models

by
Erik S. Edgar

A THESIS

Submitted to

Oregon State University

in partial fulfillment of
the requirements for the
degree of

Master of Science

Presented September 26, 2008
Commencement June 2009

Master of Science thesis of Erik S. Edgar presented on September 26, 2008.

APPROVED:

Major Professor, representing Chemical Engineering

Head of the School of Chemical, Biological and Environmental Engineering

---

Dean of the Graduate School

I understand that my thesis will become part of the permanent collection of Oregon State University libraries. My signature below authorizes release of my thesis to any reader upon request.

Erik S. Edgar, Author

ACKNOWLEDGEMENTS

Many people are to thank for helping me achieve this degree, not only in the past three years but also in the formative twenty four prior. To the thousands of people who have helped shape my life and my schooling, I thank you, and I hope that I have the opportunity to personally acknowledge you.

Thanks to Dr. Williamson and the OSU chemical engineering department for helping facilitate the bicoastal study and to Dr. Kaplan and the Tufts biomedical engineering department for welcoming me in Medford.

Thanks to Bec Conant for her support through the times and circumstances that arose during graduate school. Thanks to my grandparents who believed that education was worth the investment. And finally, mere 'thanks' does not fully capture the appreciation that I have for my parents, sister and the rest of the family. They will have to settle with my eternal gratitude for supporting me no matter the circumstances.

TABLE OF CONTENTS

CHAPTER 1: INTRODUCTION …… 1

1.1 PROBLEM STATEMENT…….. 1
1.2 BASIS FOR WORK…… 1
1.3 SUMMARY OF PREVIOUS WORK……. 2
1.4 SCOPE…….. 3

CHAPTER 2: BACKGROUND……. 4

2.1 CARDIOVASCULAR SYSTEM……. 4
2.1.1 Cardiovascular overview…… 4
2.1.2 Arteries…… 6
2.1.3 Arterial disease…… 7

2.2 ABDOMINAL AORTIC ANEURYSM……... 7
2.2.1 Abdominal aortic aneurysm overview…… 7
2.2.2 Burden of suffering……. 10
2.2.3 Clinical treatment of AAA……. 11
2.2.4 Surgical intervention……... 11

2.3 FLUID DYNAMICS…… 13
2.3.1 Fluid dynamics principles…….. 13
2.3.2 Rheology of blood……. 14
2.3.3 Pipe flow…… 15
2.3.4 Dynamic similarity……. 18
2.3.5 Infrarenal blood flow……. 18
2.3.6 Flow perturbation and separation……... 20
2.3.7 Turbulence…….. 22
2.3.8 Hemodynamic stressors…….. 24

2.4 FLUID DYNAMICS STUDY…….. 26
2.4.1 Particle tracing…… 26
2.4.2 Particle image velocimetry……. 26
2.4.3 Computational fluid dynamics…… 27
2.4.4 Turbulence modeling…….. 28

2.5 PREVIOUS ENGINEERING STUDIES……. 29

TABLE OF CONTENTS (Continued)

CHAPTER 3: METHODS…….. 32

3.1 PATIENT SPECIFIC AAA MODEL GENERATION…… 32

3.2 PHANTOM CONSTRUCTION……... 35
3.2.1 Casting techniques…….. 35
3.2.2 Modified casting method……..... 36
3.2.3 Straight tube model……. 38
3.2.4 Pressure points and air release pathways……... 38

3.3 FLOW LOOP…… 40
3.3.1 Setup and operation……... 40
3.3.2 Entrance length…….. 42

3.4 IONIC WORKING FLUID FOR PIV…….. 42

3.5 PIV METHODS…… 45
3.5.1 Illumination…… 45
3.5.2 Image capture……. 45
3.5.3 PIV hardware and control…….. 45
3.5.4 Camera and laser setup…….. 46
3.5.5 Experimental conditions…… 46
3.5.6 Image collection and data processing…… 48

3.6 PIV POST PROCESSING……. 49
3.6.1 2-D flow field assembly…… 49
3.6.2 2-D velocity profile……... 51
3.6.3 Conversion to in vivo values……. 52
3.6.4 Wall shear stress…… 54
3.6.5 2-D turbulence……... 56
3.6.6 3-D flow field analysis…….. 57

3.7 PRESSURE MEASUREMENTS…… 59
3.7.1 Flow loop and working fluid……. 59
3.7.2 Pressure measurement equipment……. 59
3.7.3 Wall pressure calibration and reporting…… 59
3.7.4 Equivalent pressure……... 61
3.7.5 Flow loop modifications…… 61

TABLE OF CONTENTS (Continued)

3.8 COMPUTATIONAL FLUID DYNAMICS…… 62
3.8.1 Governing equations……. 62
3.8.2 Turbulence computation…… 64
3.8.3 Boundary conditions……. 66
3.8.4 Computational grid…… 69
3.8.5 Computation, convergence, and post processing…….. 71
3.8.6 Fully developed turbulent pipe flow……. 72

CHAPTER 4: EXPERIMENTAL RESULTS…… 75

4.1 Inlet velocity profile……. 75
4.2 2-D velocity flow field……. 79
4.3 Maximum velocity…… 82
4.4 Maximum retrograde velocity…….. 84
4.5 Turbulence…… 86
4.6 Shear stress…… 90
4.7 Correlation rate……. 95
4.8 3-D velocity flow field……. 97

CHAPTER 5: COMPUTATIONAL RESULTS…… 103

5.1 Stream tubes……. 103
5.2 Velocity profiles……... 106
5.3 Wall shear stress……... 111
5.4 Wall pressure…… 116
5.5 Turbulence properties…….. 118

CHAPTER 6: PRESSURE RESULTS…….. 123

6.1 Pressure points……. 123
6.2 Wall pressure…… 128
6.3 Equivalent wall pressure…….. 133

TABLE OF CONTENTS (Continued)

CHAPTER 7: DISCUSSION……. 136

7.1 Experimental overview…….. 136
7.2 Computational overview…… 141
7.3 Results comparison…… 142
7.4 Experimental considerations……. 151
7.5 Computational considerations…… 152
7.6 Clinical application……. 153

CHAPTER 8: CONCLUSIONS……. 155

8.1 Conclusions…… 155
8.2 Future Study…… 156

BIBLIOGRAPHY…… 157

APPENDICES……. 162

Appendix A AAA model numeration…..……...… 163

Appendix B CFD Results……..…… 165

Appendix C Wall pressure results……...……. 172

LIST OF FIGURES

Figure		Page
2.1	The major arteries of the heart and abdomen……	5
2.2	Exposed arterial layers……..	5
2.3	Pathological types of aneurysms……	8
2.4	Aneurysms and thrombus……..	9
2.5	Endovascular AAA repair……..	12
2.6	Rouleaux formation……	15
2.7	Laminar and turbulent velocity profiles……..…	17
2.8	Oscillatory flow…….	17
2.9	Axi-symmetric AAA particle tracing……..…	21
2.10	Turbulence visualization using soap films……..…	23
2.11	Forces acting on fluid……	25
2.12	PIV schematic……	27
3.1	CT imaging from patient with AAA…….	33
3.2	AAA models…….	34
3.3	Replica development ……	36
3.4	Phantom 5 from three angles…….	37
3.5	Puncture air release ……..	39
3.6	Flow loop schematic……..	41
3.7	Dynamic viscosity for the ionic working fluid……..	44
3.8	Phantom 4 installed in the flow loop…….	47

LIST OF FIGURES (continued)

Figure		Page
3.9	Flow field assembly…….	50
3.10	Shear stress distribution……	55
3.11	3-D flow field assembly……	58
3.12	CFD AAA models……	63
3.13	Inlet conditions…….	68
3.14	Mesh cutaway……..	70
3.15	Half cylinder mesh……...	74
3.16	Velocity profiles from preliminary pipe study…….	74
4.1	Lumen examined experimentally……...	76
4.2	Inlet velocity profiles……..	77
4.3	Scaled inlet velocity profile……	78
4.4	Velocity vector maps……..	80
4.5	Maximum velocity…….	83
4.6	Maximum retrograde velocity……	85
4.7	Dimensionless turbulent velocity……	88
4.8	Turbulence intensity……	89
4.9	Shear stress distribution……..	92
4.10	Wall shear stress……	93
4.11	Correlation rate……..	96
4.12	Three dimensional flow field constructions……..	98
4.13	Axial velocity and secondary velocity……..	99

LIST OF FIGURES (continued)

Figure		Page
5.1	Stream tubes…….	104
5.2	Velocity distribution…….	109
5.3	Wall shear stress distribution……	114
5.4	Wall shear stress traces…….	115
5.5	Wall pressure distributions……	117
5.6	Dimensionless turbulent velocity……..	120
5.7	Turbulence intensity…….	121
5.8	Specific turbulence dissipation rate……..	122
6.1	Lumen with pressure points…….	125
6.2	Wall height of each pressure point……	127
6.3	Wall pressure…….	131
6.4	Equivalent pressure change……...	134
7.1	Modified wall shear stress for phantom 4……..	139
7.2	Wall pressure and wall height correction comparison……	140
7.3	2-D velocity comparison……	145
7.4	3-D velocity comparison……	147

LIST OF TABLES

Table		Page
2.1	Mean and peak flow rates in the infrarenal aorta…….	19
3.1	Model geometric parameters……	33
3.2	Experimental results derived from the inlet profile……..	52
3.3	Inlet conditions for model 8……..	67
3.4	Grid properties……..	69
3.5	Half cylinder grids corresponding to AAA models……...	73
4.1	Inlet velocity and flow rates……..	75
4.2	Experimental mean wall shear stress ……...	90
5.1	Computational mean wall shear stress …….	113
6.1	Signal fluctuations, pressure fluctuations and error estimate……...	124
7.1	Comparison of mean wall shear stress……..	144

LIST OF APPENDIX FIGURES

Appendix Figure		Page
B.1	Stream tubes ……..…….	166
B.2	Wall shear stress at Re = 500……..	167
B.3	Wall shear stress at Re = 3000……	168
B.4	Wall pressure at Re = 500 ……..	169
B.5	Wall pressure at Re = 3000…….	170
B.6	Turbulence intensity at Re = 500……	171
B.7	Turbulence intensity at Re = 3000…….	172
C.1	Phantom 1, top……	175
C.2	Phantom 1, side……..	176
C.3	Phantom 2, top……	177
C.4	Phantom 2, side……..	178
C.5	Phantom 3, top……	179
C.6	Phantom 3, side……..	180
C.7	Phantom 4, top……	181
C.8	Phantom 5, top……	182

LIST OF APPENDIX TABLES

Appendix Table		Page
A.1	AAA model numeration…….…….	164
B.1	Inlet turbulence parameters……..	173

NOMENCLATURE

α	Womersley number
B	blanking variable
C_f	Scaling factor to account for diameter variation
C_k	Inlet turbulence parameter
C_l	Laminart inlet velocity constant
C_t	Turbulent inlet velocity constant
$C_{\omega,1}$, $C_{\omega,2}$	Inlet dissipation parameters
d	diameter
d_a	non-dilated aortic diameter
ΔP	change in equivalent pressure
δt	exposure time differential
$_{ex}$	experimental values
ε	turbulent dissipation rate
g	gravitational constant
$\dot{\gamma}$	strain rate
$_{iv}$	*in vivo* values
h	height
h_o	height of the water column
h_w	wall height (pressure points)
μ	dynamic viscosity
k	turbulent kinetic energy
n	radial profile exponential
N	correlation rate
v	kinematic viscosity
ω	specific turbulence dissipation rate
ω	heart rate
p	pressure
P	equivalent pressure
Q	volumetric flow rate

r	radius
r^*	dimensionless radius
Re	Reynolds number
RI	refractive index
S	transducer signal
t	time
τ	shear stress
τ_w	wall shear stress
$\overline{\tau}_w$	mean wall shear stress
TI	turbulence intensity
$U = (u, v, w)$	velocity
$\overline{u}$	time averaged velocity
u'	turbulent velocity
U'	fluctuating, turbulent velocity
U'^*	dimensionless turbulent velocity
U^*	dimensionless velocity
U_a	mean non-dilated velocity
U_{IN}	inlet velocity
$U_{IN,max}$	maximum inlet velocity
U_{IN}^*	dimensionless inlet velocity
U_{max}	maximum velocity
$w_{max,r}$	maximum retrograde axial velocity
$X = (x, y, z)$	length scale

Computational and experimental investigation of steady flow fields, turbulence, and hemodynamic wall stresses in patient-specific abdominal aortic aneurysm models

CHAPTER 1: INTRODUCTION

1.1 PROBLEM STATEMENT

Steady flow fields and their resulting hemodynamic wall forces within a series of patient-specific abdominal aortic aneurysms (AAA) models have been characterized using computational and experimental methods.

1.2 BASIS FOR WORK

Abdominal aortic aneurysm rupture may be considered to be a mechanical failure of the diseased and weakened aortic wall. When rupture occurs, mortality reaches 90%. Surgical intervention is performed when risk is deemed great enough. However, in some instances the risks of surgery outweigh the benefits of repair. Rupture risk has proven exceptionally difficult to predict; neither biological indicators nor specific critical size or shape have been able to reliably predict rupture risk. Improved evaluation of risk would allow for better clinical treatment of AAA.

Hemodynamic wall forces and their resulting wall strains that they produce have been suggested to play significant roles in the development and progression of AAA. As other vascular diseases have been linked to areas of abnormal hemodynamic forces and strain, a similar relationship would be expected for AAA. Characterizing the flow within AAA is necessary to evaluate the magnitude, location and implications of these forces.

Non invasive imaging has not proved adequate to fully characterize the AAA flow properties *in vivo*. Further, wall pressure and wall shear may not be directly measured using non invasive techniques. For this reason, experimental and computational recreation of AAA flow allows for hemodynamic study. Computational methods are widely growing in use to study these flows in part due to their reduced cost and increasing accessibility to scientists and engineers. Yet they are numerical predictions, not reproductions of the flow, and incomplete without experimental validation. Presenting experimental and computational results in tandem results provides validation of the numerical predictions and enhances both of their studies.

While the flow fields in idealized geometries representing AAA have been well characterized both experimentally and computationally, less work has been done in patient-specific geometries. Published experimental results in patient-specific AAA are believed to be limited to the abstracts by Atkinson et al.

(2001) and Feller et al. (2001) and a recent paper by O'Rourke and McCullough (2008). More computational results have been published, though for only a limited series of patient-specific models and with experimental validation provided only by O'Rourke and McCullough.

1.3 SUMMARY OF PREVIOUS WORK

Previous work in this lab has experimentally described the flows of steady flows in idealized geometries representing AAA (Asbury 1995, Peattie 1996 part I and II). These results were presented at both low and high flow rates emulating rest and exercise conditions. These results have shown separation and vortex formation within the dilations. The magnitude of wall shear stress within the dilations was greatly reduced from the non-dilated values, and reversed in directed due to the retrograde flow. Turbulence was observed and instigated within the dilation, and increased in strength as bulge diameter increased.

The next step was characterizing pulsatile flow within the same idealized geometries, using wave forms recreating the cardiac cycles seen *in vivo* (Peattie and Bluth 1998, Peattie 2004). Some similar patterns were seen over the cycle, but separation was eliminated during systole and developed during diastole.

Patient-specific AAA geometries were created from patient CT data by Elham Aslani (2005). These were studied for geometrical features that may indicate rupture. These models were also used to generate flow through phantoms containing the patient-specific AAA models used for experimental analysis.

Steady flows within patient-specific AAA were studied experimentally by Stephanie Atkinson (2001) and Kelly Feller (2001). Velocity flow fields were evaluated using 2-D bisecting slices and 3-D representations of the entire flow field. Turbulence intensities were plotted using 2-D slices. Wall shear stress was evaluated in unpublished results by Zebulon Jones. Some similarity of the flow patterns were seen within these patient-specific geometries as the steady flows in idealized model. However, the complex geometries each developed different vortex patterns, and the ring vortices were not seen around the entire circumference. The patient-specific models seemed to amply turbulence. Pressure profiles for these AAA were determined by Aslani.

In unpublished work by Chengyan Peng, steady flow through these same patient-specific geometries was attempted computationally. While his efforts did not produce a robust final product, they paved the method and provided major contributions to the computation studies presented here.

1.4 SCOPE

In this study, steady flow through patient-specific aneurysm was characterized. Using particle image velocimetry, the flows within two phantoms containing patient-specific AAA were investigated. One contained a large, saccular aneurysm, which had not been investigated prior. The other was an isodiameteric aneurysm which had been previously characterized by Feller and Atkinson. Both 2-D and 3-D analysis were generated from these phantoms over two (3-D analysis) or three (2-D analysis) flow rates. From the flow field velocity distributions, the wall shear stress was evaluated by searching for the maximum shear in the near wall region. Turbulence within these flow fields was analyzed for 2-D slices and turbulence was found at flow rates as low as Re = 125.

Wall pressure was determined in a series of five phantoms, three of which had been previously characterized by Aslani. More pressure measurement points were used than in prior study and an additional series of pressure points characterized the pressure on a second wall, which had not been previously attempted.

Computational recreation of steady flows was performed in a series of ten patient-specific geometries. Four separate flow rates were studied and solved using both laminar and turbulent calculation schemes (k-ω). These used the computational meshes previously generated by Peng and the final computational methods were developed from his work. Inlet boundary conditions for velocity and turbulent parameters were developed based on distributions of fully developed turbulent flow. This work characterized velocity fields, wall shear stress, wall pressure and turbulence over a series of Reynolds numbers ranging from 500 to 3000.

Finally, the experimental and computational studies results were compared and evaluated for similarities and dissimilarities. This validates the computational predictions against measured results, giving an indication of the performance of the computational simulations.

CHAPTER 2: BACKGROUND

2.1 CARDIOVASCULAR SYSTEM

2.1.1 *Cardiovascular overview*

The cardiovascular system nourishes and protects the extremities of the body by circulating blood. The heart is a muscular organ the size of a fist which produces the fluidic pressure through ventricle contractions to drive blood through its conduits, the blood vessels which generates the cardiac cycle. The right ventricle expels blood to the pulmonary arteries leading to the lungs (pulmonary circulation) and left ventricle forces blood remainder of the body (systemic circulation). The heart may be described as a variable and cyclic pump, able to circulate blood at low rates during rest and high rates under exercise conditions. In the normal population, the cardiovascular output at rest is around 5 L/min (70 ml/stroke at 70 bpm) but under exercise may increase to around 20 L/min (120 m/stroke at 150 bmp), though cardiovascular output in may be as high as 40 L/min in trained athletes (210 ml/stroke at 190 bmp; Wilmore and Costill 2005).

Arteries carry blood from the heart and veins return blood to the heart (figure 2.1). Capillaries are in between and connect arterial and venous branches and are where the transport activities of the cardiovascular system occur. Both arteries and veins are branching networks which range in size from the largest vessels nearest the heart to the capillaries. The arterial system is composed of vessels ranging from large arteries (3 cm diameter for the ascending aorta), to intermediate smaller arteries and arterioles, to the microscopic capillaries (4×10^{-7} cm).

Blood is a heterogeneous mixture of red blood cells and plasma. The body contains around 5 L of blood, which closely corresponds to the volume of 1 minute of resting cardiac output. Under exercise conditions, the entire blood volume may be circulated up to 4-8 times per minute. The functions of blood are extensive, but its primary function is transportive. Blood delivers oxygen, food, other nutrients, and regulatory hormones to the cells, while removing cellular removing waste. Blood also contains substantial elements of the body's immune system, providing defense against invasive viruses, microbes and toxins. Blood is able to coagulate to stop bleeding by forming clots constructed from fibrinogen and platelets.

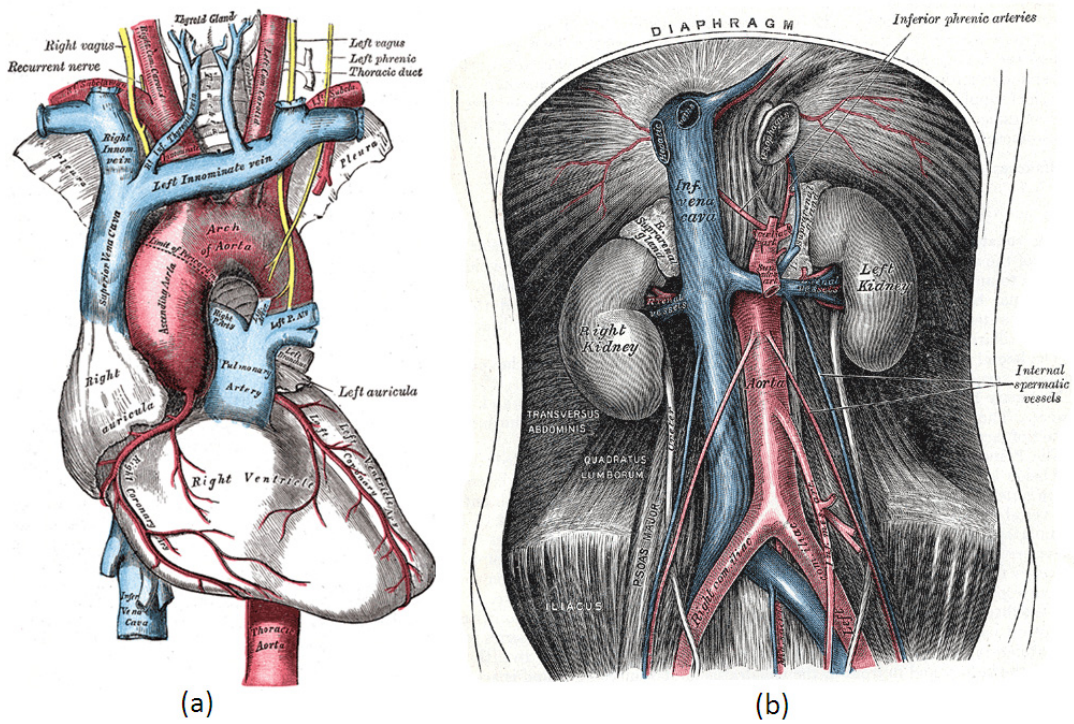

Figure 2.1 The major arteries of the heart and abdomen. The major arteries and veins (a) connected to the heart and (b) within the abdominal cavity. The abdominal aorta begins below the diaphragm. (Grey's Anatomy)

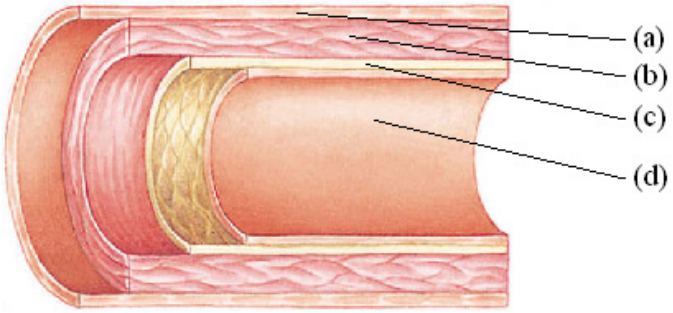

Figure 2.2 Exposed arterial layers. (a) Tunica intima. (b) Elastin lamina. (c) Tunica media. (d) Tunica adventitia. (www.dkimages.com)

2.1.2 *Arteries*

Arteries are elastic, able to conform to body motion and expand and contract in response to changing fluidic pressure or muscle tension. Muscle tension around the arteries regulates the flow of blood within each artery by dilating the vessel to increase flow (vasodilation) or contract to decrease flow (vasoconstriction). The arteries are also elastic and responsive to changing fluid pressure of the cardiac cycle. During systole, the high pressure contraction of the heart expels blood into the arteries and the arteries expand and increase in volume. During diastole this accumulated blood is released as the arteries contract due to decreased pressure. This elastic motion both dampens the pressure generated during systole and a more even delivery of blood over the cardiac cycle. Under rest conditions, flow reversals are shown during diastole due to the elastic behavior of the smaller, branching arteries. However, at exercise, these flow reversals are eliminated by the elastic behavior of the arteries (Pederson et al. 1999, Taylor et al. 2002).

Arteries of composed of three radial layers: tunica intima (innermost layer), tunica media (middle layer), and tunica externa (outermost layer). These are exposed in figure 2.2. The tunica interna contains a layer of endothelial cells supported by loose connecting elastic tissue. The endothelial cells are in contact with the arterial blood, and in the healthy aorta, form the walls of the lumen. The lumen is defined as the space within a tubular structure through which a substance passes (de Graaff 2002). Within the vascular system, the lumen refers to the interior of the blood vessels. The tunica media consists primarily of smooth muscle fibers along with elastin and collagen. The tunica adventitia is composed primarily of elastic supportive tissues. The proteins elastin and collagen are two primary components of the supportive connecting tissues. While both elastin and collagen are elastic and load bearing, elastin is the suppler component and collagen is more structural.

The aorta is the principle and largest artery. All blood flow passes through the aorta during the cardiac cycle, and all non-pulmonary arteries branch from the aorta. It is the most compliant artery due to its larger size. The aorta begins at the heart where the ascending aorta receives blood from the left ventricle of the heart. The aorta arches over the pulmonary arteries before descending through the body core to the diaphragm. This aortic section is known as the thoracic artery. The aorta below the diaphragm is the abdominal aorta, and our study focuses on blood flow here. Numerous branches from the abdominal aorta supply blood to the organs within the abdomen. The major branches non-exhaustively include celiac trunk and its branches (which supply blood to the liver, stomach and spleen), the superior mesenteric artery (to the intestines, digestive organs and other smaller organs), the renal arteries (to the kidneys), and the inferior mesenteric artery (to the digestive organs and other small organs). The aorta terminates with the iliac bifurcation, where the two common iliac arteries carry blood to the lower extremities of the body.

2.1.3 *Arterial disease*

As arteries age, a degradation of the elastin and collagen within the connective supporting occurs, resulting in a loss of elasticity and subsequent hardening of the arteries. Arteriosclerosis is the loss of elasticity and hardening of the arteries, and is a natural progression with elderly, though many other factors contribute towards it. This hardening of the arteries causes greater resistance to blood flow, resulting in increased blood pressure under the same cardiac output. Hypertension, or elevated blood pressure, is a common result from vascular degeneration due to disease or aging. Hypertension places a higher continuous strain on the heart and arteries.

In arthrosclerosis (a form of arteriosclerosis) lesions develop plaques on the arterial walls, these being known as atheroma. In addition to atheroma, thrombus may also accumulate on the arterial walls. Thrombus is a clot with a matrix-like structure which forms within the artery and is attached to its walls. As such, thrombus impedes into the arterial lumen and separates blood from the endothelial cells which traditionally form the lumen. Thrombus may be soft and pliable during early formation, but thrombus may later become calcified and harden (van de Graaff, 2002). Both thrombus and atheroma may constrict the lumen, and thus have the potential to reduce blood flow. This can lead to hypertension or potentially heart attack. In a peripheral concern, thrombus may become dislodged and obstruct the arteries (embolism), generally in the lower extremities (Silver 1983).

2.2 ABDOMINAL AORTIC ANEURYSM

2.2.1 *Abdominal aortic aneurysm overview*

An aneurysm is a localized, diseased section of an artery characterized by in irreversibly dilated arterial walls which have the potential for rupture. Abdominal aortic aneurysms (AAA) are specific to the abdominal aorta and are generally located between the renal arteries and the iliac bifurcation. An arterial dilation with a diameter exceeding 1.5 × that of the neighboring healthy vessel may be considered an aneurysm, roughly corresponding to 3.5 cm in diameter or larger for AAA (Baxter et al. 2008). Abdominal aortic aneurysms are typically asymptomatic, and a patient will not know of its incidence without screening. Many AAA are stable or grow at a controlled rate and never rupture. However, when rupture does occur, morality exceeds 90% (Johansson and Swedenborg 1986).

Three pathological types of aortic aneurysms are described. True aneurysms are fully connected with the arterial lumen, while false aneurysms (pseudoaneurysm) are dilated segments that are fully or partially separated from the lumen by tunica layers (Silver 1983). A third type, dissecting aneurysms, are

formed from separated tunica layers which fill with blood (Hurst 1990). These three aneurysm types are shown in figure 2.3. All aneurysms in this study are assumed to be true aneurysms.

Aneurysms also commonly classified based on their gross appearance as either fusiform (figure 2.4 a) or saccular (figure 2.4 b), though many aneurysms share characteristics of both. Saccular aneurysms are dilations which affect only a portion of the artery, the artery on the opposing walls remains seemingly unaffected. These tend to produce balloon like, spherical bulges which may range in size from a few millimeters to 15 cm (Silver 1983). These form sharp angles connecting the non-dilated aortic neck. Saccular aneurysms have a strong tendency for thrombus to develop on the lesion wall and partially fill the sac in a single mass (Silver 1983, Hurst 1990). Many saccular aneurysms become filled with thrombus throughout the bulge so that the lumen remains constricted (Silver 1983). In fusiform aneurysms, a more evenly distributed dilation is formed surrounding the entire aortic circumference. The areas of weakness are diffused around the entire surface. The dilated sections gradually decrease in size, slowly ramping to and from the neighboring non-dilated aortas. Fusiform aneurysms often appear spindle like in shape and may grow to 15 or 20 cm (Silver 1983). In this case, thrombus is more likely to line the entire surface of the aneurysm, than accumulate in a single mass.

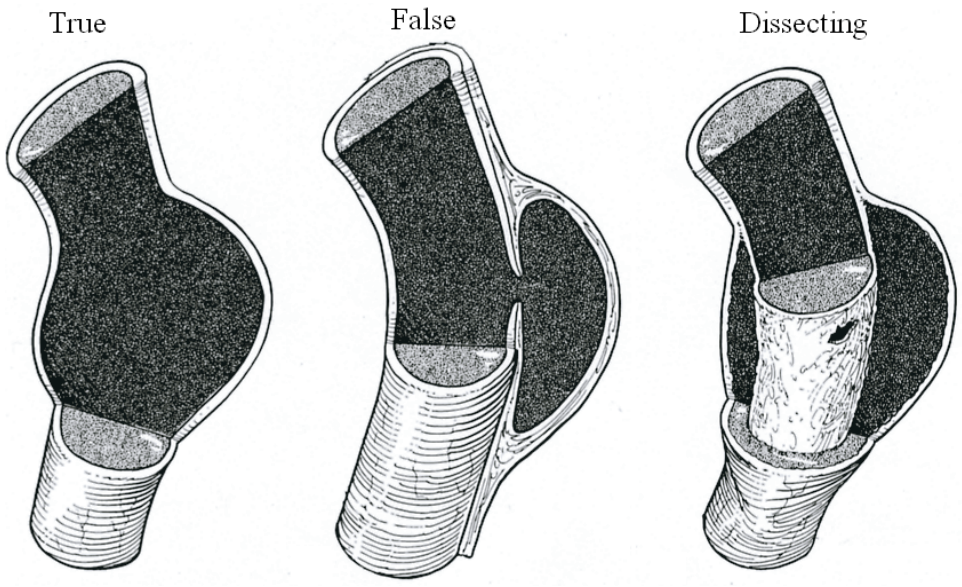

Figure 2.3 Pathological types of aneurysms. The true aneurysm (left) is fully connected to the lumen, while the false aneurysm (center) is partially blocked. The dissecting aneurysm (right) has a hole in the inner tunica layers. Blood fills the void formed by the separated tunica layers. (Cooley, 1986)

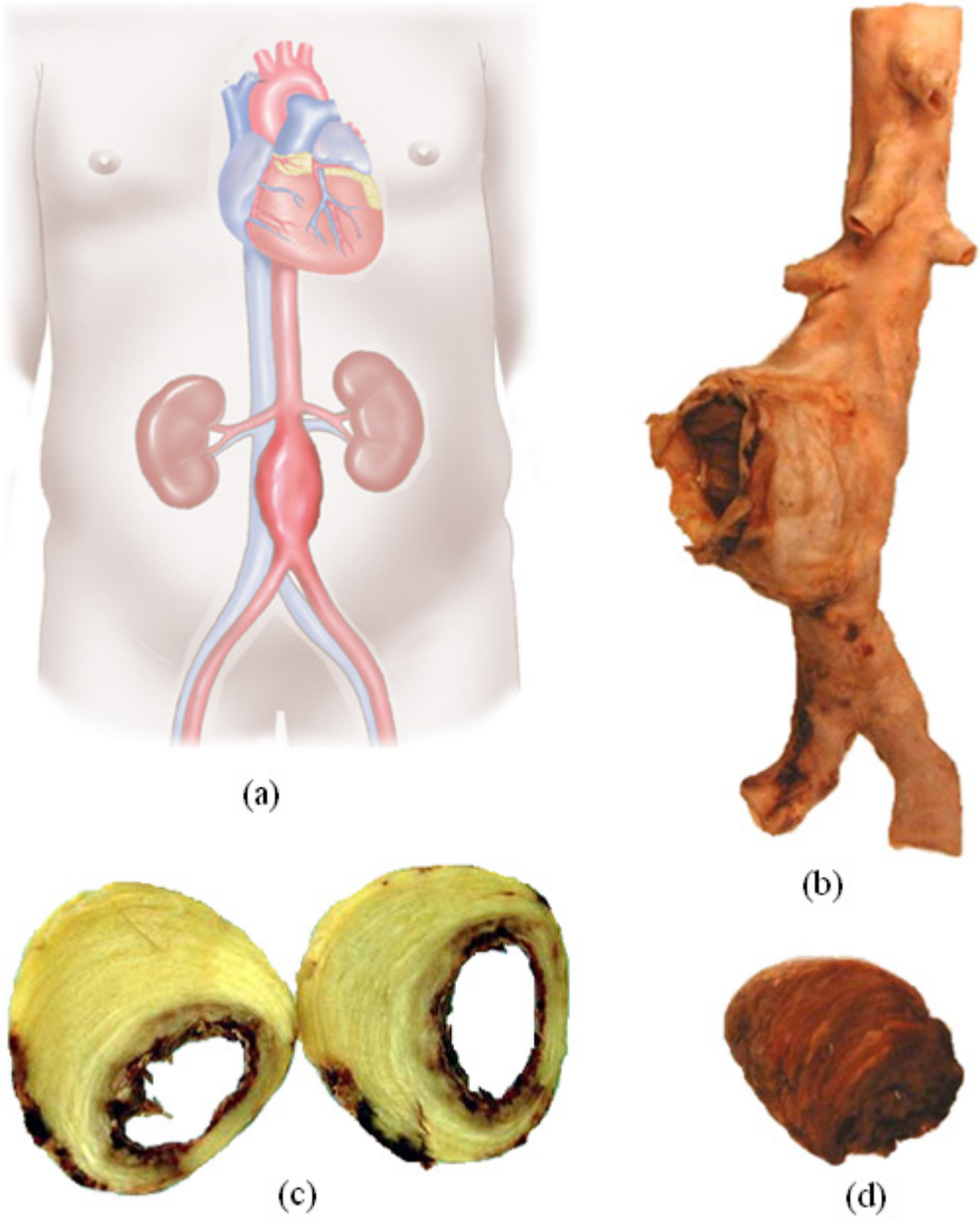

Figure 2.4 Aneurysms and thrombus. (a) Schematic with fusiform AAA. (b) Ruptured saccular AAA from cadaver. (c) Transversely sliced thrombus extracted from saccular AAA [not the AAA in (b)]. (d) Massive thrombus extracted from the above ruptured aneurysm. (a: www.dukeexechealth.org; b-d: www.actpathology.act.gov.au)

Thrombus (figure 2.4 c and d) and atherosclerosis are commonly associated with low flow, low shear regions of the vasculature. The unique geometries formed by AAA promote hemodynamic conditions highly conducive to these lesions (Fung 1997). While thrombus is not directly linked to AAA rupture, it is present in 80% of ruptured aneurysm (Darling et al. 1977). The role of thrombus within AAA is controversial. Thrombus as been suggested it to alleviate wall stress and shear by reducing the lumen diameter through the aneurysm or acting as a mechanical cushion. In these roles, thrombus may be a self healing mechanism and may prevent rupture in some cases (Roberts 1979). Others have suggested thrombus to be detrimental to the AAA wall by asphyxiating the endothelial cells and tunica tissue or that thrombus may acquire and harbor other agents which degrade arterial walls (Di Martino and Vorp 2003, Wang et al. 2002).

In spite of significant efforts, the factors associated with AAA development and ruptures are not fully understood. It is commonly agreed upon that rupture is a mechanical process and occurring when the wall stresses exceeds the wall strength. However the conditions promoting rupture are believed to be a complex interaction of mechanical stress and biologic functions. A partial and incomplete list of these factors includes lung cancer, smoking, sedentary lifestyle, age, gender (males are more susceptible), other vascular disease, thrombus within AAA, arterial wall deterioration (including elastin and collagen loss), loss of elasticity, endothelial cell inflammation, and hypertension (Crownenwett et al. 1985, Silver 1983. Baxter 2008). Of these, lung cancer and smoking are the strongest markers for advanced AAA conditions (Lederle et al. 2003).

2.2.2 *Burden of suffering*

AAA occur most often in elderly male population, with incidence rates of up to 9% in males over 65 (Newman et al. 2001, Singh et al. 2001), and mortality rates when rupture occurs may exceed 90% (Johansson and Swedenborg 1986). AAA are generally asymptomatic and in some cases not detected until rupture. When AAA rupture occurs (figure 2.4 b), blood hemorrhages from the aorta into the abdomen. The massive blood loss and complication from it flooding the abdomen will result in death without surgical intervention. Prompt surgery to close and support the ruptured wall is the only method of repair (Silver 1983). However, only 25% reach the hospital and 11% survive 30 days after rupture even with surgical treatment (Brown et al. 1999).

2.2.3 *Clinical treatment of AAA*

The diagnosis of AAA is generally performed with ultrasonography (US), magnetic resonance (MR), or computed tomography (CT) imaging (Baxter et al. 2008), though physical examination may also detect large AAA (Silver 1983). AAA screening is now routinely practiced in the elderly population in the United States. When AAA is prior to rupture, two options are considered. When risk of rupture is low, surgery is not performed. Periodic rescreening to monitor for AAA growth and increased rupture risk is done. Tobacco cessation and exercise are encouraged. Medication including statins and beta blockers are commonly administered (Baxter et al. 2008). When risk of rupture is high, elective surgery to implant a supportive graft may be performed. However, the risk of mortality from other causes including elective surgery must be weight against the benefits of repair (Lederle et. al 2002). For some patients, the risk of surgery outweighs the benefits of the repair. These cases, as would be expected, are closely monitored for further AAA progression.

Since the work of Szilagyi et al. (1972), lesion diameter has been the best predictor of rupture. AAA are considered at high risk for rupture when their diameter exceeds 5.5 cm (Lederle et. al 2002). This criterion is fails to consider any other AAA factors. Further, while large dilations are well established as high risk for rupture, some AAA as large at 15 cm are stable while some AAA smaller than 4.0 cm rupture (Darling et al. 1977). Clearly, the 5.5 cm criterion is inadequate. However, invasive measurements of AAA conditions would pose as great a threat as surgery, and the only clinical method for rupture prediction remain image based measurement. An improved rupture prediction tool is desired, but is unable to be realized without a more complete understanding of the causes rupture and indicators predicting rupture.

2.2.4 *Surgical intervention*

Surgical treatment of AAA was first performed in 1951 separately by Dubost and Freeman to patients with ruptured AAA using open surgery for direct access to the abdomen (Freeman et al. 1951, Dubost 1952). The ruptured AAA was sutured shut and a supportive fabric graft attached to the aortic wall, a similar process used to this day with open surgical treatment. Despite improvement in open surgical treatment and survival rates, the risks posed by open abdomen surgery are formidable (Zarins et al. 2004).

Parodi performed the first endovascular surgery to repair AAA in 1990 (Parodi et al. 1991). Using a catheterized delivery, a graft covered stent is implanted into the aorta supporting the diseased wall. The stents expand within the aorta, and self adhering barbs attach to the wall. The stent is ‘Y’ shaped to accommodate the iliac bifurcation (Greenhalgh 2008). By delivering the device through the femoral arteries, access through the abdominal cavity is not necessary. This procedure is commonly referred to as endovascular aortic repair (EVAR).

In the past two decades, EVAR has become commonly used for elective AAA repair and has allowed for elective surgery in patients that would not be able to tolerate the stress of open abdomen surgery. Endovascular method shows improved mortality rates and quicker recovery, but are unavailable to some patients due to their morphology (Zarins 2004). More complications arise from EVAR than open surgery, and follow screening for device function is required (Green 2008). A separate, randomized study showed similar survival rates with endovascular and open surgeries groups, but higher aneurysm related mortality rates in the open surgery group (Greenhalgh 2005).

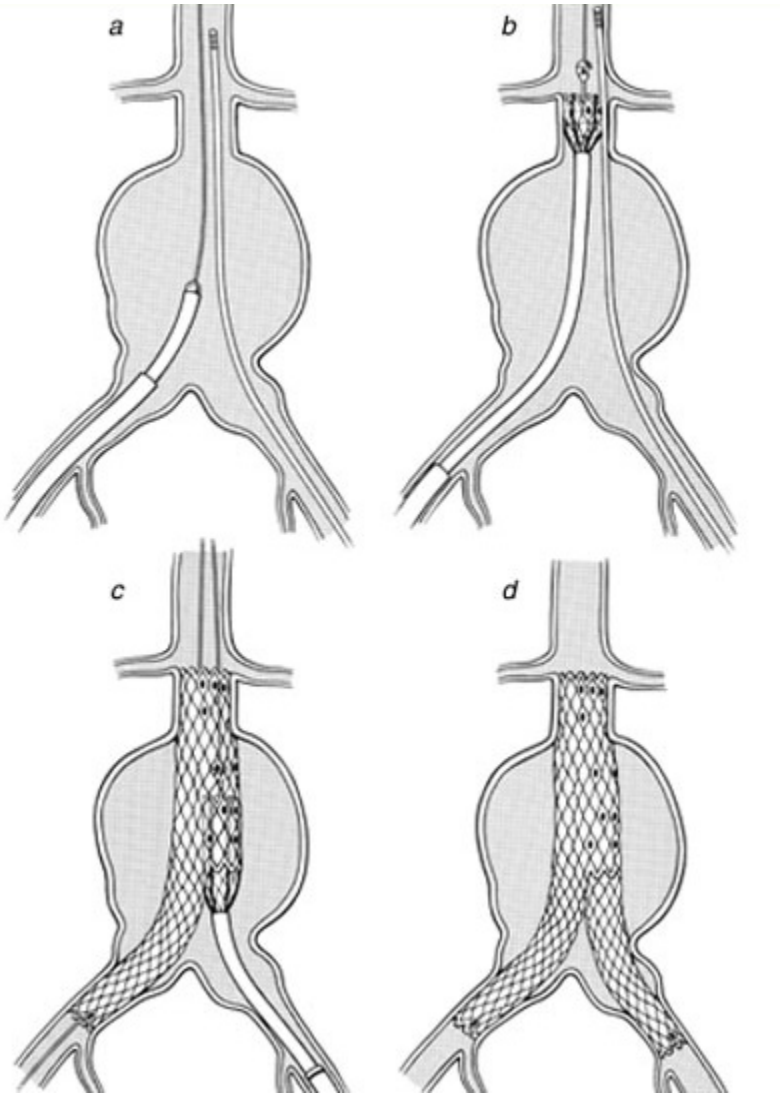

Figure 2.5 Endovascular AAA repair. Endovascular AAA repair using bifurcated, two part graph covered stent. (a) The trunk portion of the stent is delivered using a catheter through the left femoral artery. (b) Stent expands and attaches to aortic wall. (c) Contra lateral portion of the stent is expanded. (d) Stent-graft installed. (www.medscape.com)

2.3 FLUID DYNAMICS

2.3.1 *Fluid dynamics principles*

Force drives fluid motion. The principles of Newton first law (force = mass × acceleration) also apply to fluid flow. Pressure gradient and body force (such as gravity) produce fluidic motion. Shear forces, on the other hand, oppose fluid motion. Shear forces are generated by the resistance of a fluidic body to deformation. In laminar flows, shear is purely derived from the viscosity of the fluid. When turbulence is present, its eddying motion contributes to the shear forces. Shear forces diffuse through the flow, shaping the velocity profile. In this manner, shear forces counterbalance and pressure gradients and body forces.

When the sum of the shear, pressure gradient and body forces are zero, the fluid motion remains constant and no acceleration occurs. However, when these forces are out of balance, then the force must be accounted for by acceleration of the fluid. Two types of accelerations are possible, temporal and convective. Temporal accelerations occur due to flow field changes with respect to time. Convective accelerations are due to change in fluid motion as a fluid moves from one location to another. For example, the accelerations a fluid experiences through an arterial constriction are convective while the accelerations a fluid experiences during the cardiac cycle are temporal.

The forces driving and opposing fluid motion may be equated to the accelerations in the conservation of momentum. Using the incompressibility assumption and assumption of Newtonian fluid properties, used throughout this study and justified later (section 2.3.2), the conservation of momentum simplifies to a commonly used form called the Navier-Stokes equation (equation 2.1).

$$\rho\left(\frac{\partial u_i}{\partial t}+u_j\frac{\partial u_i}{\partial x_j}\right)=-\frac{\partial p}{\partial x_i}+\rho g+\mu\frac{\partial^2 u_i}{\partial x_j\partial x_j} \tag{2.1}$$

Here, $u_i = (u, v, w)$ is the local velocity, $x_i = (x, y, z)$ is the length coordinate, t is the time scale, p is the fluid pressure, μ is the dynamic viscosity, and g is the gravitational constant. The left handed terms represent momentum change from temporal and convective acceleration. On the right hand side, the terms represent pressure gradient, gravitational forces and shear forces.

A second and equally important principle is that mass is conservative. Mass is neither created nor consumed by any non-nuclear processes. This is of vital importance to physics, fluid dynamics, and cardiovascular circulation. The conservation of mass is represented in equation 2.2 for an incompressible fluid.

$$\frac{\partial u_i}{\partial x_i} = 0 \qquad (2.2)$$

The combination of the mass and momentum equation are the governing equations of fluid flow. In certain limited cases, they may be solved analytically to characterize the flow field. When analytical solutions are not possible, they may be approximated using iterative, numerical methods.

2.3.2 *Rheology of blood*

The relationship between the shear stress, τ, and shear rate, $\dot{\gamma}$, determines the fluids ability to flow under varying shear stresses. Newtonian fluids behave with linear correlation between shear stress and shear rate. This relationship may be expressed using a single constant, the dynamic viscosity, μ. The prime example of a Newtonian fluid is water, but many simple homogenous fluids exhibit these properties.

Blood does not behave in this manner. At low shear, blood thickens and becomes more viscous. Red blood cells align and aggregate to form rouleaux (figure 2.6). The rouleaux impede the ability of the blood to flow. More specifically, blood has the properties of a Casson fluid which shows both a yield stress and a non-linear correlation between stress and strain in the flow regimes (Fournier 1999).

Casson fluids exhibit three types of behavior. 1) At low shear, the yield stress of blood (0.04 dyne/cm^2) must be overcome before the blood is able to flow. If the pressure gradient is not enough to overcome the viscous yield stress, the fluid will remain stagnant. In this case, the effective viscosity is infinite since flow is completely impeded. 2) After the yield stress is overcome and the blood becomes fluidic, there is a non-linear response between stress and strain. This is seen at low to moderate strain rates ($\dot{\gamma} < 100$ s^{-1}), common in the smaller blood vessels. At low shear, the effective viscosity is widely variable. 3) At high shear ($\dot{\gamma} > 100$ s^{-1}), the shear stress and shear rate relationship becomes more linear so that a more constant effective viscosity is found. Rouleaux are entirely dissolved so that all red blood cells are individual. These conditions are observed only in the largest arteries. While the viscosity is still dependent on strain, as well as hematocrit, body temperature, it behaves in a nearly Newtonian fashion (Fournier 1999). For this reason, Newtonian behavior is assumed throughout in this study and the kinematic viscosity, ν, is constant at 0.033 cm^2/s. The dynamic viscosity, 0.03465 dyne s cm^{-2}, may be found as the product of the density (ρ, described below) and kinematic viscosity ($\mu = \rho\nu$).

Finally, blood is modeled as an incompressible fluid. While a minor variance in density would be found under extreme pressures or wide range of temperature, these are not experienced within the body.

For this reason, the density of blood at body temperature under pressures experienced within our study assumed to be constant at $\rho = 1.050$ g/cm^3.

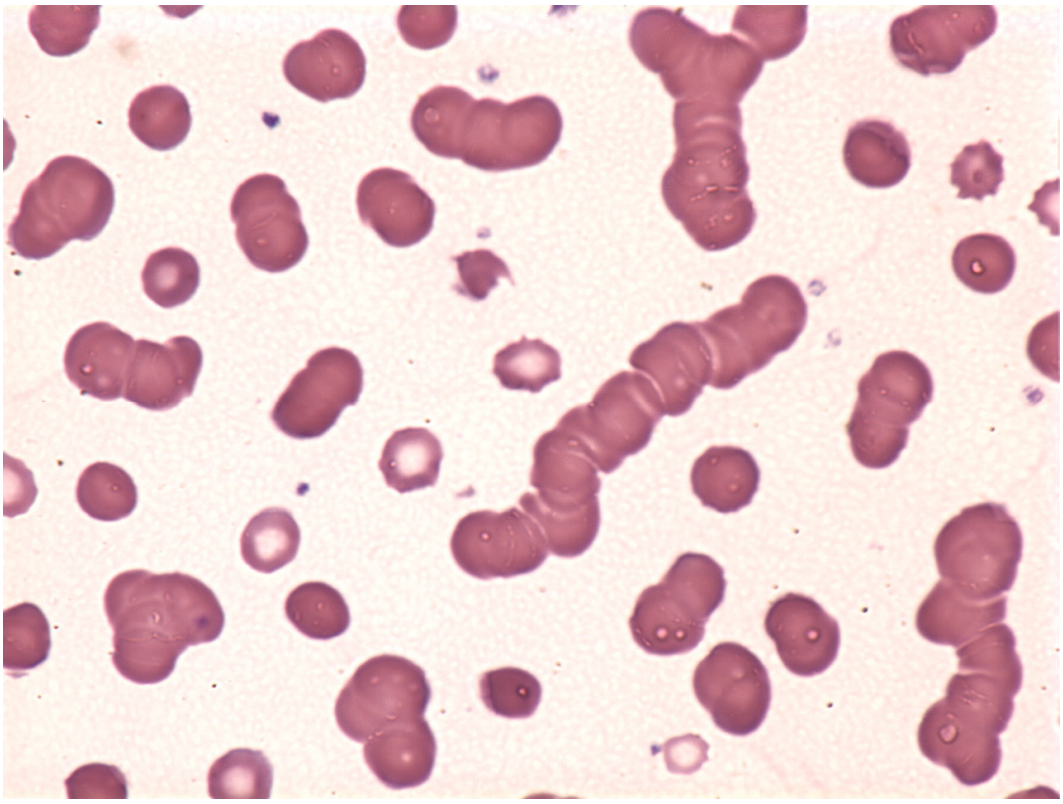

Figure 2.6 Rouleaux formation. (Maslak 2004)

2.3.3 *Pipe flow*

Arterial blood flow has often been described using pipe flow theory. Poiseuille empirically described this characteristic parabolic velocity profile (figure 2.7) generated by laminar flow of a Newtonian fluid in a cylindrical geometry (Poiseuille 1846). The boundary layer, defined first by Prandtl (1904), is continuous from the wall to flow center. It distributes shear linearly which generates the parabolic profile. No lateral/radial or rotational motion is observed here, only linear motion following the pathway of the pipe.

The Poiseuille law, equation 2.3, describes the volumetric flow rate, Q, predicted based on pressure drop, Δp, in a pipe with radius, r, and length L, with a Newtonian fluid of dynamic viscosity, μ.

$$Q = \frac{\pi r^4 \Delta p}{8 \mu L} \tag{2.3}$$

Three conclusions from this law must be drawn. First, flow rate is proportional to the pressure gradient, $\Delta p / L$, the driving force. Second, flow rate is inversely proportional to viscosity, which opposes motion. Third, the flow rate is proportional to forth power of the radius, showing lumen size has dramatic effect on flow rates.

Womersley (1955) described oscillatory flow within a pipe, also for laminar conditions (figure 2.8). The oscillatory motion of flow generates both forward motion and retrograde flow over the oscillatory cycle, with a zero net flow. In contrast to the Poiseuille flow, the shear is concentrated in the boundary layer near the wall. Due to the low shear in the flow center, a flat profile forms and is more responsive to the pressure changes driving the flow. Change in the motion in the boundary layer is delayed until the shear diffuses through the boundary layer. This develops the distinct 'M' shaped profile at low flow and a flat centerline flow at the sinusoidal peaks. A half cycle of the Womersley flow is shown in figure 2.8.

Arterial flow is neither steady nor oscillatory exclusively, rather it is combination of two. The character of the motion changes according to cardiac output. As mentioned earlier, rest conditions produce net reversal occurs during diastole while under exercise conditions, the forward motion is maintained. As such, more oscillatory character is seen in rest conditions while a more steady flow is produced during exercise. The arterial diameter, fluidic pressure, and the elasticity of the arterial walls all impact the character of the flow.

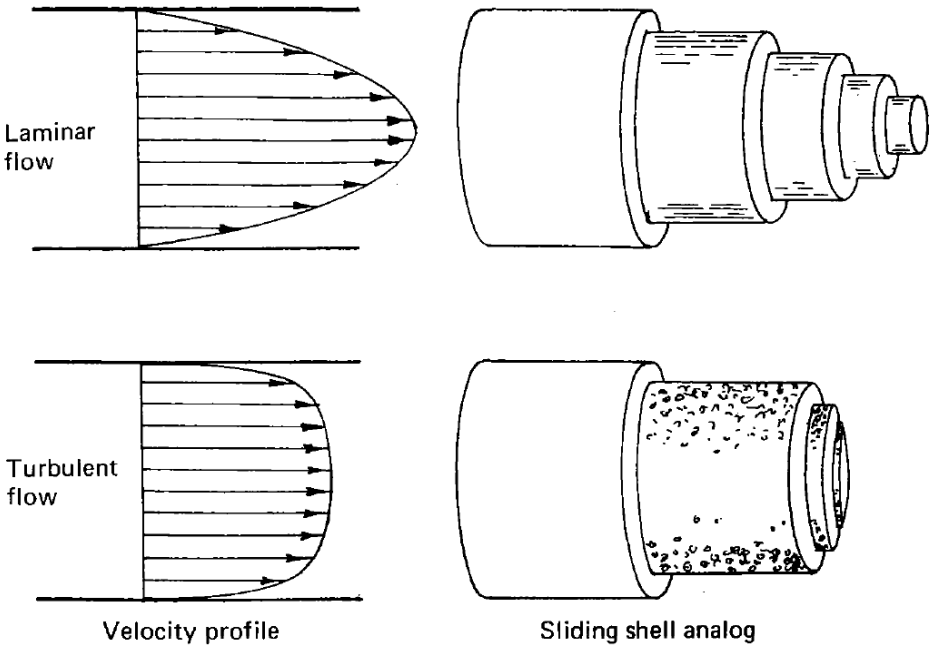

Figure 2.7 Laminar and turbulent velocity profiles. Left: velocity profiles for laminar (top) and turbulent (bottom) flows within a pipe. Both profiles proportionally represent the same flow rate. The laminar flow is shows a faster centerline velocity while the turbulent flow has a wider momentum distribution. Right: three dimensional analogs using sliding shells. (Fung 1997)

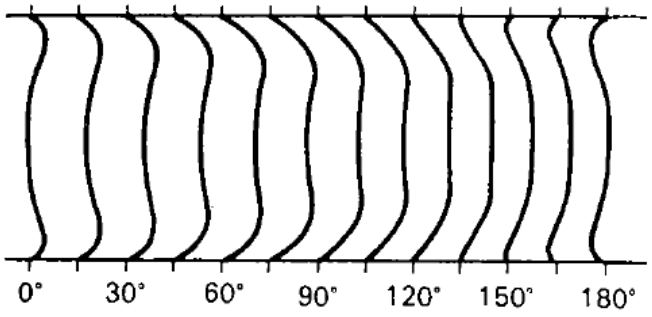

Figure 2.8 Oscillatory flow. Velocity profiles for laminar oscillatory flow for a half cycle where α = 6.67. (Fung 1997)

2.3.4 *Dynamic similarity*

Experimental reproduction of arterial flows requires matching conditions as experienced *in vivo*. Two dimensionless parameters are used to describe the conditions of these flows based on the fluidic, geometrical and flow conditions. The first is the Reynolds number, Re, which describes the ratio of the convective inertia force to the shear forces. This is represented in equation 2.4, the definition of the Reynolds number, where $\bar{u}$ is the mean velocity within a cylindrical section of diameter, d.

$$\mathrm{Re} = \frac{\bar{u}d}{\nu} \tag{2.4}$$

Similarly, the ratio of the transient inertia force to the shear forces is described by the square of the Womersley number, α. This allows replication of the temporal flow features generated by the pulsatile cardiac cycle. The definition of the Womersley number is given in equation 2.5, where ω is the heart rate.

$$\alpha = d\sqrt{\frac{\omega}{\upsilon}} \tag{2.5}$$

If these parameters are matched between two flow situations, then the flow will behave similarly. This is useful in fluids experiments, where it is often not possible to exactly match all the experimental parameters such as fluid viscosity or size. In this study, the experimental geometries were nearly identical to the *in vivo* geometries. The working fluids have lower viscosities than blood. By proportionally decreasing the experimental flow rate relative to the *in vivo* flow rate, the same Reynolds numbers were achieved.

This study is performed under steady flow conditions which do not allow the Womersley number to be matched. However, when using a pulsatile flow to emulate the cardiac cycle, the Womersley parameter must be matched by the experimental flow to reproduce the same oscillatory effects experienced *in vivo*. This is easily accomplished by adjusting the oscillatory frequency in the experimental conditions.

2.3.5 *Infrarenal blood flow*

To create physiologically reasonable conditions, it is necessary to emulate the flow through the infrarenal aorta. The flow rates in the infrarenal aorta were reported by Taylor et al. (2002) and Pedersen et al. (1999) at rest and under lower body exercise. The mean and peak flow rates (and corresponding Re and α) from these studies are compiled in table 2.1. Both studies show similar results, and both showed that overall flow reversal during diastole at rest conditions was eliminated at exercise conditions. The

infrarenal flow rates are well below the cardiovascular outputs (section 2.1.1) due to the diversion of blood to other arteries.

At rest, both studies achieved peak Re > 2200, significant as the onset of turbulence under certain conditions is commonly predicted near Re = 2200. Under exercise conditions, these overall flow rates increase, towards Re = 2000, just below the Re = 2200 criterion, though peak Re are well in excess of the transition criterion. As will be discussed elsewhere, turbulence has been seen in experimental AAA studies well below Re = 2200.

These flow rates were used to help determine the inlet boundary conditions for this study. Re = 500 was selected to emulate rest flows and is very near the resting value from Pedersen. The Re = 3000 was selected as the exercise condition, even though the mean exercise conditions from Taylor and Pedersen were slightly below this. It was hoped that a higher Re may produce more stable turbulence, while still being within the range of mean and peak values. Further, the exercise conditions in the study were relatively mild, and increased exercise effort would also increase infrarenal blood flow.

	Heart Rate (bpm)	mean Q (L/min)	mean Re	peak Q (L/min)	peak Re	α
Rest [1]	65	1.4	450	7.2	2315	11.5
Rest [2]	73	0.9	289	7	2251	12.1
Exercise [1]	115	6.4	2058	15	4823	15.2
Exercise [2]	110	5.6	1801	12	3858	14.9

Table 2.1 Mean and peak flow rates in the infrarenal aorta. Reynolds number and Womersley number were calculated with the assumptions of d_a = 2.0 cm (Liddington and Heather 1992) and ν = 0.033 cm^2/s. [1]Pederson et al. 1999, [2]Taylor et al. 2002

2.3.6 *Flow perturbation and separation*

While pipe flow studies assume constant diameters and linear geometries, arterial systems are much more complex. Bends, dilations, constrictions and bifurcations and all perturb the flow and prevent developed flow cases as suggested by Poiseuille or Womersley flow. Patient-specific studies introduce complex geometries that cause more velocity perturbations than idealized models due to the more variable wall surface.

When the lumen wall bends away from the direction of the main flow at steep enough angles, the core flow becomes separated from the wall. Between the wall and the core flow, a separation zone is formed, characterized by eddy motion and low flow velocity relative to the core flow. This zone is bounded on the upstream end by the separation point and the downstream end by the stagnation point (also called the reattachment point). Here vortices may form, with retrograde flow along the wall.

Separated flow is driven by pressure gradient. When the flow decelerates, fluid pressure elevates. This is common leaving lumen contraction (stenosis) or entering lumen dilation (such as an aneurysm). This may be explained by the conservation of momentum equation. The elevated pressure in the core flow directs some of its fluid toward these separated zones. An adverse pressure gradient is formed, and the pressure is higher at the downstream stagnation point than it is at the upstream separation point.

Separated flow is of particular interest for AAA study, as the aneurismal expansions are ideal for forming separated flows. Separated flows are not believed to produces stressors that would lead to aneurysm expansion or rupture. However, they do promote conditions that are strongly associated with vascular disease such as arthrosclerosis and thrombus formation. Low shear stress and turbulence are more common in these zones and both have been marked for vascular disease (Fung 1997).

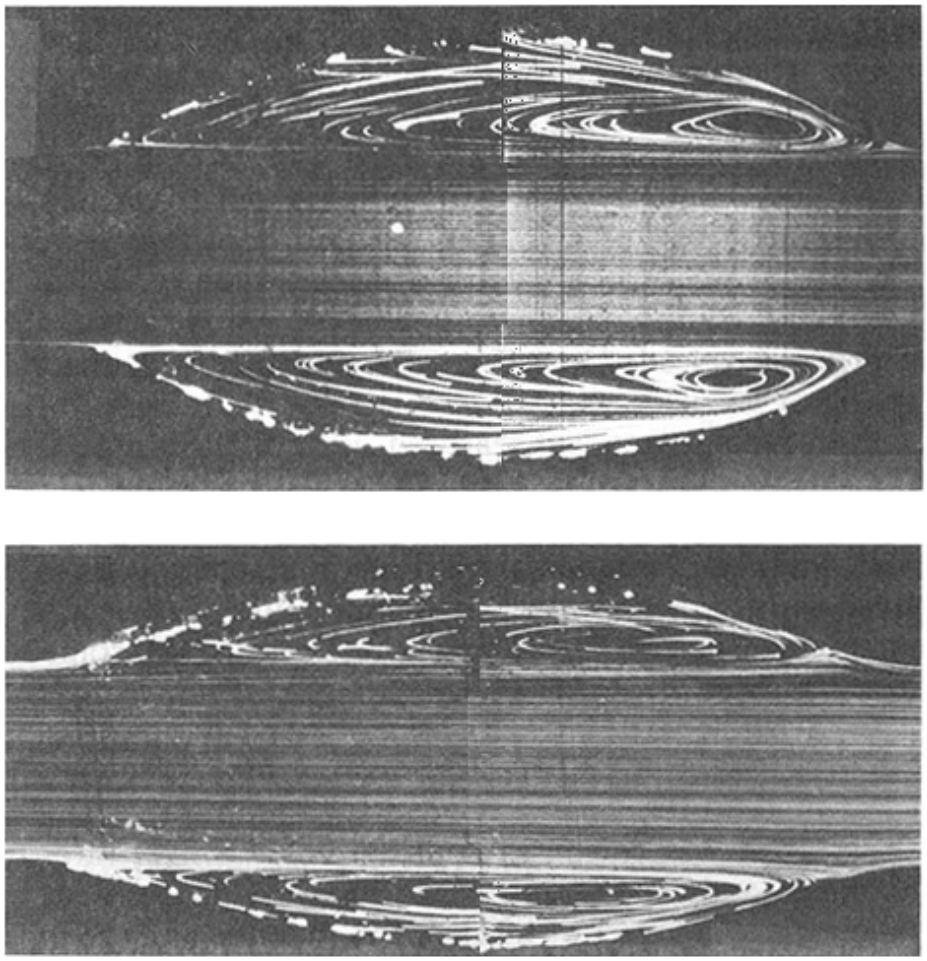

Figure 2.9 Axi-symmetric AAA particle tracing. Steady flow through axi-symmetrical dilation representing an aneurismal bulge at Re = 500 (top) and Re = 800 (bottom). Flow is from left to right. Illuminated particles captured by time lapse photography. Separated flow occurs in the dilation forming a ring vortex that is continuous around the circumference. (Budwig et al 1993. Images retouched)

2.3.7 *Turbulence*

When fluctuations in fluid flows are seemingly random, yet stochastic, they are turbulent. An example photograph of turbulence is shown in figure 2.10. Turbulence appears within all types of fluid flows including arterial blood flow. Turbulent flow contains eddies on many size and time scales. These eddies are formed, convect with the mean flow and dissipate. These eddies produce the fluctuating velocity and pressure associated with turbulence. Within a pipe flow situation, turbulence is generated within the core of the flow, and is dampened by the high shear nearest the walls. The turbulent eddies distribute momentum laterally, generating a more blunt velocity profile than seen in purely laminar flow. Figure 2.7 shows a comparison of laminar and turbulent flow profiles using sliding cylinders.

Laminar flow, by definition, is one that is not turbulent, and its velocity may be described in a single term with u_i. Turbulence, albeit random, is stochastic. Stochastic behavior is able to be quantified and described statistically. In this manner, turbulent flow is described as a sum of a time averaged component and a fluctuant component. Specifically, Reynolds decomposition (Pope, 2000) describes instantaneous velocity, u_i as the sum of time averaged velocity, $\overline{u}_i$, and fluctuating velocity component, u_i', as

$$u_i = \overline{u}_i + u_i' \tag{2.6}$$

Turbulence in pipe flow is loosely predicted to begin at Re = 2200 and be intermittent up to Re = 4000. Above Re = 4000 turbulence always present and below Re = 2200, the flow is laminar. These criterions are gross oversimplification, especially in references to flows within complex geometries such as those in this study.

Figure 2.10 Turbulence visualization using soap films. (Rutgers et al. 1996)

2.3.8 *Hemodynamic stressors*

Forces may act on the fluid in either in the normal direction (perpendicular) or in the tangential direction (figure 2.11). Normal forces are primarily due to pressure and to a lesser extent, shear contributions while tangential forces are entirely derived from shear contribution. The forces acting on the fluid at the wall boundary are transferred to the wall. In this manner, these hemodynamic stressors interact with the arterial walls.

A primary goal of this study is to describe these hemodynamic stressors acting on the arterial walls. Wall pressure is a scalar quantity that is relatively simple to measure and describe. Pressure is either measured directly from the flow or computed simultaneously with the velocity flow field. Wall shear stress is a vector, containing both a directional and a magnitude component. It is a more complicated to measure, which may be performed with strain gauges. Direct wall shear stress measurement was not feasible in this study, so the shear stress was evaluated from the velocity flow field. Wall shear stress is defined as the gradient of the velocity at and normal to the wall times the dynamic viscosity.

$$\tau_w = \mu \nabla u_t \cdot \hat{n}\big|_{wall} \tag{2.7}$$

To evaluate wall shear, three measurements are required. 1) The dynamic viscosity must be known. 2) The velocity near the wall must be determined in fine detail to accurately evaluate the gradient. 3) The normal direction of the wall must be found. The Casson properties of blood and its coagulation outside the body make the viscosity evaluation problematic, but the Newtonian assumption simplifies this portion of the calculation. Experimental and computational measurements determine the gradients used to determine the wall shear stress nearby. However, the normal direction was not able to defined systematically, so alternative calculations are used for the wall shear stress calculations which are explained in the methods.

Turbulence causes temporal variations in these stressors. Turbulent eddies cause fluctuant pressure and wall shear stress. Instantaneous wall shear stress and pressure can vary greatly from time averaged values. Asbury et al. (1995) reports instantaneous wall shear stress up to 20 × times the mean values due to fluctuations. These turbulence forces are believed to degrade arterial walls by subjecting to high vibrations (Johansson and Swedenborg 1986). However, all results are presented in time averaged terms. As a result, this study is unable to investigate the temporal variation in forces due to turbulence.

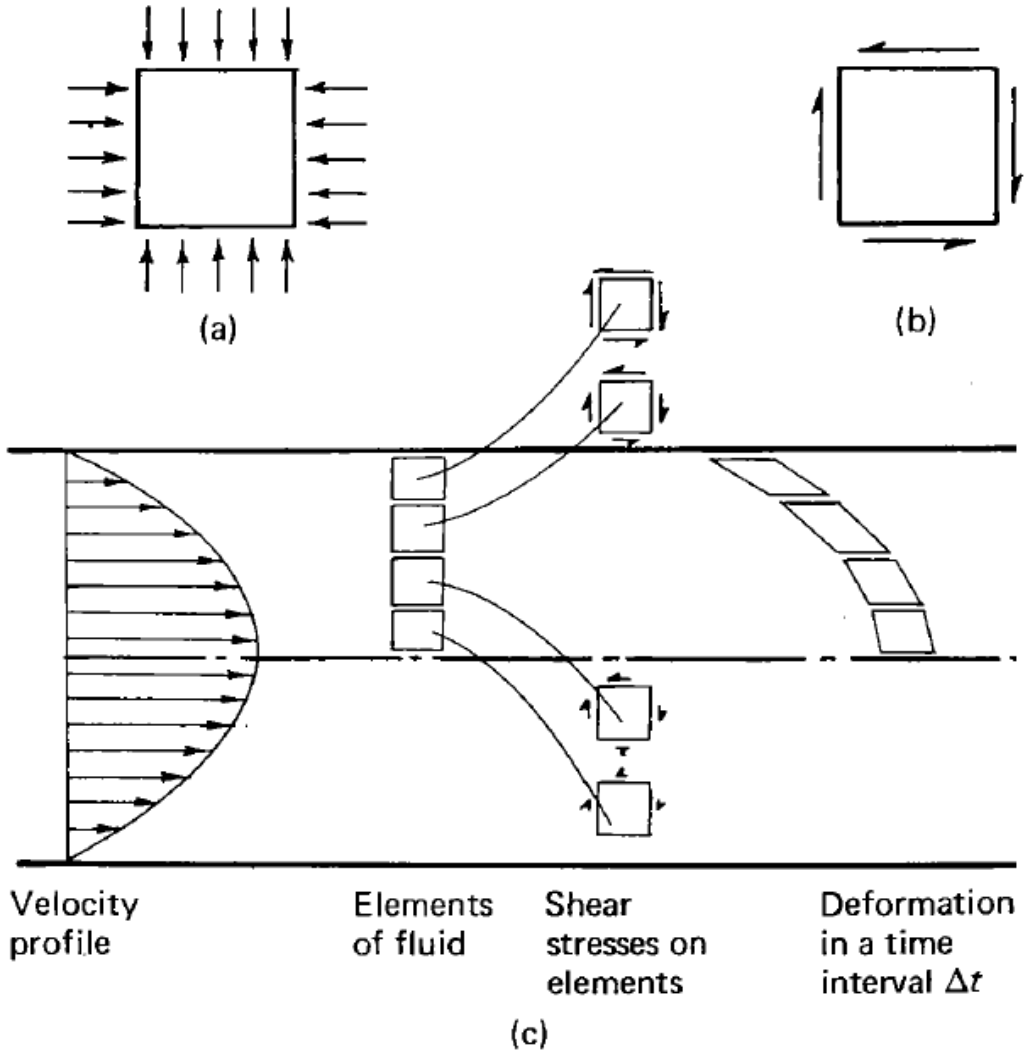

Figure 2.11 Forces acting on fluid. (a) Normal forces acting on a volumetric element. (b) Tangential forces acting on a volumetric element. (c) From left to right: laminar velocity profile within a pipe; volumetric elements within the flow; demonstration of the shear stress on each element; deformation of each element due to shear over a period of time. (Fung 1997)

2.4.1 *Particle tracing*

Fluid dynamics studies have used particle tracing methods to study the motion of flows. This has generally been accomplished using illuminated particles and time lapsed photography. An example of this is provided by Budwig et al. (1993) of steady flow through a symmetrical dilation (figure 2.9). This provides qualitative results demonstrating flow patterns, as well as aesthetically pleasing images. Quantitative details of the flow fields, velocities, turbulence, strain and shear, are not reliably generated from this method of analysis since specific particle displacement is measured.

2.4.2 *Particle image velocimetry*

Particle image velocimetry is a technique of measuring the LaGangian flow field by tracing the motion of suspended particles within the flow field between two separate visual measurements over a known period of time. This has been performed manually by interpolating the motion of particle between images by hand, though this is an extremely time intensive and subjective method. Modern methods have been introduced to digitalize and automate the process, made possible in part by the digital charged couple device (CCD) camera and modern computing.

In this study, silver coated glass beads are suspended in the fluid. These particles are illuminated by a Nd:YAG laser emitting bluish/green light (512 nm), which is optically refracted into a thin sheet to only illuminate a thin slice of the flow. Two rapid lasing pulses are emitted creating a stroboscopic effect by freezing the reflections from the suspended particles in sequential images by a CCD camera. Cross correlation techniques determine the mean motion within an array of interrogation areas, subdividing the images. By acquiring and correlating many image sets, both timed averaged velocity and velocity variance are described. This process is illustrated in figure 2.12 and explained in further detail elsewhere (Dantec 1998).

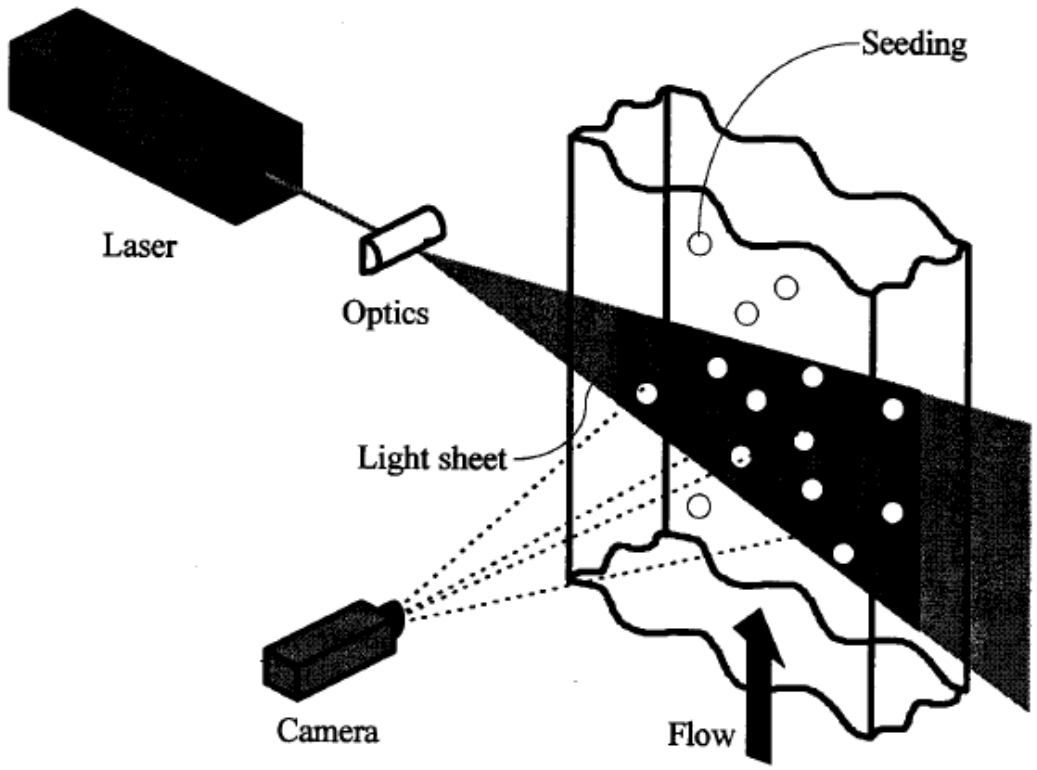

Figure 2.12 Particle image velocimetry (PIV) schematic. (Dantec 1998)

2.4.3 *Computational fluid dynamics*

Computational fluid dynamics (CFD) modeling is a technique that uses numerical methods to predict flow fields that may not be determined analytically. The flow properties are estimated by solving the conservation of mass and momentum equations (equations 2.1 and 2.2).

CFD techniques are becoming more widely used to study all types of fluid motion, augmenting or even replacing experimental studies. Due to the inability to take direct *in vivo* measurements, CFD is a useful tool for hemodynamic modeling. Its application spans from general modeling of the arterial system, to regionalized sectors of the arteries to localized specific application. Some of these include flow within aneurysms, stenosis, bifurcations and heart values.

It must be cautioned that the solutions provided by CFD are, with varying degrees of success, only predictions of the flow fields. To be complete, CFD analysis requires experimental validation. The accuracy of CFD analysis is subject to numerous factors, some of which include accurate modeling the fluid, proper description of boundary conditions, the effects of turbulence, and the generation of a appropriate computational grid.

CFD solutions are very sensitive to the computational grid generated from discretization of the flow field. These grids may either structured, with ordered and repetitive grid elements, or unstructured, which more fill the grid with less pattern. Patient-specific geometries necessitate an unstructured grid to accommodate the complex surfaces. These impose a significant increase in computational demand over structured grids. To test the performance of grids, flow structure and velocities are compared between grids of increasing cell density. When the flow remains the same upon further refinement, grid independency has been achieved. However, in complex situations, grid independency is often sacrificed for computational economy (Prakash and Ethier 2001).

2.4.4 *Turbulence Modeling*

The presence of turbulence also creates a great difficulty in computational study of fluid flow. A century of turbulence study has provided relatively little understanding to the properties of turbulence. The classic paper of Reynolds (1883) described 'sinuous motion,' now known as turbulence, and introduced the correlation that would become the Reynolds number (equation 2.4) to predict the onset of turbulence. Boussinesq (1877) introduced the concept of eddy viscosity, a mathematical approximation to estimate the additional shear generated by turbulence. Mathematical approximations have simplified modeling so that turbulence is modeled in conjunction with the mean flow field, known as Reynolds averaging. Predictions of turbulent flow fields began with simple algebraic models modeling turbulence. Further refinement has allowed for empirically defined one and two equation models, widely used tools academically and commercially.

Two equation models represent a significant improvement in turbulence modeling. They are described as complete since they are able to predict both turbulent kinetic energy and turbulent dissipation, while less sophisticated methods neglect the later. The first two equation model of turbulence, Kolmogorov's k-ω model (Kolmogorov, 1942), described two components of turbulence, k, and the specific turbulent dissipation rate, ω. The numerous Wilcox modifications to Kolmogorov's original model are considered the standard k-ω turbulence models.

The k-ε model is a similar two equation model that alternatively describes the turbulent dissipation, ε, though its immediate relationship to ω bears mentioning: $\varepsilon = k \times \omega$. The Jones and Launder

(1972) developed the standard k-ε model and it and its modifications remain the most widely used turbulent models to date (Pope 2000). Other two equation models and innumerous further refinements have been made, though none have proven to be superior over a wide range of application.

The k-ω models have shown particular utility in internal flows, with improved prediction compared to k-e models in comparison to experimental results. Arterial stenosis have been previously modeled by a few groups with k-ω techniques, and Khanafer et al. (2008) showed the first publication known to this author using k-ω methods in AAA study. The Wilcox (1993) modification is used for this study and the transport equations for k and ω and the closure parameters are stated in that reference.

Advanced modeling allows for time dependent, high detail modeling able to resolve turbulent eddies on their time and spatial scales. Direct numerical simulation is able to describe turbulent eddies on all size and time scales resolved by the grid and time steps. Large eddy simulation is a similar technique, but to save computational resources, predicts the behavior of smaller eddies to be isotropic while only resolving eddies at a larger scale. Both tend to provide improved solution quality relative to Reynolds averaged methods but are in limited application due to extraordinary computational demands.

2.5 PREVIOUS ENGINEERING STUDIES

In vivo analysis of AAA flow fields, wall stresses and turbulence remains difficult since the invasive measurements needed to quantify these parameters cannot be performed. Current techniques in ultrasound are able to partially determine velocities, though wall shear and pressure distributions cannot be directly measured. Turbulence, while having been qualitatively observed, has not been well quantitatively observed *in vivo*. For these reasons, *in vitro* experimentation or computational modeling is needed to characterize these flow fields.

To replicate the aneurismal flow *in vitro*, two different methods have commonly been to generate flow through models. The earlier experiments used glass tubes which have been specially blown with an axi-symmetric dilation, and in a few experiments, non axi-symmetric dilations. Flow-through models (phantoms) containing lumen representing aneurysms have been used for experimental study. These phantoms were generated by lost wax casting within optically transparent elastomer. While idealized geometries have been used here, rapid prototyping has allowed for the replication of detailed models, allowing phantoms to be constructed with patient-specific aneurysm geometries.

Experimental modeling of aneurismal flow has been performed by many groups. Numerous groups have studied steady flow in axi-symmetric dilations within straight tube models, with the common agreement of separated and retrograde flow forming a ring vortex which fills the aneurismal dilation. An

inverse pressure gradient is found in separated flow, with maximum pressure distal at the stagnation point and minimum pressure proximal at the separation point. The wall shear is shown to be greatly reduced and reversed in these areas, though with high shear in the distal end of the aneurysm. Under pulsatile conditions, studies have consistently shown retrograde flow being flushed out during systole, but to appear during diastole.

Dye injection (Stehbans, 1974) and illuminated particle tracing using time-lapsed exposed photographs (Fukushima et al. 1989, Budwig et al. 1993, Egelhoff et al. 1999, O'Rourke and McCullough 2008) were the visual methods used to study AAA flow. However, these but provided only qualitative assessment of the flow fields. In a somewhat unique pair of studies, color Doppler flow imaging was also used to investigate *in vitro* flow (Schrader et al. 1992, Peattie et al. 1994, Asbury et al. 1995, Peattie et al. 1996 part I).

More recent studies have used Laser Doppler Velocimetry (LDV; Asbury et al. 1995, Egelhoff et al. 1999, Peattie et al. 1996 part I and II, Peattie et al. 2004, O'Rourke and McCullough 2008). LDV principle is measuring the apparent change in wave length in reflected laser signals from a point within a flow field. This method is able to produce and instantaneous, accurate and non invasive localized velocity measurements. LDV is able to perform hundreds of measurements in a short period in a localized spot, making it ideal for turbulence evaluation and determining mean flow velocities. For this reason, LDV is considered the gold standard in fluid velocity measurements. LDV's main drawbacks are its inability to analyze more than one point simultaneously and failure to determine the directional component of velocity. Thus evaluating an entire flow field in two or three dimensions becomes a time consuming task.

Particle image velocimetry (PIV), is another velocity measurement technique to compliment LDV. It has been used increasingly in past years by many groups (Bluestein et al. 1996, Yu 2000, Yip and Yu 2001, Atkinson et al. 2001, Feller et al. 2001, Salsac et al. 2004). Unlike LDV, PIV is able to analyze large sections of flow fields rapidly. Like LDV, PIV may also be used serially to provide time averaged flow fields and turbulence determinations, though computational limits somewhat prevent high number of evaluations that LDV allows. PIV is prone high measurement error and noise relative to LDV.

Of the experimental studies using idealized geometries, several have observed turbulence in vitro (Bluestein et al. 1996, Budwig et al. 1993, Egelhoff et al. 1999, Fukushima et al. 1989, Peattie et al. 2004, Schrader et al. 1992, Yip and Yu 2001, O'Rourke and McCullough 2008). Several note the onset of intermittent turbulence within the AAA at Reynolds number, Re, below the expected onset criterion of around Re = 2200 in pipe flow. For example Asbury found intermittent turbulence occurring at starting Re = 1750 in steady flow while Egelhoff found turbulence present in pulsatile conditions emulating exercise. Egelhoff suggested that AAA encourage turbulence by breakdown of the vortex structure.

Experimental study of AAA flow within patient-specific models has been performed by only one group outside of the Peattie lab known to the authors at this time, O'Rourke and McCullough (2008). Using LDV and particle visualization, complex flow patterns were seen within the patient-specific geometries with little resemblance to axi-symmetric ideal models. Notably, turbulence intensity of up to 0.70 was observed on the centerlines, and turbulence intensity of over 1.0 was seen elsewhere. Within the Peattie lab, Atkinson et al. (2001) showed highly rotational flow fields exist within the AAA bulge, but developed and uni-directional flow occurs distal of the bulge contraction. Feller et al. (2001) showed highly instable flow fields within the AAA bulge at Re = 1200.

Computational methods in AAA study have become widely used in AAA study. Two major branches of AAA study have evolved in the past 15 years: the study of dynamic flow fields and the wall strain and deformation studies which use changing cardiac pressures but with quiescent flow fields. This study and literature review is focused on the former, though the later is an emerging and vital contribution to the field of AAA study, most notably with the Vorp Lab (Rhaghavan et al. 2000, Wang et al. 2002, Di Martino et al. 2003). Some more recent studies have coupled the two in the Fluid Structure Interaction (FSI) technique, which is performed by evaluating dynamic flow fields with deformable walls (Di Martino et al. 2003, Wolters et al. 2005, Scotti et al. 2007, Khanafer et al. 2007)

The earliest studies use 2-D finite element analysis to study idealized aneurysm approximations (Wille 1981, Perktold et al. 1984, Fukushima et al. 1989, Budwig et al. 1993, Bluestein et al. 1996). All studies are in general agreement of the presence and location flow separation and vortex formation within the dilations of the AAA. Further, a general agreement between the computational results and experimental results was seen for the simple geometries (Fukushima et al. 1989, Budwig et al. 1993, Bluestein et al. 1996). Bluestein utilized the k-ε turbulence model, the first AAA study incorporating turbulence computationally.

Three dimensional modeling was first performed in AAA study by Taylor and Yamaguchi (1994) showed different vortex structure in asymmetric geometries and what was observed previously. Further studies by many authors (Viswanath et al. 1997, Yu et al. 1999, Breeuwer et al. 2004, Scotti et al. 2007) have further considered 3-D axi-symmetric and asymmetric geometries. Patient-specific modeling has recently been incorporated into an increasing number of computational studies (Di Martino et al. 2001, Finol and Amon 2003, Wolters et al. 2005, Genevès et al. 2005, Leung et al. 2006). Significantly different flow patterns and stress distributions were seen as a result of these geometries. While Wolters showed similar magnitude of wall shear stress within these models, Finol and Amon showed peak values at up to 64 × those seen in idealized models.

CHAPTER 3: METHODS

3.1 PATIENT SPECIFIC AAA MODEL GENERATION

All procedures were carried out with full approval from the Institutional Review Boards of Hartford Hospital, Oregon State University and Tufts University. Abdominal aortic aneurysm models were derived from CT image series from the presenting population of Hartford Hospital (Hartford, CT). Abdominal scans were obtained from 50 patients using a spiral CT imaging system (model 9800 High Speed Scanner, General Electric Healthcare Inc.). Nominal slice thickness for these scans was 0.6 mm, with a helical pitch of 1.5:1. Images were obtained from one end of the abdomen to the other during a single sustained breath hold by the patients to minimize respiratory-induced artifacts, after intravenous administration of standard nonionic contrast enhancement agent. All AAA imaging contained non-dilated aorta proximal to the bulge, while those from lesions not crossing the femoral bifurcation contained non-dilated aorta distal to the bulge as well.

Prior to model construction, the CT series were truncated proximally at the plane of the T11 or T12 vertebra and distally at the coccyx. The resulting image series provided an entrance length of three to five aorta diameters proximal to the bulge, depending on the AAA location and aorta curvature. The iliac bifurcation and short sections of the common iliac arteries were also included in each model, though other arteries branching from the aorta were not. After truncation, the aortic lumen, wall and any mural thrombus present were identified in each image and individually masked. Commercial software (*MIMICS* v9.0, Materialise; Leuven, Belgium) was then used to create separate 3-dimensional models of the AAA clear lumen and thrombus (figure 3.1). Ten of these assembled lumens are depicted in figure 3.2. This process is described in further detail by Aslani (2005).

Table 3.1 presents the major geometric properties of the three representative models focused on in the results (Aslani 2005). These characteristics include the non-dilated aortic diameter immediately proximal to the bulge, d_a, maximum bulge diameter, d_{AAA}, maximum lumen diameter, d_l, (which differ due to the presence of thrombus), bulge length, L_{AAA}, and the volumes of the lumen, thrombus and bulge, V_l, V_t and V_{AAA} (where $V_{AAA} = V_l + V_t$), curvature, κ, and tortuosity, T. To calculate the bulge length, its upper boundary was taken as the most proximal level at which the lumen diameter exceeded, and remained greater than, 1.2 × its value in the non-dilated entrance tube. Similarly its lower boundary was defined as the distal level at which it became less than 1.2 × its non-dilated value.

Model	Phantom	d_a (cm)	d_{AAA} (cm)	d_l (cm)	L_l (cm)	V_l (cm)	V_t (cm)	V_{AAA} (cm)	κ (cm^{-1})	T
1	4	2.32	5.50	5.50	6.70	135.1	0	135.1	0.453	1.38
7	3	2.77	4.56	3.01	5.52	34.8	69.9	104.7	0.504	1.33
8	1	2.25	3.90	3.70	6.10	73.8	14.1	87.9	0.218	1.06

Table 3.1 Model geometric parameters.

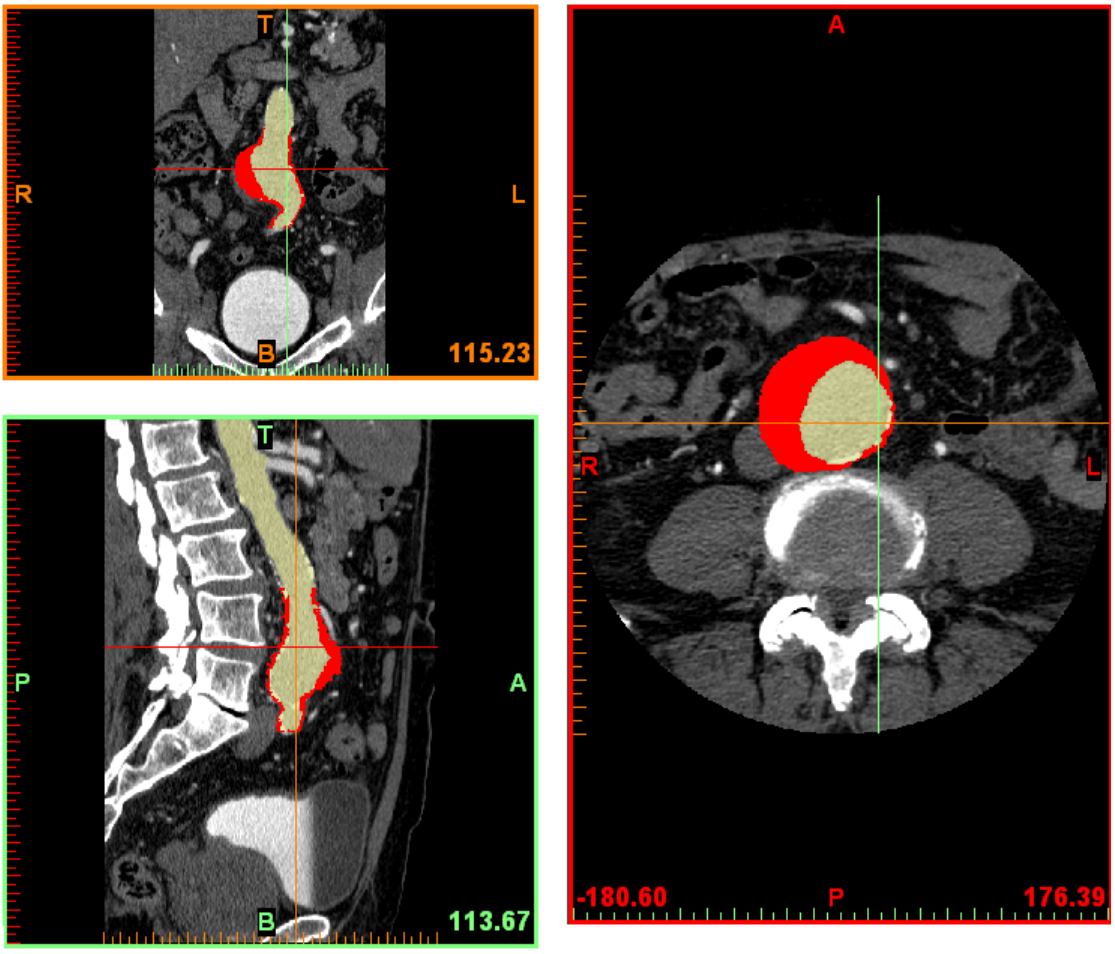

Figure 3.1 CT imaging from patient with AAA. Aortic lumen (tan mask) and thrombus (red mask) from coronal (top left), transverse (right), and sagittal (bottom left) slices. (Aslani 2005)

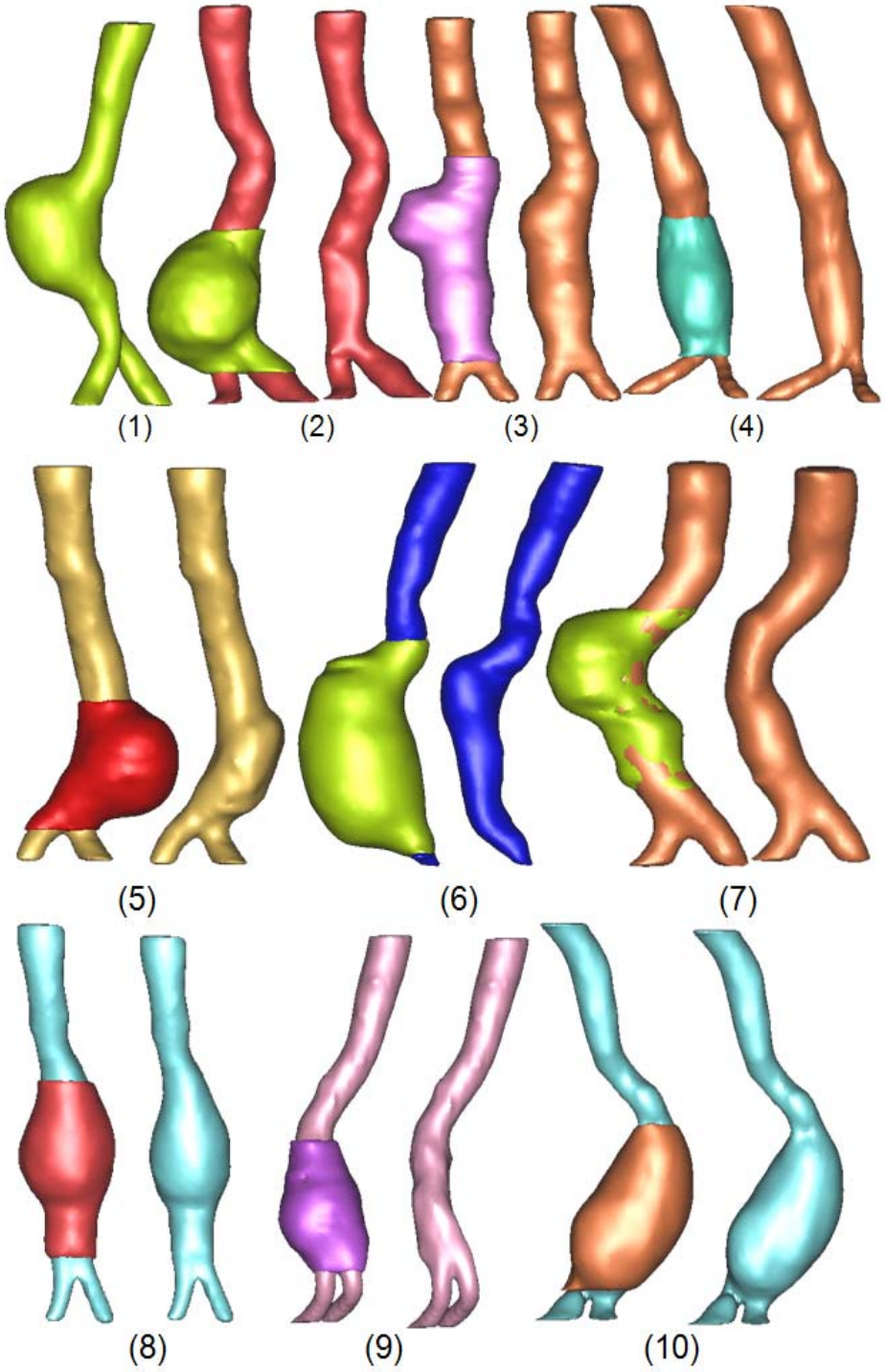

Figure 3.2 AAA models. 3-D representation of the lumen and thrombus of ten aortas containing AAA generated from patient CT scans. Images on left include thrombus, while images on right show the lumen only. The aorta of patient number 1 contains no thrombus, so only a lumen image is shown.

3.2 PHANTOM CONSTRUCTION

3.2.1 *Casting techniques*

The method for the construction of the flow through phantoms is based on previous work within the lab using lost wax casting techniques (Atkinson et al. 2001, Feller et al. 2001, Aslani 2005). The lumens of the patient specific AAA models were exported into .STL files, and a prototype model was produced via stereo lithography (AARK Industries). The models were scaled so that the mean diameter of the inlet was 2.54 cm (1”), matching flow loop. The prototype models were truncated proximal to the iliac bifurcation and to their entrance and exit sections, a 1” diameter solid resin cylinder was adhered with quick setting epoxy. The junctions were filleted to produce smooth transitions.

To produce wax replicas, an investment cast of the prototype model was made. To facilitate this, a open top casting jig was made from a plastic container with the internal dimensions of 40 cm × 10 cm × 10 cm. Holes 2.54 cm (1") in diameter were drilled at the axial ends to suspend the prototype model. The walls of the casting jig and the entire surface of the prototype model were coated with a thin layer of mold release compound formulated by petroleum jelly dissolved in hexane and the model.

Room temperature vulcanizing (RTV) silicone rubber encapsulant (Dow Corning, RTV 3110) was poured into the jig, up to the midpoint of the prototype model and resin cylinders creating the bottom half of the investment cast. This was incubated at 50 °C to cure while the unused portion of the RTV silicone was refrigerated at 4 °C to prevent curing. The exposed top face of the cured bottom half with mold release and the RTV silicone was poured into the casting jig so to cover the prototype, creating the top half of the investment cast. After the top cured, the investment cast was removed from the jig, split, and the prototype removed.

The voided investment cast was compressed and an axial end was sealed with clay. Water soluble jewelers wax (Contenti Co.) was gently warmed in a covered beaker partially submerged in a water bath. The wax was slowly poured into the open end of the investment cast in multiple stages to prevent bubble formation. After the wax solidified, the investment cast was opened and the wax replica removed. The wax replica was trimmed to 14” in length with the AAA lesion centered. Segments of 2.54 cm ID, 3.33 cm (1” ID, 1 5/16” OD) tubing were placed on the replica ends to create shoulder in the phantoms to mate with the flow loop.

A five piece, open top rectangular jig with internal dimensions of 35.5 cm × 10 cm × 10 cm (14” × 4” × 4”) was constructed from 1.27 cm (½”) thick acrylic sheets to cast the phantoms. Recessed tabs in the axial ends supported the tubing covered ends of the wax replica. The surfaces of the jig and the wax replica were coated with mold release.

An optically translucent, polydimethylsiloxane (PDMS) elastomer (Dow Corning, Sylgard 184) was mixed from the two part solution and degassed in a 10 mmHg vacuum for 20 minutes. The PDMS elastomer was poured to cover the wax replica and incubated at 50 °C to cure. The unused portion could be refrigerated at -17 °C for future use. After curing, the phantom was removed from the jig and placed in an aqueous solution of 10 g/L acetic acid solution to dissolve the wax. After the wax was removed and the phantom cleaned, the phantom was wrapped with Saran Wrap to prevent surface damage prior to use. An example of this process and the final product are shown in figures 3.3 and 3.4.

3.2.2 *Modified casting method*

The first attempts at creating phantoms were stymied by bubble formation during curing at the wax and PDMS elastomer interface. To circumvent this problem, the PDMS elastomer was cast in a two parts, using the prototype model to form the lumen. After both halves were cured, the prototype was removed and a wax replica inserted to the lumen. A thin coating of elastomer was placed on one of the bottom face, and the halves were joined. The wax replica prevented internal runoff. The phantom was placed into the jig to cure.

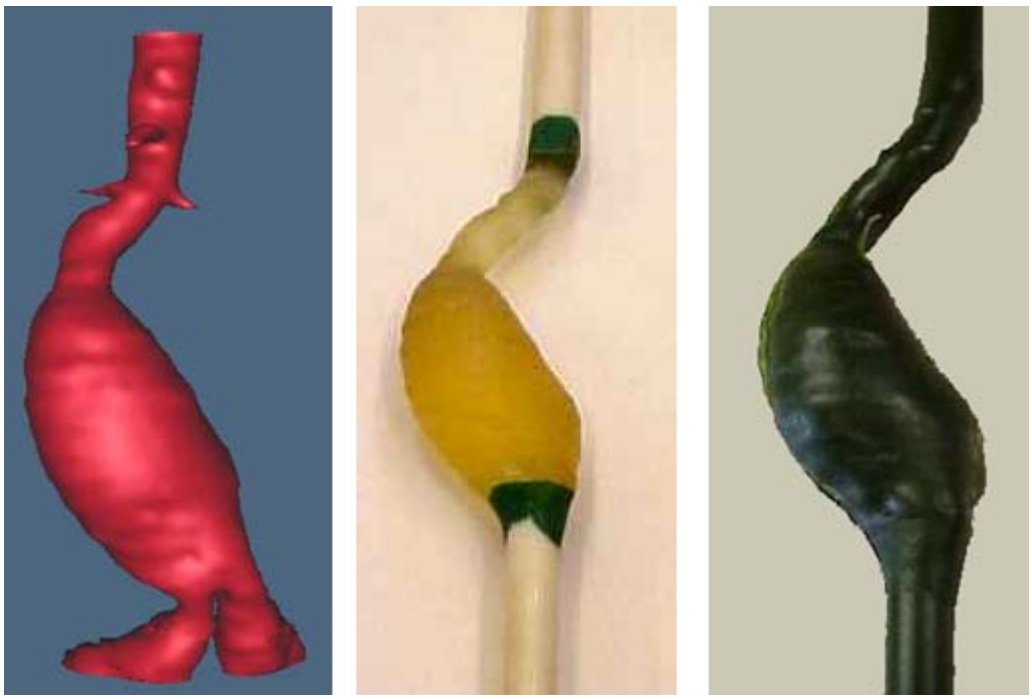

Figure 3.3 Replica development. Left: lumen geometry generated from patient CT images (phantom 5). Center: prototype with resin cylinders installed proximal and distal to the lesion. Right: wax replica.

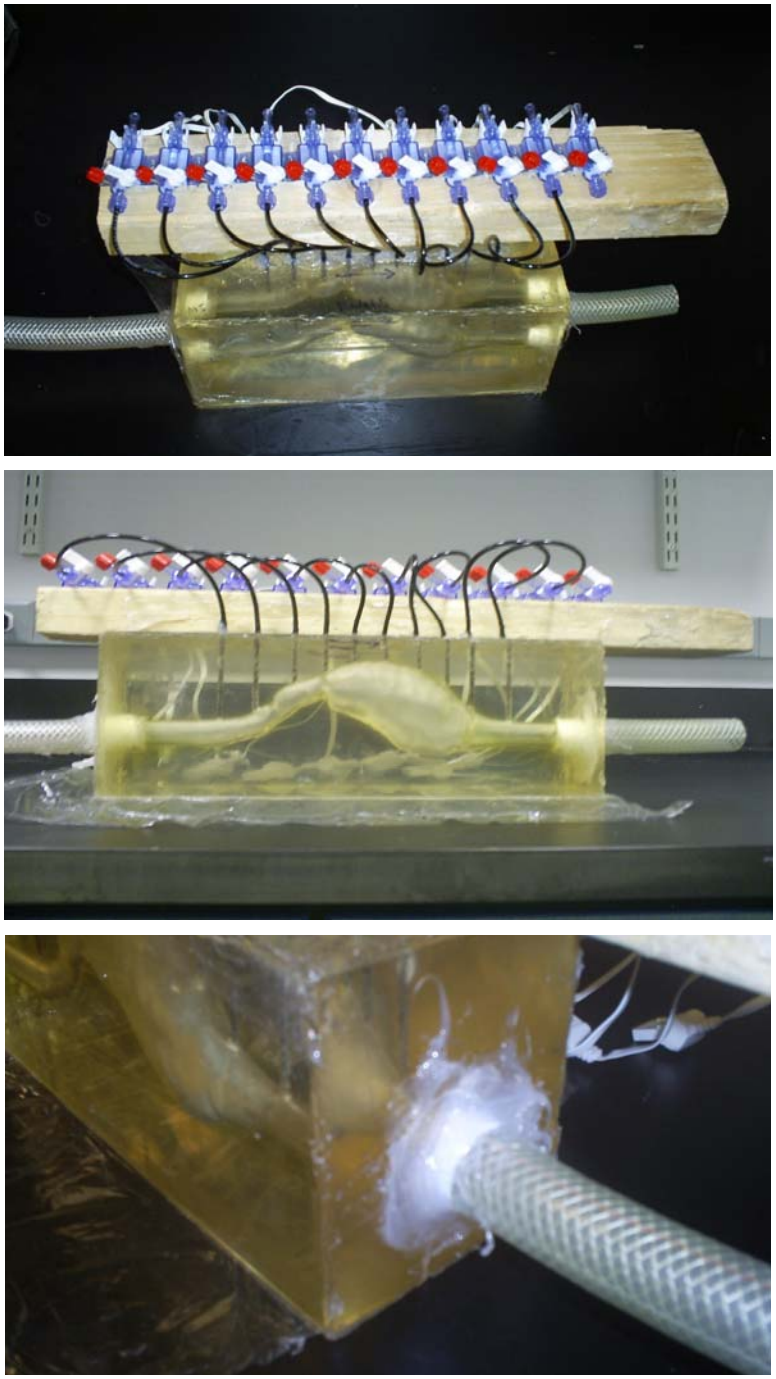

Figure 3.4 Phantom 5 from three angles. Top and center images show the pressure points installed into the pressure transducers. Bottom shows the caulking at the tubing and elastomer block interface.

3.2.3 *Straight tube model*

In addition to the AAA models, a straight tube phantom was constructed. An investment cast fabricated using a 2.54 cm (1") resin cylinder and a wax replica was made. During elastomer casing, bubbles formed along the lumen wall, destroying the optical clarity of the majority of the phantom. A section on the bottom side of the lumen was identified as optically acceptable for preliminary PIV study.

3.2.4 *Pressure points and air release pathways*

To allow for pressure measurement in the flow through model, a portal from the model's lumen to a pressure transducer was required, these being known as pressure points. A series of 8-11 spaced locations were identified along the centerline of the lumen and marked on the external face of elastomer. Using a drill press and a 1/8" bit, holes were cut through the elastomer to the lumen. Flexible, 1/8" polyurethane tubing (AIR Industries) was inserted into these holes with excess tubing to later be connected to pressure transducers. The junction of the tubing and elastomer was caulked (DAP, Aquarium Sealant). For phantoms 1-3, two series of 9-11 pressure points were made, one on a lateral wall and one on either the anterior or posterior wall. For phantom 4 and 5, only one series of pressure points was made.

Entrained air must be removed from the lumen. While most air could be purged with alternating high/low flow cycles in the flow loop and some jostling of the phantom, this method was not always sufficient. Air may be bled through the pressure points, useful during pressure measurement. However, these pressure points were not available during PIV analysis.

An alternative method was devised to create a small, controlled puncture through the elastomer to the lumen of the model through which entrained air in the lumen may be bled (figure 3.5). A diagonal pathway out of the view of optics was punctured using the back end of a 1/16" drill bit. At the external surface, a countersink hole was with a 3/32" and a 1/8" polyurethane tubing was inserted and caulked. The pressure transducers were used to regulate the air bleeding. These punctures became optically invisible when the void spaces filled with working fluid. Additionally, these punctures were less invasive to the phantom than the pressure taps since they did not remove any elastomer.

When the pressure points were not used, the tubing was disconnected from the transducers and clamped. Alternatively, the polyurethane tubing could be removed and the holes into the phantom were filled with silicone sealant. Although this process could not restore the optical clarity for imaging, it was satisfactory for laser light illumination. This process was performed on the posterior wall of phantom 3.

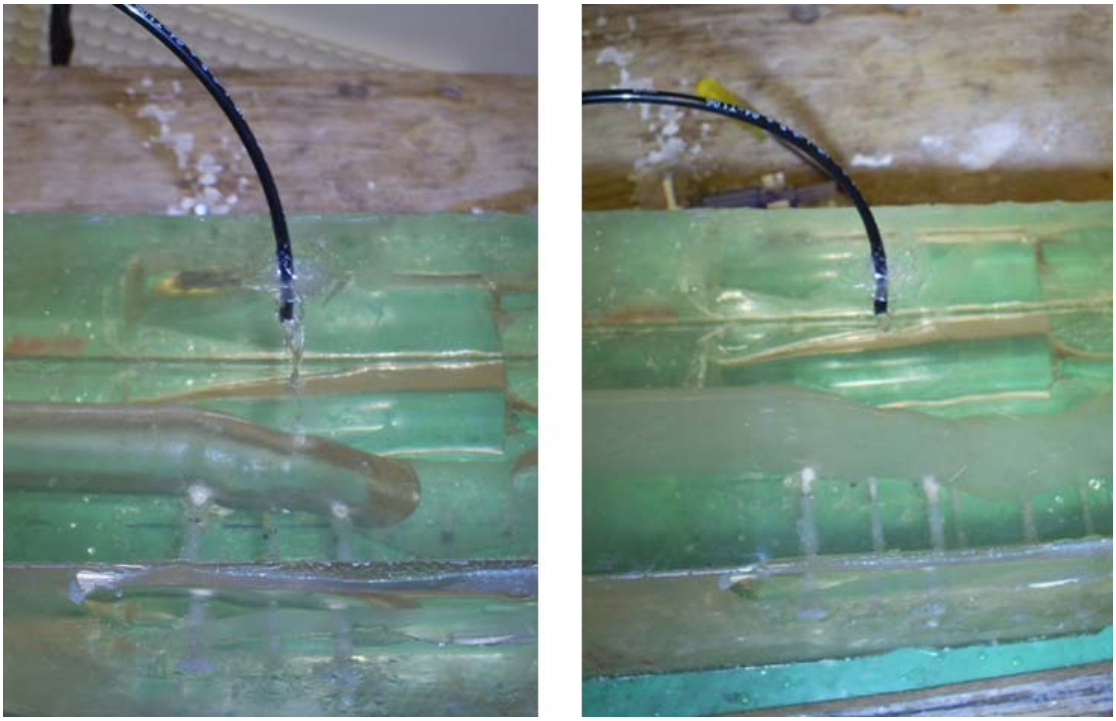

Figure 3.5 Puncture air release. Puncture air release in the elastomer block of phantom 3. Left image: air is in the model and pathway. Right image: the air has been bleed and the working fluid has entered the pathway. The puncture becomes optically invisible when the working fluid fills the void space of the punctures. Additionally on the perpendicular face at the bottom of the image, pressure points which were sealed with silicone may be seen.

3.3 FLOW LOOP

3.3.1 *Setup and operation*

A gravity driven flow loop was constructed from vinyl tubing to deliver steady, fully developed flow to the phantom. A schematic of this loop with is provided in figure 3.6. The flow loop was supported by a frame constructed of steel channels. A working surface was constructed from three 4' × 2' × 3/4" plywood sheets and bolted to the frame. The surface was leveled by adjusting the 14 feet supporting of the frame.

Fluid was stored in a floor level reservoir constructed from a 20 L carboy. Fluid was pumped from the floor reservoir by a geared pump (Ismatec SA, 7617-70) to an elevated constant head tank. The constant head tank, allows for continuous overflow, effectively generating a water column of constant height and pressure in the test section. Overflow was collected in a surrounding container and returned to the floor level reservoir.

The test section of the flow loop was constructed from 2.54 cm (1") braided vinyl tubing. The test section started with a 3 meter decent, prior to leveling into a horizontal, entrance section proximal to the phantom. A second tube was distal of the phantom, forming the exit section. Fluid was then returned to the floor reservoir. The flow loop tubing was inserted into shoulders of the phantom so that the lumen was continuous. The tubes were wrapped in electrical tape to create a watertight seal. For additional sealing and structural support, the junction was generously caulked (DAP Chemicals, Aquarium Sealant).

To create fully developed pipe flow proximal and distant to the flow through model, the entrance and exit sections must be long, straight and level. To accomplish this, the tubing was tightly encased with 1.5 meter rigid PVC pipe to ensure an elongated and straight path. These sections were supported and leveled by a series of wooden platforms suspended between the tangs of 'U' shaped threaded steel bars.

The flow rate through the test section was regulated by an electromagnetic valve (.375" orifice, 24 V; Teknocraft Inc.) distal of the exit section. The valve was controlled by a variable DC power supply (GW, GPR-6030D). Manual valves were placed proximal to the entrance section and distal to the exit section. The flow rate through the test section was measured with a non-invasive ultrasonic flow meter (Transonic Systems Inc., T109) distal of the exit section. When water was used as the working fluid, the flow meter was calibrated using a timed collection method. When the sodium iodide/sodium chloride solution was used as the working fluid, the volumetric flux was estimated using PIV analysis.

A static line for head measurements originated from a 'T' junction in the downward tube proximal to the entrance section. A self adhesive measuring tape was placed adjacent to the static line channel for measuring the water column height relative to the working surface. A reservoir was placed atop this static

line to provide extra fluid capacitance for stability during pressure measurements. A manual valve on this line was opened only during pressure tests.

An inline filter was placed upstream of the pump. However, when using the ionic working fluid at high flow rates, air was introduced to the fluid forming tiny bubbles in the low pressure section upstream of the pump, presumably at the filter, causing the working fluid to turn opaque. This filter was bypassed when working with the ionic solution during PIV operation, which prevented bubble formation.

When the flow loop was not in use for a short period, the working fluid remained in the flow loop. The downstream manual valve was shut and the power supply and flow meter were turned off. For longer term shut down, the flow loop was drained. When using the sodium iodide/sodium chloride solution, the flow loop was more prone to micro leaks, and was drained when ever not in use to prevent fluid loss and mess. The flow loop was also rinsed multiple times with clean water after tests using the sodium iodide/sodium chloride were finished to dilute and remove the ionic solution from the flow loop.

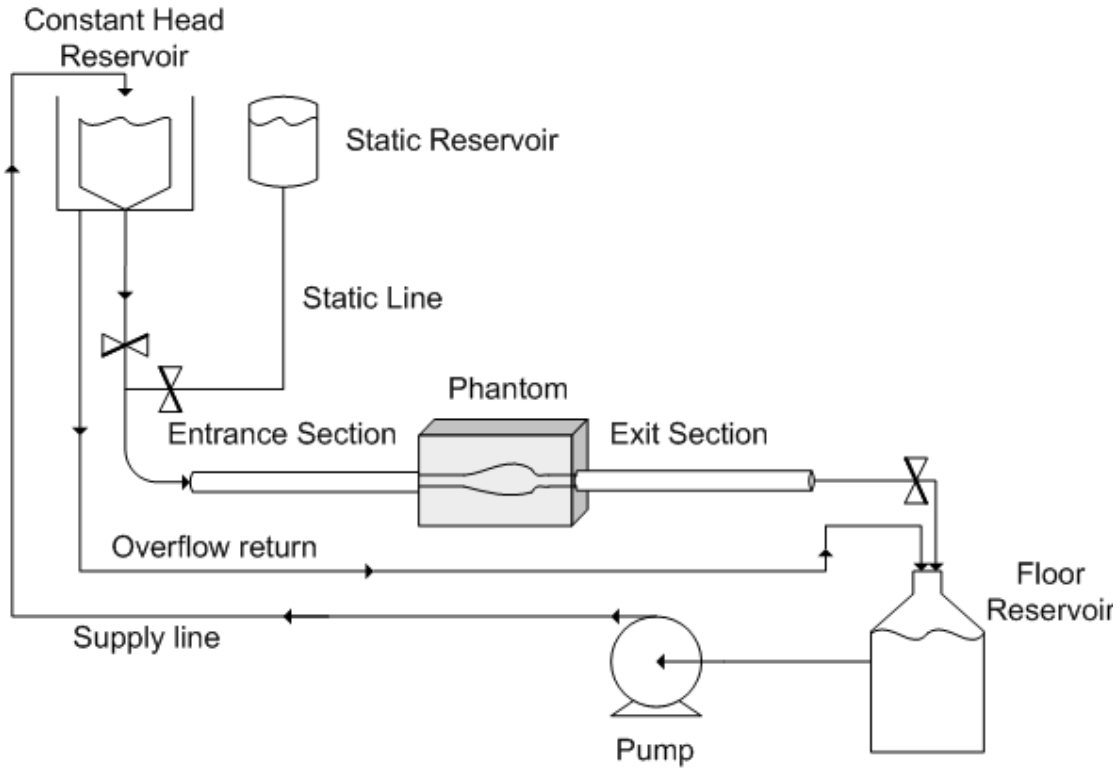

Figure 3.6 Flow loop schematic.

3.3.2 *Entrance Length*

According to Dombrowski *et al*. (1993), the entrance length, L_{ent}, required for a laminar flow to achieve a 99% developed profile from an initially uniform profile may be predicted by

$$L_{ent}/d = 0.370\exp(-0.148\,\mathrm{Re}) + 0.055\,\mathrm{Re} + 0.260 \tag{2.1}$$

For a turbulent flow to achieve a 99% developed profile from an initially uniform profile, the entrance length is predicted to be about

$$L_{ent}/d = 40. \tag{2.2}$$

For our 2.54 cm diameter entrance sections, the entrance length at Re = 500 is predicted to be 70.5 cm using equation (top), and our 150 cm entrance section is well in excess of this length. At Re = 3000, the entrance length is predicted to be 401 cm using equation (top) and 101 cm using equation (bottom). Since the flow is intermittently turbulent, is can be assumed that the length with be in between these values. Given that flow proximal to the entrance section is somewhat developed, the length requirement would be reduced. It is reasonably safe to say that flow will be well developed, or nearly so at both Re = 500 and Re = 3000 prior to the phantom entrance.

3.4 IONIC WORKING FLUID FOR PIV

In order to eliminate visually distorting refraction, the refractive index, *RI* of the working fluid must match that of the elastomer of the flow through model. The *RI* of the PDMS elastomer is near 1.41. Though some organic fluids match or closely match this *RI*, none were considered acceptable for use as a working fluid do to their intrinsic properties. Alternatively, aqueous mixtures may be used to raise the *RI* above that of water (*RI* = 1.33).

In previous experiments in Peattie's group used a the working fluid comprised of glycerol and aqueous sodium thiocyanate (NaSCN) for PIV and LDV analysis (Atkinson et al. 2001, Feller et al. 2001, Peattie et al. 2004, Peattie et al. 1996 part I and II, Asbury et al. 1995). However, the sensitivity of viscosity to temperature of glycerol prevented working fluid highly concentrated in glycerol from being practical in an environment without precise temperature control. Further, the corrosiveness, safety concerns and general difficulty of use of aqueous sodium thiocyanate made this previously used recipe unattractive.

Based on the use of aqueous sodium iodide used by Budwig et al. (1994) and Narrow et al. (1992), aqueous sodium iodide (NaI) was considered as the working fluid. The sodium iodide aqueous solution

had more acceptable viscous behavior then that of glycerol and handling and safety characteristics were better than aqueous sodium thiocyanate. Narrow further recommended the addition of sodium thiosulfate ($Na_2S_2O_3$) to inhibit the formation of the triiodide ion, which causes the characteristic iodine discoloration. Sodium iodide's cost, however, made it somewhat imposing for use. Sodium chloride (NaCl), was considered as a cost saving dilutent, added to its solubility point. The solubility of sodium chloride in water is 359 g/L, which was reduced with further addition of sodium iodide to the solution. A 42 wt % sodium iodide (724 g NaI : 1000 g water) solution was required to achieve a *RI* of 1.41 (Narrow et al. 1993), matching that of the elastomer.

The proper recipe for the working fluid was determined experimentally using a visual test. A scarp piece of PDMS elastomer was submerged in the aqueous mixture, and the optical distortion was observed. When the *RI* of the aqueous solution matched that of the elastomer, the optical distortion through of the swatch was be eliminated. The recipe was found to be 1 L water : 517 g NaI : 150 g NaCl (31.0 wt% NaI, 9.0 wt% NaCl), conservatively below the precipitation point of sodium chloride.

To prepare a large enough volume for the flow loop, a stock solution of 150 g/L sodium chloride (Diamond Crystal Kosher Table Salt) and 1.5 g/L sodium thiosulfate (Arcos) was prepared with tap water in a 20 L carboy and stirred until all salts had dissolved. In another 20 L carboy, sodium iodide (VWR) and 10 L of the stock solution were mixed until the solution matched the *RI* of scrap PDMS elastomer, producing approximately 15 L of solution.

The flow loop was primed and purged with a separate 200 g/L NaCl. The carboy containing the ionic working solution was then inserted to the flow loop, in place of the floor reservoir. While running continuously through the flow loop to mix the solution, the composition of the working fluid was altered by the addition of sodium iodide until the optical distortion was eliminated. The final adjustments of the concentration of the working fluid were performed using a He:Ne laser pointed through the top of the cylindrical model inlet of the lumen in the flow through model as described by Asbury et al. (1995). When the *RIs* of the fluid and elastomer do not match, the laser light would diverge into two separate points visible on the back wall. Sodium iodide or water was added until the laser points converged, indicating the *RIs* matched.

The viscosity of the working fluid was determined using a calibrated glass capillary kinematic viscometer (Technical Glass Products Inc., Size 50) submerged in a water bath. The results over a small temperature window are presented in figure 3.7. The temperature for of the lab was reasonably constant at 24 °C (+/- 1 °C) and the working fluid was believed to be the same temperature. Thus, 24 °C was assumed as constant for all tests and the kinematic viscosity of the working fluid at this temperature was found to be .01107 cm/s. The density of the working fluid was found to be 1.411 g/mL at 24 °C and constant within the temperature window. The dynamic viscosity was found to be .01562 dyne s cm^{-2}.

Sliver coated glass beads with a mean diameter of 13 um (Potters Industries Inc.) were suspended in a small solution of working fluid, and injected into the floor reservoir. Due to bead settling, continuous replenishment was required to keep a proper suspension for quality imaging. Steady addition of beads in small quantities during experimentation yielded better results than a single large dose. Due to the settling of the beads on the surface of the phantom, optical quality would decrease, resulting in marginal images. To suspend some of the settled beads, the flow loop was run at maximum flow rate. Deeper cleaning of the phantoms required removal from the flow loop and spraying the lumen with pressurized tap water.

After extended periods in the flow loop, the working fluid became cloudy and slightly opaque. To restore optical clarity, the working fluid was cleaned using a disposable 1L, vacuum filter system with a .45 um cellulose acetate filter (Corning Inc., 430516). The filter was rinsed and reused for the entire volume of the working fluid. The working fluid was reseeded with silver coated glass beads after filtration.

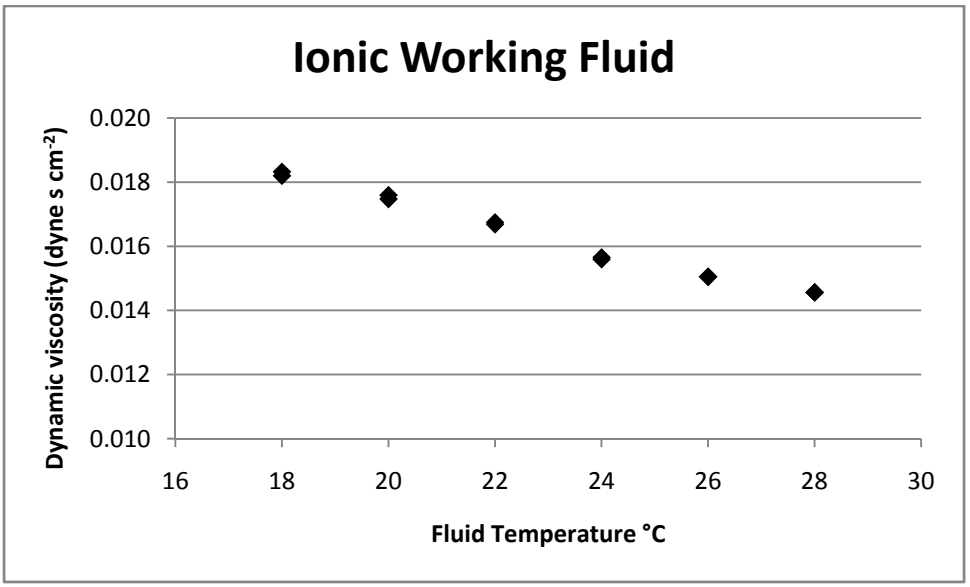

Figure 3.7 Dynamic viscosity for the ionic working fluid. Approximate concentration: 31 wt% NaI, 9 wt% NaCl, and 60 wt% water.

3.5 PIV METHODS

3.5.1 *Illumination*

Illumination for the flow field was provided by paired Nd:YAG laser (New Wave Optics, Solo I). Duel lasing units were able to prudence two rapid, high intensity bursts as required by PIV. The Nd:YAG laser generates photons at the 1064 nm wavelength but a harmonic generator combines the 1064 nm photons, producing in 532 nm bluish/green light. The lasing energy was generated by a flash lamp and released using a Q-switch, permitting 15 mJ emissions with 4 ns duration. A second burst follows from the second laser, at a timed interval, δt.

3.5.2 *Image Capture*

A digital charged coupled device (CCD) camera (Kodak Megaplus ES 1.0) capable of recording images with 1008 H x 1016 V resolution and 8 bit grayscale detail was used for image capture. The camera uses an electronic shutter with flash memory to allow for collecting two images (A and B) rapidly. The δt was adjust for each flow rate, so that the particle displacement between images was roughly the same between the different flow rates (δt = 32500 μs for Re = 125, δt = 8000 μs for Re = 500; δt = 1500 μs for Re = 3000). As opposed to conventional camera technique, the timing of the exposure is dictated by the laser pulse, not the camera shutter. The duration of the lasing pulse was short enough so that no particle motion during the individual exposures was detected.

A 60 mm macro lens (Nikon Inc., AF Micro Nikkor) was attached to the camera, and the relative aperture set at f/8. Manual focusing of the lens was required whenever the laser sheet height was adjusted.

3.5.3 *PIV Hardware and Software Control*

The PIV system is run by a proprietary processor (Dantec, FlowMap 2100). The processor controls the timing of the camera and the laser flashlamps and Q-switches. The processor is connected to a PC via peer to peer Ethernet connection and operated by proprietary software (Dantec, FlowManager 3.40) on the PC.

3.5.4 *Camera and laser setup*

The camera was mounted on an aluminum tubing frame approximately 30 cm above the vertical midpoint of the flow through model (figure 3.8). The frame allowed the camera horizontal and axial motion to capture separate portions of the flow field. To provide a structured grid for the camera measurements, tick marks in 30 mm increments were marked along the axial direction of the aluminum tubing, and up to eight separate zones were studied in the axial direction. Horizontal marks were also used when a horizontal shift was needed to capture the entire flow field.

The laser was mounted to a gutted milling machine, which provides very precise and steady vertical adjustment of the laser light sheet. The emitted laser light plane was aligned so that it measured the same height on tape strips placed on the aluminum tubes closest to the laser, ensuring that it was parallel to the working surface. This vertical height of the laser light plane was measured on this scale. Using the sliding camera and vertical adjustment of the laser, the entire flow field was able to be captured for PIV analysis.

The field of view was measured at the vertical midpoint of phantom 4 was 4.90, which was used for the whole study. The resulting object of the camera images was 45.0 mm H x 45.4 mm V. Using 30 mm imaging grid resulted in 15 mm of over lap from neighboring images.

During image collection, the overhead fluorescent lighting was turned off and windows were covered to eliminate reflective glare and background light that would otherwise be captured during the long exposure (B) images. Two computer monitors and a 40 watt incandescent bulb from a desk lamp generated ambient light, though these light sources were shown to have no effect to the images.

3.5.5 *Experimental conditions*

With the phantoms installed into the flow loop and air purged from the lumen, the flow was adjusted for a stable flow rate near the predicted Reynolds number target. Using the PIV system, data was collected for two different analysis techniques.

For 2-D flow field analysis, a bisecting slice though the flow field was identified to demonstrated the entire flow field. A coronal slice (left to right) was found within phantom 3 and while a sagittal slice (anterior to posterior) was used for model 4. Images were collected at three different flow rates, corresponding to Re = 125, 500, and 3000. Image collection occurred at either 9 (phantom 3) or 10 (phantom 4) different zones to capture the entire flow field.

For 3-D recreation of the flow field, data sets were taken from the entire flow field. To reduce the computational demand, only fifty image sets were taken at each zone. The flow field was captured in multiple vertical levels in 5 mm increments. After the data for the entire field was collected, the phantom was rotated 90° and process was repeated at the perpendicular angle. For the 3-D analysis, images were taken at Re = 500 and 3000 only.

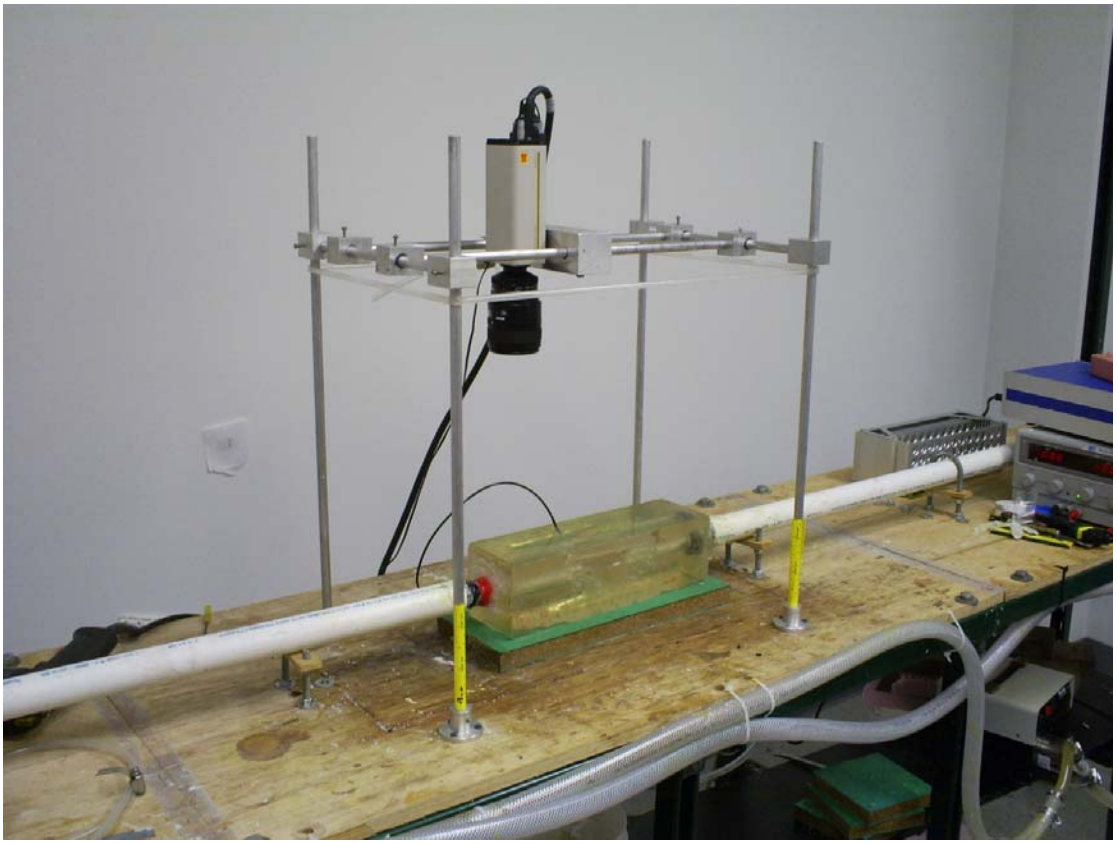

Figure 3.8 Phantom 4 installed in the flow loop. Phantom sat atop a cork slab and the working surface. The working surface was attached to a steel channel frame. Fluid in the test section flowed from left to right. Entrance and exit tubes were supported by the wooden platforms on 'U' shaped threaded rods. Surgical tubing compressed the aluminum frame to increase rigidity. The camera was attached to an aluminum block which slid axially along the aluminum dowels. Measuring tape was adhered to the front tubes to align and measure the height of the laser light sheet. The single black tube was connected to an air bleeding puncture. Tubes on the bottom were the supply and overflow lines.

3.5.6 *Image collection and data set processing*

Once these image sets were collected, a series of steps were performed to generate the final vector map complied for the set of images.

- Mask Definition: Portions of the images outside the flow field were masked.
- Mean image map: A composite image for images A and B were made by averaging the each image in the data set.
- Subtract mean image map: The mean image map was subtracted from each dataset image, ideally leaving only the illuminated particles against a blank background.
- Adaptive correlation: A single refinement step is used for each correlation area, performing an initial correlation at low resolution and then repeating at the final vector resolution.
    - For the 2-D analysis, the interrogation areas were 32 pixels × 32 pixels. Correlation areas were overlapped by 50% on both horizontally and vertically. The resulting spacing between interrogation areas was 1.43 mm both horizontally and vertically.
    - For 3-D analysis, the interrogation areas were 64 pixels × 64 pixels with 50% overlap horizontally and vertically. The final spacing between interrogation areas was 2.86 mm both horizontally and vertically.
- Masking Validation: The mask was applied and vectors under the mask were disabled.
    - For 2-D analysis, a single mask was generated at each zone and used at all flow rates.
    - For 3-D analysis, masks were generated for each zone at each flow rate.
- Peak Velocity Validation: Validates vectors by comparing the strength of the best solution generated by correlation to the strength of the second best solution. Vectors below the peak validation ratio value 1.2 were disabled.
- Moving Average Validation: Each vector was compared with its neighbors for relative accuracy. Non-compliant vectors are disabled. For each correlation area, the surrounding grid points making up a 3x3 grid were used, with an acceptance factor of 0.1, with 3 iterations.
- Range Validation: Each vector was checked for compliance within a set window of valid lengths. Vector range was for each zone to match the velocities seen locally. Vectors not within the prescribed range were disabled.
- Vector Statistics: At each location, the vector statistics are averaged from the remaining valid vectors, producing the time averaged flow field velocity map. The final data included the location of the interrogation area counterpoints (x and y), the velocity components (u and v), the standard deviation of the velocity, (σu and σv), and the number of valid vectors per location, N.
- Export data: The vector statistics were exported into a Tecplot compatible .dat file.

3.6 PIV POST PROCESSING

3.6.1 *2-D flow field assembly*

Data visualization and manipulation was performed with Tecplot 9.2. The data from each of the PIV zones were compiled to produce a single 2-D zone containing the entire flow field. To do this, the data files for each zone within a single vertical layer were opened simultaneously and arranged to match the grid used by the camera. A new zone was produced that would contains the entire flow field data, and would match the spatial density of the interrogation areas (46 × 180 grid points for phantom 3, 52 × 180 grid points for phantom 4). This process is depicted in figure 3.9.

Due to the adaptive correlation process, some of the boarder rows and columns produced invalid results, and these interrogation areas must be removed. This was indicated using a blanking variable B, all valid data was assigned $B = 1$ and invalid data was assigned $B = 0$. Using value blanking, all cells where $B = 0$ were deactivated. With these invalid cells deactivated using value blanking, the remaining valid data was complied into the new zone using a linear interpolation routine.

The axes of the new zone were adjusted so that the axial direction, z, was oriented upwards, with descending flow. The field was also shifted so that $z = 0$ correlated with the transition from the cylindrical inlet to the aortic segment.

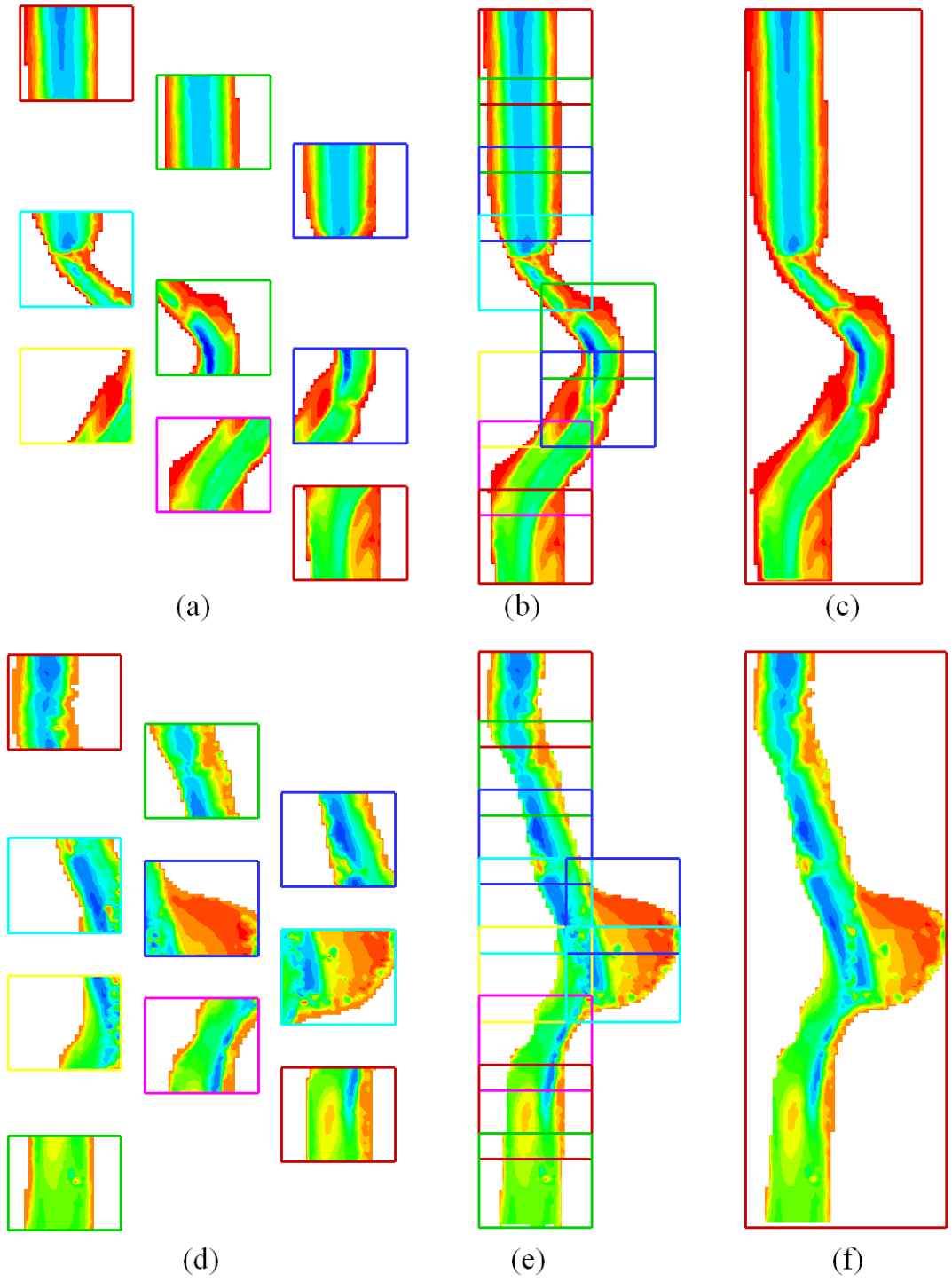

Figure 3.9 Flow field assembly. Consolidation of PIV data into a single, 2-D zone in phantoms 3 (a-c) and 4 (d-f). (a,d): The separate zones from PIV. (b,e): The zones were aligned. (c,f): A single zone containing the entire evaluated flow field was generated by interpolation of data from the original nine zones.

3.6.2 *2-D velocity profile*

Within the cylindrical entrance zone, the velocity profile from a horizontal cross section was isolated. This velocity data was know as the inlet velocity profile, U_{IN},. The maximum velocity in the profile identified and set as the $U_{IN,max}$. The dimensionless inlet velocity, U^*_{IN}, was determined by

$$U^*_{IN} = \frac{U_{IN}}{U_{IN,\max}}. \tag{3.4}$$

The horizontal position of the left and right lumen wall, x_l and x_r were identified and the horizontal data was scaled into the dimensionless inlet radius, r^*, with r^* = -1 and r^* = 1 at the left and right walls respectively by

$$r^* = \frac{2x - \left(x_r + x_l\right)}{x_r - x_l}. \tag{3.5}$$

Using the power law approximation (equation 3.6) and the variable exponent, n, the dimensionless velocity was curve fit.

$$U^*_{IN}\left(r^*, n\right) = 1 - \left(r^*\right)^n. \tag{3.6}$$

The best fit was determined by least squares error reduction method by altering x_l, x_r, and n to best fit the approximated profile to the data. Fully developed laminar pipe flow has a n value of 2 (Pouiselle-Hagen flow). Fully developed, turbulent pipe flow is commonly associated with the seventh power law (n = 7).

An estimation of the flow rate, Q, was made by integrating the power law profile over the inlet cross sectional area. Here the diameter, d, was constant at 2.54 cm and the radial dimensionless radius was set so that r^* = 0 the center point and r^* = 1at the wall (1/2 d).

$$\begin{aligned} Q &= \oint U_{IN}\left(r^*, n\right) dArea \\ Q &= 2\pi U_{IN,c} \int_0^{1/2d} \left(1 - \left(\frac{r}{1/2d}\right)^n\right) r\,dr \\ Q &= 2\pi U_{IN,c} \left(\frac{\left(1/2\,d\right)^2}{2} - (1/2\,d)^{-n} \frac{\left(1/2\,d\right)^{n+2}}{n+2}\right) \\ Q &= \frac{\pi n d^2 U_{IN,c}}{4n+8} \end{aligned} \tag{3.7}$$

The mean aortic velocity, U_a, was found from the flow rate by

$$U_a = \frac{4Q}{\pi d^2}. \tag{3.8}$$

This may also be found from the power law approximation,

$$U_a = \frac{U_{IN,c} n}{n+2}. \tag{3.9}$$

With the flow rate determined, the actual inlet Reynolds number (Re_{ex}) was found by solving the Reynolds' number equation by

$$\mathrm{Re}_{ex} = \frac{U_a d}{\nu}. \tag{3.10}$$

This experimental Reynolds numbers were found to be close, but not entirely accurate to the target Reynolds numbers, Re_t, of Re_t = {125, 500, and 3000}. The summary of the experimental inlet results are compiled in table 3.2.

Model	Re_t	n	$U_{IN,max}$ (cm/s)	U_a (cm/s)	Q (ml/s)	Re_{ex}
3	125	1.61	1.356	0.605	3.07	139
3	500	2.23	5.89	3.10	15.72	712
3	3000	2.53	19.76	11.04	55.9	2533
4	125	1.68	1.255	0.573	2.90	131
4	500	2.81	6.45	3.77	19.10	865
4	3000	2.86	20.40	12.00	60.8	2753

Table 3.2 Experimental results derived from the inlet profile

3.6.3 *Conversion to in vivo values*

The velocities and length scales were converted from experimental values (temporary subscript '*ex*') into more physiologically useful *in vivo* values (temporary subscript '*iv'*). The initial length scale estimations of the physical models were performed using the inlet diameter approximation as 2.54 cm as the characteristic diameter, without consideration to the lumen geometry as defined by Aslani (2005). The

computational geometries were matched to the reported lumen characteristics, and are assumed to be at the *in vivo* scale. The flow fields generated from the experimental analysis were compared side by side with the computational flow fields, and scaled to match. The length conversion to in vivo was found to be X_{iv} / X_{ex} = 1.18 for phantom 3 and X_{iv} / X_{ex} = 1.08 for phantom 4.

To covert the velocity scales, Reynolds dynamic similarity principles were used, accomplished with equation 3.11.

$$\frac{U_{iv}}{U_{ex}} = \frac{d_{ex}\nu_{iv}}{d_{iv}\nu_{ex}} \tag{3.11}$$

In equation 3.11, the diameter ratio is the inverse of the length scale conversion above. Arterial blood is assumed to be accurately represented by a Newtonian fluid (ν = 0.033 cm^2/s and ρ =1.050 g/ cm^3).

Additionally, it was desired to scale the experimental velocity results so that they directly match the target Reynolds numbers, Re_t. Thus, a linear velocity conversion was added to equation 3.11, producing

$$\frac{U_{iv}}{U_{ex}} = \frac{d_{ex}\nu_{iv}}{d_{iv}\nu_{ex}} \frac{\mathrm{Re}_t}{\mathrm{Re}_{ex}} \tag{3.12}$$

A minor discrepancy in Reynolds number calculation exists between Reynolds number calculation of the experimental and computational results. The computational results assume the characteristic diameter to be calculated within the aortic entrance section, while the experimental study has used the inlet pipe diameter as the characteristic geometry. The experimental values were scaled to approximately match the computational results by comparing velocity at a series of points. A fudge factor, C_f, was added to equation 3.12 to finalize the velocity conversion, equation 3.13.

$$\frac{U_{iv}}{U_{ex}} = \frac{d_{ex}\nu_{iv}}{d_{iv}\nu_{ex}} \frac{\mathrm{Re}_t}{\mathrm{Re}_{ex}} C_f \tag{3.13}$$

Given no direct computational comparison was available for the Re = 125 case, the C_f from the Re = 500 was used for the Re = 125 cases. For phantom 3, C_f was 0.93 at Re = 125 and 0.835 at Re = 3000. For phantom 4, C_f was 0.855 at Re = 125 and 0.750 at Re = 3000.

From this point, any length or velocity is assumed in *in vivo* terms, and the subscript '*iv*' dropped.

3.6.4 *Wall Shear Stress*

The wall shear stress, τ_w, is defined as the product of the dynamic viscosity with the gradient of the tangential velocity normal to the wall (equation 2.7). Since identification of the wall normal was problematic the wall shear stress was approximated by an alternative method. The shear stress distribution within the flow field was determined by the product of the dynamic viscosity of blood (0.03465 dyne s cm^{-2}), μ, and the field strain rate.

$$\tau = \mu\left(\left(\frac{du}{dx}\right)^2 + \left(\frac{dw}{dx}\right)^2 + \left(\frac{du}{dz}\right)^2 + \left(\frac{dw}{dz}\right)^2\right)^{.5}. \tag{3.14}$$

From the distribution, the maximum values within three correlation areas from the left and right wall were identified at each horizontal level (figure 3.10). Using the assumptions 1) the maximum shear stress in developed pipe flow will be at the wall and 2) the strain rate normal to the wall will be the maximum strain, this maximums were called the wall shear stress, τ_w, and were calculated separately for the two walls.

Since these calculations are made from 2-D data in the *x* and *z* plane, the out of plane derivative, *dy*, and velocity, *v*, were neglected. The calculation also provides shear stress values in absolute terms without the directional component.

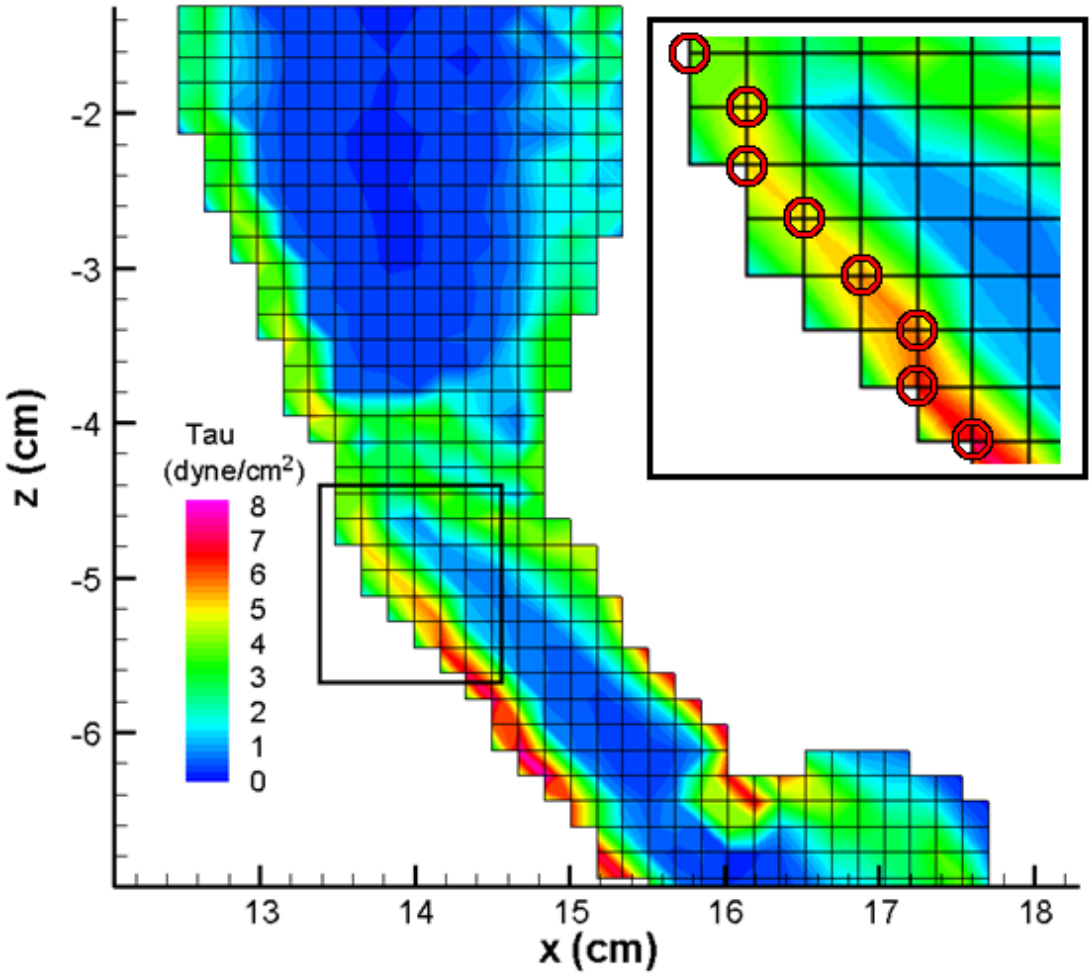

Figure 3.10 Shear stress, τ, distribution. Shear stress distribution from phantom 3 at Re = 3000. On both the right and left wall, the maximum shear stress within three points of the wall was determined and assumed to be the wall shear stress, τ_w. Inset: the red circles indicate maximum values at each horizontal level on the left wall.

3.6.5 *2-D Turbulence*

The total magnitude of the standard deviation of the velocity, σU, was determined by

$$\sigma U = \left(\left(\sigma u \right)^2 + \left(\sigma v \right)^2 \right)^{.5} . \tag{3.15}$$

The σU was comprised of 1) the fluctuating, turbulent velocity, U', 2) the systematic background noise from computational analysis, U'_{nosie}, and 3) experimental error. However, experimental error cannot be isolated and remains associated with U'. To isolate the turbulent fluctuating component, the systematic background noise background noise was subtracted from the σU by

$$U' = \sigma U - U'_{noise} . \tag{3.16}$$

To determine the U'_{nosie}, the lowest flow rate case (Re = 125) was inspected at the inlet. Here, the turbulence is assumed to be zero and any σU was believed to be entirely noise. The lowest σU values observed here were consistently $2.3 - 2.6 \times 10^{-2}$ cm/s. The value was estimated to be U'_{nosie} 2.5×10^{-2} cm/s was then selected for the Re = 125 case. The noise is predicted to increase inversely to the image exposure time differential, δt, so that

$$U'_{noise}\left(\delta t\right) = U'_{noise}\Big|_{\mathrm{Re}=125} \frac{\delta t}{\delta t\big|_{\mathrm{Re}=125}} . \tag{3.17}$$

The resulting U'_{nosie} at Re = 500 and 3000 were 1.01×10^{-1} cm/s and 5.42×10^{-1} cm/s respectively.

The turbulent velocity was then divided by the mean aortic inlet velocity, U_a, to produce the dimensionless turbulent velocity, U'^{*}, by

$$U'^{*} = \frac{U'}{U_a} . \tag{3.18}$$

The turbulent velocity was dived by the local velocity, U, to produce the turbulence intensity, TI, by

$$TI = \frac{U'}{U} . \tag{3.19}$$

For the TI calculation, a negligible 1×10^{9} cm/s was added to U in the denominator to prevent undetermined solutions due to zero division in the regions outside of the flow field. This addition had no noticeable effect on the flow field results.

3.6.6 *3-D flow field analysis*

The PIV data was compiled from individual zones into larger single zones. These zones were assigned heights corresponding to the vertical level of the laminating plane during experimentation. These 'layers' were then arranged in their 5 mm increments in 3-D graphical space. The perpendicular data was also assembled into single zones, 'slices,' in a similar method. The layers and slices were aligned in 3-D space, and at the entrance, exit, and mid model, the slices were manipulated to accommodate geometry formed by the layers (figure 3.9).

A 3-D rectangular grid was generated (23 × 15 × 86 for model 3, 19 × 26 × 86 for model 4). The velocity and N data was interpolated from the source data to the new grid using a Kriging method within Tecplot. Transverse slices were generated by taking slices through the grid at constant z values.

The length scale was corrected for *in vivo* values in a manner similar to the conversion in section 3.6.2. The length scale conversions were the same ($d_{iv} / d_{ex} = 1.18$ for phantom 3, $d_{iv} / d_{ex} = 1.08$ for phantom 4), but the velocity scale matched to the 2-D experimental results by direct velocity comparison (for phantom 3, U_{iv} / U_{ex} = {1.66 at Re = 500; 2.1 at Re = 3000}; for phantom 4, U_{iv} / U_{ex} = {1.48 at Re = 500; 2.62 at Re = 3000}).

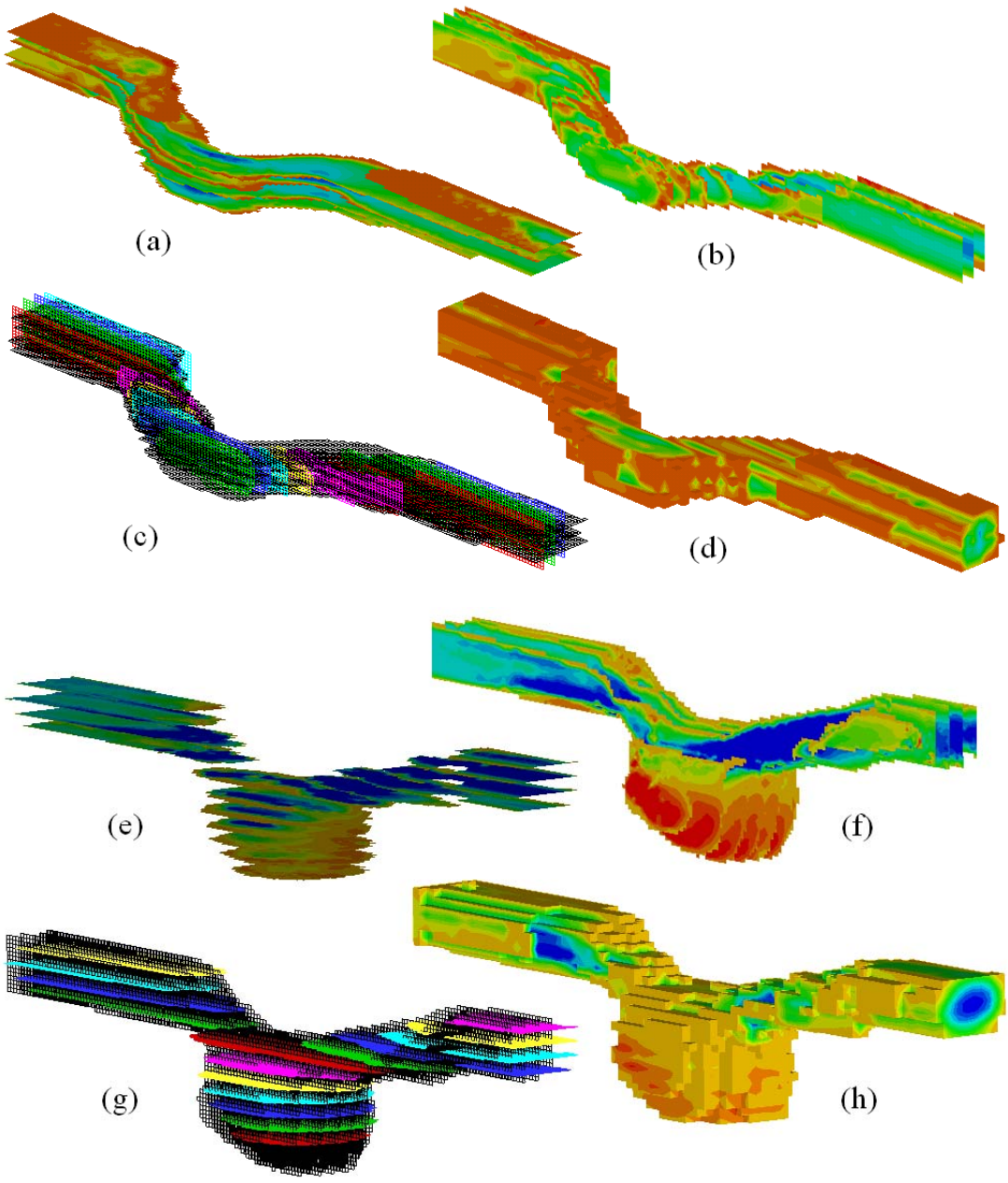

Figure 3.11 3-D flow field assembly. Consolidation of 3-D PIV data for phantoms 3 (a-d) and 4 (e-f). (a,e): The x-z planes were compiled, and aligned. (b,f): The y-z planes were compiled and aligned. (c,g): The x-z and y-z planes were merged and aligned. (d,h): A single zone was created by interpolating the data from all the planes.

3.7 PRESSURE MEASUREMENTS

3.7.1 *Flow loop and working fluid*

Physical phantoms were installed in the flow loop as previously described. Tap water was used as the working fluid, and the temperature was assumed to be constant at 22 °C (≈ 75 °F). At this temperature, the kinematic viscosity was $\nu = 9.52 \times 10^{-3}$ cm^2/s and the density was approximated as 1 g/cm^3. Assuming the 2.54 cm (1") diameter entrance section to be the characteristic diameter (0.75" for phantom 5), d_a = 2.54 cm, the desired flow rate, Q, for each test was determined from the Reynolds number. The flow rate was monitored using so that it maintained a steady flow rate near the target Re. The flow loop was allowed to stabilize for 15 minutes prior to testing once the desired flow rate was achieved.

3.7.2 *Pressure measurement equipment*

Disposable medical pressure transducers (Utah Medical Products, DPT-400) were used to convert the physical strain due to fluid pressure to a digital signal. A hemodynamic monitor (Hewlett Packard), provided a course graphical display of pressure vs. time, and amplified the pressure signal for reading by a digital multimeter. A twelve pin cable was used to connect the transducers and monitor while a wire with a ¼" plug and banana plugs on the opposite ends was used to connect the monitor and the multimeter. Twelve transducers were mounted to a 2" × 4" wooden block, which was adhered o the top of the phantom (figure 3.4). The polyurethane tubing was trimmed to an appropriate length and inserted into the transducers. The transducers designed to permit bleeding to remove air from the tubing lines.

3.7.3 *Wall pressure calibration and reporting*

The multimeter reported the signal potential, S, in terms of votalge which was linearly proportional to the pressure. Only a single connection on the hemodynamic monitor was available. The cord connecting the monitor and transducers was manually connected and disconnected to make each signal measurement. The reading was taken as soon after connecting the transducer as reasonably possible, as a slight decrease in signal voltage was observed when the transducer was plugged in for an extended period. At flow rates above Re = 1500, the output signal was fluctuant. In these cases, the signal was reported as a time averaged value. Below Re = 1500, the reported signal was stable enough so that a single, direct reading was adequate.

For simplicity, the water density, ρ, was assumed to be 1.00 g/cm^3, so that water column height, h, could be directly converted to pressure, p, from the vertical height length scale, h, by

$$\frac{dp}{dh} = -\rho g = -1\frac{mmH_2O}{mm} = -0.07353\frac{mmHg}{mm} \quad . \tag{3.7.1}$$

The pressure was reported relative to the ambient atmosphere so that the pressure is zero at the open air/water interface of the constant head reservoir. A vertical coordinate system was defined so that $h = 0$ at the working table surface. The height of the open air/water interface, h_o, was found using the measuring tape adjacent the static line in reference to the working surface.

The vertical locations of the pressure points were measured with a caliper from the base of the elastomer block to the pressure point. For the side series pressure points, the caliper directly measures the top of the urethane tube as it leaves the elastomer, while the top series was measured externally by visually aligning the caliper with the at the lumen/pressure point interface. The phantoms were supported by a 2.81 cm cork slab which sat atop the working surface. The sum of the height of the cork slab and the height of the pressure point within the elastomer block determined the wall height, h_w, for each pressure point. The product of $-h_w\rho g$ is referred to as the wall height correction.

Previous studies in this lab have used a drop point measuring tool for measuring pressure point wall height, which has been suggested as more accurate for the top measurements. While measurement with a caliper increase the error of local wall height measurements, the estimated maximum error for the top series pressure points is below .005 cm (~.06 mmHg), and the effect of error is decreased by systematic practices. Any measurement error appears in the wall pressure results only, and is small in comparison to the range of pressures observed due to range of wall heights. This measurement and any corresponding error cancelled out for the equivalent pressure results.

Equation 3.7.1 was integrated with the boundary condition of zero pressure at the top of the water column, ($p = 0$ at $h = h_o$) resulting in

$$p = \rho g(h_o - h)\Big|_{Q=0} \quad . \tag{3.7.2}$$

Equation 3.7.2 describes the pressure at any point within the flow field at static condition as a function of height. The wall pressure at the pressure points at the static condition was determined using $h = h_w$ (equation 3.7.3).

$$p = \rho g(h_o - h_w)\Big|_{wall,Q=0} \tag{3.7.3}$$

Using equation 3.7.3, a calibration was performed for each transducer by varying the height of the water colum, h_o, in the static line. Pressure, p, as determined by 3.7.3, was plotted against the multimeter signal, S, and a linear regression was performed. Each calibration reported an r-squared value of greater than

0.9999. Calibrations were performed immediately before testing the flow rate series of one side of one phantom, and repeated if the flow loop or pressure tubing were disturbed. The experimental signal results were then converted using the calibration to report the wall pressures.

3.7.4 *Equivalent pressure*

The equivalent pressure, P, a composite of local pressure and relative height, and may be stated as

$$P = p + \rho g \Delta h \quad . \tag{3.7.4}$$

Here, Δh is the difference between the local height and a constant height datum. With the constant height datum, the equivalent pressure is constant through the entire flow field under a quiescent condition. This makes the equivalent pressure especially useful for comparing flow induced pressure trends between pressure points of different height.

The height datum is defined at the working surface where $h = 0$. Under a static condition, the equivalent pressure is equal to pressure generated by the water height at all points within the flow field,

$$P = \rho g h_o \Big|_{Q=0} \quad . \tag{3.7.5}$$

The equivalent pressure at the each pressure point is calculated directly from the wall pressure by subtracting the wall pressure correction ($-\rho g h_w$) to provide equation 3.7.6.

$$P = p + \rho g h_w \Big|_{wall} \quad . \tag{3.7.6}$$

3.7.5 *Flow loop modifications*

Two modifications were made to the flow loop that should have an improved effect on the quality of the pressure measurements. The tubing proximal to the entrance section was refit with larger, 1” ID tubing and directed in a more linear configuration, which reduced pressure drop proximal to the phantom. An extra reservoir tank was placed atop the static line which acted as a fluid capacitor for the flow loop. The extra fluid capacity helped stabilize the pressure, both in dynamic and static conditions.

3.8 COMPUTATIONAL FLUID DYNAMICS

The basis of CFD is the iterative solution of governing fluid equations under a series of explicitly stated boundary conditions, made possible by a descritized computational grid. The CFD-ACE software suite (ESI Group, 2006; Paris) was used for grid generation, solution, and post-processing.

3.8.1 *Governing Equations*

The governing equations for fluid flow are the conservation of mass and momentum equations. With the assumptions of incompressible, Newtonian fluid, these equations simplify. Under these conditions, the conservation of mass is called the continuity equation (equation 3.8.1) while the conservation of momentum is specifically called the Navier-Stokes equation (equation 3.8.2).

$$\frac{\partial u_i}{\partial x_i} = 0 \text{, and} \tag{3.8.1}$$

$$\frac{\partial u_i}{\partial t} + u_j \frac{\partial u_i}{\partial x_j} = -\frac{1}{\rho}\frac{\partial p}{\partial x_i} + \nu \frac{\partial^2 u_i}{\partial x_j \partial x_j} + g \text{.} \tag{3.8.2}$$

Here, $u_i = (u, v, w)$ is the local velocity, $x_i = (x, y, z)$ is the length coordinate, t is the time scale, p is the fluid pressure, and g is the gravitational constant. Blood in the arteries is modeled under isothermal conditions and as incompressible and Newtonian where ρ is the fluid density (1.05 g/cm^3) and v is the kinematic viscosity of (3.3×10^{-2} cm^2/s).

For all computations, steady flow was assumed so that the time derivative was negated. With gravitational body force integrated into pressure in terms of equivalent pressure, $P = p + \rho g$, the Navier-Stokes equation may be stated as

$$u_j \frac{\partial u_i}{\partial x_j} = -\frac{1}{\rho}\frac{\partial P}{\partial x_i} + \nu \frac{\partial^2 u_i}{\partial x_j \partial x_j} \text{.} \tag{3.8.3}$$

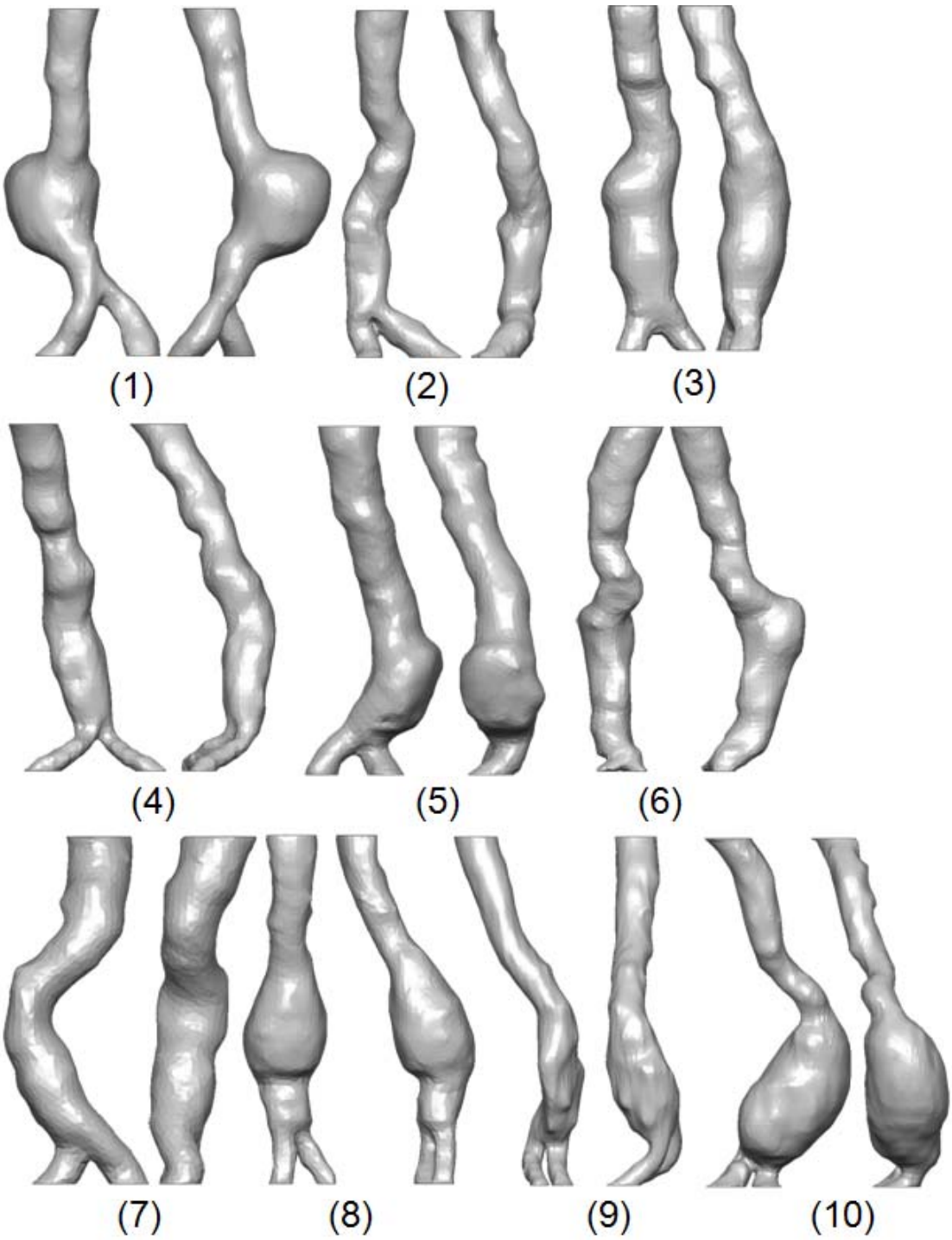

Figure 3.12 CFD AAA models. Posterior view (left), and right lateral view (right) of the 10 representative AAA models in which flow field development has been analyzed. Models 1 (saccular model), 7 (isodiameteric model), and 8 (fusiform model) are investigated in depth.

3.8.2 *Turbulence computation*

Reynolds decomposition describes instantaneous velocity, u_i as the sum of time averaged velocity, $\overline{u}_i$, and fluctuating velocity component, u_i', as

$$u_i = \overline{u}_i + u_i' . \tag{3.8.4}$$

Under laminar flow, the fluctuating component is zero, and the Navier-Stokes equation may be solved as stated above where velocity is implicitly non-fluctuant. When turbulence is present, the fluctuating component u_i' is non zero and dynamic. By definition, the time averaged values of the fluctuating components always equals zero ($\overline{u'}_i = 0$). However, the time averaged values of the product of turbulent components are non-zero when turbulence is present ($\overline{u_i' u_j'} \neq 0$). To mathematically quantity these values, the turbulent kinetic energy, *k*, is defined as

$$k = \frac{1}{2}\overline{u_i' u_i'} = \frac{1}{2}(\overline{u'^2} + \overline{v'^2} + \overline{w'^2}) . \tag{3.8.5}$$

The assumption of isotropic turbulence, $\overline{u'^2} = \overline{v'^2} = \overline{w'^2}$, is made for computational simplicity. As such, *k* may be represented by a singular dimension fluctuating velocity as

$$k = \frac{3}{2}u'^2 . \tag{3.8.6}$$

Equation 3.8.6 rearranged may be stated as,

$$u' = \sqrt{2/3\, k} . \tag{3.8.7}$$

This relationship (equation 3.8.7) is computationally useful for representing the fluctuant magnitude, and is used later in reporting the strength of turbulence. It is equivalent to the root mean squared turbulent fluctuations or standard deviation of the velocity as determined from experimental measurements.

Under turbulent conditions, it is convenient to restate Navier-Stokes equation by simplifying the convective acceleration with the continuity equation so that, as

$$\frac{\partial}{\partial x_j}\left(u_i u_j\right) = -\frac{1}{\rho}\frac{\partial p}{\partial x_i} + \nu \frac{\partial^2 u_i}{\partial x_j \partial x_j} . \tag{3.8.8}$$

Equation 3.8.4 is substituted into the Equation 3.8.8 under Reynolds averaged conditions. This modification of the Navier-Stokes equation is known as the Reynolds Average Navier-Stokes (RANS) equation and may be stated as

$$\frac{\partial}{\partial x_j}\left(\overline{u}_i\overline{u}_j + \overline{u_i'u_j'}\right) = -\frac{1}{\rho}\frac{\partial p}{\partial x_i} + \nu\frac{\partial^2\overline{u}_i}{\partial x_j\partial x_j}. \tag{3.8.9}$$

This is restated using the Reynolds stress tensor, $\tau_{i,j} = -\overline{u_i'u_j'}$, as

$$\overline{u}_j\frac{\partial\overline{u}_i}{\partial x_j} = -\frac{1}{\rho}\frac{\partial p}{\partial x_i} + \nu\frac{\partial^2\overline{u}_i}{\partial x_j\partial x_j} - \frac{\partial}{\partial x_j}\left(\tau_{i,j}\right). \tag{3.8.10}$$

The *k*- ω turbulence model (Wilcox 1993) was used to evaluate the Reynolds stress tensor. With the Boussinesq assumption, the Reynolds stress tensor is alternatively defined as

$$\tau_{i,j} = 2\nu_T S_{i,j} - \frac{2}{3}k\delta_{i,j}. \tag{3.8.11}$$

Here ν_T is the kinematic eddy viscosity, $S_{i,j}$ is the mean strain tensor and $\delta_{i,j}$ is the Kronecker delta ($\delta_{i,j} = 1$ when $i = j$, $\delta_{i,j} = 0$ when $i \neq j$). The mean strain tensor be stated as

$$S_{i,j} = \frac{1}{2}\left(\frac{\partial\overline{u}_i}{\partial x_j} + \frac{\partial\overline{u}_j}{\partial x_i}\right). \tag{3.8.12}$$

The *k*-ω model assumes that the kinematic eddy viscosity may be solved by

$$\nu_T = \frac{k}{\omega}. \tag{3.8.13}$$

The RANS equation may be solved simultaneously with the *k* and ω transport equations, specified with their closure coefficients elsewhere (Wilcox 1993).

3.8.3 *Boundary conditions*

Inlet flux was defined by a steady volumetric flow rate, Q, as

$$Q = \frac{\mathrm{Re}\pi\nu d_a}{4}, \tag{3.8.14}$$

where Re is the Reynolds number and d_a is the mean diameter in the non-dilated aorta. The Reynolds number is defined here as

$$\mathrm{Re} = \frac{u_a d_a}{\nu}, \tag{3.8.15}$$

where u_a is the mean non-dilated velocity. Table 3.3 details the conditions used for model 8.

The inlet geometry of the patient specific models was not perfectly round, and a fully developed velocity conditions were not able to be directly applied. To generate repeatable and consistent entrance flows between the models, the inlet of each model was approximated as an ellipse. For each model, the left, right, anterior, and posterior wall extrema points (x_1, x_2, y_1, and y_2) were identified, and then the dimensionless radius, r^*, was then defined as

$$r^*(x,y) = \sqrt{\left(\frac{2x-(x_1+x_2)}{x_1-x_2}\right)^2 + \left(\frac{2y-(y_1+y_2)}{y_1-y_2}\right)^2}. \tag{3.8.16}$$

Notably, $r^* = 0$ indicates the inlet center, while $r^* = 1$ indicates the wall approximation. For laminar simulations, a second order, Poiseuille velocity distribution, $\left(r^*\right)^2$, normal to the inlet was then established within the ellipse (equation 3.8.17). For turbulent simulations, a fourth order velocity distribution, $\left(r^*\right)^4$ was imposed (equation 3.8.18). The fourth power distribution was a best reasonable fit between the Re = 500 and Re = 3000 cases in the fully developed turbulent pipe flow side study (section 3.9). The laminar and turbulent entrance conditions are normal to the inlet plane and stated in terms of the power law as

$$u_{inlet}\left(r^*\right) = Re\, C_l\left(1-\left(r^*\right)^2\right), \text{ and} \tag{3.8.17}$$

$$u_{inlet}\left(r^*\right) = Re\, C_t\left(1-\left(r^*\right)^4\right). \tag{3.8.18}$$

The constants for laminar and turbulent flow, C_l and C_t, were determined by matching the reported inlet flux, Q, to the desired flow rate as calculated by Equation 3.8.14. The maximum inlet velocities were determined by product of Re and C_l or C_t. Due model wall irregularities, some areas of the model wall did not extend fully to $r^* = 1$, while some areas extended past $r^* = 1$. Some undesired flow artifacts occurred here, with abnormally rapid forward flows near the wall in the former case and retrograde flows in the later case. These artifacts were absorbed by the bulk flow, and had no effect on the flow field shortly downstream of the inlet.

To approximate fully developed turbulent conditions at the inlet, fully developed pipe flow was modeled in a preliminary side study (section 3.9). Approximations of these results were applied to the inlet. For the turbulent solutions, inlet distributions of k and ω needed to be specified. Stepwise approximations with were generated and implemented using the same elliptical approximation as the velocity profiles. The inlet k and ω conditions were

$$\log_{10}\left(k_{inlet}\left(r^*\right)\right)=\begin{cases}C_k, & 0\le r^*\le 0.9\\ C_k-20\left(r^*-.9\right), & r^*>0.9\end{cases}$$

(3.8.19)

$$\log_{10}\left(\omega_{inlet}\left(r^*\right)\right)=\begin{cases}C_{\omega,1}, & 0\le r^*\le 0.5\\ C_{\omega,1}+2\left(C_{\omega,2}-C_{\omega,1}\right)\left(r^*-0.5\right), & r^*>0.5\end{cases} \tag{3.8.20}$$

with C_k, $C_{\omega,1}$, and $C_{\omega,2}$ are the inlet turbulence parameters, unique for each flow rate and model. Example turbulent inlet values from model 8 (fusiform) are provided in table 3.8.1, while a complete listing is available in section 3.9. At the outlets, the velocity and turbulence were unbound while the fluid pressure was constant across the outlet planes. Inlet conditions are shown in figure 3.12 for model 8, Re = 3000.

Re	Q (ml/s)	u_a (cm/s)	C_l (cm/s)	C_t (cm/s)	C_k	$C_{\omega,1}$	$C_{\omega,2}$
500	29.2	7.33	1.83×10^{-4}	2.40×10^{-4}	-4.3	0	2.1
3000	174.9	44	1.83×10^{-4}	2.40×10^{-4}	-2.8	0.4	2.2

Table 3.3 Inlet conditions for model 8. Q and u_a are valid for both laminar and turbulent inlet flows. The inlet velocity constants C_l and C_t were used for laminar and turbulent computations respectively. The turbulent parameters C_k, $C_{\omega,1}$, and $C_{\omega,2}$ were only used for turbulent simulations.

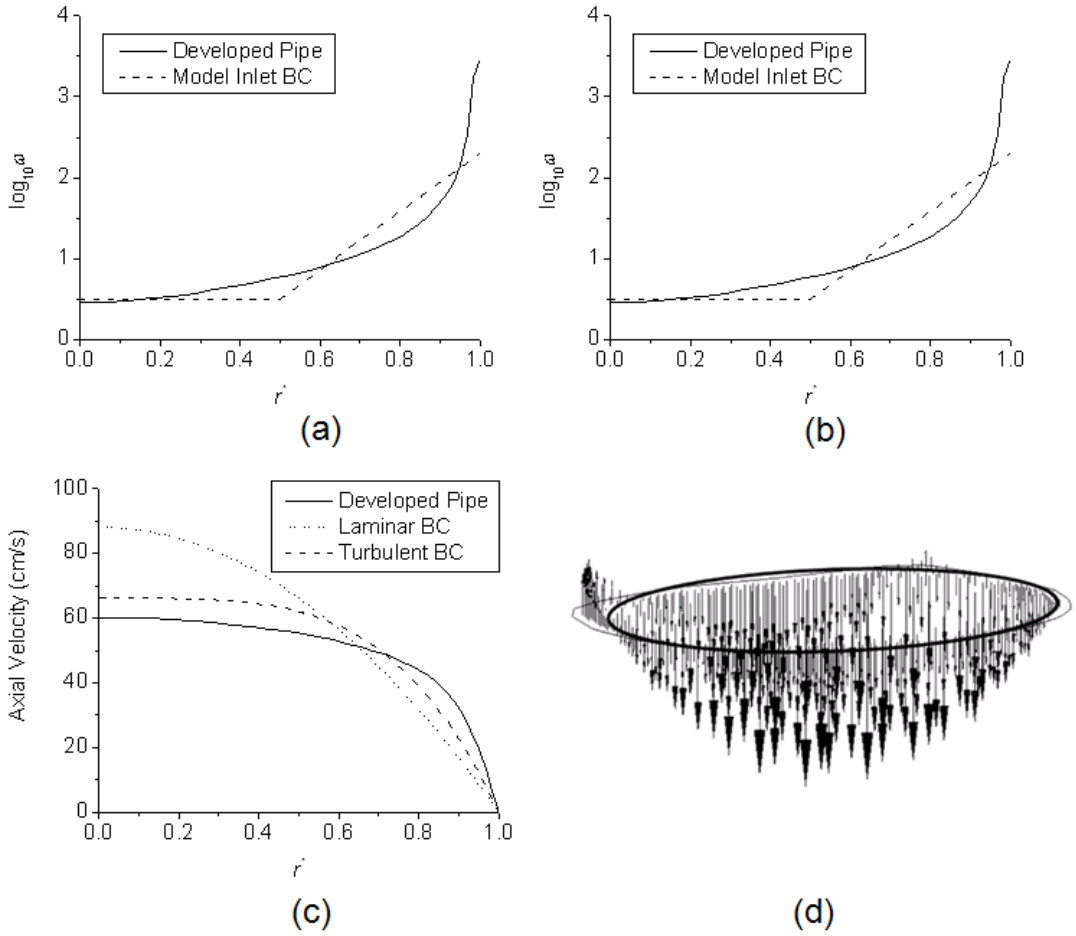

Figure 3.13 Inlet conditions. Flow field inlet conditions for simulation at Re = 3000 for fusiform model. Solid line: preliminary computation of fully developed turbulent flow. Dashed line: turbulent profile applied to fusiform model. Dotted line: laminar profile applied to fusiform model. (a) Inlet axial velocity distribution. (b) Turbulent kinetic energy, k, distribution. (c) Specific turbulent dissipation rate, ω, distribution. (d) Entrance velocity distribution as imposed in the fusiform model for turbulent analysis at Re = 3000. Maximum velocity is 48.1 cm/sec. The approximated inlet wall position, r^* = 1, is shown by the wide line, while the actual position is shown by the thinner line. Flow is in the retrograde direction in regions for which $r^* > 1$.

3.8.4 *Computational grid*

Unlike analytical solutions, CFD generally requires a discretization of the flow field, creating a grid of small cells within the studied geometry. In an unpublished method, Chengyan Peng and Peattie created a series of non uniform, finite volume grids. These grids were a hybrid of structured and non structured elements. The near wall regions were composed of non structured elements, while the interior elements were structured, and varied in mesh density with cell length increasing inwards. This progressive cell enlargement reduced the total number of cells within the mesh. These meshes allowed for optimizing the convergence speed by using the greatest possible number of structured grids (which are less computationally demanding) and placed the highest grid resolution in the near wall region, where the highest shear would be expected to occur. An example mesh is shown in figure 3.14. While formal grid independence study was not performed, preliminary turbulent calculations were performed to determine if convergence could be achieved. The resulting grids had between 2-4 $\times 10^5$ elements. Details for the three exemplar models are listed in table 3.4.

Model	d_a (cm)	d_{AAA} (cm)	Mesh cells
1	2.32	5.50	330,392
7	2.77	4.56	221,280
8	2.25	3.90	202,254

Table 3.4 Grid properties. Non-dilated diameter, d_a, maximum bulge diameter, d_{AAA}, and number of mesh cell per grid.

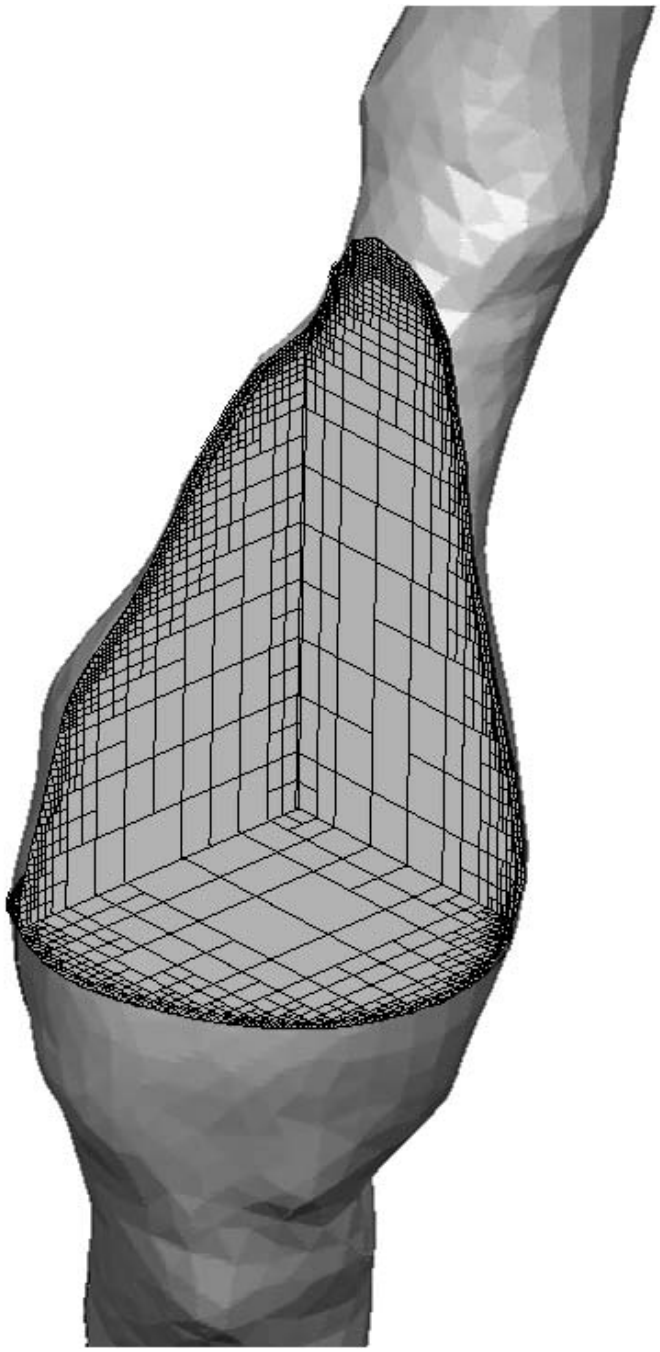

Figure 3.14 Mesh cutaway. Computational mesh from the fusiform model, cutaway to display interior cells.

3.8.5 *Computation, convergence, and post processing*

Solutions to the series of equations described above were generated within the discretization grids. Both laminar and turbulent solutions were determined for the flow rates of Re = 500, 1000, 2000 and 3000. Initial conditions for laminar solutions used a quiescent condition except at the inlet. For the turbulent computation, the converged laminar solution was used as the initial velocity and pressure conditions as it helped prevent divergent calculations that were more frequent from quiescent conditions. The model and flow rate specific C_k and $C_{\omega,1}$ constants were used as the initial conditions for k and w. Upon convergence, both laminar and turbulent solutions were insensitive to initial conditions. Solutions were assumed fully converged when all residuals were reduced four orders of magnitude from maximum values. The number of iterations require for convergence varied from around 200 to 20,000. While the default relaxation parameters were used for the majority of the solutions, they were adjusted in some cases to either 'stiffen' the solution to expedite convergence or to 'soften' solver parameters when solutions were unstable. Calculations were carried out on a personal computer with dual 2.4 GHz Intel Xeon processors and 4 GB RAM. Solutions took from around 1 hour up to 48 hours to converge, though the 4-8 hour range with 1000-2000 iterations was typical. Turbulent solution took longer than laminar solutions, and on rare occasion would have one or more variable not fully converge to the fourth order reduction of residuals. In these cases, residuals 'flat lined' and further reduction was not possible, though all solutions achieved at least three orders of magnitude reduction in residuals. These were assumed as fully converged, and their results did not appear compromised.

After convergence, some derivation of the flow field was required to generate the turbulence intensity and wall shear stress. Using the post processing software (CFD-View), the shear stress distribution, τ, was derived from the velocity as

$$\tau = \mu \left. \frac{du_i}{dx_j} \right|_{i \neq j} \tag{3.8.21}$$

The wall shear stress, τ_w was then generated as the absolute value of the shear stress values at the border cells.

Turbulent intensity was defined as the standard deviation of the fluctuating velocity component (equation 3.8.4) over the mean velocity and calculated as

$$TI = \frac{\sqrt{2/3\, k}}{\overline{u}_i}. \tag{3.8.22}$$

Likewise, the dimensionless turbulent velocity, U'^{*}, was found by

$$u'^{*} = \frac{\sqrt{2/3\,k}}{u_a}. \tag{3.8.23}$$

3.8.6 *Fully developed turbulent pipe flow*

To determine the proper inlet conditions for the turbulent simulations within the AAA models, a set of fully developed pipe flow simulations was performed. A structured grid, shown in figure 3.15, corresponding to a half cylinder was generated. The grid was composed of 44,000 nodes and 40,194 cells, with the number of nodes (30 x 15 x 100) corresponding to radius, theta, and length. The radial spacing was set so that higher grid density was near the walls, mimicking that of the AAA grid. The length of the grid was set at 50 cm, and the diameter was set at 2.5 cm. This half cylinder grid was scaled to five different sizes to closely match the non-dilated aortic diameter, d_a, for each AAA model.

According to each of the 10 model's d_a, they were organized into five groups corresponding to closely related values. Approximate median values were assessed for each group, d_p, and for each group the half cylinder grid was rescaled to match that median value. Using the $n = 4$ assumption for inlet turbulent velocity profiles, the C_t value, which when multiplied with the Reynolds number equal the centerline velocity, was also determined for each d_p. These values are compiled in table 3.5.

The same techniques, parameters and boundary conditions used for the AAA models were used for this sub-study. Newtonian, incompressible assumptions were made for the modeled fluid ($\rho = 1.050$ g/cm^3, $\upsilon = 0.033$ cm^2/s). The k-ω model (Wilcox 1993) was used to predict turbulence. No penetration and no slip were assumed at the cylindrical walls and constant pressure was assumed at the outlet. Symmetry was assumed on the rectangular face. The inlet velocity condition was defined using equation 3.8.18 while the k and ω conditions were defined as using equations 3.8.19 and 3.8.20. To accommodate this cylindrical geometry, r^* was alternatively defined as

$$r^{*} = \frac{2r}{d_p}. \tag{3.8.24}$$

The values of C_k and $C_{\omega,1}$ and $C_{\omega,2}$ were found by an iterative method. After each simulation converged, the outlet values of C_k, given by $log_{10}(k)$ at $r^* = 0.5$, $C_{\omega,1}$, given by $log_{10}(\omega)$ at $r^* = 0$, and $C_{\omega,2}$, given by $log_{10}(\omega)$ at $r^* = 0.95$ were found. These values were used as the inlet conditions of the next iteration. This was repeated until the inlet and outlet were in good agreement. These values were then used for the inlet values of the models corresponding to that pipe diameter. These values from the $d_p = 2.25$ cm

simulation at Re = 500 and 3000 are presented in table 3.8.1, which were used for the fusiform model. A full compilation of the inlet turbulent parameters are in appendix A.

The normalized velocity profiles (U / (C_t Re)) from each flow rate from the d_p = 2.25 cm simulation are presented in figure 3.16. It should be apparent that the n = 4 profile was not a perfect match to each flow rate. However, it is a useful best estimation for the entire range of flow rates as a median profile. By using the same velocity profile for each flow rate, the inlet velocity conditions are much simpler to develop when using multiple flow rates.

Model	d_a (cm)	d_p (cm)	C_t (cm/s)
9	2.11		
8	2.25	2.25	0.0219
6	2.26		
1	2.32		
10	2.32	2.32	0.0213
2	2.35		
11	2.42	2.42	0.0204
5	2.68	2.68	0.0184
4	2.84		
		2.96	0.0167
7	2.96		

Table 3.5 Half cylinder grids corresponding to AAA models.

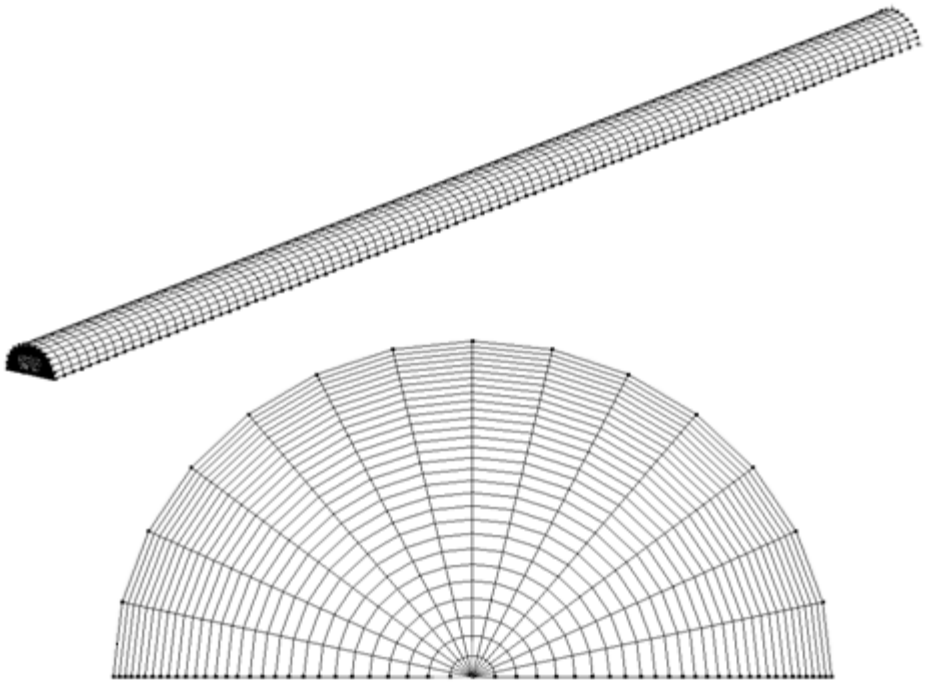

Figure 3.15 Half cylinder mesh. Mesh used for fully developed turbulent pipe flow study assuming symmetry on the face.

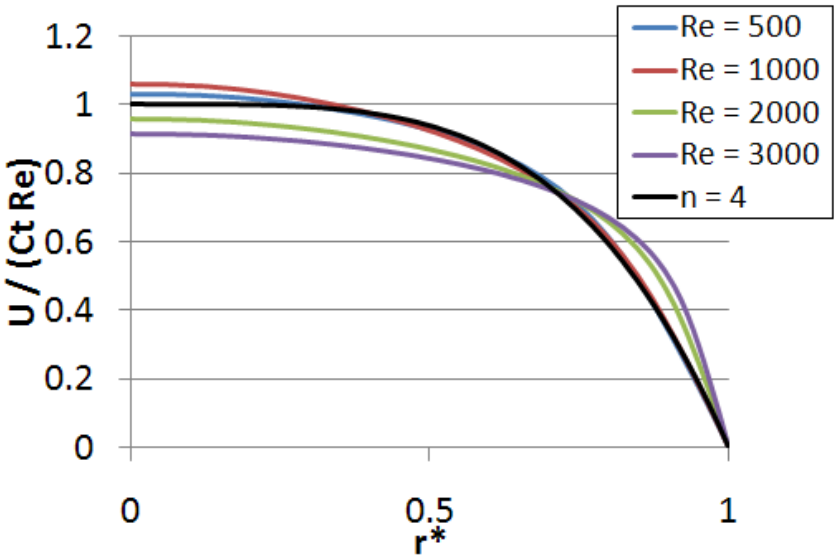

Figure 3.16 Velocity profiles from preliminary pipe study.

CHAPTER 4: EXPERIMENTAL RESULTS

Flow field measurements were carried out in phantom 3 (figure 4.1 left) and phantom 4 (figure 4.1 right) at the flow rates of Re = 125, 500 and 3000 for 2-D analysis which consisted of velocity, turbulence and wall shear stress measurements. Velocity measurements were performed at Re = 500 and 3000 for 3-D analysis in these phantoms.

4.1 INLET VELOCITY PROFILE

From the experimental 2-D velocity results, the inlet velocity, U_{IN}, was extracted from the flow fields at z = +3.2 cm for phantom 3 and z = +3.0 cm for phantom 4 (figure 4.1). The experimental inlet velocity values (figure 4.2, diamonds) were matched to idealized approximations of each inlet velocity profile (figure 4.2, solid line). The inlet velocities were divided by the mean inlet aortic velocity, U_a, to render the scaled inlet velocity, U_{IN}^* (figure 4.3). The target Reynolds number (Re_t) and the actual experimental Reynolds number (Re_{ex}) differed somewhat for all cases. Results of the inlet study are summarized in table 4.1.

Phantom	Re_t	n	U_{cl} cm/s	U_a cm/s	Q ml/s	Re_{ex}
3	125	1.61	1.356	0.605	3.07	139
3	500	2.23	5.89	3.10	15.72	712
3	3000	2.53	19.76	11.04	55.9	2533
4	125	1.68	1.255	0.573	2.90	131
4	500	2.81	6.45	3.77	19.10	865
4	3000	2.86	20.40	12.00	60.8	2753

Table 4.1 Inlet velocity and flow rates. All values are in experimental terms without scaling to the target Re or *in vivo* conditions.

In phantom 3, at Re = 125, the shape of the inlet profile was found to be n = 1.69 using least square error reduction methods. This profiles showed more conic character (n = 1) than the expected parabolic shape (n = 2). At Re = 500, the profile was more parabolic, n = 2.23, much closer to the expected parabolic shape. At Re = 3000, the profile was more widely dispersed, n = 2.53, though an unusual

reverse concave profile was seen on either side of the centerline. The U_{IN}^{*} showed the change of profiles between the flow rates as with flatter profiles as flow rates increased.

In phantom 4, a similar progression was observed in the development of the shape of the inlet profile. At Re = 125, n = 1.68; this again shows a somewhat conic element to the velocity profile, unexpected at any Re. At Re = 500, n = 2.81 while at Re = 3000, n = 2.86. These showed much flatter profiles, which show less laminar character than the low flow rate. The U_{IN}^{*} were strikingly similar between the Re = 500 and Re = 3000 flow rates.

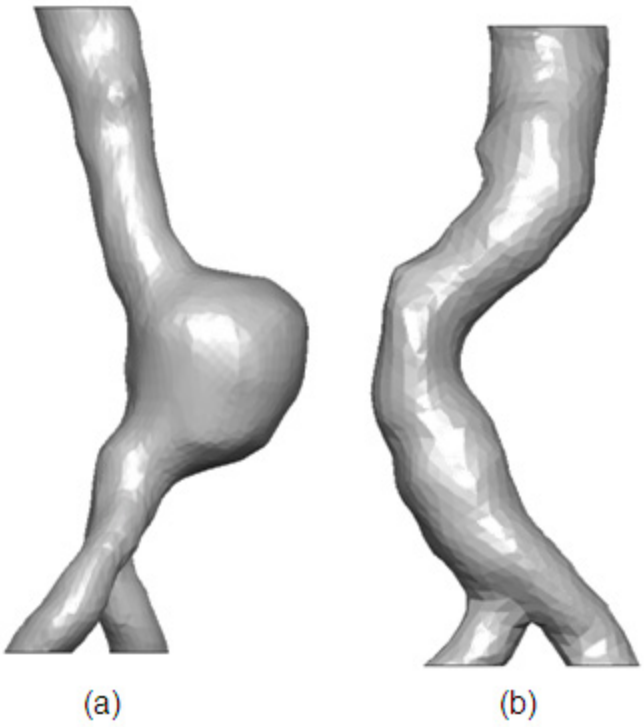

Figure 4.1 Lumen examined experimentally. Lumen of phantom 3 (a) and phantom 4 (b) oriented as viewed by the PIV camera during 2-D analysis.

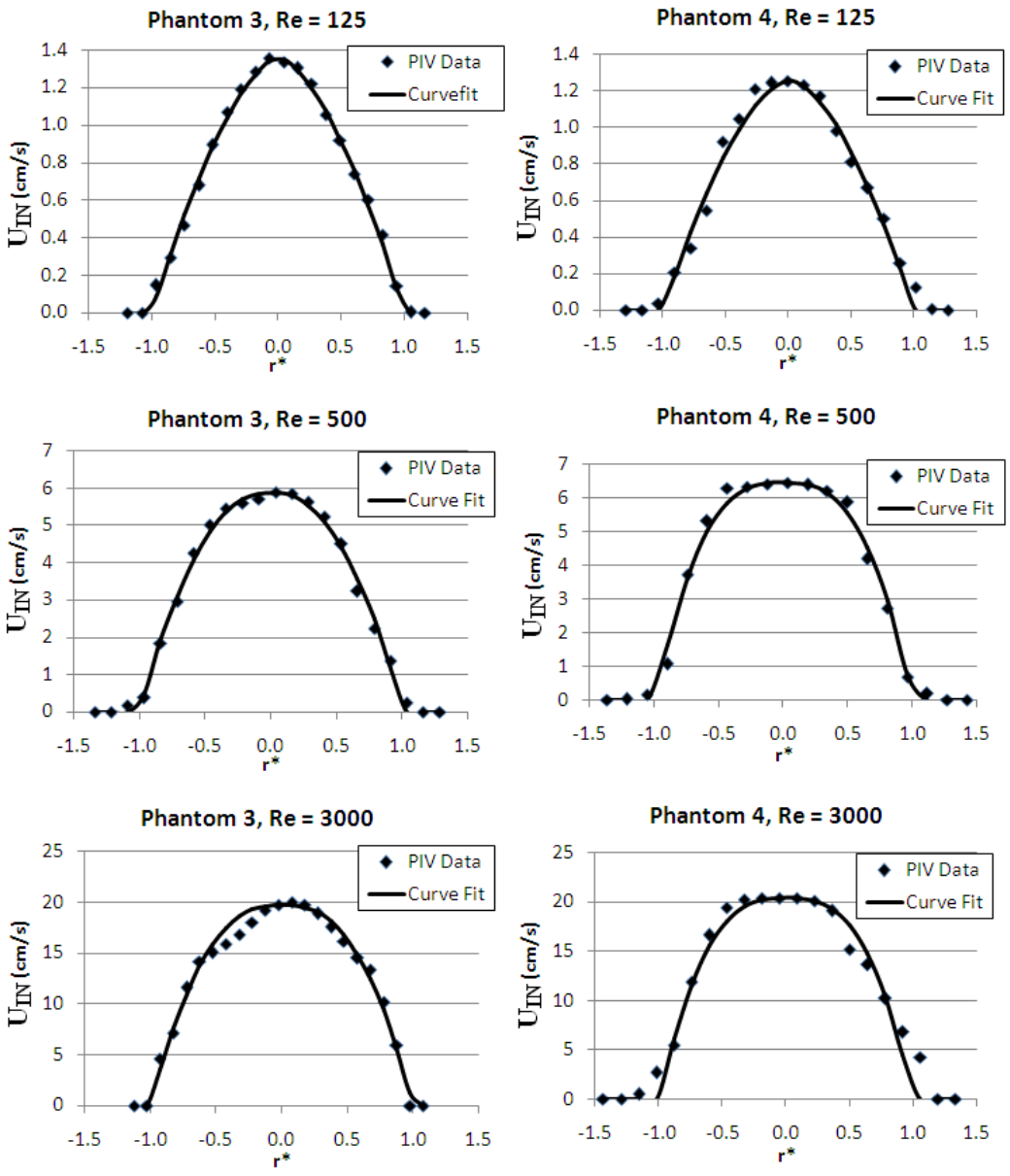

Figure 4.2 Inlet velocity, U_{IN}, profiles. Experimental velocity (diamonds) and the profile approximation (solid line) from the phantom entrance sections. Results are presented in terms of experimental velocity values, without *in vivo* conversion.

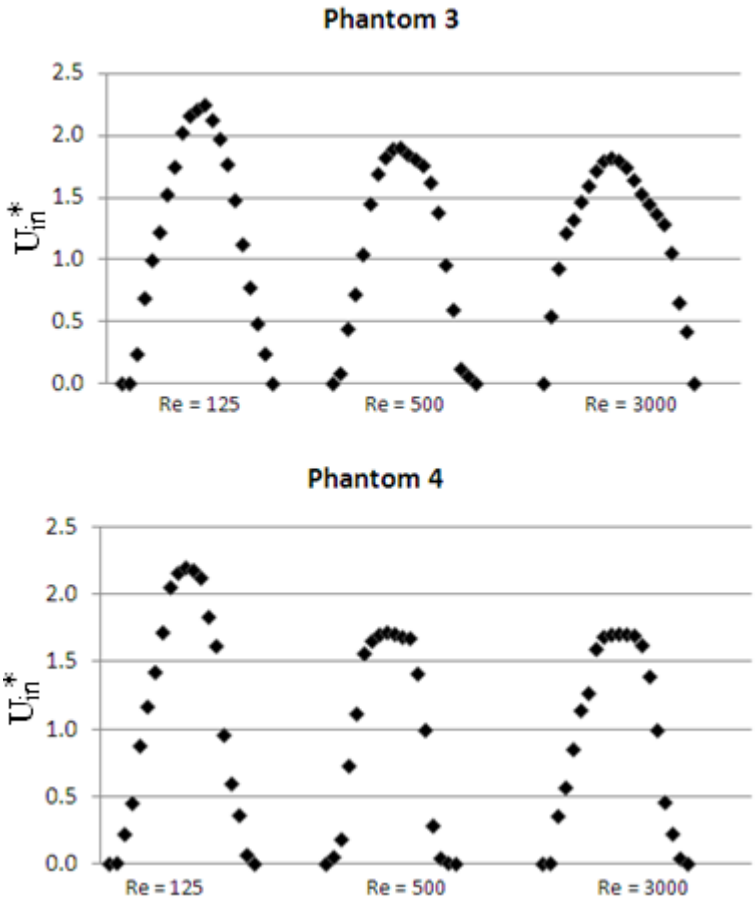

Figure 4.3 Scaled inlet velocity, U_{in}^* profile.

4.2 2-D VELOCITY FLOW FIELD

The velocity flow fields of phantom 3 (figure 4.4) show a well developed flow profile in the cylindrical inlet from z = +8 cm to z = 0. Through the first bend of the lumen near z = -3 cm, the flow remains directed on a straight axial path causing the core momentum to impact the right wall. As the lumen bends in its isodiametric 'C' shape, the bulk of the momentum shifted from the right wall to the left wall. As the momentum shifts leftwards, a small pocket of low flow forms in on the right wall between z = -10 cm to z = -13 cm. Here, a slight retrograde characteristic is seen at Re = 500, while the velocity remains low but forward directed for Re = 125 and 3000. As the bends terminated, a small pocket of separated and recirculating flow formed on the right wall at all flow rates as the core flow was focused on the opposite wall there. The flow exited the bends into the cylindrical exit section and the core momentum moved from the left wall with skewed velocity profiles. In all flow rate cases, low flow occurred on the left walls while a somewhat exaggerated high velocity in the center maximum velocity was formed, but the flow profiles began returning towards the developed, parabolic profile.

The inlet flow of phantom 4 (figure 4.4) was generally parabolic and developed. In comparison to phantom 3, the flow within the inlet phantom 4 showed blunter profiles at Re = 500 and 3000. As the flow entered the aortic section at z = 0 cm, the anterior tilt of the walls forced the momentum of the core flow to the posterior wall. At Re = 125, the core flow remained developed and remained generally centered. At Re = 500, the profile was strongly skewed to the posterior wall while at Re = 3000, the profile was less skewed but showed very wide velocity distribution. At z = -8 cm, immediately proximal to entrance to the aneurismal dilation, the velocity profiles for each flow rate returned to a nearly parabolic distribution. The direction of flow here matched the slant formed by the entrance section.

As the flow entered the aneurismal dilation, the flow field displayed two parts: forward core flow on the posterior wall and a large vortex filling the dilation on the anterior. The core flow remained attached to and followed the path of the posterior wall. Impacted flow occurred on the distal surface of the bulge, where the flow separated into the recirculating flow or exited the bulge. While the recirculation appears well defined at Re = 125, the flow patterns at Re = 500 and Re = 2500 show more variability in the fluid motion with less pronounced vortex structure.

As flow exits the aneurysm, it is entirely attached to the walls and skewed profiles arise from the convergence of the separated flow. At Re = 125, the flow is reasonably developed with the core flow mostly centered. At Re = 500 and Re = 3000, a flat profile formed at the aneurysm outlet, but downstream a bimodal profile was developed. Low flow areas formed on the posterior wall of the exit tube at all flow rates, and further downstream the flow profile began returning towards a developed profile.

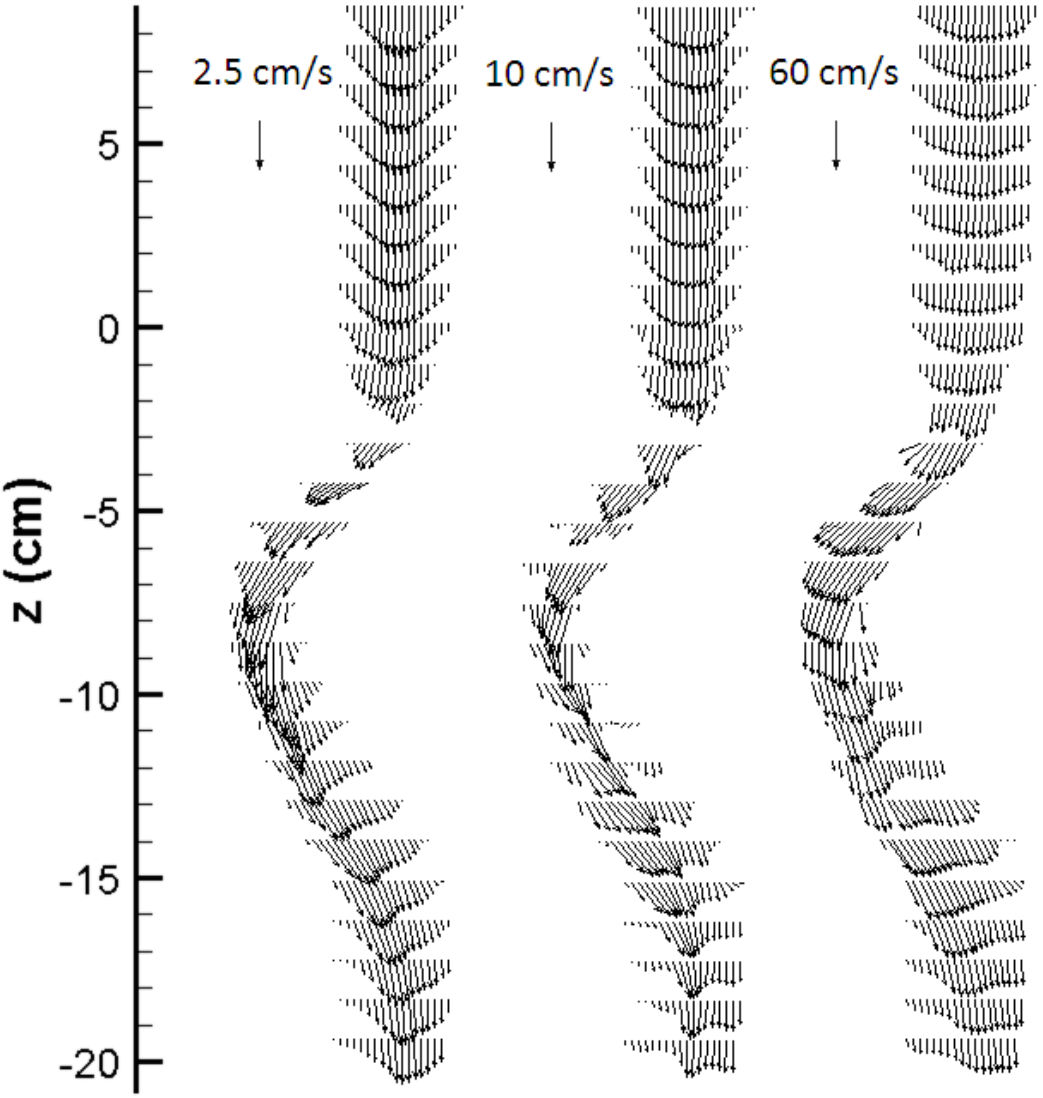

Figure 4.4 (part 1/2) Velocity vector maps for phantom 3 at Re = 125 (left), Re = 500 (center), and Re = 3000 (right).

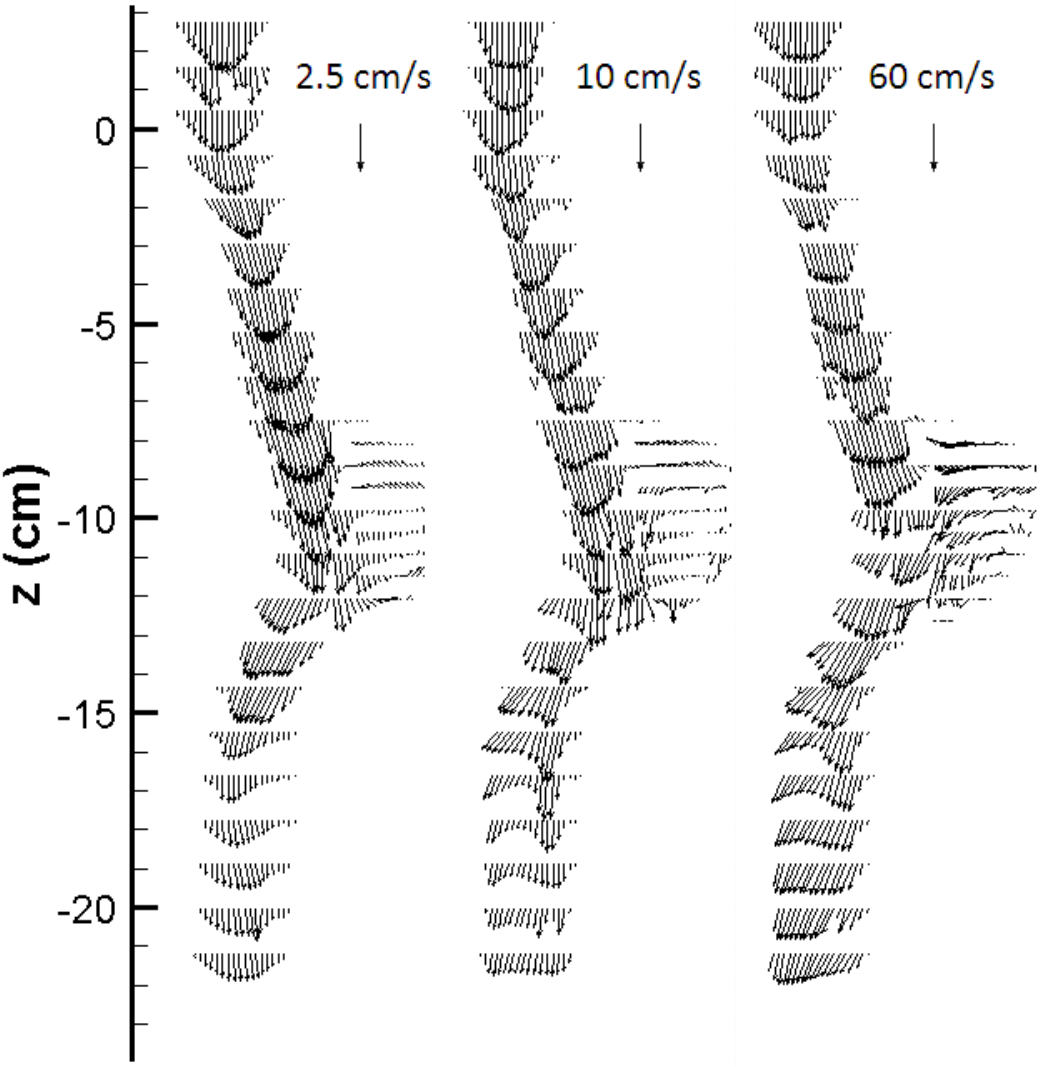

Figure 4.4 (part 2/2) Velocity vector maps for phantom 4 at Re = 125 (left), Re = 500 (center), and Re = 3000 (right).

4.3 MAXIMUM VELOCITY

From the flow field results, the maximum value of the local velocity magnitude, U_{max}, was identified at each horizontal level. To remove spurious data resulting from poor correlation, only U_{max} values resulting from correlation of resulting from $N = 7$ or better (of a possible 200) were accepted. To this data, a three point boxcar averaging routine was performed to smooth minor noise, and these results are presented in figure 4.5.

While the majority of the U_{max} results were from robust correlation, a few sections were compromised by significant correlation error. These generally formed spiking reductions in U_{max} values due to the tendency of noisy results to under-report velocity magnitude. Major erroneous data in the U_{max} results for phantom 3 were local minima near z = -4 cm at Re = 125 and Re = 500, local minima near z = -9 cm at Re = 500, local minima near z = -12 cm at Re = 500 and local minima near z = -14 cm at Re = 500. Major erroneous data in the U_{max} for phantom 4 results were local minima near z = 0 for Re = 3000, local minima near z = -7 cm for Re = 500, and local maxima near z = - 22 cm for Re = 500 and Re = 3000.

In phantom 3, the U_{max} at the start of the studied flow field at z = +8.6 cm was 2.78 cm/s at Re = 125, 9.76 cm/s at Re = 500, and 51.3 cm/s at Re = 3000. From these initial values, there was a steady decrease in U_{max} through the cylindrical inlet and the aortic entrance section between z = +8 cm to z = -5 cm at Re = 125 and Re = 3000. The overall minima U_{max} for the flow field at Re = 125(approx 2.0 cm/s) and Re = 3000 (37.3 cm/s) occurred near z = - 2 cm. At Re = 500, a slight decrease in U_{max} occurred in the section, achieving a local minima of 9.23 cm/s at z = 4 cm. A steady and rapid increase in U_{max} occurred between the first and second bend, and the overall maxima U_{max} at all flow rates occurred near z = -9 cm with 3.85 cm/s at Re = 125, 12.33 cm/s at Re = 500, and 63.8 cm/s at Re = 3000. The maximum centerline velocity gradually decreases to the aortic terminus at z = -15 cm, and then continues decreasing at a slightly reduced rate through the cylindrical exit section. The overall minima U_{max} at Re = 500 of 7.14 cm/s occurred at the flow field terminus and while 2.28 cm/s at Re =125 and 41.4 cm/s at Re = 3000 also occurred here.

In phantom 4, the U_{max} at the start of the studied flow (z = +3.1 cm) was 2.80 cm/s at Re = 125, 10.70 cm/s at Re = 500, and 52.2 cm/s at Re = 3000. From the entrance, U_{max} decreased to a local minima of 2.13 cm/s at Re = 125, 9.40 cm/s at Re = 500, and around 45 cm/s at Re = 3000 (obscured by error) near z = -2 cm. The U_{max} increases as the flow accelerates through the first bend. An acceleration occurs and near z = -5 cm, the overall U_{max} maxima of 3.48 cm/s was achieved at Re = 125, while only local maxima of 11.63 cm/s at Re = 500 and 64.6 cm/s at Re = 3000. Near the bulge midpoint at z = -13 cm local U_{max} minima of 2.05 cm/s at Re = 125, 9.09 cm/s at Re = 500 were found. Also, at Re = 3000, the overall U_{max} minima of 36.8 cm/s was found. The U_{max} increased through the constriction of the dilation, achieving overall U_{max} maxima at z = -15 cm of 11.83 cm/s at Re = 500 and 70.17 cm/s at Re = 3000, while the Re =

125 flow produced a local U_{max} maxima of 2.45 cm/s. The U_{max} decelerates distal of the aneurysm, decreasing rapidly through the terminus of the aortic section at z = -17 cm, and into the cylindrical outlet section. The overall U_{max} minima occurred near z = -20 cm at Re = 125 with 1.32 cm/s and near z = -22 cm at Re = 500 with 4.65 cm/s. In contrast, a local minima for Re = 3000 occurred at the flow field terminus at z = -23.8 cm with 39.0 cm/s.

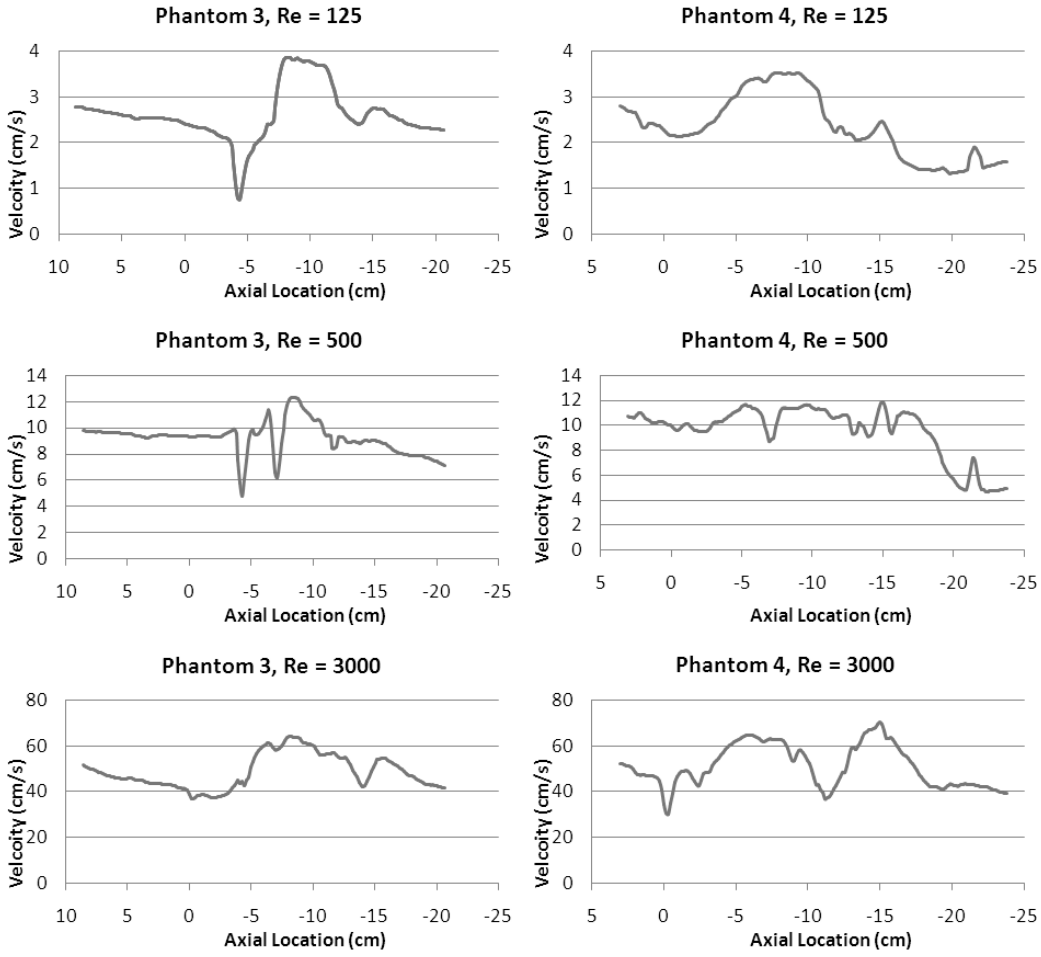

Figure 4.5 Maximum velocity for phantoms 3 and 4.

4.4 MAXIMUM RETROGRADE VELOCITY

The maximum retrograde axial velocity, $w_{max,r}$ (figure 4.6), was determined by identifying the greatest retrograde axial velocity component w at each horizontal level. Only $w_{max,r}$ values associated with correlation rates of $N = 7$ or better (of a possible 200) were accepted to remove inconsistent and spurious velocities. The recirculation results were particularly sensitive to correlation error, especially at higher flow rates. As such, the magnitudes of $w_{max,r}$ may be somewhat suspect in some cases, but the presence and reported locations of retrograde flow are of high confidence.

In phantom 3, retrograde flow occurred in all flow rate cases in a pocket in the upper left corner of the third bend, near $z = -15$ cm. A slight separation of flow occurs here opposite the core flow, which is concentrated near the right wall. The maximum $w_{max,r}$ in this flow were 0.0112 cm/s at Re = 125, 0.659 cm/s at Re = 500 and 3.75 cm/s at Re = 3000. An additional recirculation in the Re = 500 case was observed near $z = -12$ cm with a maximum $w_{max,r}$ of 0.708 cm/s.

In phantom 4, a single, large recirculation occurred in the saccular dilation. The structure of the recirculation flow with the aneurismal dilation is best demonstrated with the Re =125 flow rate. The vortex was well defined at Re = 125. The $w_{max,r}$ maxima peaks of 0.303 cm/s and 0.586 cm/s occurred at the upstream reattachment point ($z = -13$ cm) and t the downstream separation point ($z = -10$ cm). Between these peaks, a well defined $w_{max,r}$ minima occurred mid-bulge ($z = -11.5$ cm) of 0.171 cm/s. The Re = 500 and Re = 3000 flows showed similar trends as $w_{max,r}$ maxima occurred near the separation and attachment points and reduced mid-bulge. However, higher correlation error obscured much of the recirculation flow field, causing choppy $w_{max,r}$ results. Again, $w_{max,r}$ maxima were found at the separation (0.274 cm/s at Re = 500 and 7.11 cm/s at Re = 3000) and attachment points (0.892 cm/s at Re = 500 and 11.76 cm/s at Re = 3000). The local mid-aneurysm $w_{max,r}$ minima at Re = 500 and Re = 3000 could not be determined.

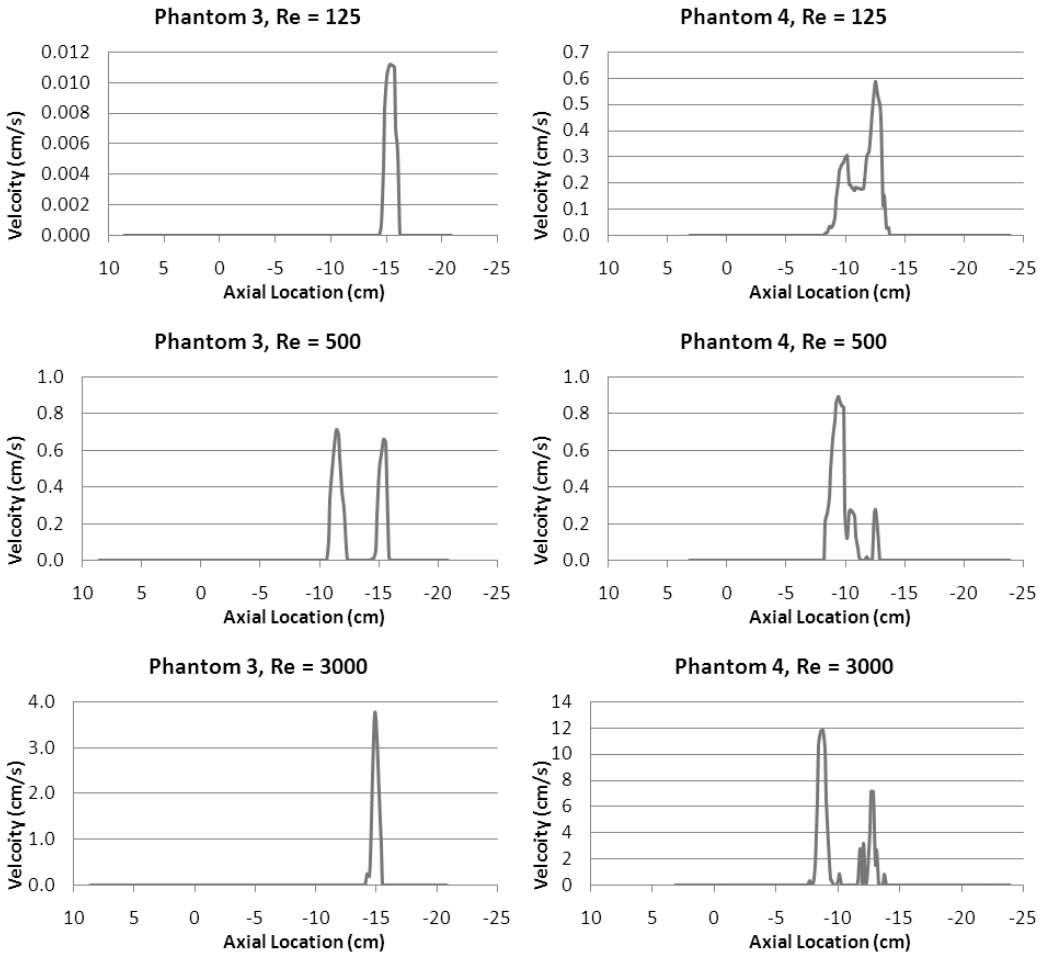

Figure 4.6 Maximum axial retrograde velocity for phantoms 3 and 4.

4.5 TURBULENCE

The dimensionless turbulent velocity, u'^*, and the turbulence intensity, *TI*, distributions are shown in figures 4.7 and 4.8, respectively. The u'^* and *TI* distributions are very similar, and should be given that the difference in computation is only in the denominator. While in the core flow, the u'^* and *TI* values closely matched, but in the low flows areas, the *TI* values may appear exaggerated in comparison to the u'^* values. These written results give an emphasis to u'^* values. While *TI* and u'^* both achieved values in excess of 1 (equal instability and velocity magnitudes), the scale was limited to a maximum of 1.

Since correlation error often manifests itself in terms of velocity instability, the turbulence results were particularly sensitive to correlation error. Where localized peak *TI* and u'^* values were present, these were often due to correlation error. The lower, background values are believed to be more accurate representations of actual instability.

Upstream of the lumen bends in phantom 3 (z = +8 cm to z = -3 cm), low u'^* values were seen in the developed flow. At Re = 125, the centerline values were near zero, with u'^* values around 0.1 near the walls. The Re = 500 flow showed greater turbulence near the walls with u'^* consistently near 0.2, but near zero values in the centerline. At Re = 125 and 500, these centerline values held throughout the majority of the flow field as baseline u'^* values remained near zero and were not sustained above 0.1. However, the Re = 3000 flow produced higher turbulence at nearly all points. Within the entrance section, centerline u'^* values ranged from 0.1 to 0.2 while near wall values increased to the neighborhood of 0.3. Elsewhere, baseline u'^* values were universally above 0.2 at Re = 3000 and turbulence increased within the aortic bends of the flow field.

Throughout the first bent to second bend (z = -4 cm to z = -8 cm), optical distortion produced erroneously higher instability, but correlation was otherwise adequate. Through the bends, unusual turbulence patters were formed compared to the straight tube section. At Re = 125 and Re = 500, the flow remained generally stable on the right wall, while higher turbulence was found on the left wall where u'^* values were between 0.5 and 0.7 at both flow rates. At Re = 3000, the low flow area was much more unstable, and u'^* values in excess of 0.7 across the flow cross section. After the final bend, there was elevated turbulence in the high shear areas surrounding the core flow. At Re = 125, the surrounding areas showed u'^* values of around 0.1 to 0.2 in the shear regions and below 0.1 in the core. The Re = 500 case was similar to the Re = 125 case; u'^* values were between 0.1 and 0.3 in the shear regions and below 0.1 in the core. The Re = 3000 case showed greater turbulence with u'^* values between 0.4 and 0.6 in the shear regions and 0.2 to 0.4 in the core.

The turbulence developed and behaved similarly in phantom 4 as in phantom 3, with the major exception of the saccular bulge. However, greater optical distortion within phantom 4 caused less

consistent results with more areas erroneously high turbulence readings. Throughout the flow field start into the first bend of the model (z = +3 cm to z = -8) cm, the Re = 125 and 500 flows produced near zero turbulence in the core flow and near wall of u'^* values around 0.1 at Re = 125 and around the 0.1 to 0.2 window at Re = 500. At Re = 3000, the u'^* values were between 0.2 to 0.4 near the walls and 0.1 to 0.2 in the core flow. Elsewhere, the baseline u'^* values remained below 0.1 for Re = 125, but at Re = 500 the background u'^* values were generally in the 0.1 to 0.2 region. The Re = 3000 case showed background u'^* values nearly universally above 0.2.

Within the aneurysm, the turbulence level increased as the core flow convects through the bulge with u'^* values near 0.2 at Re = 125, 0.3 at Re = 500 and 0.6 at Re = 3000. Optical distortion cause by the phantom fusion seam compromised turbulence results, most notably at Re = 125 and Re = 500. In the vortex section in the bulge near the anterior wall, the u'^* values generally remain at their background levels for Re = 125 and Re = 500. At Re = 3000, the instability is rampant and throughout most of the bulge, u'^* values were in excess of 1. Distal of the bulge, the turbulence decayed from the elevated aneurysm values back to baseline levels.

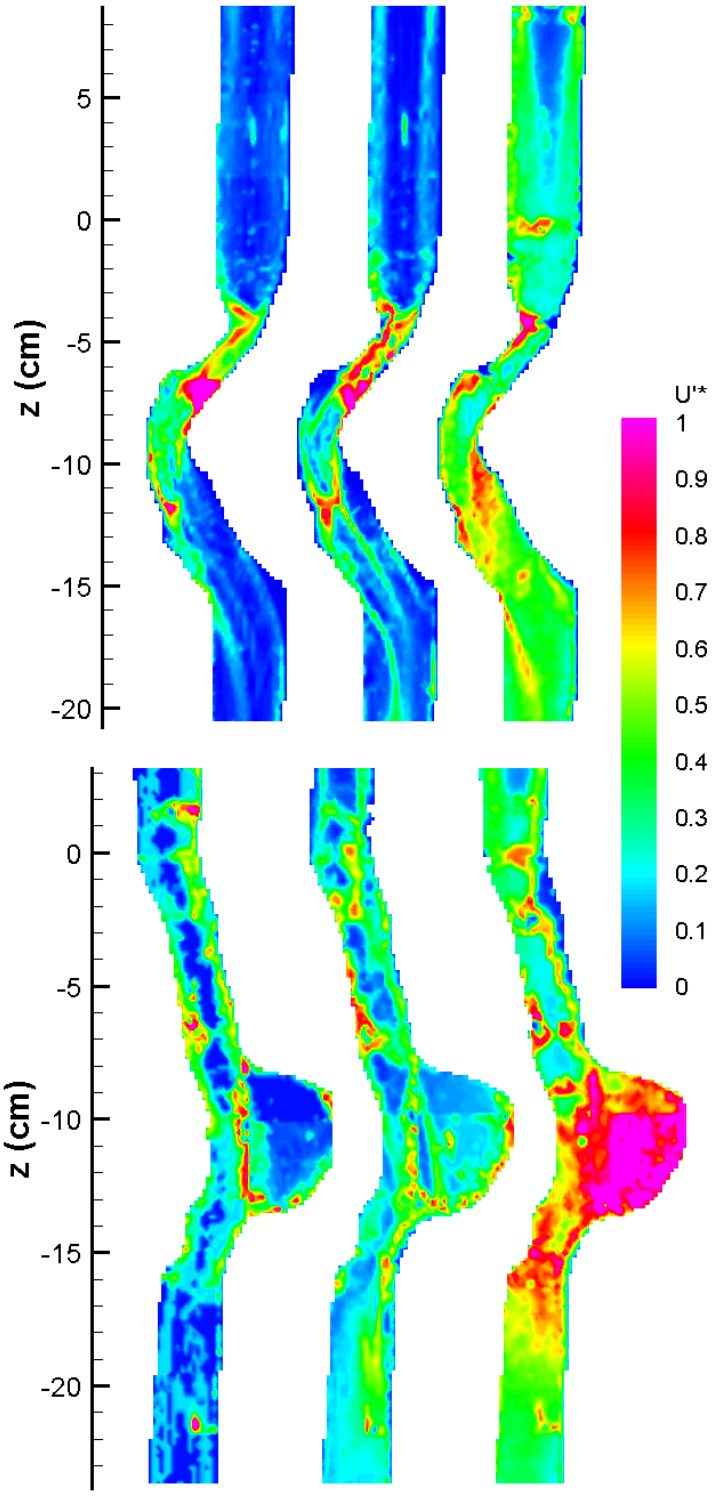

Figure 4.7 Dimensionless turbulent velocity, u'^{*}, distributions for phantom 3 (top) and 4 (bottom) at Re = 125 (left), Re = 500 (center), and Re = 3000 (right).

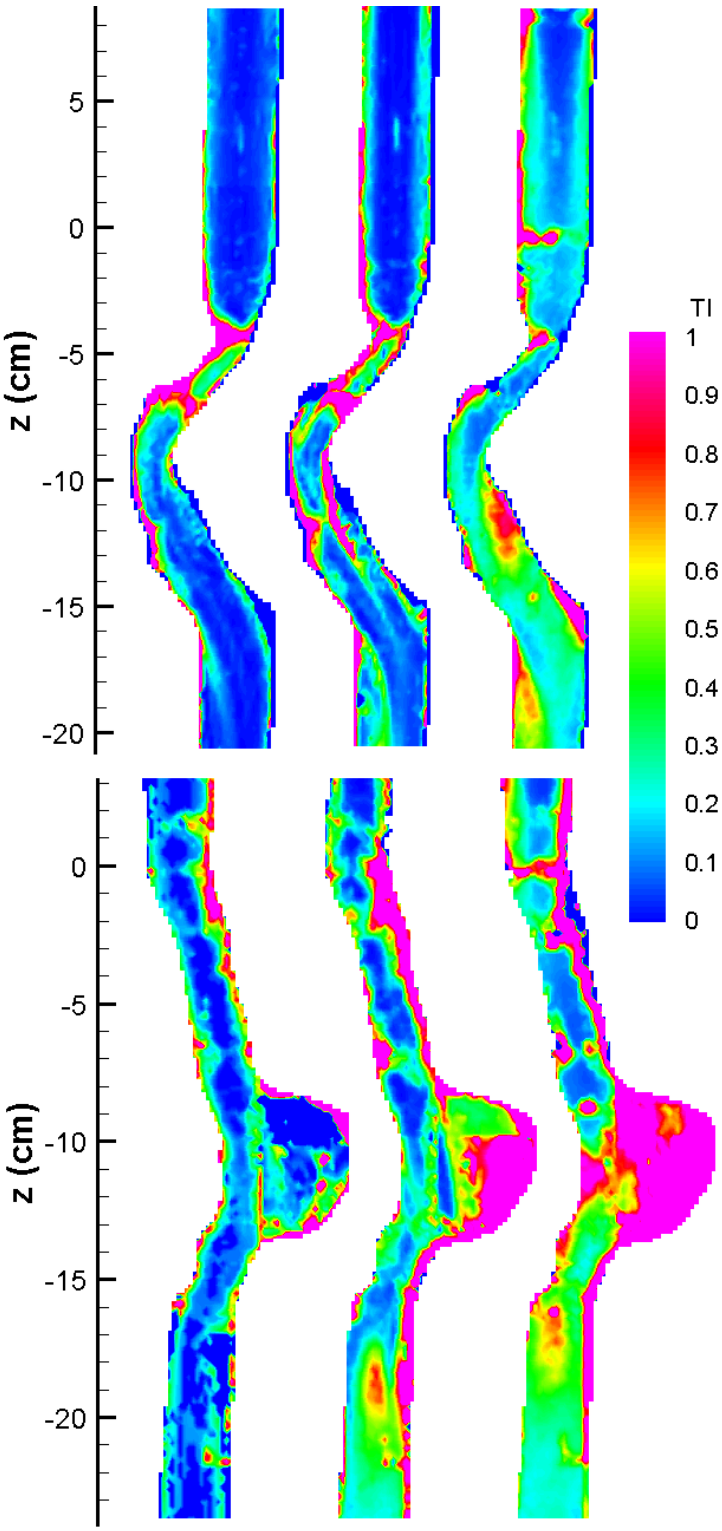

Figure 4.8 Turbulence intensity distribution for phantom 3 (top) and 4 (bottom) at Re = 125 (left), Re = 500 (center), and Re = 3000 (right).

4.6 SHEAR STRESS

The shear stress, τ, distributions (figure 4.9) were derived from the velocity profiles, and from these distributions, the wall shear stress was identified (figure 4.10). The mean wall shear stresses are reported in table 4.2. Due to the 2-D analysis techniques, these results did not include the contribution to overall shear of the out of plane velocity component, *v*, nor the out of plane spatial derivative, *dy*. However, since the flow fields are examined in a general vertical mid point, the contributions from the out of plane derivatives are expected to be minimized. Further, since only phantom 4 at Re = 3000 shows highly rotational secondary velocities (section 4.8), the out of plane velocity contributions are also expected to be low.

Phantom	Re	$\overline{\tau}_w$, wall 1 dyne/cm^2	$\overline{\tau}_w$, wall 2 dyne/cm^2
3	125	0.087	0.091
3	500	0.374	0.446
3	3000	2.50	2.93
4	125	0.066	0.117
4	500	0.223	0.614
4	3000	5.10	6.37

Table 4.2 Mean wall shear stress. For phantom 3, wall 1 is the left wall and wall 2 is the right wall. For phantom 4, wall 1 is the anterior wall and wall 2 is the posterior wall.

The flow rates between the phantoms show a general agreement of shear distributions. Overall, higher shear was concentrated closer to the walls at the higher flow rates, while shear was more evenly distributed at the lower flow rates. The bends typically caused high shear on one wall alternating with low shear on the opposing wall. The shear was generally at its lowest within low flow areas and recirculations. The combined mean wall shear stress tended to increase slightly faster than linearly with respect to the flow rate. Between Re = 125 and Re = 500, a 4 × increase would fit the linear prediction. However, in phantoms 3 and 4, a 4.6 × and 4.7 × increase in wall shear stress was found. Similarly, between Re = 500 and Re = 3000, a 6 × increase would fit the linear prediction, but experimentally, a 6.8 × and 6.6 × increase was found in phantoms 3 and 4.

The wall shear stress in the entrance of phantom 3 was mostly constant on both sides throughout the cylindrical inlet sections on both walls. Downstream of the first bend, the wall shear stress on the left and right walls showed opposing high and low values, dependent on which wall was impacted by the core flow. In the first bend, the wall shear stress on the right wall was elevated, while the wall shear stress on the left wall would be low. Through the bends, the momentum shifted and then the magnitudes were reversed so that wall shear stress values were elevated on the left wall and low on the right. In the exit section, the magnitudes switched yet again, with high values on the right wall and low on the left. In all flow rates, the maximum wall shear stress was seen on the right wall through the first bend in the lumen. These values were 0.33 dyne/cm^2 at Re = 125, 1.49 dyne/cm^2 at Re = 500, and 7.30 dyne/cm^2 at Re = 3000. Some notably low, near zero occurred in multiple locations where the flow was either separated or showed very low velocity in the wake of a bend. In all instances, the wall shear stress was elevated on the opposing wall.

In phantom 4, the wall shear stress was concentrated on the posterior wall throughout the entrance section and generally remained until near the bulge entrance where the anterior and posterior values would converge. Within the bulge, the wall shear stress was greatly reduced on the anterior wall adjacent to the separated and recirculating flow. Though it is not qualitatively represented in these absolute terms, the wall shear orientation is reversed throughout the bulge on the posterior wall due to the retrograde flow. On the anterior wall, the wall shear stress remained high until mid-aneurysm, when the wall shear reduced greatly as the lumen bent away from the core flow. Just proximal to the bulge constriction, the wall shear stress increased rapidly on both walls as the flow converged. In the exit sections, the wall shear stress decreased at Re = 125 and 500, but remained elevated at Re = 3000. The maximum wall shear stresses of 0.26 dyne/cm^2 at Re = 125, 1.20 dyne/cm^2 at Re = 500, and 6.91 dyne/cm^2 at Re = 3000 was observed on the posterior wall either just before the bulge entrance (Re = 500), just distal of the bulge opening (Re = 125) or nearly equal maxima values were seen at both sites (Re = 3000).

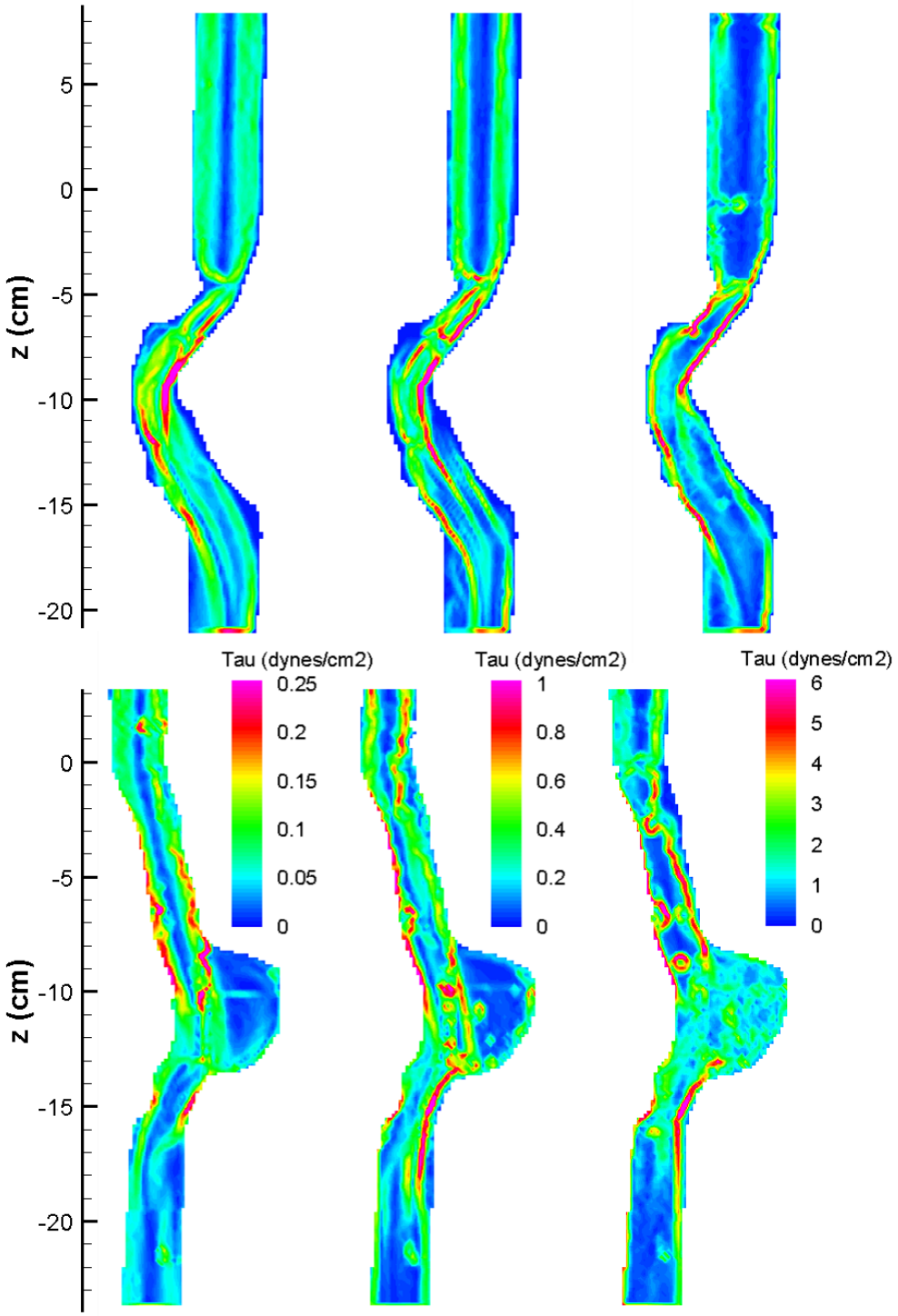

Figure 4.9 Shear stress distributions for phantom 3 (top) and 4 (bottom) at Re = 125 (left), Re = 500 (center), and Re = 3000 (right). Note that the shear stress scales are shared between phantoms but different at each flow rate.

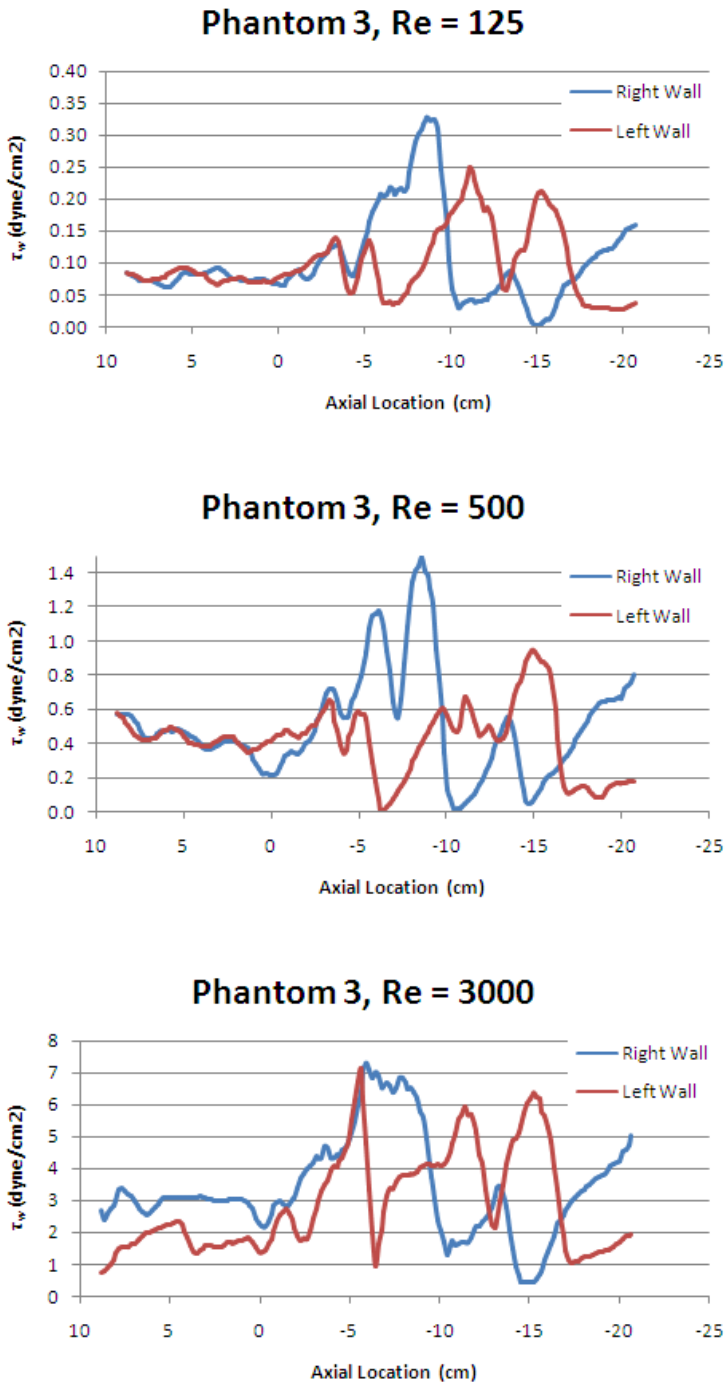

Figure 4.10 (part 1/2) Wall shear stress for phantom 3 in *in vivo* values.

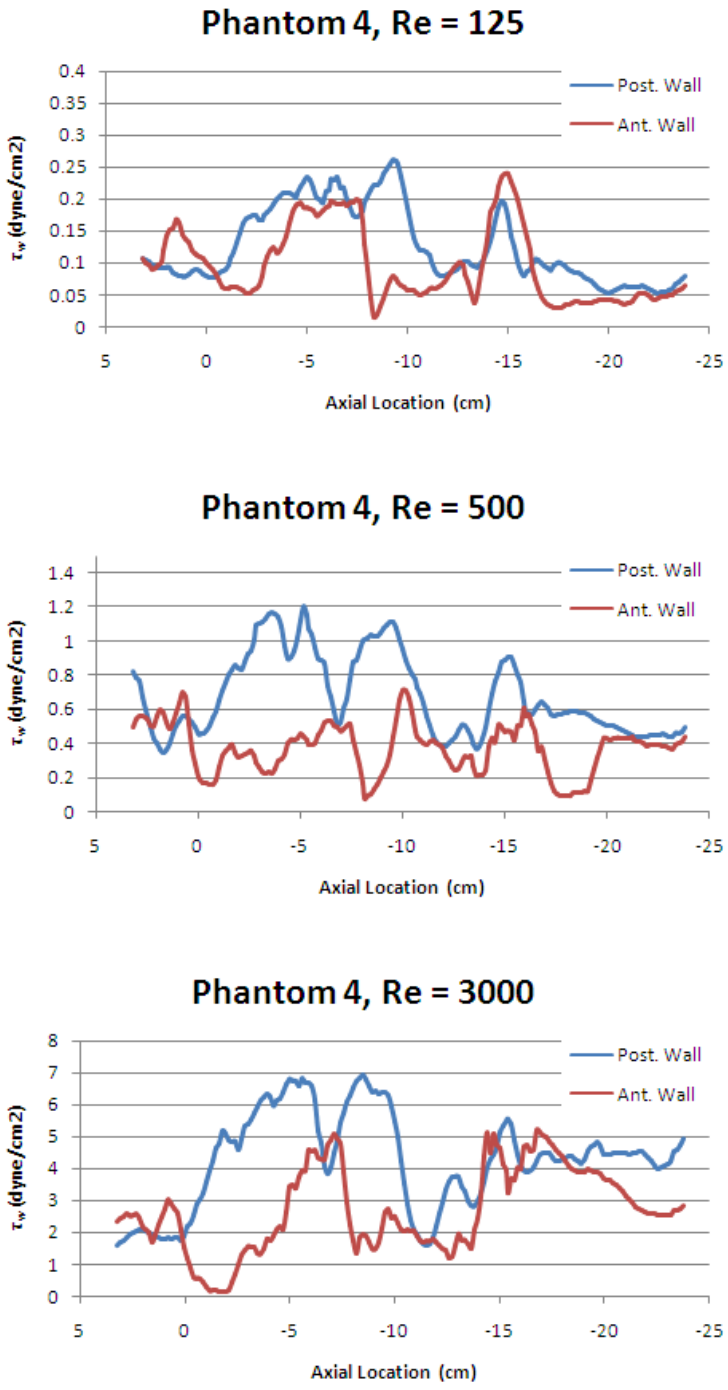

Figure 4.10 (part 2/2) Wall shear stress for phantom 4 in *in vivo* values.

4.7 CORRELATION RATE

The number of accepted vectors per interrogation area (or correlation rate), *N*, was determined during the vector validation process as unsuitable vectors were removed. The *N* distributions are presented in figure 4.11, however in contrast to the other contour plots, these were generated without blanking the out of flow field interrogation areas where *N* was universally 0. While the correlation rate cannot be directly associated with quality results, higher correlation rates were often indicative of better results. In this 2-D analysis, the *N* values ranged from 0 (no accepted vectors) to 200 (all vectors accepted). The average *N* values from the interrogated flow field of phantom 3 were 157 at Re = 125, 148 at Re = 500, and 99 at Re = 3000. For phantom 4, the average *N* values were 148 at Re = 125, 97 at Re = 500 and 80 at Re = 3000.

In phantom 3, the *N* distribution is reasonably consistent in the inlet section, except for some minor areas of low correlation near $z = 3$ cm and $z = 0$ cm. The correlation rate was compromised in near the first and second bend between $z = -4$ cm and $z = -8$ cm where phantom imperfections distorted the optics. The correlation increased downstream, especially at Re = 125 and Re = 500. Otherwise, the correlation rate remains high through the flow field.

In phantom 4, the *N* distribution showed choppy distributions and overall lower correlation rates and more choppy patterns than phantom 3. Correlation was inconsistent within the the entrance sections between $z = +2$ cm and $z = -8$ cm and was especially low near the right wall. An optically impeding deformity of the phantom exterior caused very low correlation area within the bulge center, with $N > 20$ seen at all flow rates. While reasonably high *N* values were seen elsewhere in the bulge at Re = 125 and Re = 500, very low correlation rates were in the bulge at Re = 3000. Downstream of the bulge, the correlation was at a higher and more consistent rate.

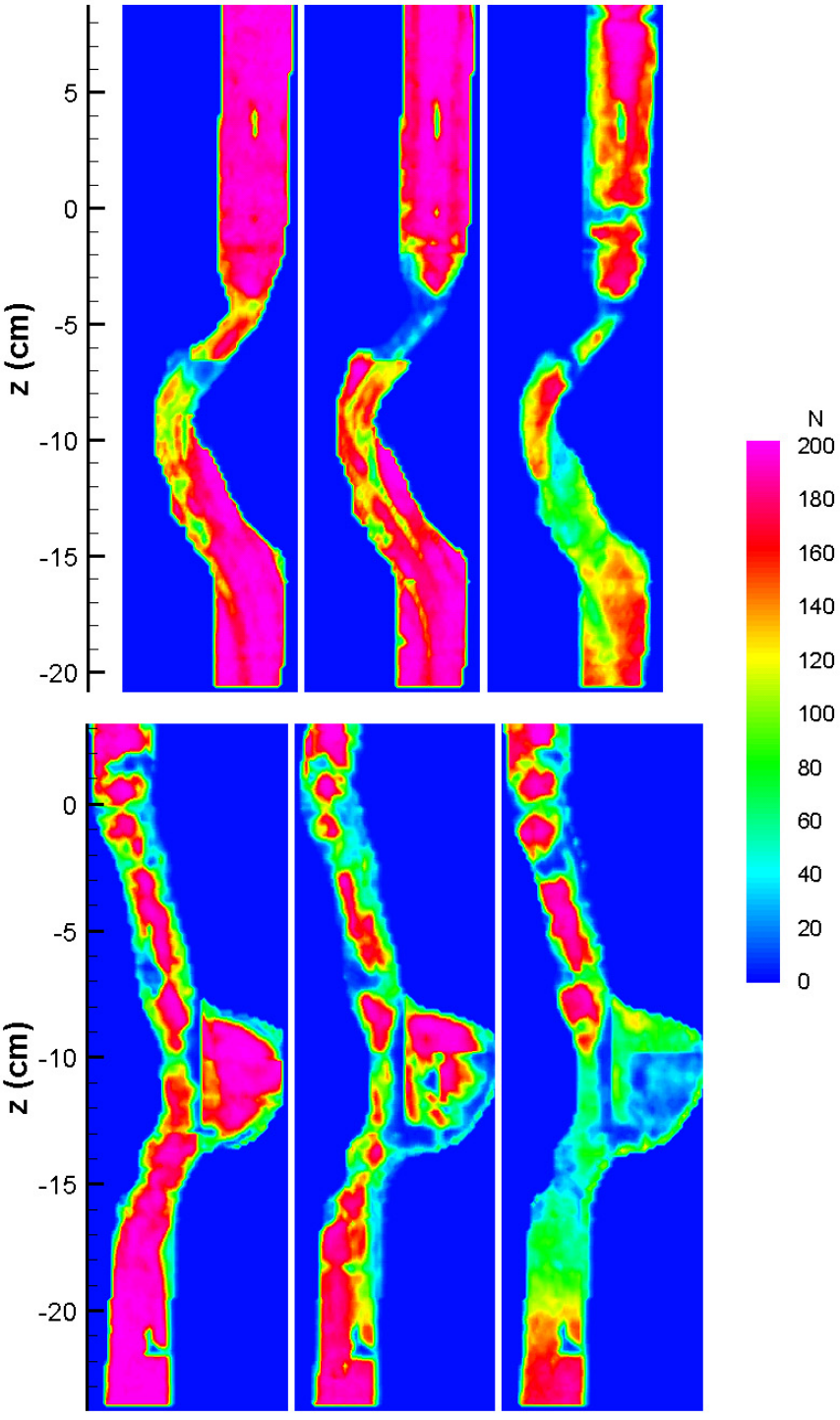

Figure 4.11 Correlation rate, *N*, distribution in phantom 3 (top) and phantom 4 (bottom) at Re = 125 (left), Re = 500 (center), and Re = 3000 (right).

4.8 3-D VELOCITY FLOW FIELD

From the 3-D flow field constructions of phantom 3 and phantom 4 (figure 4.12), transverse slices were taken at multiple locations (colored boundaries, figure 4.12). Their axial velocity distributions (w; figure 4.13, top row) and secondary velocities (u and v; figure 4.13, bottom row) were exposed at Re = 500 and Re = 3000. The point of view in these transverse slices is vertically down so that the core flow is traveling away from the figure. The anterior wall is on the figure top and the posterior wall is on the bottom, while the left and right walls are on the left and right sides of the figures.

In phantom 3, the flow field progresses as described in the 2-D results. With the inherent exception of the velocity magnitudes, both flow rates behaved essentially similarly. A centered, well developed core flow is shown within the entrance sections. Through the bends, the momentum is focused on the right wall (z = -2.5 cm), then shifts back through center (z = -5.0 cm) towards the left wall (z = -8.5 cm and -12.0 cm) before shifting back to the right wall in the exit section (z = -16.0 cm). No significant retrograde motion was captured in any of these transverse slices. Through the lumen bends, the flow shows lateral motion in the x direction, but little evidence of motion in the y direction. No swirling or rotational motion was seen in the non-axial velocity components. At Re = 500, the non-axial velocity (u, v contribution only) reached a peak of 7.2 cm/s within the z = -8.5 cm slice while at Re = 3000, the peak non-axial velocities was 41.3 cm/s at z = -2.5 cm.

In phantom 4, the 3-D flow fields were also behaved as described in the 2-D results. Transverse slices provided much more detail of the vortex structure and showed slightly different patterns at the different flow rates. At Re = 500, the recirculation within the bulge was strongest on the anterior wall (z = -8.5 cm through -11.5 cm) while at Re = 3000 the retrograde flow was more focused on the left wall. The retrograde axial velocities in the separated flow appeared proportionally greater at Re = 3000. The core flow also shifted from the mid posterior wall at Re = 500 to the right posterior corner at Re = 3000 and it appear to be much wider than at Re = 500. At Re = 500, some non axial motion was seen within the bulge, but did not appear to have distinct structure patterns other than accommodating the bulge walls and the maximum non-axial velocity (u, v contribution only) was 5.1 cm/s within the z = -15.0 cm slice. In striking contrast, at Re = 3000, a very strong out of plane rotation is formed. A counterclockwise rotation throughout the entire bulge was formed. The vortex center moved from the bulge anterior/center position (z = -8.5 cm and -10.0 cm) towards the posterior wall and the bulge outlet (z = -11.5 cm). The maximum out of plane velocity was 66.8 cm/s within the z = -11.5 cm/s slice. This clockwise motion was maintained distal of the aneurysm and remained intact in the exit section (z = - 19.0 cm).

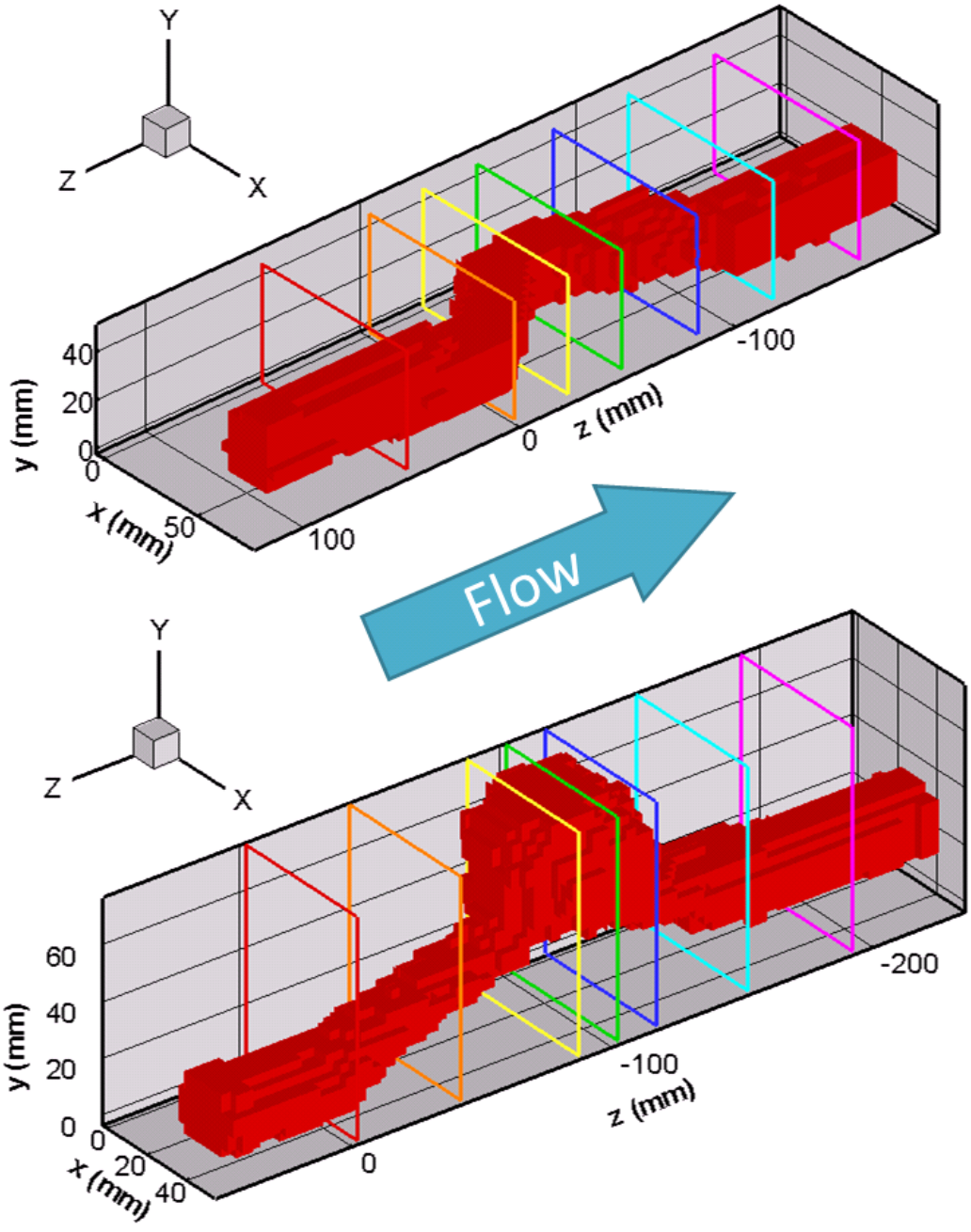

Figure 4.12 Three dimensional flow flied constructions for phantom 3 (top) and phantom 4 (bottom). The multicolored boundaries indicate the locations of the transverse slices used in figures 4.13 to 4.14.

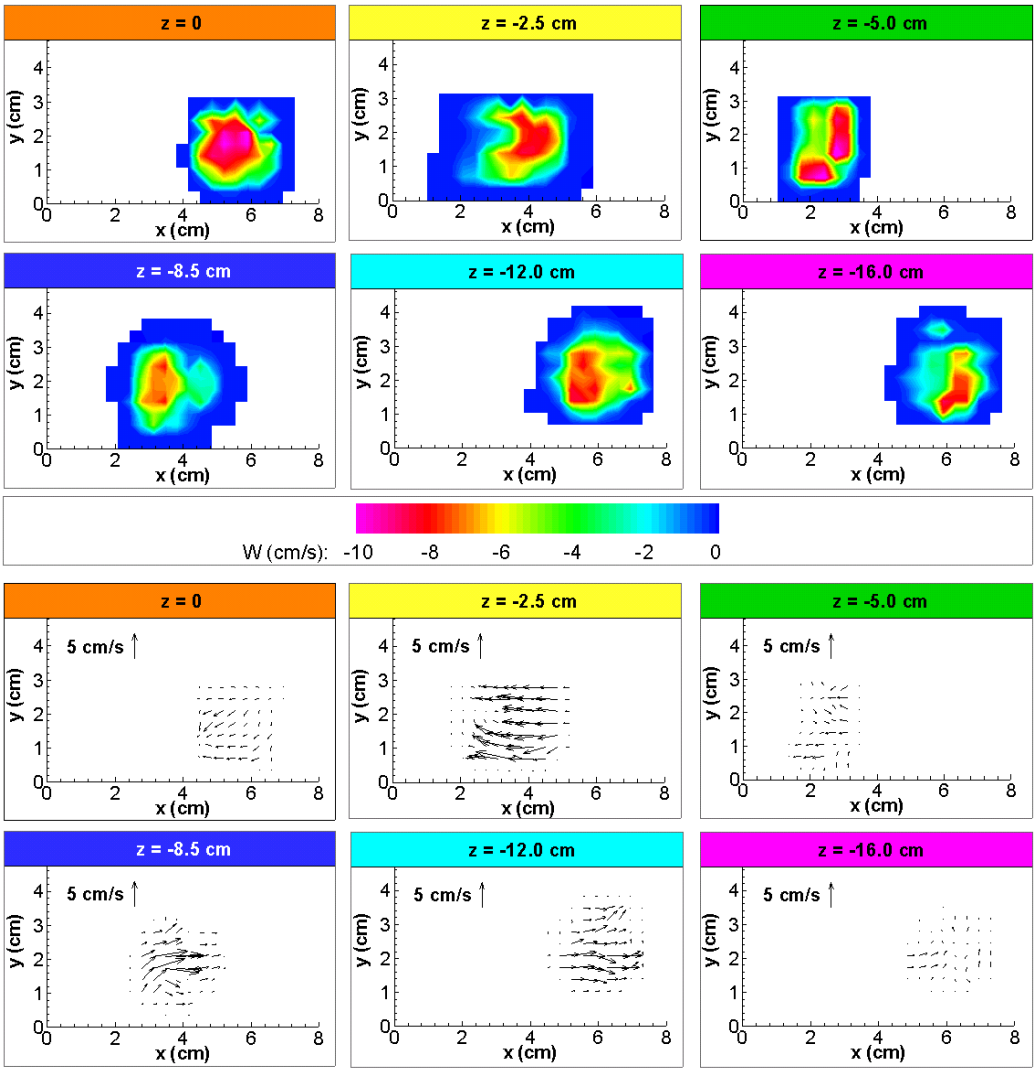

Figure 4.13 (part 1/4) Axial velocity (*w*; top two rows) and secondary velocity (*u* and *v*; distributions) distributions from transverse slices of phantom 3 at Re = 500.

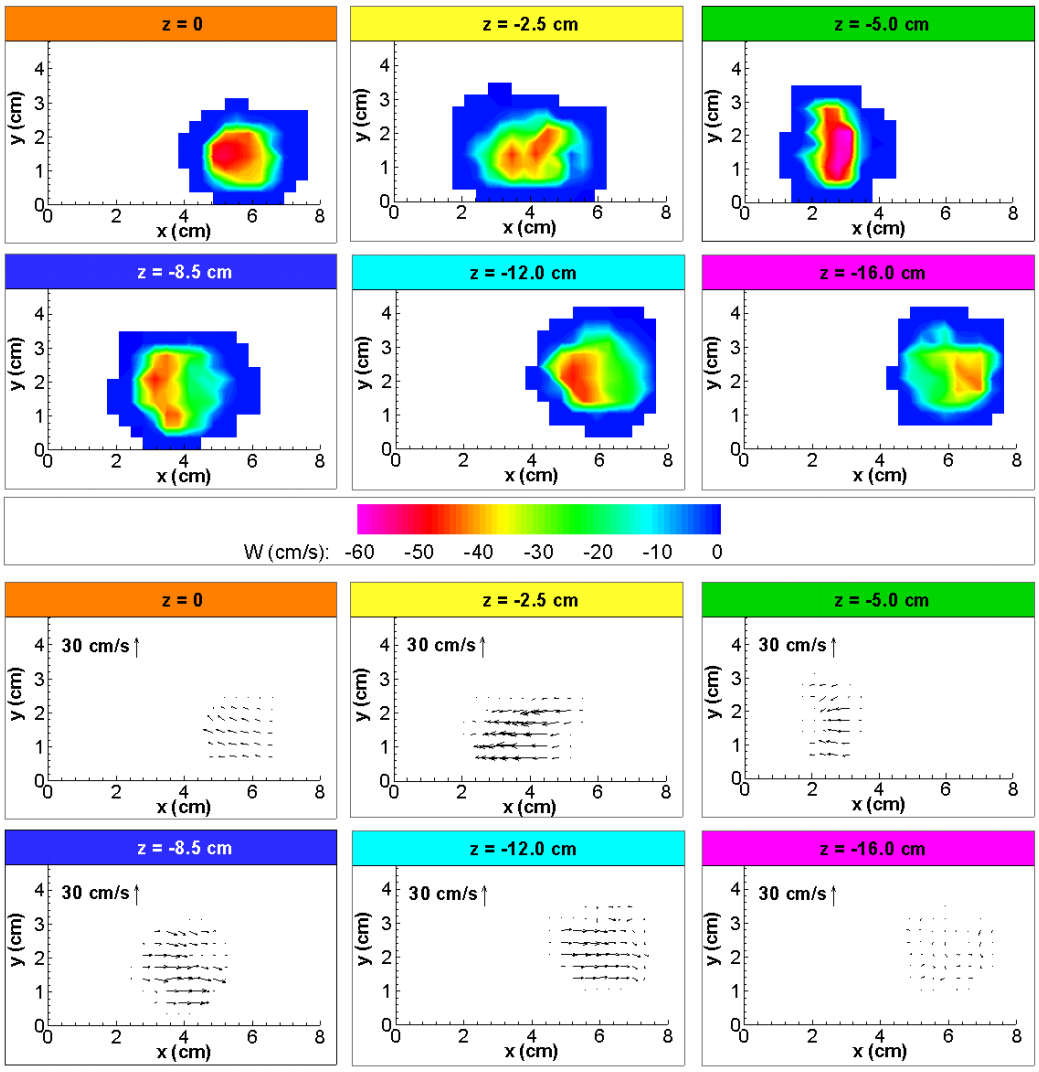

Figure 4.13 (part 2/4) Axial velocity (*w*; top two rows) and secondary velocity (*u* and *v*; distributions) distributions from transverse slices of phantom 3 at Re = 3000.

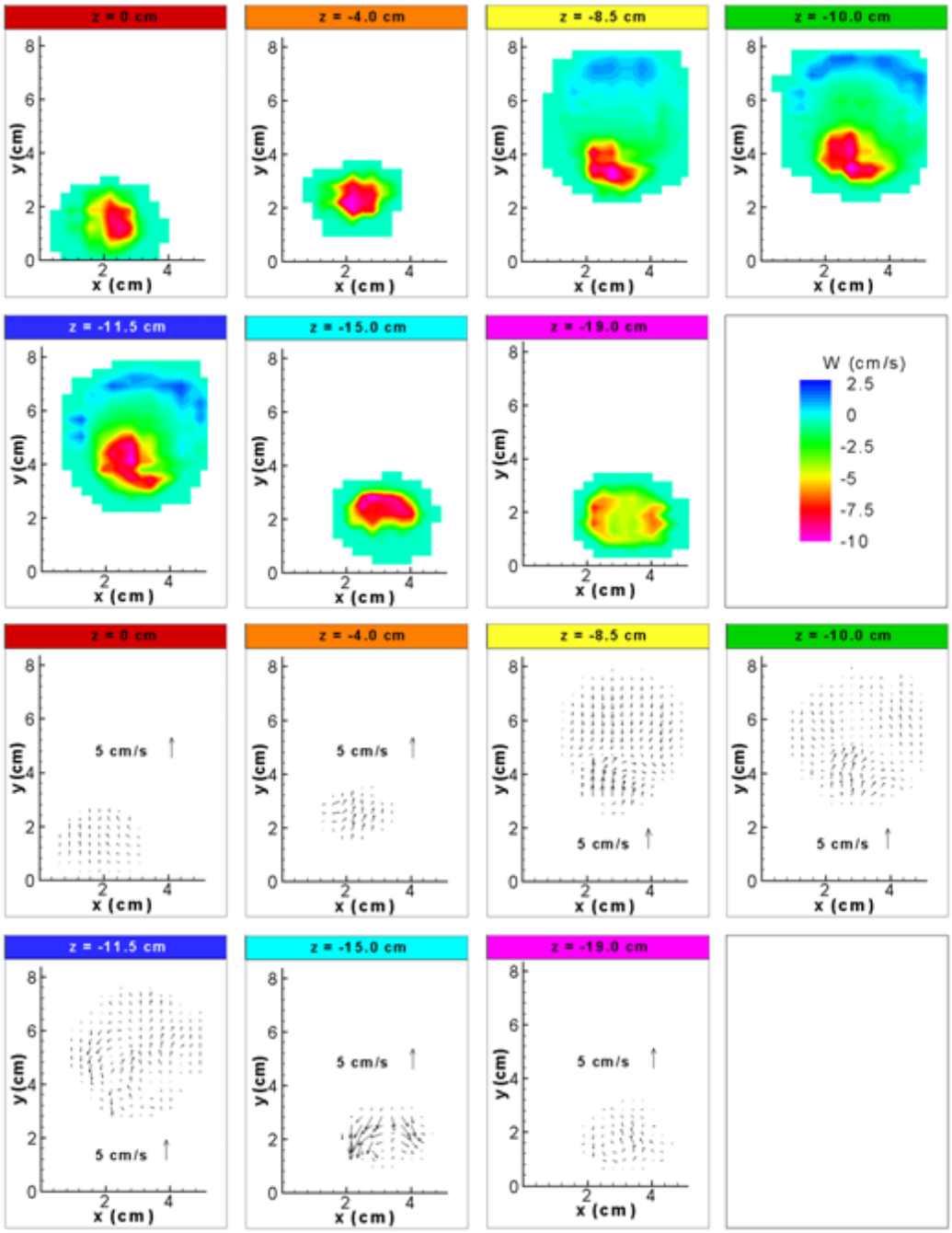

Figure 4.13 (part 3/4) Axial velocity (*w*; top two rows) and secondary velocity (*u* and *v*; distributions) distributions from transverse slices of phantom 4 at Re = 500.

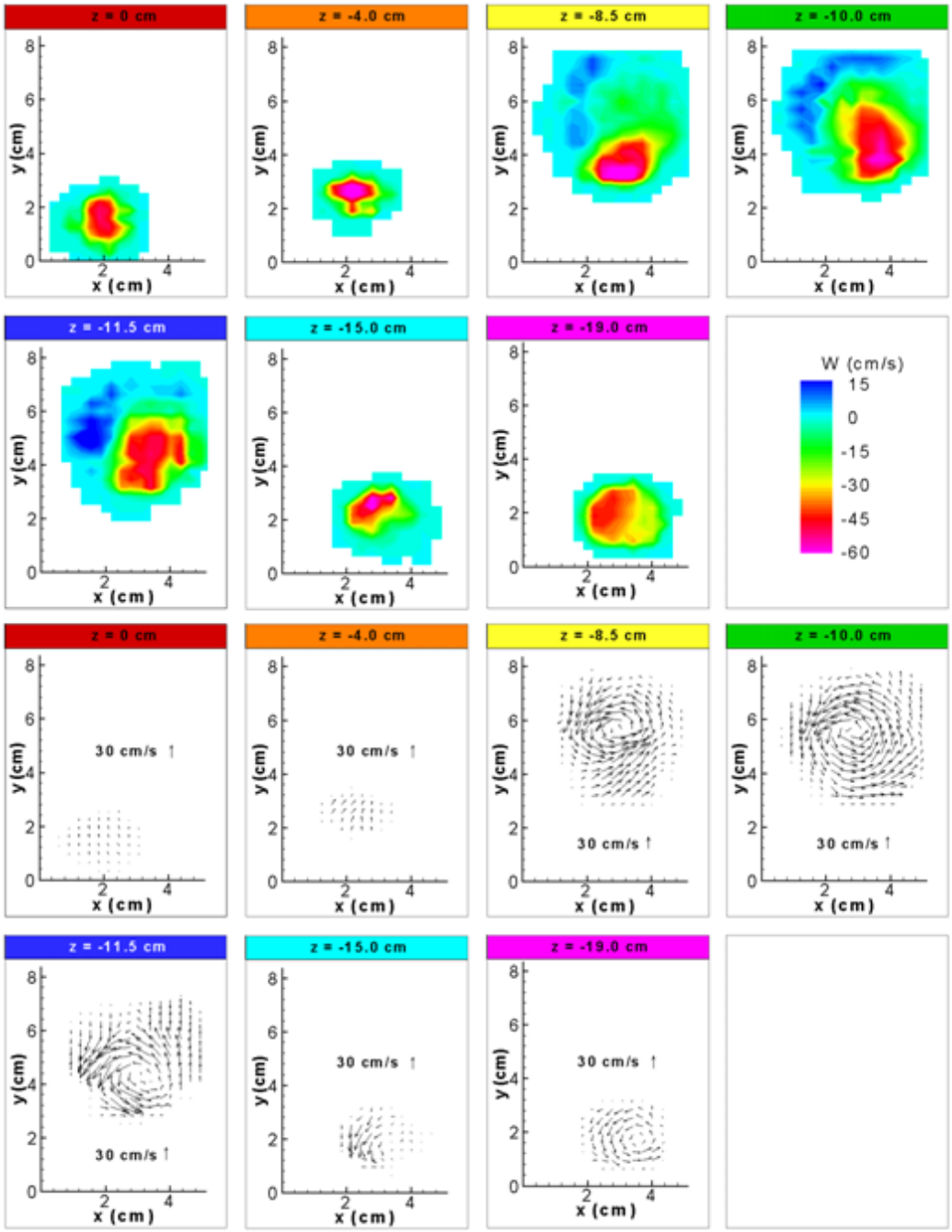

Figure 4.13 (part 4/4) Axial velocity (*w*; top two rows) and secondary velocity (*u* and *v*; distributions) distributions from transverse slices of phantom 4 at Re = 3000.

CHAPTER 5: COMPUTATIONAL RESULTS

Steady flow fields in the series of ten models (figure 3.12) were computationally analyzed under laminar and turbulent schemes for Reynolds numbers of 500, 1000, 2000 and 3000. For brevities sake, each of these 80 simulations will not be investigated in depth. Analysis here is restricted to Re = 500 and Re = 3000 and laminar and turbulent comparisons are limited. Three models (1, 7 and 8) were selected to be studied in detail to provide representative results for the series. Results for phantoms 1-10 under the same flow rates are shown in appendix B. Model 8 contained a nearly axi-symmetrical, fusiform aneurysm, with mild thrombus deposits. It is referred to as the 'fusiform model.' Model 1, the 'saccular model,' has a highly bulged, saccular aneurysm with no thrombus. This model also corresponds to phantom 4 of the experimental studies. Model 7 contained a saccular aneurysm had high thrombus accumulation, constricting the lumen. For this reason it is referred to as the 'isodiameteric model.' This model corresponds to phantom 3.

5.1 STREAM TUBES

The turbulent flow fields at Re = 3000 of each of the ten models were examined with stream tubes (figure 5.1). Stream tubes were placed to accentuate the separated flow and strong non-axial motion, but as a consequence the core flow is underrepresented by these figures. All are presented from the posterior point of view.

Model 1 contains a very pronounced, saccular bulge with no thrombus deposits. The flow remained attached to the walls in the non-dilated section between the entrance and the bulge inlet. Here, the stream tubes were essentially parallel to the aortic wall and nearly no lateral motion was observed. Within the bulge, flow separated along the left and anterior walls forming a single large vortex with both lateral and retrograde motion characteristics. The core flow remained attached to the right, posterior wall and widened somewhat throughout the dilation, in part due to additional forward flow opposing the retrograde flow. Some of the core flow impacted the distal surface, in evidence by the sharply bent stream tubes. Here the flow either both separated and reversed into retrograde motion or it remained attached and exited the distal end of the bulge. Distal of the bulge, the flow remained attached and showed little lateral motion. As the flow approached the bifurcation, the flow split laterally into each leg of the iliac arteries.

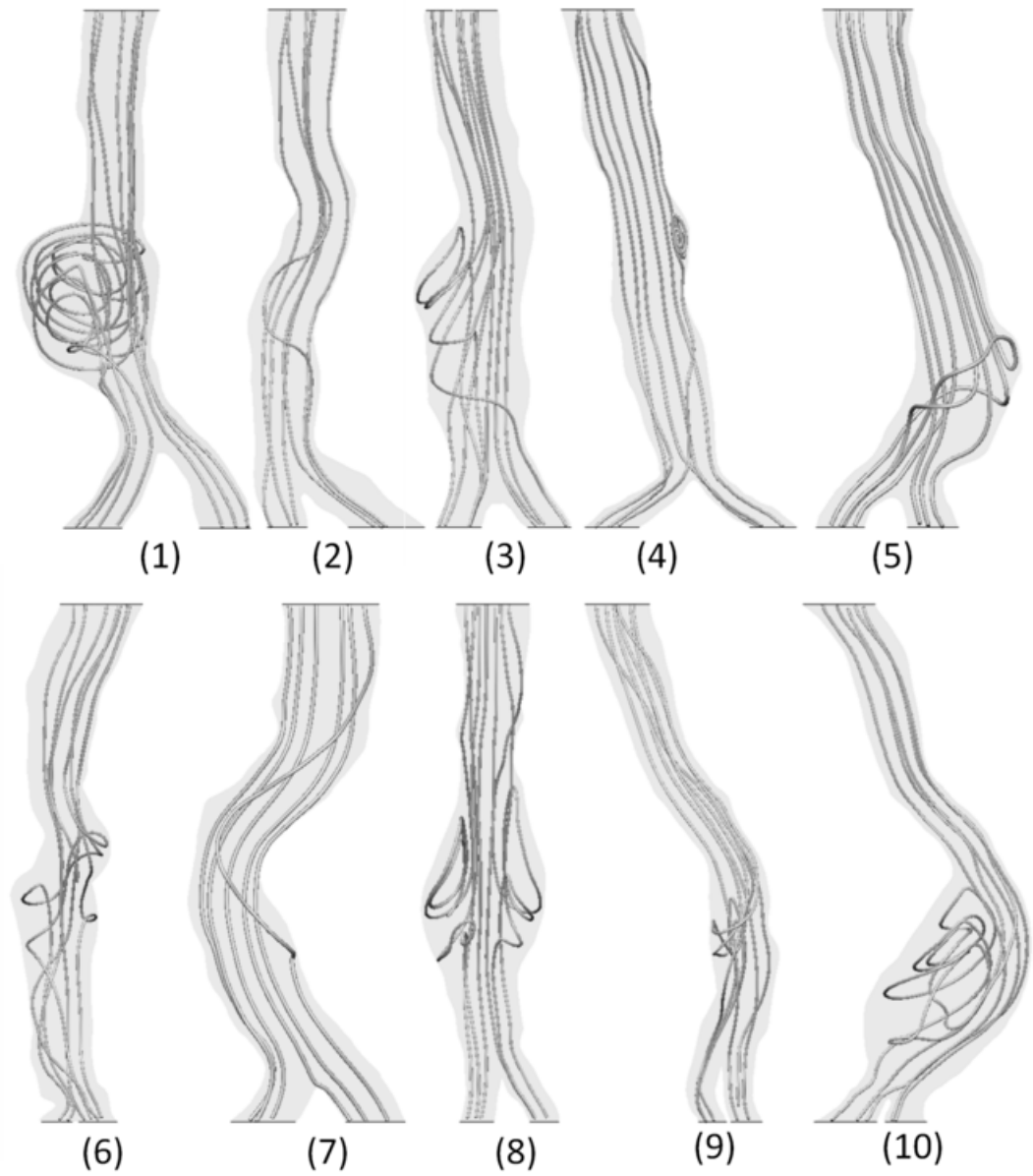

Figure 5.1 Stream tubes within turbulent flow fields at Re = 3000 for models 1-10, viewed from the posterior point of view.

Model 2 contains a saccular aneurysm, filled with thrombus and which constricts the lumen making it generally isodiameteric. Sharp bends in the lumen cause significant lateral motion. These bends are both from non-dilated sections as well as tunneling through the intralumenal thrombus. While the flow remains attached through the vast majority of the model, a minor flow separation occurs 7 cm downstream of the inlet (not visible in this image). However, much less vortocicy was present in this model due to the lack of dilation.

Model 3 contains a somewhat unique lumen, which has a double 'hump' in the dilation due to a slight constriction mid bulge; nothing similar is seen within this aneurysm series. The aneurysm is mostly fusiform, except a small thrombus filled sac is present on the left wall of the top hump. Separation occurs on the left wall at the proximal end of the aneurysm with lateral and retrograde flow occurring here. The core flow reattaches well before the lumen constriction. No separation is observed elsewhere in the model.

Model 4 contains a fusiform aneurysm with moderate thrombus deposits that constrict the lumen yielding a mostly isodiameteric lumen. A small but pronounced separation occurs on the right wall which proximal to the aneurismal dilation. Otherwise the flow is entirely attached throughout the model.

Model 5 contains a saccular AAA, with mild thrombus deposits that leave a less prominent sac on the lumen. A single vortex forms on the right and posterior wall within this sac.

Model 6 contains a large saccular aneurysm, filled with thrombus yielding an unusual, tortuous lumen. While the view in figure 5.1 fails to capture the sharp bends, these generate numerous flow separations, all of modest size. Three distinct separations are visible here: one on the left, two on the right. Downstream of the recirculations, a mild lateral fluid motion remains in the straightened section.

Model 7 contains a saccular AAA on the left wall, though it is filled with thrombus constricting the lumen throughout the aneurysm. The lumen forms a sweeping arc, but remains in a planer configuration without showing significant thoracic bend. The flow remains attached from the entrance to the exits other than two some minor separations downstream of some sharper lumen bends (not visible in this figure). Otherwise, lateral acceleration occurs as the momentum shifts from walls due to the arcing lumen. Very small separations occur at two bends within this model, though they are not visible in this figure. Model 7 contains the widest arteries of the series.

Model 8 contains a fusiform AAA with mild thrombus deposits. Within this aneurysm, a unique phenomenon occurs: two separate vortices form on the left and right aneurysm wall, which are nearly mirror images in regards to their size, position and flow patterns. The flow remains attached to the walls on both the anterior and posterior walls, effectively separating the recirculation in two equal halves.

Model 9 is a fusiform aneurysm, but its lumen is somewhat constricted due to thrombus. A single small but well formed recirculation occurs on the left wall while the flow remains attached on the rightmost wall. Highly lateral motion occurs between the aortic bends but flow remains attached. Model 9 has the narrowest aorta of the series.

Model 10 contains a large, saccular AAA with mild thrombus deposits. Model 10 provides an unusual aortic path, with a long and relatively thin winding pathway proximal to a large dilation. While the aneurysm is slightly smaller than the saccular aneurysm in model 1, it has the largest bulge diameter in relation the non-dilated aorta. Due to the lumen curvature, the core flow remains attached to the right wall. Opposite the core flow, a single large vortex forms on the entire left wall and most of the anterior and posterior wall. The flow within the vortex has only mild retrograde character but highly lateral motion. The core flow widens within the dilation until it reattaches, just proximal to the constriction.

5.2 VELOCITY PROFILES

To display flow field properties, visualization slices from the coronal planes were used to bisect the models. A single plane was not well contained within the models, and as such was not able to depict features from the entirety of the flow field. Most models contained an approximately 10° bend in the aorta was present to accommodate the thoracic spine. Consequently, the flow field results were generated by combining data from two intersecting planes, and were able to contain the majority of the flow field. These planes were viewed from the posterior, always the acute angle, as extraneous ‘leafs’ formed on the obtuse side behind the target visual. The lone exception was model 7 for which which a single visualization slice was able to demonstrate the flow field.

Vector maps were generated for the saccular, fusiform, and isodiameteric model under laminar and turbulent schemes for the flow rates of Re = 500 and Re = 3000 (figure 5.2). Primary vectors were spaced evenly at 1.25 cm intervals, while secondary vectors were added to provide more detail within the vortices at 0.625 cm intervals between the primary vectors. The vectors lengths were scaled so that the same reference vector was used for both flow rates, with a six fold increase in magnitude matching the flow rate increase. The reference vector length was the same for all models. The extraneous leafs were manually erased to display only the target vectors and front most wall traces. Additionally, maximum velocities were chosen as the parameter to describe the profile. When used in comparison to other flows at the same location, they can provide a rough comparison of profile between conditions.

The fusiform model showed very similar, but not identical, flow fields for the laminar and turbulent cases. As would be expected, at Re = 500 the laminar calculation produced a rounder, more nearly parabolic entrance profile than did the turbulent calculation, for which the inlet profile was flatter

and more blunt. The centerline, maximum velocity at the inlet was 11.0 cm/sec for the laminar field, whereas it was 9.1 cm/sec for the turbulent field. However, as fluid convected through the aorta and into the proximal bulge, the turbulent profile gained momentum in the center and lost momentum near the wall. Consequently, the difference between the laminar and turbulent profiles decayed, so that the two profiles were nearly identical shortly downstream of the inlet and the differences in maximum velocities were below 1 percent. At 6 cm downstream of the inlet, the maximum velocity was 12.2 cm/s for the both the laminar and turbulent case. Within the bulge, the two nearly symmetrical recirculations flanked the core flow. Core flow in the bulge in this model was nearly identical for both laminar and turbulent calculations. The maximum velocity in the core at the widest level of the aneurysm, 11 cm downstream from inlet, was 6.4 cm/s for both cases. The maximum retrograde velocity in the outer vortices at the same level was 2.1 cm/sec for both cases. Constriction of the wall at the bulge exit led to a rapid shear layer near the wall with a nearly uniform profile across the core. Maximum velocity in the core downstream of the bulge at 2 cm proximal to the bifurcation were 8.5 cm/s and for both cases. As the flow approached the bifurcation, its core then began to skew due to fluid accelerations caused by the lumen constriction and curvatures.

A similar evolution of the flow field occurred in this model at Re = 3000, though with 6 times larger velocities and flow rate at the inlet. The maximum inlet velocity was 66.0 cm/sec for the laminar case and 54.4 cm/sec for the turbulent case. A blunter profile was seen at the higher flow rate, and greater velocity differences were present between the laminar and turbulent flow fields. At 6 cm downstream of the inlet, the maximum velocities were 67.9 cm/s for the laminar case and 64.1 cm/s for the turbulent case. The maximum velocity at the widest point was 43.8 cm/sec for the laminar case and 40.1 cm/sec for the turbulent case while the maximum retrograde velocities in the outer vortices were 15.4 cm/sec and 16.4 cm/sec. Maximum velocities 2 cm proximal to the bifurcation were 46.5 cm/sec for the laminar case and 46.8 cm/sec for the turbulent case.

Inlet flow in the saccular model was similar to that in the fusiform model. At Re = 500, the maximum centerline velocities of 9.9 cm/sec for the laminar case and 8.0 cm/s for the turbulent case. The differences in velocities between the laminar and turbulent cases decayed rapidly from the inlet so that at 6 cm downstream of the inlet, the maximum velocities were 11.2 cm/s for the laminar case and 11.1 cm/s for the turbulent case. Within the bulge, the single large vortex showed an expanded core on the right most side and prominent recirculation on the left most side. The maximum velocities at the widest plane of the aneurysm, 10 cm downstream of the inlet, were 9.3 cm/s for the laminar case and 9.2 cm/sec for the turbulent case, while the maximum retrograde velocities at this level were 1.7 cm/s for both cases. Downstream of the aneurysm, the flow showed a nearly flat velocity profile due to the rapid constriction. The maximum velocity in this region, 2 cm proximal to the bifurcation, was 12.1 cm/sec for both cases.

Again, similar patterns developed at Re = 3000, but with larger velocities. At the inlet, the maximum velocities were 59.4 cm/s for the laminar case and 48.1 cm/s for the turbulent case. Greater differences were seen between the laminar and turbulent cases. At 6 cm downstream of the inlet, maximum velocity was 62.8 cm/s for the laminar case and 59.5 cm/s for the turbulent case. The maximum velocity at the widest plane of the aneurysm was 55.9 cm/sec for the laminar case and 54.1 cm/sec for the turbulent case, and the maximum retrograde velocities at this level were 12.6 cm/s and 13.7 cm/s. The maximum velocities 2 cm proximal to the bifurcation were 71.6 cm/s for the laminar case and 72.9 cm/s for the turbulent case.

A well developed profile was maintained throughout the isodiametric model, perturbed only by lateral accelerations as the flow followed the bends of the lumen. Two minor recirculations were seen: one on the left wall at 7 cm downstream of the inlet and one on the right wall at 13 cm downstream of the inlet (both accented by secondary vectors). At Re = 500, the maximum inlet velocities were 8.4 cm/sec for the laminar case (not shown) and 6.5 cm/sec for the turbulent case. Differences between the laminar and turbulence cases decayed shortly downstream of the inlet and became indistinguishable throughout the remainder of the model. Maximum velocities 9 cm downstream of the inlet, the widest point of the aneurysm (which was not the widest point of the lumen), were 9.5 cm/s for the laminar case and 9.4 cm/s for the turbulent case; no retrograde flow occurred here. The maximum velocities 2 cm proximal to the bifurcation were 8.4 cm/s for both cases.

At Re = 3000 in the isodiameteric model, the two small vortices remained, and were more intense and marginally larger than at the lower flow rate. Otherwise, the flow had more momentum near the walls and a flatter profile throughout the model. Greater differences between the laminar and turbulent cases occurred, though still much less than the differences observed in the bulged models. The inlet velocities were 50.5 cm/s for the laminar case and 39.3 cm/s for the turbulent case. At 6 cm downstream of the inlet, the maximum velocities were 54.3 cm/s for the laminar case and 52.2 cm/s for the turbulent case. At the widest point of the aneurysm, the maximum velocities were 55.4 cm/sec for the laminar case and 53.5 cm/sec for the turbulent case with no separation. The maximum velocities 2 cm proximal to the bifurcation were 46.7 cm/s and 46.6 cm/s.

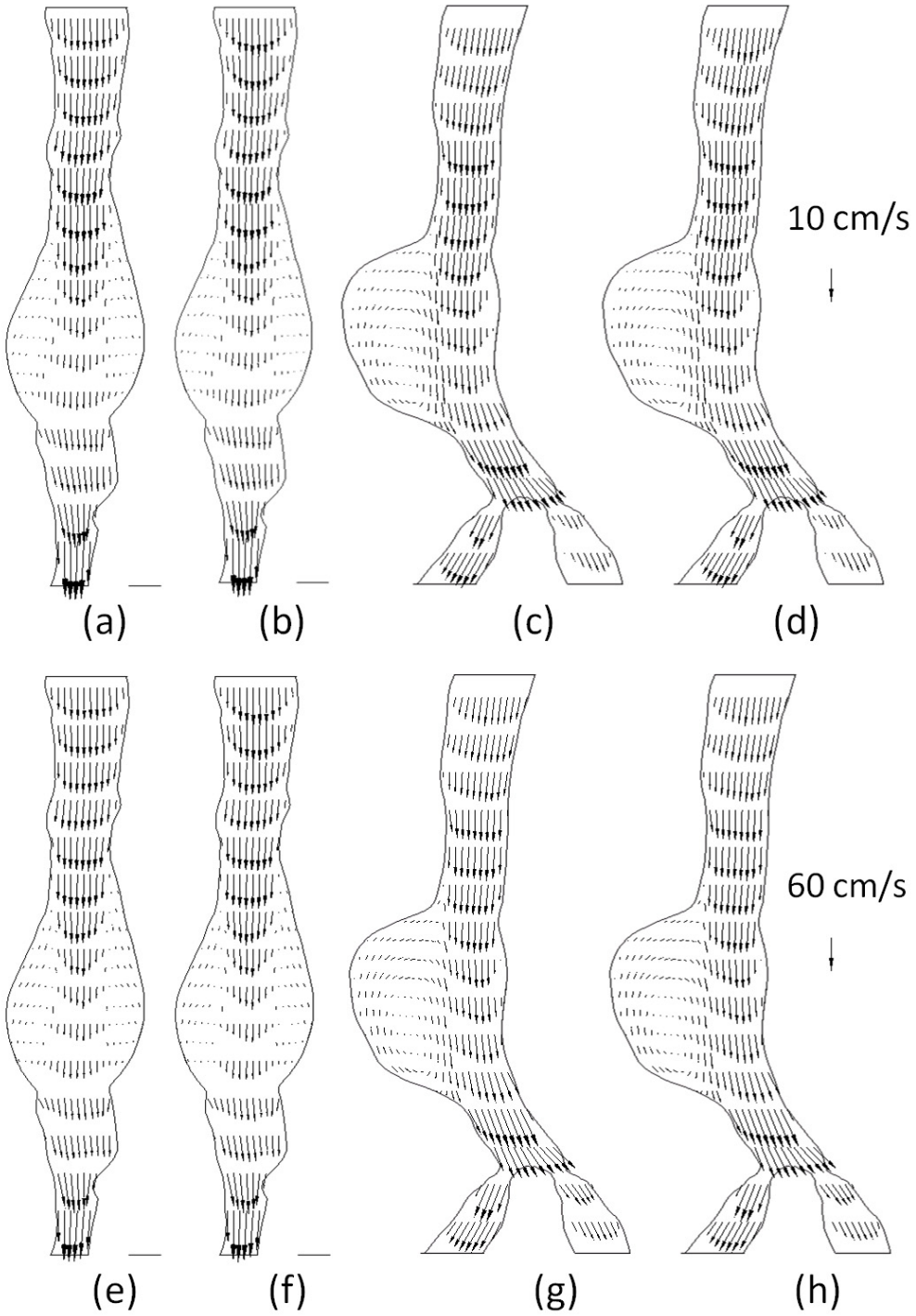

Figure 5.2 (part 1/2) Velocity distribution in (a-b, e-f) fusiform model, (c-d, g-h) saccular model for Re = 500 (top row: a-d), and Re = 3000 (bottom row: e-h) under turbulent solutions (left: a, c, e, g) and laminar solutions (right: b, d, f, h).

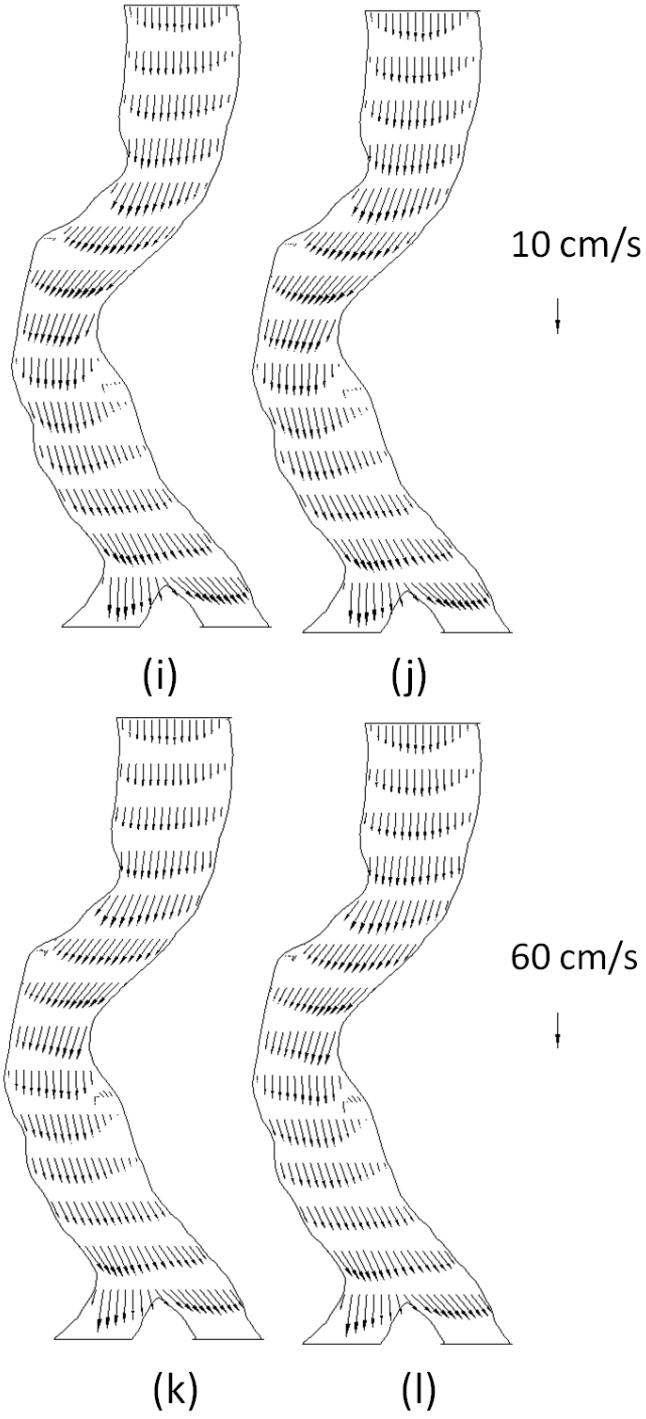

Figure 5.2 (part 2/2) Velocity distribution in (i-l) isodiameteric model for Re = 500 (top row: i-j) and Re = 3000 (bottom row: k-l) under turbulent solutions (left: i, k) and laminar solutions (right: j, l).

5.3 WALL SHEAR STRESS

The wall shear stress, τ_w, was determined by calculating the shear stress within the flow field and reporting the values of the outermost elements of the lumen. The wall shear stress was calculated in scalar, absolute terms without indicating direction. Two passes of 90% surface reduction were performed on the wall shear stress distributions to smooth the results while three passes of a five boxcar averaging routine were performed on the traces. These distributions are shown in figure 5.3 for the three exemplar models. The similarity of the laminar and turbulent cases made presenting both at each flow rate redundant. For this reason, the wall shear stress distributions are only shown for the laminar case at Re = 500 and turbulent case Re = 3000.

From these wall shear stress distributions, traces along the center of the proximal wall of the three example models for laminar and turbulent at Re = 500 and 3000 were plotted (figure 5.4). From these traces, mean wall shear stress values for each wall were presented in table 5.1. For the wall shear stress color contour distributions and trace plots, a six fold increase in wall shear stress magnitude of the scales matched the six fold increase in flow rate between Re = 500 and Re = 3000.

Each model showed very similar τ_w distributions for the laminar (Re = 500: blue line, Re = 3000: green line) and turbulent (Re = 500: red line, Re = 3000: purple line) calculations at both flow rates, except at the inlet due to the wider momentum distribution of the turbulent inlet velocity condition. This differential between the laminar and turbulent cases decayed rapidly at Re = 500 and at a slightly slower rate at Re = 3000. The laminar cases produced marginally higher wall shear stress on the posterior wall in the fusiform and saccular models while the shear in the turbulent cases were greater on the anterior walls. The net of the differences seemed to balance so that neither the laminar or turbulent fields developed significantly larger overall wall shear stress. All these wall shear stress differences between the laminar and turbulent cases were proportionally greater at Re = 3000.

The wall shear stress patterns in all models developed at Re = 3000 in near lockstep relative to those at *Re* = 500, though higher wall shear resulted from increased flow rate and wider momentum distribution at the higher flow rate. The wall shear stress increased more in proportion to the flow rate. Rather than a six fold increase in wall shear between Re = 500 and Re = 3000, approximately 10 × increases were seen in the non-dilated sections while near 14 × increases were present in the bulges.

Within the fusiform model, four different wall shear sections seemed to appear as a result of the local geometry: elevated shear proximal to the bulge, low values intra-aneurysm, return to elevated values distal to the bulge, and greatest shear at the bifurcation and iliac arteries. The inlet and non-dilated aorta proximal to the bulge showed alternating high and low shear due to minor surface elevation changes. The shear was higher on the posterior wall due to the impacted core flow there resulting from the anterior tilt in

the aorta. In this section, maximum values of 1.77 dyne/cm^2 at *Re* = 500 (laminar case) and 18.5 dyne/cm^2 at Re = 3000 (turbulent case) were found. At 6 cm downstream of the inlet, the circumferential mean wall shear stress was 0.86 dyne/cm^2 at Re = 500 and 8.4 dyne/cm^2 at Re = 3000 at 5 cm downstream from the inlet. Within the bulge, wall shear stress values dropped around 70% compared to the non-dilated sections. Where the flow is separated adjacent to the left and right walls, the τ_w direction is reversed due to the separated flow, but not graphically shown due to scalar τ_w reporting. Much higher momentum was near the center of the proximal and anterior walls at Re = 3000, elevating the wall shear. At the widest point of the bulge, the circumferential mean τ_w was 0.153 dyne/cm^2 at Re = 500 and 2.23 dyne/cm^2 at Re = 3000. The τ_w increased on the distal surface of the bulge near the constriction. In the iliac arteries, the wall shear was the highest, with peak values reaching up to 3.8 dyne/cm^2 at Re = 500 and 29 dyne/cm^2 at Re = 3000.

The wall shear stress distribution in the saccular model was irregular and non-symmetric at both flow rates. In the inlet tube, higher shear stresses developed on the posterior wall than on the anterior wall at both Reynolds numbers, with mean circumferential wall shear stress at 6 cm downstream of the inlet of 0.84 dyne/cm^2 at Re = 500 and 8.59 dyne/cm^2 at Re = 3000. Within the bulge, shear stress was low and nearly uniform on the anterior wall at both Reynolds numbers, but the core jet produced at strip of higher shear values on the posterior wall. At the widest point of the bulge, the circumferential mean τ_w was 0.126 dyne/cm^2 at Re = 500 and 2.25 dyne/cm^2 at Re = 3000. Irregular, non-uniform spots of high shear stress formed in the outlet legs, up to 3.44 dyne/cm^2 at Re = 500 and 32. dyne/cm^2 at Re = 3000. These were the maximum within the saccular model.

Wall shear stress in the isodiametric model had low magnitude with irregular fluctuations over the length of the lumen, a pattern similar to that in the entrance tubes of the other models. Without any significant dilation of the lumen, τ_w showed neither extended areas of low magnitude nor extended areas of high magnitude. The wider diameter of this model (d_a = 2.77 cm) caused much lower overall wall shear stress than seen in the fusiform (d_a = 2.25 cm) and saccular models (d_a = 2.32 cm) since the shear was wider distributed over the larger cross section. At 5 cm downstream of the inlet, the mean circumferential wall shear stress was 0.69 dyne/cm^2 at Re = 500 and 5.5 dyne/cm^2 at Re = 3000. At the widest point of the aneurysm (but not the lumen), 9 cm downstream of the inlet, the circumferential mean τ_w was 0.76 dyne/cm^2 at Re = 500 and 5.4 dyne/cm^2 at Re = 3000. The arching geometry of this model resulted in the core flow impacting the right wall near 10 cm downstream of the inlet. The momentum then shifted towards the left wall and remained focused there through the remainder of the model due to the sweeping arch.

Fusiform Model

Re	Scheme	$\overline{\tau}_w$, posterior wall	$\overline{\tau}_w$, anterior Wall
500	Laminar	0.986	0.912
500	Turbulent	0.959	0.948
3000	Laminar	9.53	7.64
3000	Turbulent	8.85	8.32

Saccular Model

Re	Scheme	$\overline{\tau}_w$, posterior wall	$\overline{\tau}_w$, anterior wall
500	Laminar	0.891	0.674
500	Turbulent	0.882	0.701
3000	Laminar	8.15	5.50
3000	Turbulent	8.00	6.05

Isodiameteric Model

Re	Scheme	$\overline{\tau}_w$, left wall	$\overline{\tau}_w$, right wall
500	Laminar	0.549	0.391
500	Turbulent	0.555	0.388
3000	Laminar	5.220	3.885
3000	Turbulent	5.350	3.748

Table 5.1 Computational mean wall shear stress, $\overline{\tau}_w$, from traces along two walls for the three models.

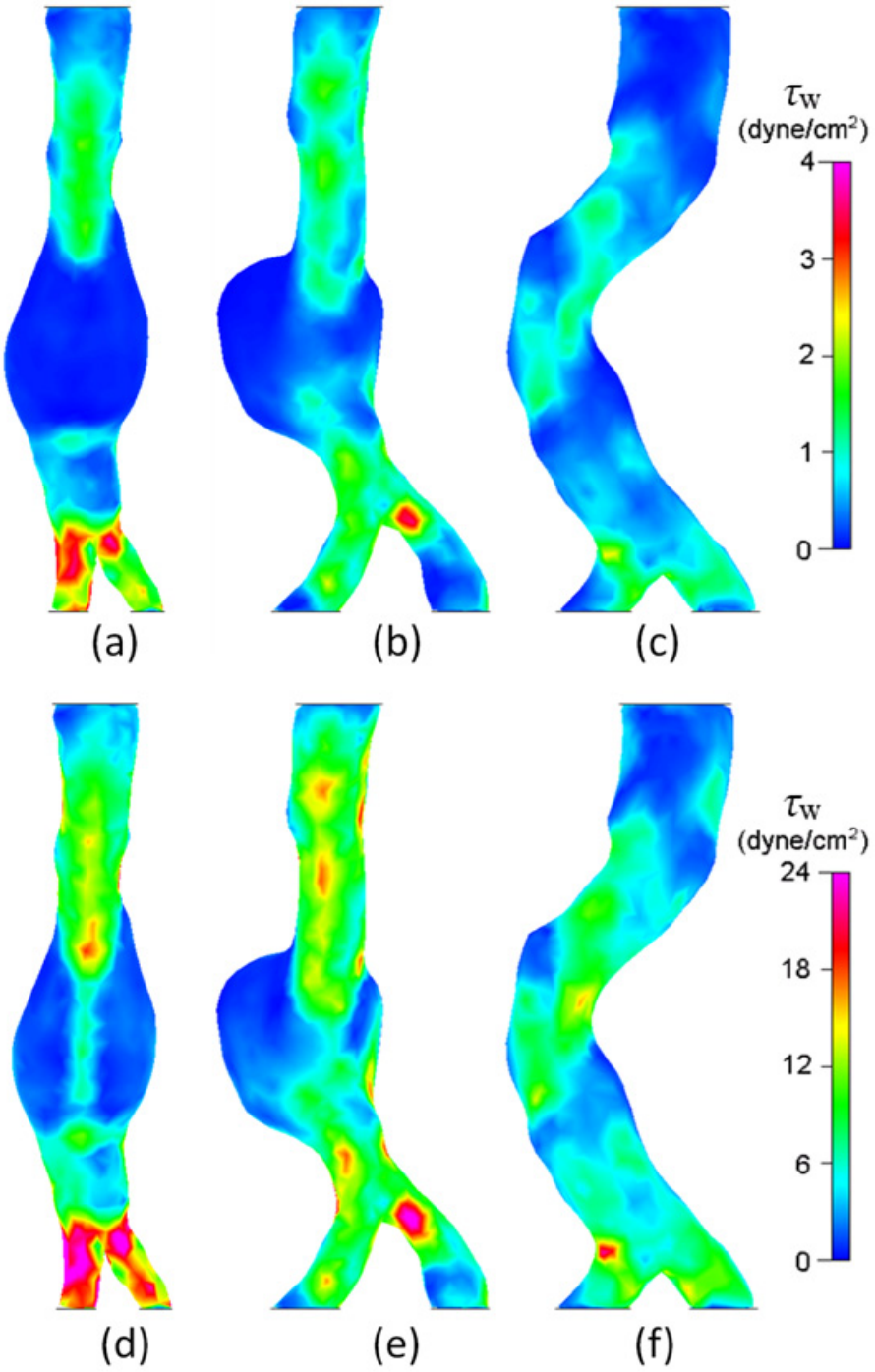

Figure 5.3 Wall shear stress, τ_w, distributions from the posterior point of view for laminar solutions at Re = 500 of (a) fusiform model, (b) saccular model, (c) isodiameteric model, and for turbulent solutions at Re = 3000 for (d) fusiform model, (e) saccular model, and (f) isodiameteric model.

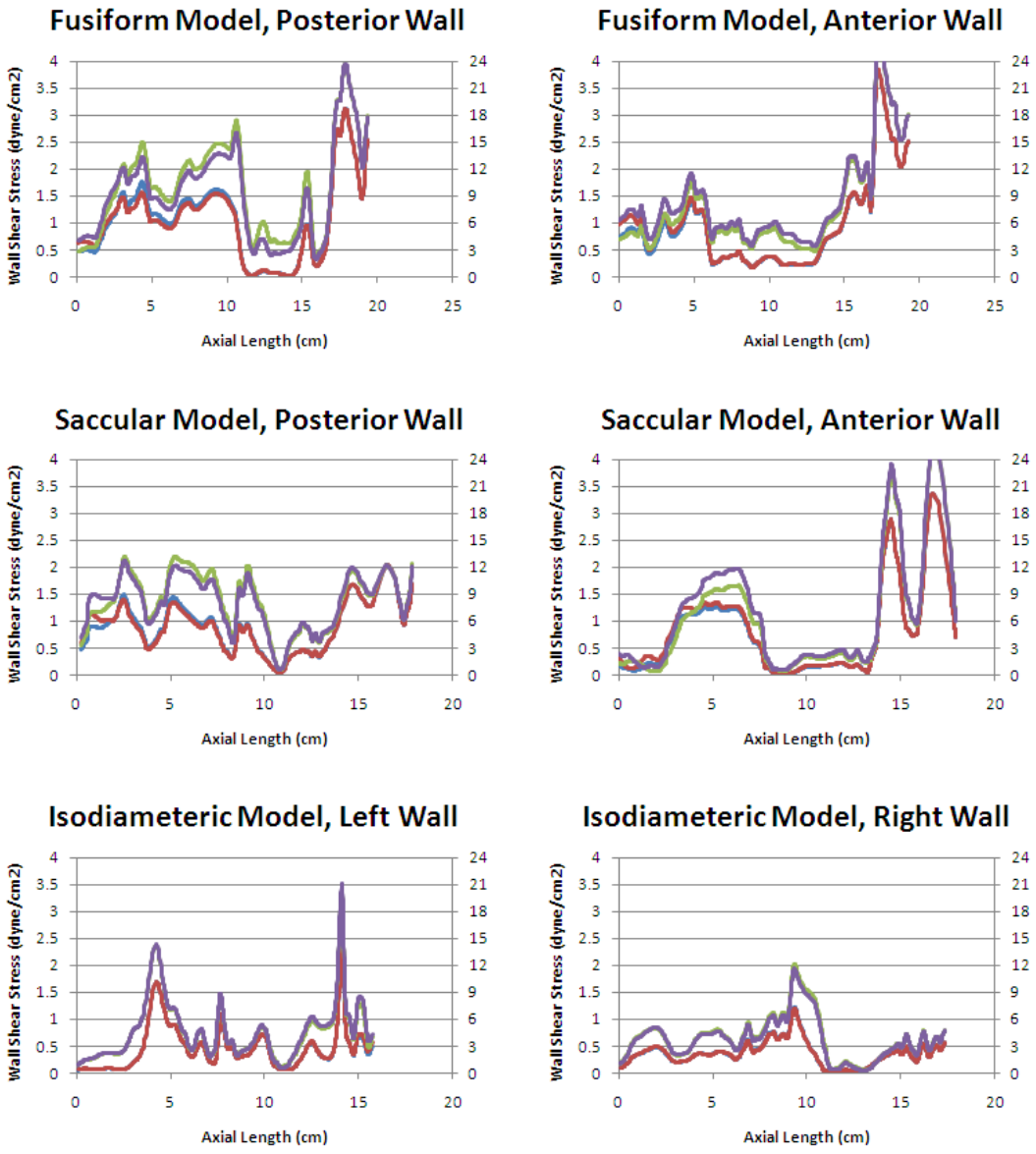

Figure 5.4 Wall shear stress traces from the center of the anterior and posterior wall of the three studied models. The inlet corresponds to axial length = 0. In each plot, solutions for turbulent solution at Re = 500 (red line), laminar solution at Re = 500 (blue line), turbulent solution at Re = 3000 (purple line), and laminar solution at Re = 3000 (green line). The Re = 500 cases use the left vertical axis (0 – 4 dyne/cm^2) while the Re = 3000 cases use the right vertical axis (0 – 24 dyne/cm^2).

5.4 WALL PRESSURE

Wall pressure distributions (figure 5.5) for *Re* = 500 (laminar cases) and *Re* = 3000 (turbulent cases) were generated from the pressure in the border cells of the exemplar models. Pressure magnitude was set relative to the maximum pressure in a given model at a given flow rate, which normally occurred at the model entrance. To enhance contrast, the results were presented using 30 flooded contours. The pressure scales were selected to best display the series of models at each flow rate.

Wall pressure patterns in the fusiform model were generally very similar regardless of flow rate or solution scheme, though pressure drops grew as flow rate increased and the pressure drop in the turbulent solutions was slightly greater than of the laminar solutions (comparison not shown). This was due to the lower overall kinetic energy in the turbulent profile at the inlet relative to the laminar profile. In each case, wall pressure decreased monotonically through the entrance tube. It then increased in the bulge as the area expanded and flow decelerated, with an adverse gradient developing along the bulge wall. At *Re* = 500, the minimum pressure within the bulge was -0.060 mmHg occurring near the bulge entrance while the maximum pressure was -0.032 mmHg near the bulge terminus. At *Re* = 3000, minimum pressure was -1.87 mmHg and maximum was -0.41 mmHg. Distal to the maximum, the pressure decreased monotonically, outside of local maxima at the bifurcation. The overall pressure change from the inlet to 15 cm downstream was -0.054 mmHg at Re = 500, while at *Re* = 3000, it was -1.13 mmHg. Within the iliac arteries, the pressure dropped as the mean velocities increased due to the more constricted arteries.

In the saccular model, the wall pressure distribution was highly non-symmetric. In the inlet tube, pressure was higher along the posterior wall than along the anterior wall at both *Re* = 500 and *Re* = 3000. At *Re* = 500, the wall pressure on the posterior wall declined slightly within the entrance section, then increased within the aneurysm. There was a rapid drop at the bulge exit, with a small local maximum at the bifurcation point. In contrast, along the anterior wall, there was a rapid drop in the entrance tube, reaching a minimum of -0.056 mmHg immediately before the bulge entrance. Pressure was larger and nearly uniform over the anterior bulge surface, but with a local maximum of -0.032 mmHg at the bulge exit, then a rapid decrease into the exit tubes. The mean wall pressure in the aneurysm was -0.048 mmHg. A similar, but less uniform pattern developed at *Re* = 3000. Mean pressure in the bulge was -1.26 mmHg, and the local minimum and maximum of the anterior bulge wall were -1.60 mmHg and -0.65 mmHg. The overall pressure change from the inlet to 15 cm downstream was -0.092 mmHg at Re = 500 and -2.50 mmHg at *Re* = 3000.

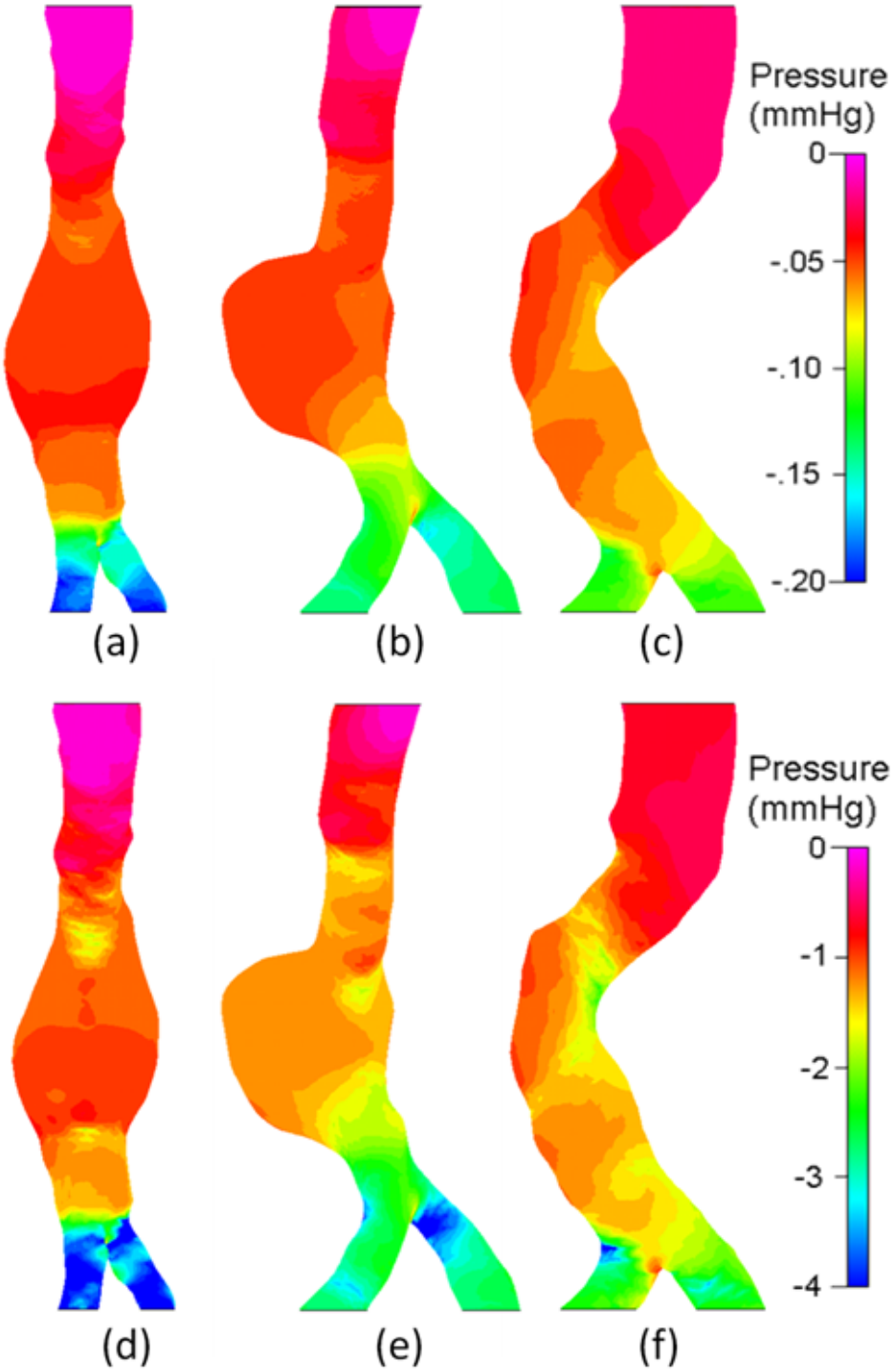

Figure 5.5 Wall pressure distributions from the posterior point of view for laminar solutions at Re = 500 of (a) fusiform model, (b) saccular model, (c) isodiameteric model, and for turbulent solutions at Re = 3000 for (d) fusiform model, (e) saccular model, and (f) isodiameteric model.

In the isodiametric model, pressure followed the contours of the lumen wall. Lumen curvature led to lateral accelerations of the flow that produced local wall pressure maxima and minima at the lumen bends. Near 8 cm downstream of the entrance, there was a local maximum of -0.035 mmHg at *Re* = 500 and -0.80 mmHg at *Re* = 3000 on the left lateral wall, with a corresponding local minimum of -0.073 mmHg at *Re* = 500 and -2.52 mmHg at *Re* = 3000 facing it on the right lateral wall. Pressure reversals accompanied the recirculations at 7 and 13 cm downstream of the inlet. Unlike the saccular and fusiform model, no adverse pressure gradients were sustained around the lumen circumference. The overall pressure change over the initial 15 cm downstream of the entrance was -0.070 mmHg at *Re* = 500 and -1.60 mmHg at *Re* = 3000, and was notably lower than the other models due to the wider vessel.

5.5 TURBULENCE PROPERTIES

The dimensionless turbulent velocity, u'^*, and the turbulence intensity, *TI*, results for the three demonstrative models are shown in figure 5.6 and 5.7. The specific turbulence dissipation rate, ω, results are shown in figure 5.8. These figures were generated from the same planes as the velocity profiles. Here, the 'leafs' formed by the intersecting coronal planes are visible from the proximal view around the edges of the bulge.

At the inlet of all the models, the turbulence intensity showed an 'M' shaped profile at the inlet of each model, with a maximum near $r^* = 0.90$ and a local minimum on the centerline, $r^* = 0$. In areas around $r^* = 1$, the *TI* surged due to near zero velocity even though *k* was relatively low there; these artifacts were caused the irregularly shaped inlets combined with the applied inlet conditions. In the fusiform model, the centerline *TI* at the inlet was 0.06 at both *Re* = 500 and 3000, representative of the other model's results. The turbulence intensity was generally greatest at the inlet or immediately downstream at all flow rates. In all models, the *TI* decayed within the non-dilated sections, achieving in some cases TI below 0.01. As would be expected, the *TI* was greater downstream at Re = 3000. In all cases, the turbulence present did not appear self sustaining was very sensitive to the inlet turbulence conditions. Within the dilations, separation seemed to encourage and promote turbulence, and an overall increase in *TI* was noted. Downstream of the dilations, turbulence again dissipated, returning to very low values. Again, throughout the dilations and the turbulence intensity was significantly higher at Re = 3000.

Within the fusiform model at *Re* = 3000, local regions of high *TI* also developed around the centers of the recirculation vortices. Background *TI* was near zero in each model, but regions of non-zero, elevated turbulence intensity tended to follow the main flow, particularly in the upstream halves of the models. Those regions expanded significantly in both area and strength as flow rate increased. Immediately downstream of the inlet, *TI* decreased significantly from its inlet values at both flow rates.

However, within the dilation, the turbulence intensity increased. In the plane shown in figure 5.7, the maximum *TI* was found in the vortex centers, and was 0.062 at *Re* = 500 and 0.33 at *Re* = 3000. Similar inlet values occurred in the saccular model with a steady decrease in *TI* as flow convected downstream. Maximum *TI* within the lesion occurred near the beginning of the dilation and was 0.038 at *Re* = 500 and 0.095 at *Re* = 3000. In the isodiametric model (figure 8e-f), *TI* was elevated in the entrance but much lower outside the entrance. Downstream of the entrance region, the maximum turbulence intensity was 0.059 at *Re* = 500 and 0.089 at *Re* = 3000, which developed approximately 8 cm downstream of the inlet. Elevated *TI* was not distributed over as wide an area in the isodiametric model as it was in the other models.

At each flow rate in each model, the specific turbulent energy dissipation rate had a high value in a very thin layer along the wall (figure 5.8) with lower values in the core. As would be expected, dissipation rates grew in strength as flow rate increased. In all three models, the dissipation rate was more uniform at high *Re* than at low *Re*. In center of the dilations of the saccular and fusiform models, the dissipation was approximately 1 sec^{-1} at *Re* = 500 and 4 sec^{-1} at *Re* = 3000, while in the non-dilated sections, including the entire aortic section of the isodiametric model, the dissipation in the core flow ranged from 2 to 6 sec^{-1} at *Re* = 500 and from 5 to 20 sec^{-1} at *Re* = 3000. The dissipation near the walls was relatively consistent for all models, peaking near 1000 sec^{-1} at *Re* = 500 and *Re* = 3000.

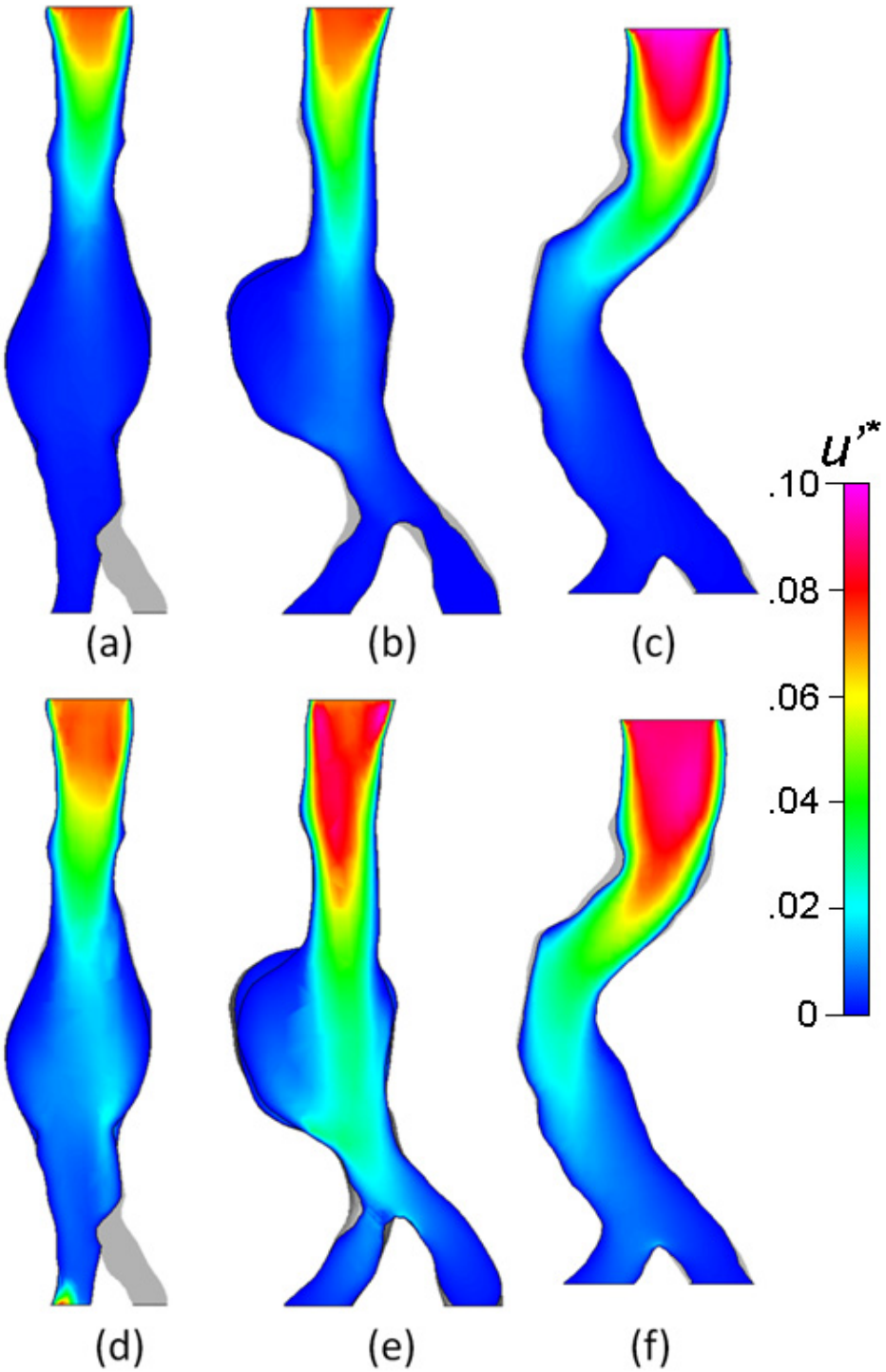

Figure 5.6 Dimensionless turbulent velocity u'^{*} distributions from the posterior point of view for turbulent solutions at Re = 500 of (a) fusiform model, (b) saccular model, (c) isodiameteric model, and at Re = 3000 for (d) fusiform model, (e) saccular model, and (f) isodiameteric model.

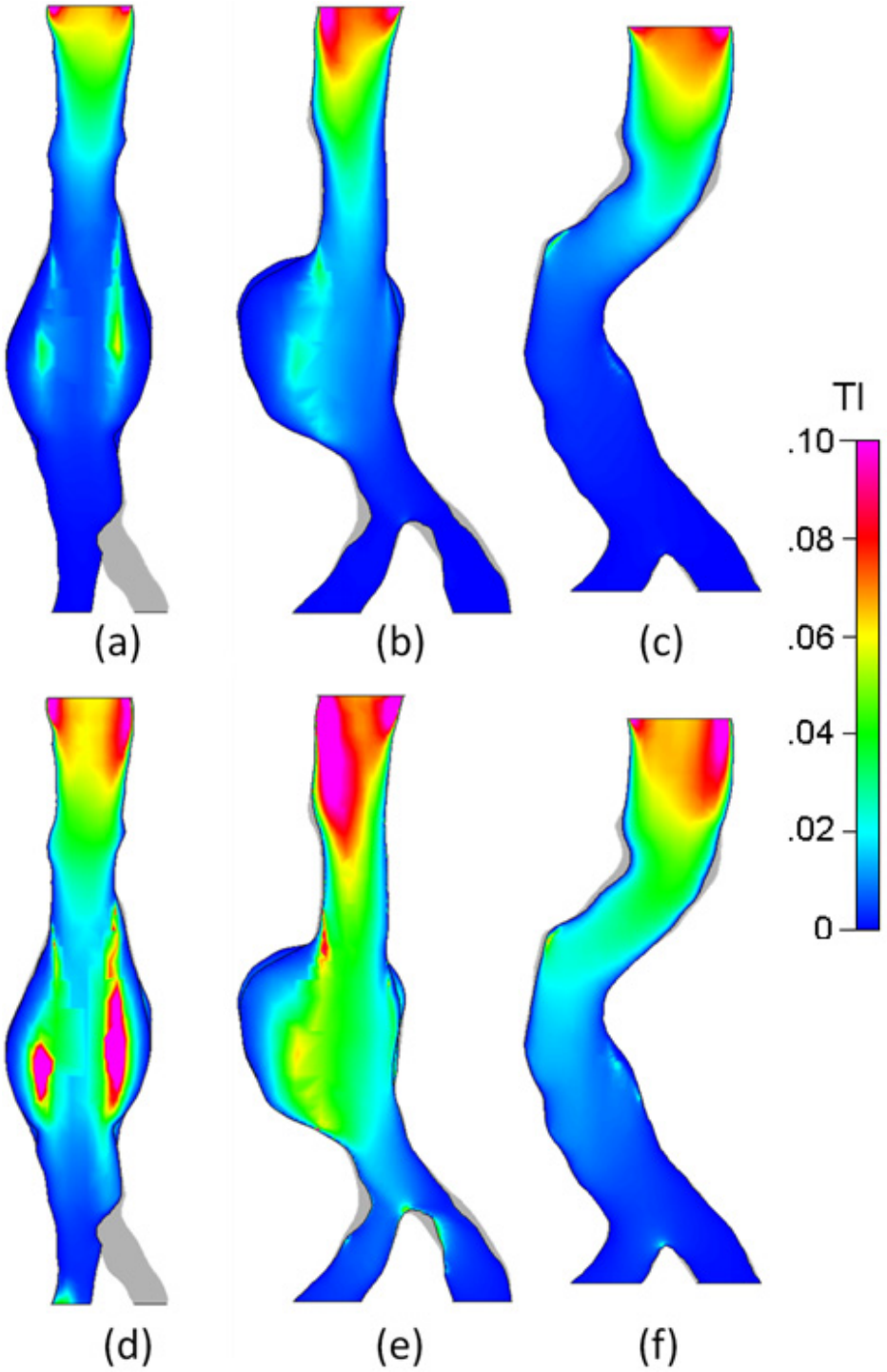

Figure 5.7 Turbulence intensity, *TI*, distributions from the posterior point of view for turbulent solutions at Re = 500 of (a) fusiform model, (b) saccular model, (c) isodiameteric model, and at Re = 3000 for (d) fusiform model, (e) saccular model, and (f) isodiameteric model.

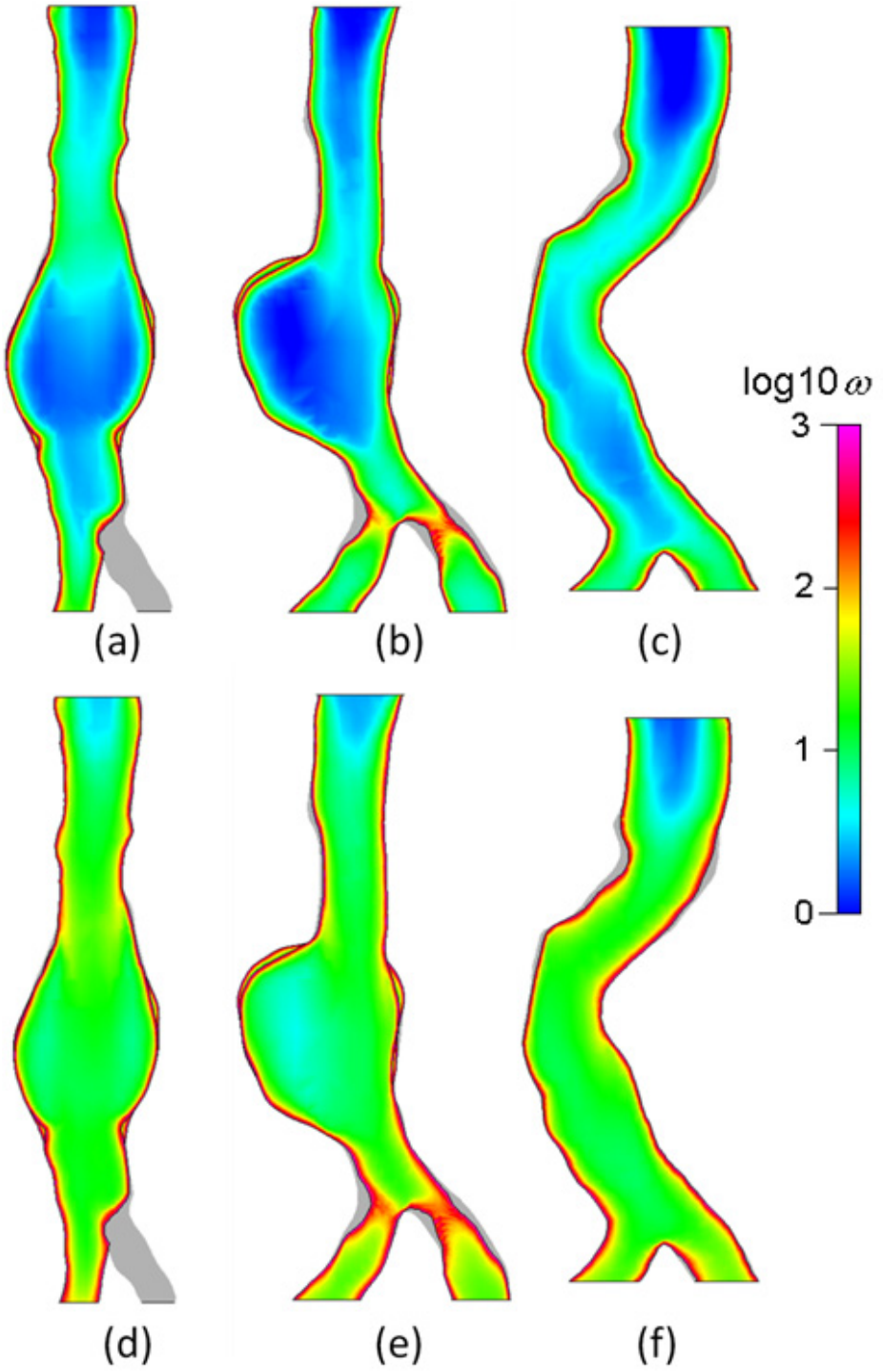

Figure 5.8 Specific turbulence dissipation rate, ω, distributions from the posterior point of view for turbulent solutions at Re = 500 of (a) fusiform model, (b) saccular model, (c) isodiameteric model, and at Re = 3000 for (d) fusiform model, (e) saccular model, and (f) isodiameteric model.

CHAPTER 6: PRESSURE RESULTS

6.1 PRESSURE POINTS

The locations of the pressure points in relation to the lumen of phantoms 1-3 are displayed in Figure 6.1. Phantoms 1-3 had a series of pressure points on the lumen top and side wall while phantoms 4 and 5 had pressure points on the top wall only. Eleven pressure points were installed in each series in phantoms 1, 2, and 4 (top series only), ten pressure points were set up in phantom 5 (top only), and nine pressure points were set up in each series of phantom 3. However, some pressure points became inoperable during experimentation and their results were not reported (grey background, figure 6.1). The pressure points in each series were numerated sequentially with P1 at the most proximal point. The lumens displayed in figure 6.1 do not indicate the location of the truncated bifurcation and cylindrical entrance and exit sections, and some points (P1 and P11 of phantom 4, and P10 of phantom 5) are within these cylindrical sections. The axial position of each phantom determined and reported as the axial length, with the most proximal pressure point, P1, set as zero. For phantoms 1-3, the axial location of the most proximal pressure point on the top and side walls was the same though the vertical height was different. Axial length values were reported in experimental values, though the *in vivo* length scale was nearly the same (d_{iv}/d_{ex} =1.18 for phantom 3, d_{iv}/d_{ex} =1.08 for phantom 4).

The vertical height of each pressure point relative to the working surface is reported in figure 6.2. The top profiles of phantoms 1-5 follows the highest vertical point of the lumen in the configuration within the flow loop. The side profiles of phantom 1-3 follow the vertical mid point of the lumen, creating a less dynamic height profile than the top series.

During experimentation, the signal output, S, was not always steady. The cumulative effect of a variety of instability sources, including alternating current instability, flow loop instability, environmental (building, working surface, experimental equipment) vibration contributed to background signal noise. However, background signal noise was low, as observed by the very low fluctuations observed under quiescent condition, on the order of less than 0.01 mmHg. These fluctuations were at or below the measurement threshold, and this noise was neglected in this present study. At flow rates above Re = 1500, the signal fluctuations increase due to flow instability and some margin of error in pressure analysis must be assumed. This increase of fluctuations between Re = 1500 and Re = 2000 corresponds to onset of intermittent turbulence in steady flow under similar conditions occurring near Re = 1700 as observed by Asbury et al (1995). The magnitude of the fluctuations seemed insensitive to any factors outside of flow rate such as lumen geometry or pressure point position.

The range of signal fluctuations, $\{S\}$, and the corresponding pressure fluctuation range, $\{p\}$, as determined from the slope (0.01 mmHg/V) are reported in table 6.1. While these values do not directly

correlate as the experimental error, the range of the fluctuations are displayed as error bars in figures 6.2 and 6.3 for the Re = 3000 case. Error bars are not displayed on the other flow rates because they are too small to be significant on the plots as presented. A rough approximation of the potential measurement error was predicted using two assumptions: 1) a Gaussian distribution of the fluctuations and 2) that 95% of the fluctuations observed occur within the range of $S \pm \{S\}$, and in turn $p \pm \{p\}$. Thus, the magnitude of the reported pressure fluctuations was equal to the second standard deviation, $\{p\} = 2\sigma$. The error is often reported as magnitude the first standard deviation, σ, which in this case would be half the recorded pressure fluctuations, $\{p\}/2$, also reported in table 6.1. Since signal fluctuations were found to be insensitive to location, the potential error is blindly applied for all pressure point results in all phantoms as a function of Re only. While this is certainly a subjective measurement, it is a reasonable approximation of the potential measurement error due to the fluctuations.

Re	$\{S$ (V)$\}$	$\{p$ (mmHg)$\}$	p Error (mmHg)
0	< 0.0001	< 0.01	< 0.005
500	0.0001	0.01	0.005
1000	0.0001	0.01	0.005
1500	0.0001	0.01	0.005
2000	0.0002	0.02	0.010
2500	0.0005	0.05	0.025
3000	0.001	0.10	0.050

Table 6.1 Signal fluctuations, pressure fluctuations and error estimate.

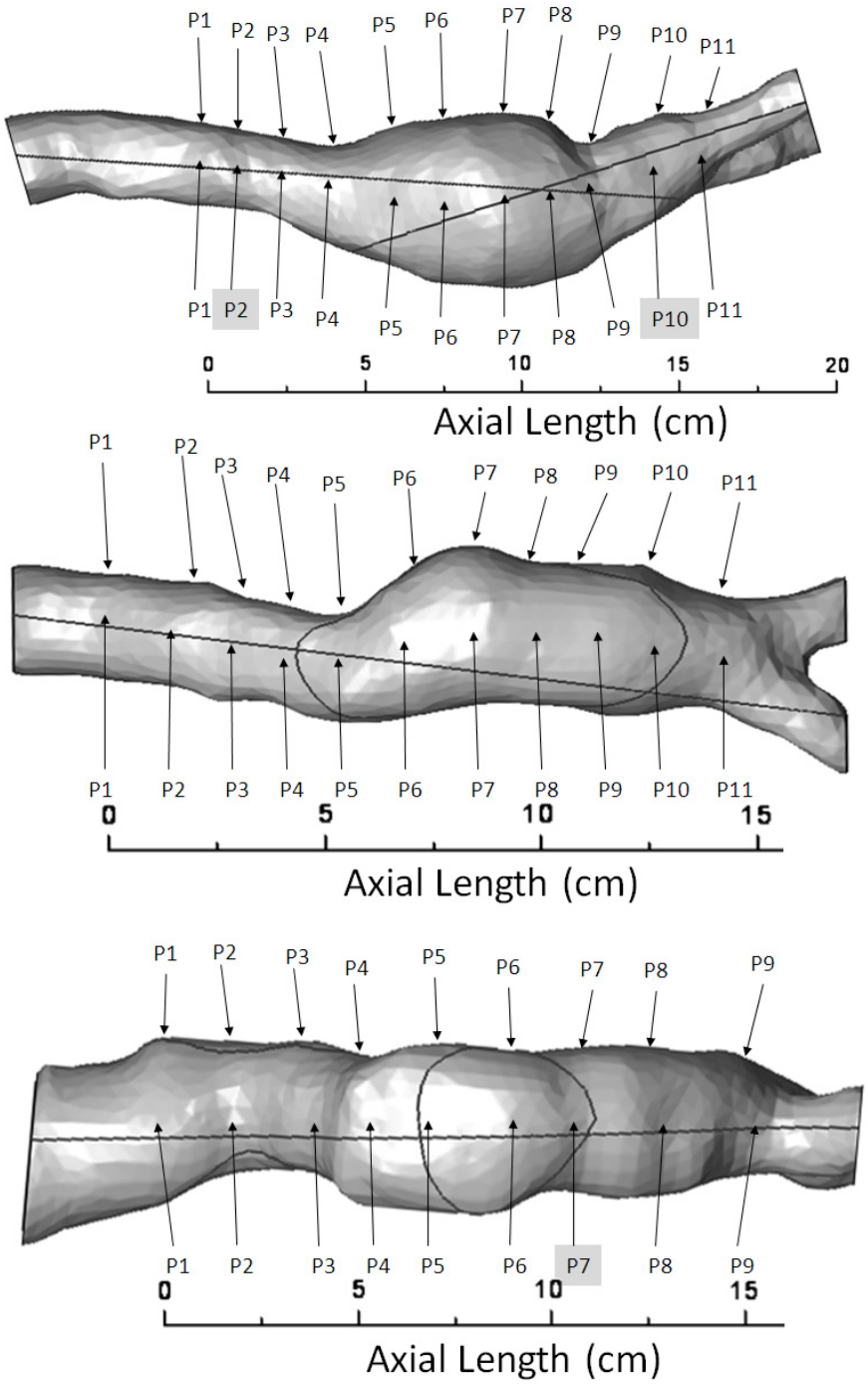

Figure 6.1 (part 1/2) Lumen with pressure points. Lumen of phantoms 1 (top), 2 (middle), and 3 (bottom) with the locations of each pressure point. Grey background indicates pressure point which failed during experimentation.

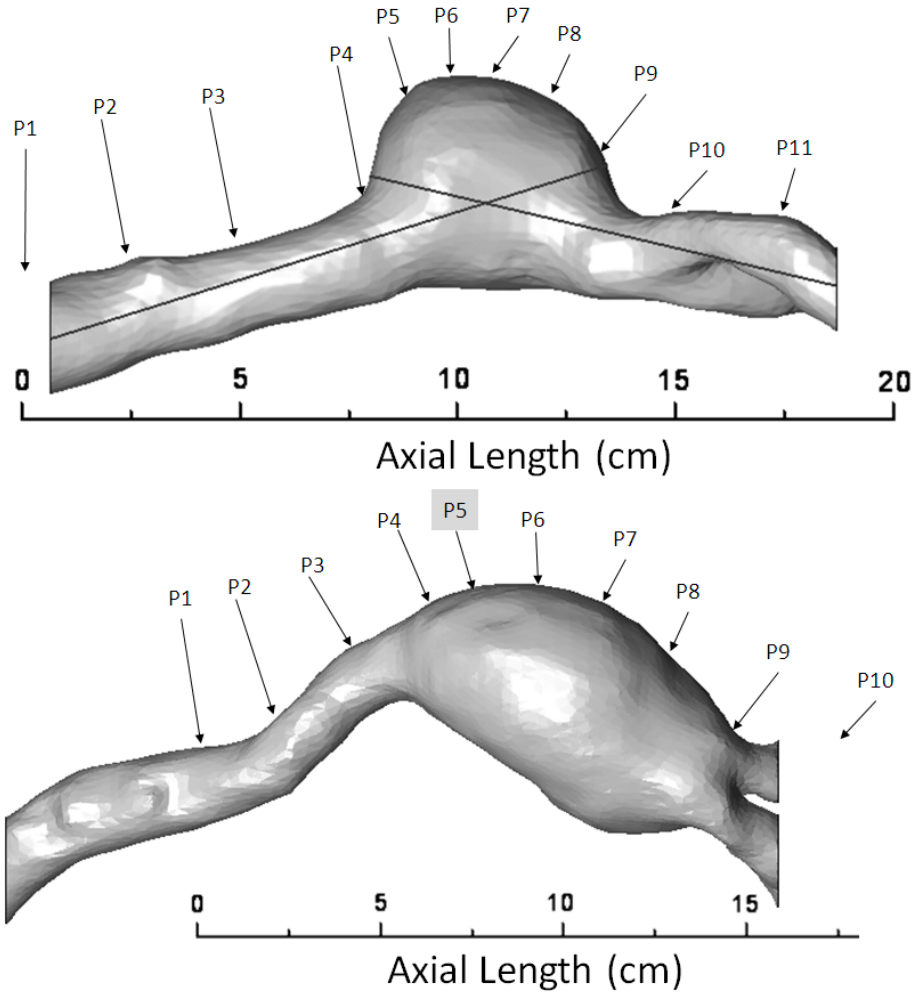

Figure 6.1 (part 2/2) Lumen with pressure points. Lumen of phantoms 4 (top) and 5 (bottom) with the locations of each pressure point. Grey background indicates pressure point failed during experimentation.

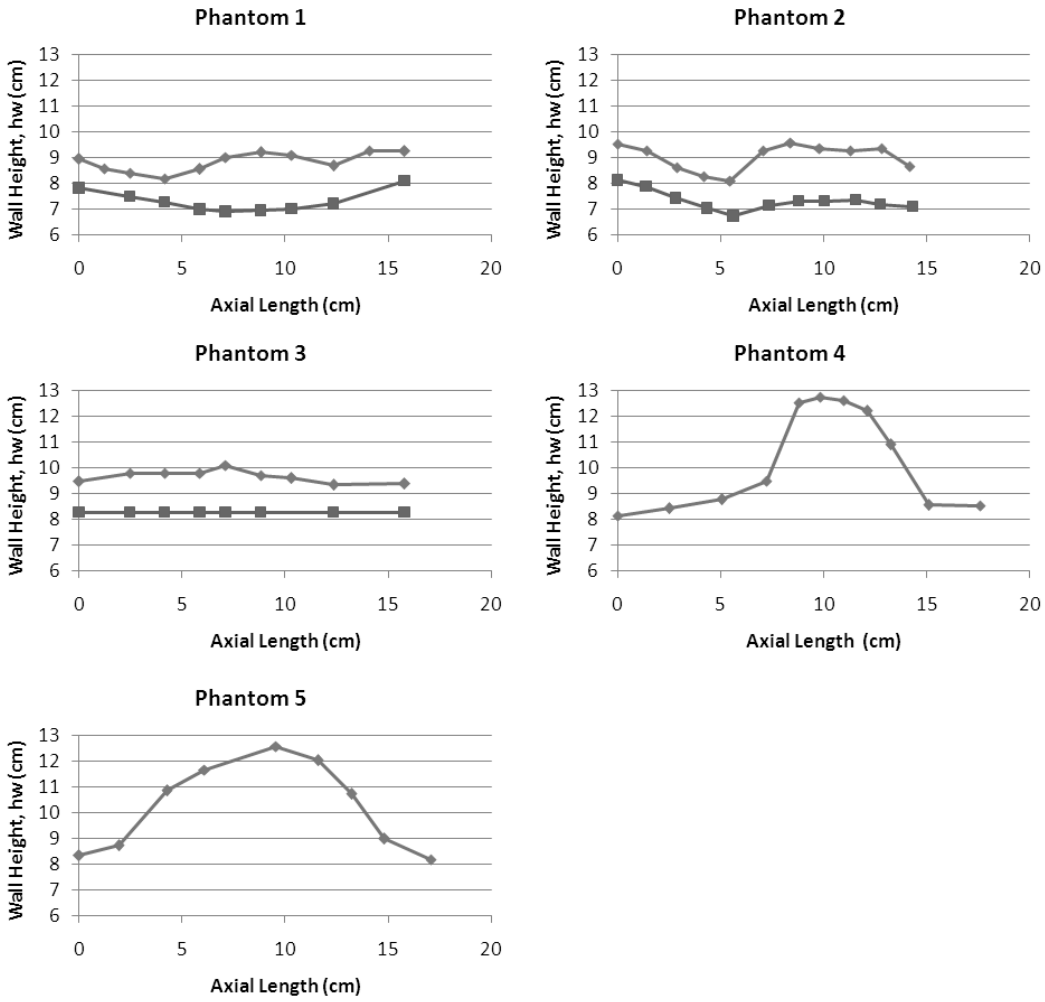

Figure 6.2 Wall height, h_w, of each pressure point relative to the working surface. In phantoms 1-5, diamonds indicate the locations of the pressure points in the top series while in phantoms 1-3, the squares indicate the locations of the pressure point in the side series.

6.2 WALL PRESSURE

The wall pressure for each phantom for the flow rates corresponding to Re = 500 and Re = 3000 are reported in figure 6.3 and for the series of Re = {500, 1000, 1500, 2000, 2500, and 3000} in appendix C. The wall pressure and length values are presented in experimental values. The wall pressure for the top and side pressure point series phantoms 1-3 are presented simultaneously in figure 6.3, while for phantoms 4-5, only top series measurements were performed. At the time of testing, it was not considered that the side and top pressure would be reported simultaneously, and the flow rates between the top and side trials were not identical as achieving a steady flow was priority over perfectly replicating the precise Reynolds number specified flow rate. While a minor deviation in flow rate between tests near Re = 500 produced negligible change to the overall wall pressure, the same deviation is amplified and would cause a significant pressure shift at Re = 3000, resulting in results that make the top and side series appear too close (Phantom 2) or too far apart (Phantoms 1 and 3). The lower flow rate is assumed to be accurate regarding the pressure differential between the top and side profiles.

Phantom 1 was oriented so that the top pressure point series was on the posterior wall and the side pressure point series was on the left lateral wall. This orientation suggests that the patient would be lying prone. The wall pressure profiles of the top and sides pressure point series of phantom 1 at Re = 500 very closely matched the inverse of their wall height profiles. This likeness suggests that the wall height was the most significant factor in determining the wall pressure profile, while flow inducted effects were minimal. In the top profile, the pressure steadily increased between P1 and P4, corresponding to a vertical drop in the lumen in the phantom. Between P4 and P8, the pressure decreased as the dilation expanded and the lumen height rose. A sharp increase in wall pressure occurred between P8 and P9 due to the rapid constriction of the dilation. The wall pressure decreases between P10 and P11 as the constricted lumen is vertically elevated distal of the aneurysm. The range of pressure for the top series at Re = 500 was {0.77 mmHg}.

A similar progression was seen for the side pressure profile at Re = 500. The wall pressure nearly exactly matches the inverse wall height, again suggesting that the wall pressure profile was function more of wall height than of flow induced effects. The side pressure points follow the approximating vertical middle of the lumen, and are off higher wall pressure than the top points due to the lower elevation. A gradual increase in pressure from P1 to P6 occurred, following the gradual vertical decline of the mid level height of the lumen through the entrance tube and into the aneurysm. The wall pressure then decreased from P6 to P11 as the lumen bent back vertically upward. P2 and P10 were inoperable during experimentation, and their values not reported. The range of pressure for the side series at Re = 500 is {0.95 mmHg}.

At Re = 3000, the overall wall pressure was reduced as compared to the Re = 500 case due to increased pressure drop in the flow loop. The top profile was highly skewed between P1 and P4. Although

P2 and P3 functioned properly at the lower flow rate, they seemed to provide erratic values at Re = 3000. For this reason, these suspect points are highlighted (yellow background, figure 6.3). Otherwise, the top and side profiles followed the same trends seen at the lower flow rate, and flow induced pressure change seem to be minor.

The pressure fluctuations at Re = 3000 are on the order of ±0.1 mmHg (error bars, figure 6.3) from the time averaged, reported values. The magnitude of these were slightly significant in comparison to the range of wall pressure in the top, {1.30 mmHg}, and side, {0.91mmHg} profiles. The range of the top is exaggerated due to the outlying point P2; with P2 negated, the range would be become {0.79 mmHg}.

The overall mean drop of all pressure points from Re = 500 to Re = 3000 was slightly less for the side profile, -7.9 mmHg, than the top profile, -8.8 mmHg. As suggested earlier, this was believed to stem from slightly different flow rates between the top and side series. While the overall magnitude of the pressure drop was clearly affected, the wall pressure profiles of the top and side series was believed to remain consistent. This is the most exaggerated case of the three phantoms studied with top and side series.

The wall pressure measurements in phantom 2 were taken from the right lateral wall (top series) and the posterior wall (side series). This orientation suggests that the patient would be lying on their left side. At Re = 500, the side and top pressure profiles inversely followed the same geometrical trends as seen in phantom 1. The top pressure profile decreased as the lumen dilated, and inversely followed the somewhat wavelike patterns on the top wall. The side pressure showed a more moderate change in pressure, while still inversely following the geometrical pattern established by the mid wall. The range of wall pressure is {1.16 mmHg} for the top profile and {0.94 mmHg} for the side profile.

At Re = 3000, the same profile trends were seen in the top and side series as at Re = 500. The pressure fluctuations are somewhat significant in comparison to the range of wall pressures, but still much smaller. The range of wall pressure was {1.23 mmHg} for the top profile and {0.97 mmHg} for the side profile. The overall differential between the top and side wall pressures was smaller than those at Re = 500, due to the difference in flow rates, making the pressure profiles appear compressed at Re = 3000. The mean overall wall pressure change from Re = 500 to Re = 3000 was -7.6 mmHg for the top series and -8.1 mmHg for the side series.

The wall pressure measurements in phantom 3 were taken from the posterior wall (top series) and the left lateral wall (side series). This orientation suggests that the patient would be lying prone. The side pressure taps were configured slightly differently in this phantom than in phantoms 1 and 2. Rather than precisely following the vertical midpoint, these were set up in a line vertically parallel to the working surface so that each pressure point would have an identical h_w, and the same wall pressure correction ($-\rho g h_w$) was applied to each point. This does, incidentally, nearly follow the vertical mid point due as the

lumen due to the planer geometry of the lumen. During experimentation on the side series, P7 failed and was not reported.

At Re = 500, the top wall pressure profile inversely follows the geometrical pattern of the lumen, showing much less pressure change between points due less vertical change in the lumen in this configuration. The range of top wall pressure series is {0.62 mmHg}, which is less than any of the other phantoms. The side series showed very consistent wall pressure, with a pressure range of {0.08 mmHg}.

At Re = 3000 the same pressure trends were seen in the side and top profile relating to lumen geometry and pressure point height. The range of the top wall pressure series was {0.61 mmHg} and the range of the side wall pressure series is {0.19 mmHg}. The mean pressure change between Re = 500 and Re = 3000 was -7.5 mmHg for the top series and -7.1 mmHg for the side series. The greater drop of the top series makes the profiles at Re = 3000 appear exaggeratedly wide.

The wall pressure measurements in phantom 4 were taken from the anterior wall (top series) only. This orientation suggests that the patient would be lying in a supine position. At Re = 500 and Re = 3000, the pressure profile showed a larger pressure decrease in the aneurysm, as a result of the highly saccular bulge. The pressure profiles very precisely follow the inverse of the vertical height of the top wall. The range of wall pressure is {3.04 mmHg} at Re = 500 and {3.11 mmHg} at Re = 3000. At Re = 3000, the pressure fluctuation are the same as in phantoms 1-3, but appear less prominent here due to the larger range of wall pressures experienced within this phantom. The wall pressure drop of the top series between Re = 500 and Re = 3000 was -8.1 mmHg.

The wall pressure measurements in phantom 5 were taken from the left lateral wall (top) only. This orientation suggests that the patient would be lying on their right side. At Re = 500 and Re = 3000, the pressure profile shows a large pressure decrease in the aneurysm, as a result of the unusually large dilation. The pressure profile matches the inverse of the top wall height very closely. The range of wall pressure is {3.58 mmHg} at Re = 500 and {3.49 mmHg} at Re = 3000. The pressure fluctuations observed at Re = 3000 were on the same order of magnitude as those seen in the other phantoms.

The mean pressure change from Re = 500 to Re = 3000 was -4.3 mmHg, significantly less than seen in phantoms 1-4. Since the inlet diameter is smaller in phantom 5 (0.75”) was smaller than in phantoms 1-4 (1.0”), the flow rate was reduced to achieve the same Re. However, the remainder of the flow loop remained at 1.0”, which provided less pressure drop at the comparably lower flow rate for phantom 5. Thus, this reduced pressure change between flow rates was an artifact of the flow loop and not the phantom. During experimentation, P5 failed and was not reported.

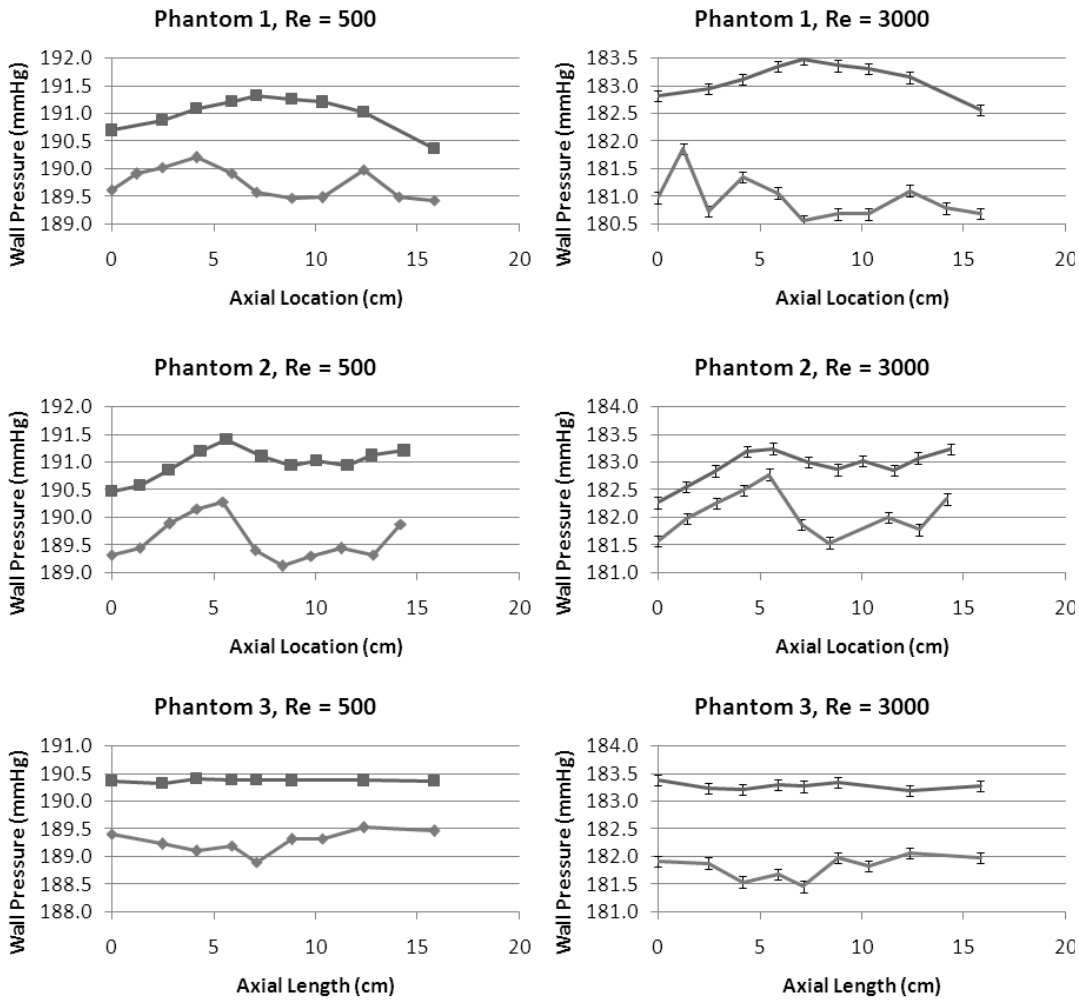

Figure 6.3 (part 1/2) Wall pressure for phantoms 1-3 at Re = 500 and 3000. For each plot presented, the lower pressure data set (diamonds at Re = 500) are from the top pressure point series while the higher pressure data set (squares at Re = 500) are from the side series. Error bars in the Re = 3000 plots indicate range of pressure fluctuations.

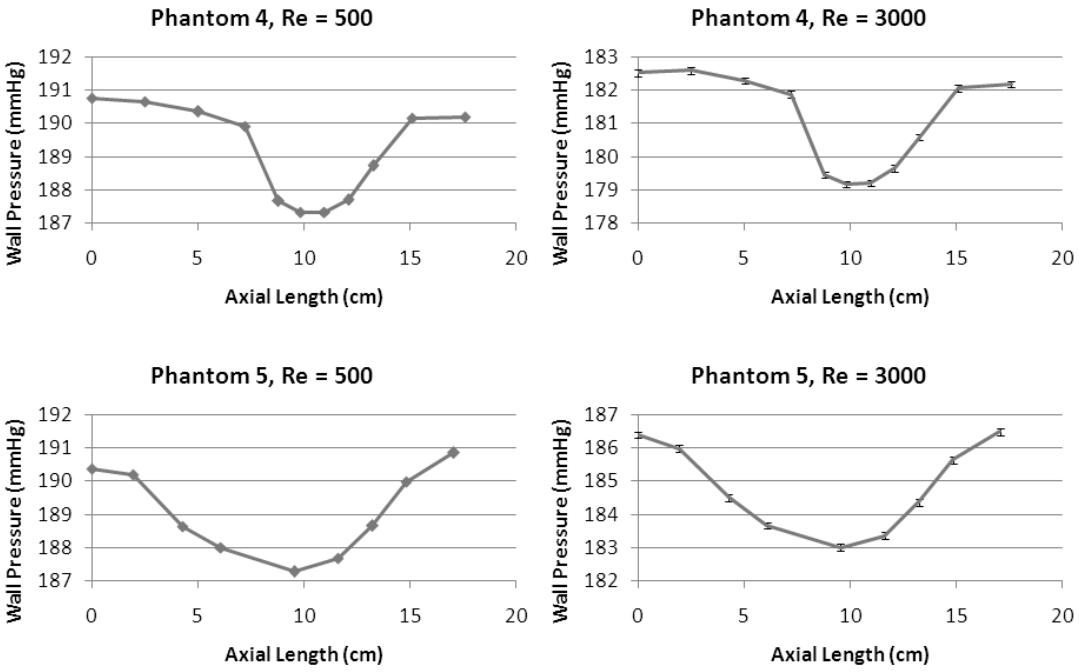

Figure 6.3 (part 2/2) Wall pressure for top series of phantoms 4 and 5 at Re = 500 and 3000. Error bars in the Re = 3000 plots indicate range of pressure fluctuations.

6.3 EQUIVALENT WALL PRESSURE

In phantom 1 at Re = 500, the change of equivalent pressure remains fairly steady around zero at all pressure points on the top series, other than a minor increase at P9 ($\Delta p'$ = 0.17 mmHg) and P10 (0.11 mmHg) on the top series. On the side series, the ΔP tends to hover around -0.05 mmHg between P3 and P11. No discernable trends were observed for side and top profile and the distribution appears somewhat random but centered around $\Delta P = 0$.

In phantom 1 at Re = 3000, the top profile is much more jagged than at the low flow rate. While P2 and P3 on the top series were reported in the wall pressure measurements and suggested to be outlier, they were significantly outside the ΔP range of the other points. Removing these two outlier points does not entirely smooth the trends, and a jagged profile with another abnormally low value at P6 of -0.38 mmHg that would normally also be considered an outlier. The distal points P9 - P11 are back near zero. Pressure fluctuations were indicated by error bars, and were significant in comparison to the ΔP ranges. The side profile of phantom 1 at Re = 3000 however shows a more convincing results. A tighter ΔP distribution was seen here in comparison to the top series. The magnitude of fluctuations was greater than the reported ΔP range. Again, the profiles seemed random.

In phantom 2 at Re = 500, the top and side ΔP profiles showed similar profiles which were focused around -0.1 mmHg. At Re = 3000, the top and side ΔP values tend to be higher, hovering around 0.1 mmHg. Both show slightly jagged profiles in the proximal P2 – P6 points but the distal P7-11 points showed a more steady increase in ΔP.

In phantom 3 at Re = 500, the ΔP distribution was very tight around zero for both the top and side series. No significant deviation from $\Delta P = 0$ occurred aside from a few points 0.05 mmHg away from zero. At Re = 3000 in phantom 3, the ΔP distribution was more dynamic, with a somewhat jagged profile above $\Delta P = 0$ while the bottom series was a slightly smoother and below $\Delta P = 0$.

In phantom 4, the ΔP profile for the top series at Re = 500 closely matches that of the top series at Re = 3000. Since the lumen of phantom 4, is more dilated and saccular than in phantoms 1-3, this ΔP profile may be due to greater flow disruption. However, since this trend was not observed elsewhere suggests incorrect calibration. The wider ΔP pressure swing made the fluctuations at Re = 3000 appear less significant than in the other phantoms.

In phantom 5, the ΔP at Re = 500 was a very smooth profile which stayed near 0.05 mmHg, except for the most distal point, P10 which jumped to 0.37 mmHg. A similar pattern happened at Re = 3000, where the profile was more jagged, but with a large change from P9 to P10. This suggests that P10 may be an outlying point.

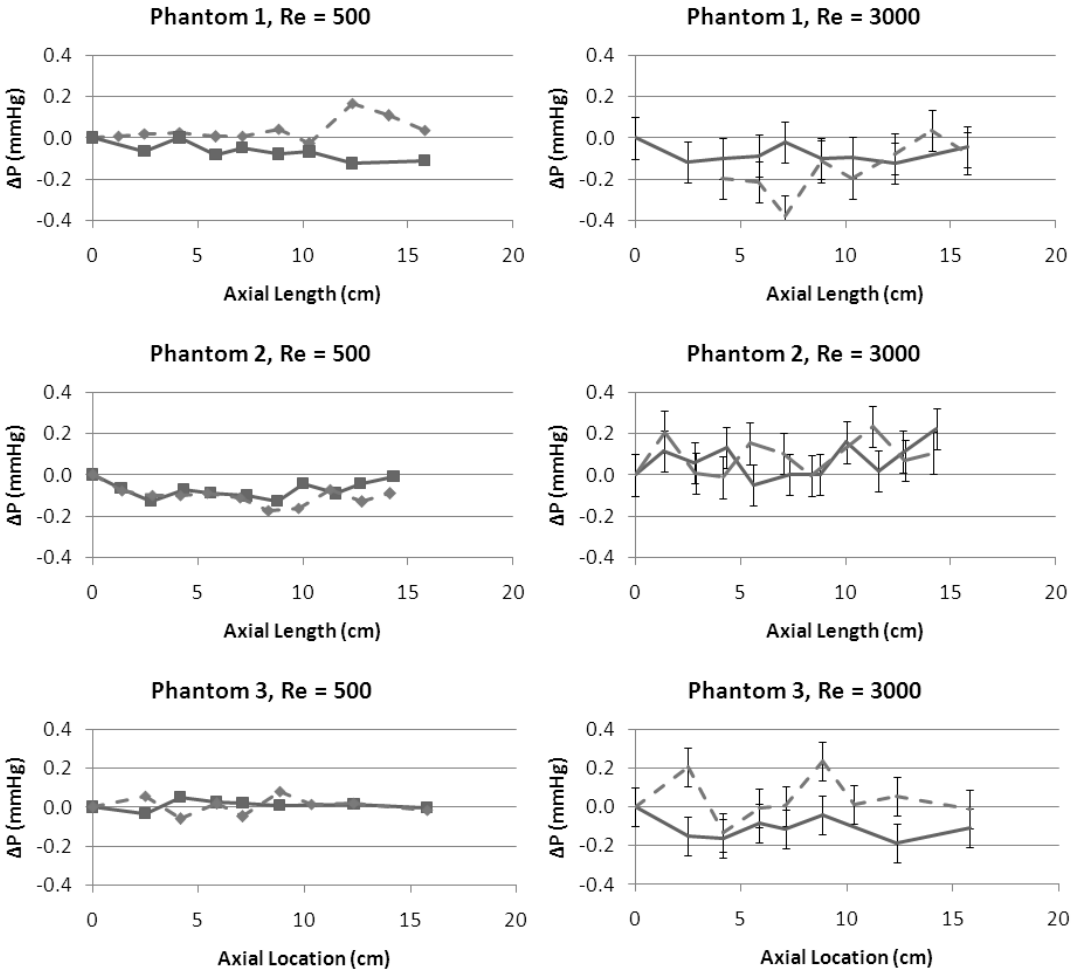

Figure 6.4 (part 1/2) Equivalent pressure change, ΔP, relative to pressure point 1 for phantoms 1-3 at Re = 500 and 3000. Top series are represented by dashed lines (and diamonds at Re = 500) while side series are represented by solid lines (and squares at Re = 3000). Error bars in the Re = 3000 plots indicate range of pressure fluctuations.

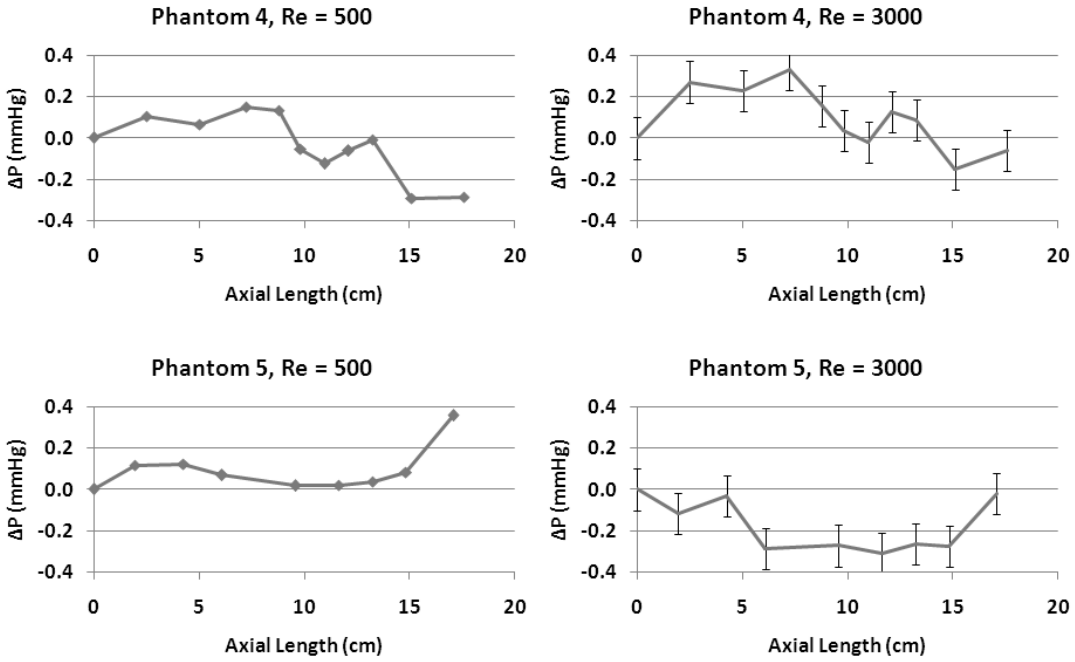

Figure 6.4 (part 2/2) Equivalent pressure change, *ΔP,* relative to pressure point 1 for the top series in phantoms 4 and 5 at Re = 500 and 3000. Error bars in the Re = 3000 plots indicate range of pressure fluctuations.

CHAPTER 7: DISCUSSION

7.1 EXPERIMENTAL OVERVIEW

Flow was evaluated in two models. As would be expected, each model generated different flow patterns. In phantom 3, the flow remained attached almost throughout the entire model though the momentum shifted from wall to wall due to the tight bends. When recirculations did occur, they were minor and did not affect the majority of the flow field. Downstream of the aortic bends, the flow showed signs of perturbation as the velocity profiles were skewed leaving the final bend.

Over the range of flow rates examined the flow showed evolution as the flow rates increased. The Re = 125 showed more conic character, noted with the $n < 2$ inlet profile. At the higher flow rates, the profile was decidedly more parabolic at Re = 500 and much blunter at Re = 3000. Within the aortic bends, the flow remained in a somewhat parabolic shape at Re = 125, and the flow seemed to accommodate the bends more readily. At Re = 500, the flow was less accommodating to the bends, and a minor recirculation was formed on the middle of the right wall, downstream of the first bend. Downstream of this, a slightly bimodal velocity profile was generated as the flow left the field of study. At Re = 3000, the low flow and recirculation was eliminated, possibly due to the wider momentum distribution. The core flow velocity profile hinted at generating a bimodal velocity profile, but it was eliminated as the flow impacted the wall downstream of the last bend.

Transverse imaging confirmed the results shown by the 2-D profiles, but did not greatly add to the observations. The core flow showed high momentum from the anterior to posterior walls throughout. The core flow carved a very specific channel through the lumen, leaving low flows on the opposing walls. Non axial motion was confined to accommodating the lumen bends. The lateral motions were maintained past the end of the bends as the inertia did not change until the core flow impacted the walls. Essentially no lateral to posterior motion was seen, though this could be expected since the lumen mostly confined to a single plane in the lateral and axial directions.

Turbulence evolved between flow rates, increasing between Re = 125 to Re = 500, then significantly increasing from Re = 500 to Re = 3000. Given that turbulence is only predicted to occur starting around Re = 2000 in straight tubes, it was somewhat surprising to see it at the lower flow rates. While certainly the noise from PIV recording resulted in elevated turbulence, notably within the first bend, there was no question about the presence of instability elsewhere. Given the very mild turbulence within the entrance section, it could be inferred that the flow through the bends helped induce the turbulence. Most apparent was at the final bend, where high turbulence near the shear area of the flow moved into the core.

The wall shear stress of this phantom alternated between high and low values based on the location of the core flow momentum. Due to the exchange between the walls, the shear was generally very high on one wall and low on the opposite. The wider flow profile at Re = 3000 had two effects. It increased the overall wall shear, as would be expected from higher flow rate, somewhat but also decreased the areas of low shear. The low shear spots did occur, but covered less area, and generally did not achieve as proportionally low values. The wall shear stress results reported positive values every due to the absolute, directionless calculation. Generally, recirculation areas are shown with a negative wall shear due to the adverse motion. The minor recirculations produced essentially zero values, so even if these sections were reported negatively, no real difference would be noted.

Phantom 4 produced a large vortex within the dilation that was maintained at all flow rates. Attached, forward moving core flow was found on the anterior wall and retrograde flow found on the posterior wall. At Re = 125, the vortex was very well defined, and showed continuous recirculation along the entire posterior wall. At Re = 500 and Re = 3000, the recirculation was still present, but the flow fields were choppy. This is probably an artifact generated by PIV analysis in part due to highly fluctuant motion of the flow here and inadequate correlation by PIV. None the less, there was no question of a significant recirculation within the bulge. The core flow showed different flow at Re = 125 and Re = 500 versus that of Re = 3000. At the low flow rates, the core flow generally maintained the same direction throughout the bulge and low, but forward moving momentum was on the distal half of the aneurysm anterior wall. At Re = 3000, it more closely followed the anterior wall, bending at the midpoint and remaining firmly attached. It appears that the momentum from the vortex forced the core back towards the anterior wall. The flow downstream of the model was fairly well developed at Re = 125 but very perturbed at Re = 500 and Re = 3000.

Transverse imaging confirmed the major separation and retrograde flow on the posterior wall. At Re = 500, the retrograde flow spanned from the left wall to the right wall, though at Re = 3000 it shifted heavily towards the right wall. The core flow showed a similar motion on the anterior wall. At Re =500 it was centered, but at Re =3000, the core moved up the left wall. The transverse slices showed that the core flow was significantly wider within the dilation and forward moving flow of high velocity extended further into the flow center. The non-axial velocity showed little motion other than to accommodate the lumen at Re = 500. However at Re = 3000, a strong counter clockwise circulation was generated within the bulge. Its rotational strength carried downstream. The flow was significantly changed between the lower and high flow rates.

Turbulence was much greater in phantom 4 in comparison to phantom 3. The caveat to that assessment is that optical quality of phantom 4 was less than that of phantom 3, which produced noisy results which exaggerated the turbulence values. If a little reading between the lines is allowed for the

turbulence results, the evolution of turbulence can be seen. While turbulence was present at each flow rate, the flow within the bulge became very turbulent at Re = 3000. The separated, recirculating flow became more chaotic, which was reflected both by high standard deviation of velocity (and thus high turbulence) and the failure to capture a well articulated, time averaged velocity profile.

Unlike phantom 3, extended and more intense adverse wall shear stress was generated on the posterior wall of phantom 4. Were a negative wall shear reported, it would show negative values on the posterior wall between z = 8 cm and 14 cm. This has been recalculated simply assuming negative values between the separation and stagnation points in figure 7.1. Here it is more apparent the major change in wall shear stress on the posterior wall relative to the remainder of the phantom. Re = 125 and Re = 3000 show a more typical wall shear distribution with the low, negative and constant values through this section. However, the spiking negative wall shear mid wall at Re = 500 is questionable.

Wall pressure results very definitively showed a pressure profile that was the inverse of the wall height. Figure 7.2 shows a comparison of the wall height correction to the pressure profiles for the side series pressure profile for phantom 1 and the top pressure profile for phantom 4. In each case, the wall height correction nearly matches the pressure profile. While some minor deviations between the wall height correction and the pressure profiles were present, they are minimal. The deviations are represented by the equivalent pressure plots in figure 6.4.

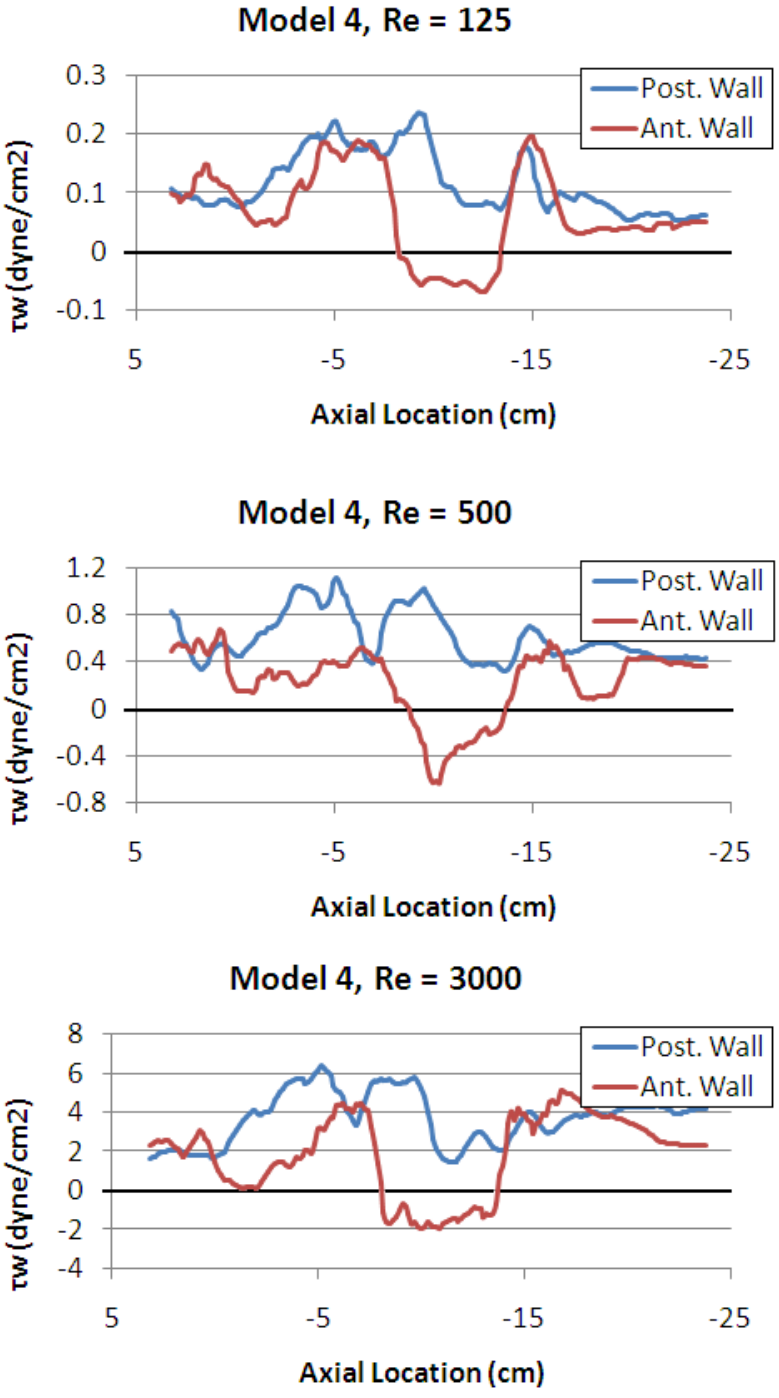

Figure 7.1 Modified wall shear stress for phantom 4 modified. Negative WSS values occur on posterior wall where flow is adverse.

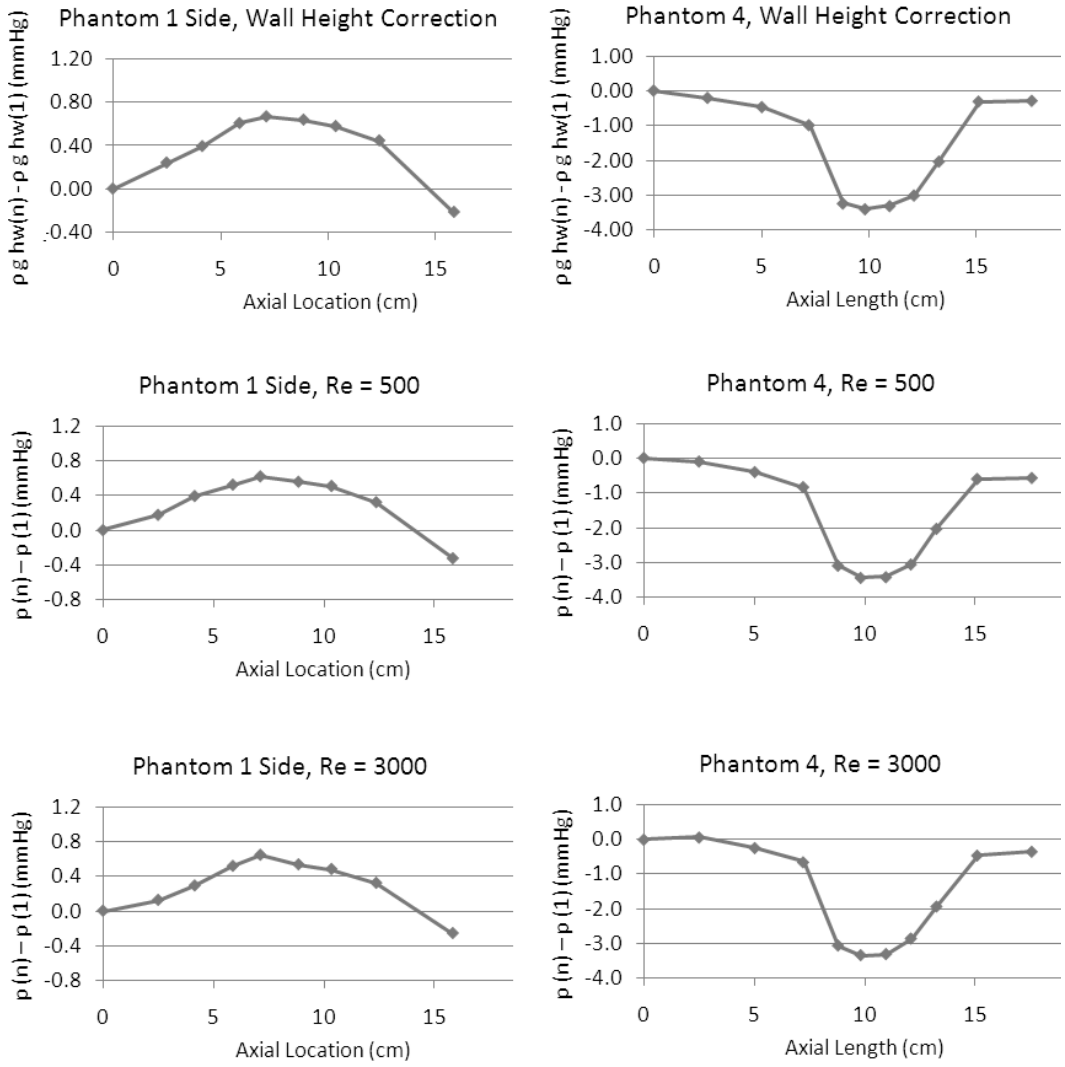

Figure 7.2 Pressure and wall height correction comparison. Wall height correction (top), pressure profile for Re = 500 (middle) and pressure profile for Re = 3000 (bottom) comparison for the phantom 1 side series pressure profile and the phantom 4 top series pressure profile. Each profile has been normalized to the first pressure point.

7.2 COMPUTATIONAL OVERVIEW

The flow field kinematics in the computational models reflected the lumen geometry, with vortices developing in bulged regions. The saccular model produced a single large vortex filling its bulge, while the fusiform model produced two separate, nearly mirrored vortices on the left and right wall (a unique phenomena among the 10 models studied). The strength of these vortices increased with Re, but their position and size were independent of flow rate. Because of the presence of these vortices, wall shear stress in the bulges was significantly reduced in magnitude and reversed in direction relative to shear generated by the core flow outside of the bulges. Within the dilations, the wall pressure showed an adverse gradient, with a local maximum near the distal end. In contrast, in the isodiametric model the flow generally remained attached and well developed, and local pressure maxima were found at the lumen bends.

As Re increased from 500 to 3000, the velocity and wall shear stress distributions did not simply increase six-fold in magnitude due to the increased flow rate, but otherwise remain unchanged. Instead, momentum transport was redistributed as flow rate varied, so that the velocity increase was not constant at every position. Near-wall velocities were more than proportionally larger at high Re. As a result, though the wall shear stress distributions were structurally similar for the two flow rates (figure 5.3 and 5.4), wall shear was proportionally greater at the higher flow rate. In non-dilated sections, the mean wall shear stress increased 10-fold, but non-uniformly. In contrast, within the bulged sections, the recirculation strength was relatively greater at the higher flow rate, accelerating both forward directed and retrograde flows, which augmented wall shear. In the bulges, the mean wall shear stress increased 14-fold or more. This disproportional increase suggests that larger sections of the aneurismal wall may be subject to shear-mediated effects than would be thought based on low Re observations.

The flow fields produced by the laminar computations were very similar to those obtained in turbulent simulations, particularly in the isodiametric model (figure 5.2). Differences became apparent only within the aneurysm dilations, where maximum forward velocities were nearly always faster in laminar results than in turbulent results because of radial dispersion of momentum by turbulence. A strong similarity between laminar and turbulent results might not be unexpected at Re = 500, since turbulence is not expected to be dominant at low Reynolds numbers. However, the similarity was striking even at Re = 3000. One possible explanation of this is that turbulent calculations produce mean velocity rather than instantaneous velocity, potentially obscuring larger differences in instantaneous velocities. Alternatively, momentum transfer in the k-ω computation may be more highly dependent on core mesh density than was initially realized.

There were measurable quantitative differences in the laminar and turbulent results at Re = 3000. For example, recirculation velocities in the turbulent simulations differed by 5-10% from those in the

laminar calculation. In spite of this, the wall shear stresses were not significantly altered between laminar and turbulent results (figure 5.4). If a trend for the wall shear stress between the laminar and turbulent results could be generalized from this work, it would be that the laminar results provided greater peak values while the turbulent results provided slightly higher values overall.

7.3 RESULTS COMPARISON

A more important issue than differences in the laminar and turbulent calculations *per se* is whether either approach gave results comparable to experimental measurements. Flow fields derived from PIV measurements are compared to laminar computational results at Re = 500 and turbulent calculations at Re = 3000 in figures 7.3 and 7.4. Qualitatively, the computations reproduced major features of the flow fields well. In general, computational flow fields seemed to produce higher wall shear rates and more uniform interior velocity profiles than did the experimental measurements, and to not evolve as expected as flow rate increased. Aside from those issues, the qualitative correlation between computationally and experimentally derived flow fields was reasonable, and the basic structure of core flow as well as separation and recirculation were well replicated.

In the saccular model (figure 7.3 a-d, shown in lateral view), the core jet was well replicated at both Re in the entrance tube and through the bulge, though the experimental measurements showed a more perturbed velocity profile in the exit tube than did the computations. The size and position of the bulge vortex was also similar. The measurements showed more rapid forward momentum transport in the bulge than the computations, though at Re = 3000 the accuracy of the measurements was limited by flow instability within the bulge. Since the experimental phantoms did not contain the iliac bifurcation, the flow downstream of the dilation was different.

The transverse slices (figures 7.4) showed the locations and magnitude of the core and vortex flow were reasonably well matched, though the computational model failed in two points. First, the computational model predicted strong counterclockwise rotation at both Re = 500 and Re = 3000 that was seen experimentally at Re = 3000 but not at Re = 500. Second, the experimental results showed the core flow within the dilation moved from the left posterior corner at Re = 500 towards the right posterior wall at Re = 3000 and the recirculation areas made a similar shift. These were not captured by the computational predictions.

In the isodiametric model (figure 7.3 e-h), gross features of the measured velocity profiles were in agreement with the computations. Notably, the computations replicated the two small, separated recirculation zones along the inner wall at the bends of the phantom at both Reynolds numbers. However, in the experiments forward momentum was confined to channels along the outer wall, around the

recirculation zones. As a result, flow along the outer wall was convectively accelerated to relatively high velocities downstream of the bends. This convective acceleration pattern was not duplicated in the computational flow fields.

The transverse slices did not reveal significant discrepancies between experimental and predicted flows. The core flow showed the same motion alternating between the left and right walls. Disagreement between the secondary vectors was seen at $z = 0$ for $Re = 3000$. Neither flow showed great change between the flow rates, but wider momentum distributions were seen for each.

While the computational predictions clearly predicted adverse pressure gradients within the bulges, these were not confirmed experimentally. Many of the predicted pressure changes at $Re = 500$ were near the experimental measurement threshold, so these would not be expected to be resolved. At the higher flow rate, the predicted pressure changes were on the scale that would have been resolved experimentally, however this was not found. Turbulent fluctuations may have obscured some of the pressure trends, but none of the experimental results strongly indicated the adverse pressure gradients or significant maxima or minima predicted by CFD.

Unfortunately, quantitative disparities between the measured and computed flow fields were not trivial, particularly with regard to wall shear stress magnitude. CFD predictions of wall shear stress were 40% greater than their experimental counterparts at $Re = 500$ and 98% greater at $Re = 3000$. Mean wall shear stress values are compared in table 7.1. However, part of this difference may be due to under evaluation of the experimentally measured wall shear stress because of inadequate near wall resolution and 2-D limitations inherent in PIV techniques. In addition, the maximum core velocities of the computed flow fields were approximately 10% less than the experimental measurements, while maximum computed retrograde velocities were 10-50% greater than the measurements. Thus it seems likely that at present although computational evaluation of AAA flow fields is qualitatively accurate, it is not yet sufficient for quantitatively accurate prediction of flow field and wall behavior.

Poor agreement between was seen between the turbulence distributions of the measured and computational flows. Experimentally, the turbulence was low through the entrance section and was increased when the flow became more complex, either within the dilation or the bends. Computationally, these increases occurred were locally contained, and did not greatly fuel turbulence downstream. The computational results seemed to underpredict turbulence by an order of magnitude.

Model	Re	$\overline{\tau}_w$, exp dyne/cm^2	$\overline{\tau}_w$, comp dyne/cm^2
Saccular	125	0.091	-
Saccular	500	0.418	0.782
Saccular	3000	2.78	7.02
Isodiameteric	125	0.089	-
Isodiameteric	500	0.410	0.472
Isodiameteric	3000	2.72	4.55

Table 4.2 Comparison of mean wall shear stress, $\overline{\tau}_w$ between experimental (exp) and computational (comp) results. Wall shear stress was derived from laminar fields at Re = 500, and from the turbulent fields at Re = 3000.

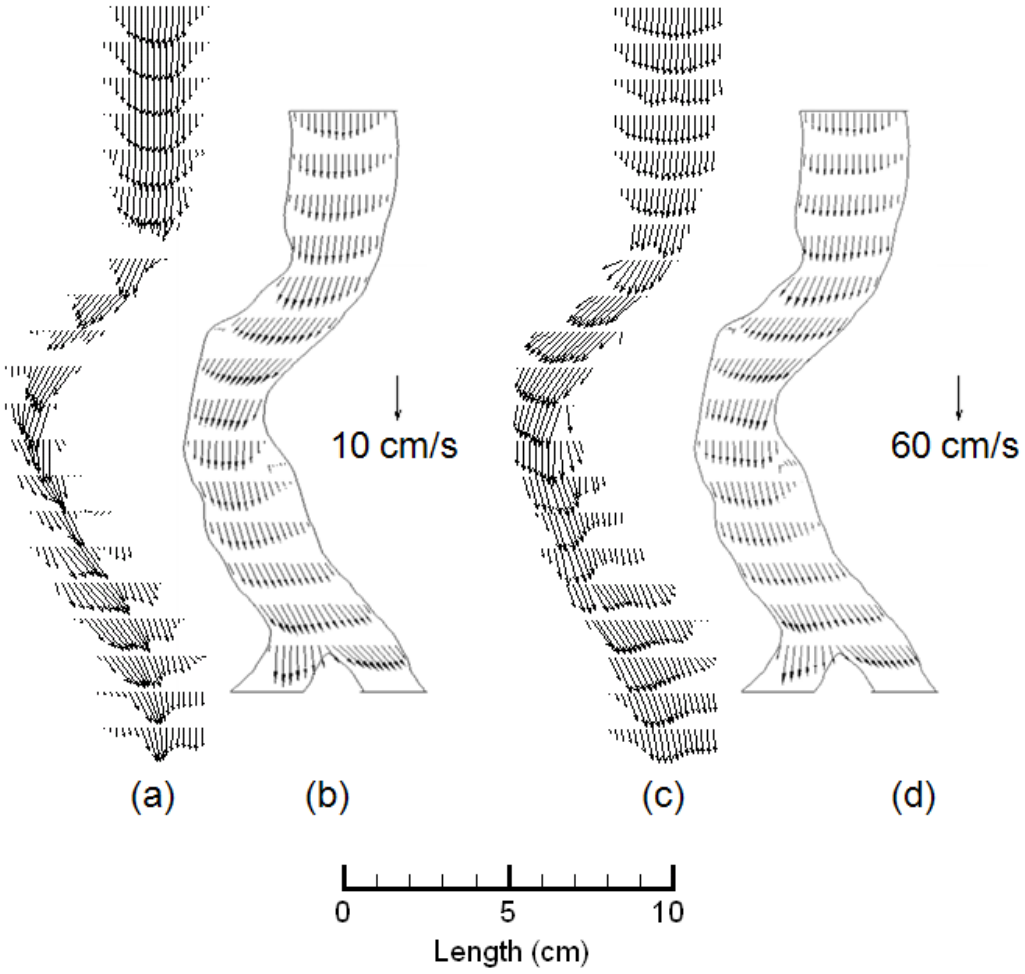

Figure 7.3 (part 1/2) 2-D velocity comparison. Comparison of velocity distributions for phantom 4 from the posterior point of view for (a) experimental flow field at Re = 500, (b) laminar computation at Re = 500, (c) experimental flow field at Re = 3000, (d) turbulent computation at Re = 3000.

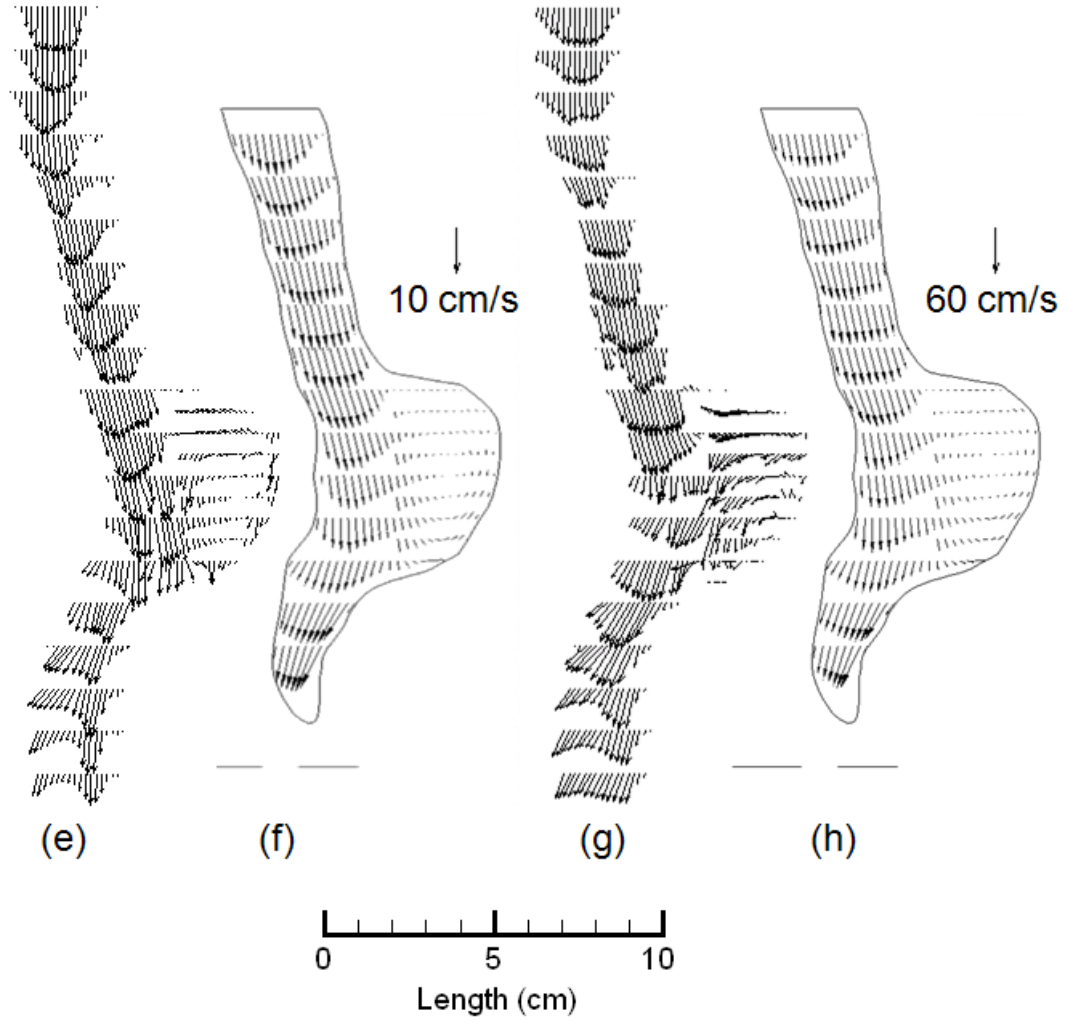

Figure 7.3 (part 2/2) 2-D velocity comparison. Comparison of velocity distributions for phantom 4 from the lateral point of view for (e) experimental flow field at Re = 500, (f) laminar computation at Re = 500, (g) experimental flow field at Re = 3000, (h) turbulent computation at Re = 3000.

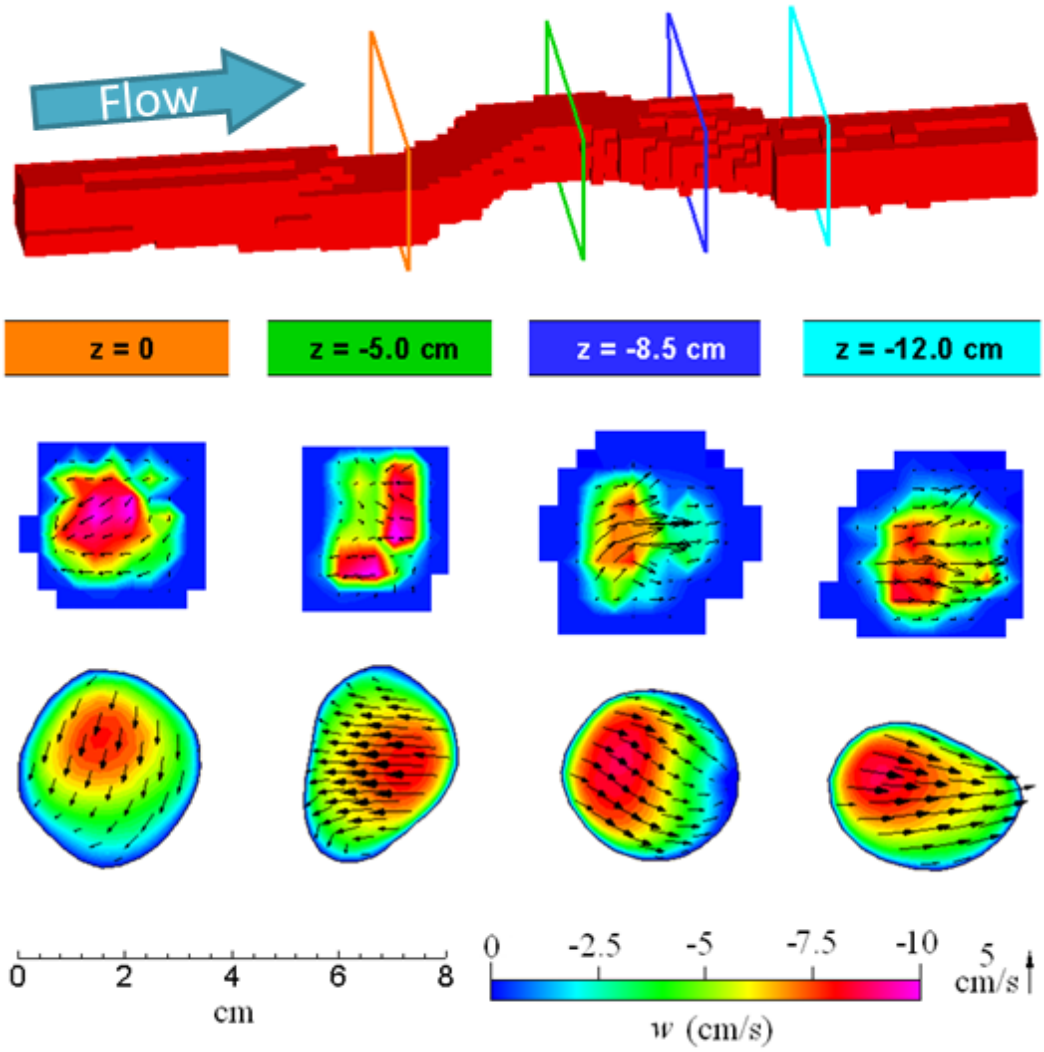

Figure 7.4 (part 1/4) 3-D velocity comparison. Comparison of experimental measurements (top row) and computational predictions (bottom row) of combined axial (colored contours) and non axial (vectors) velocities, extracted from transverse slices from phantom 3 at Re = 500.

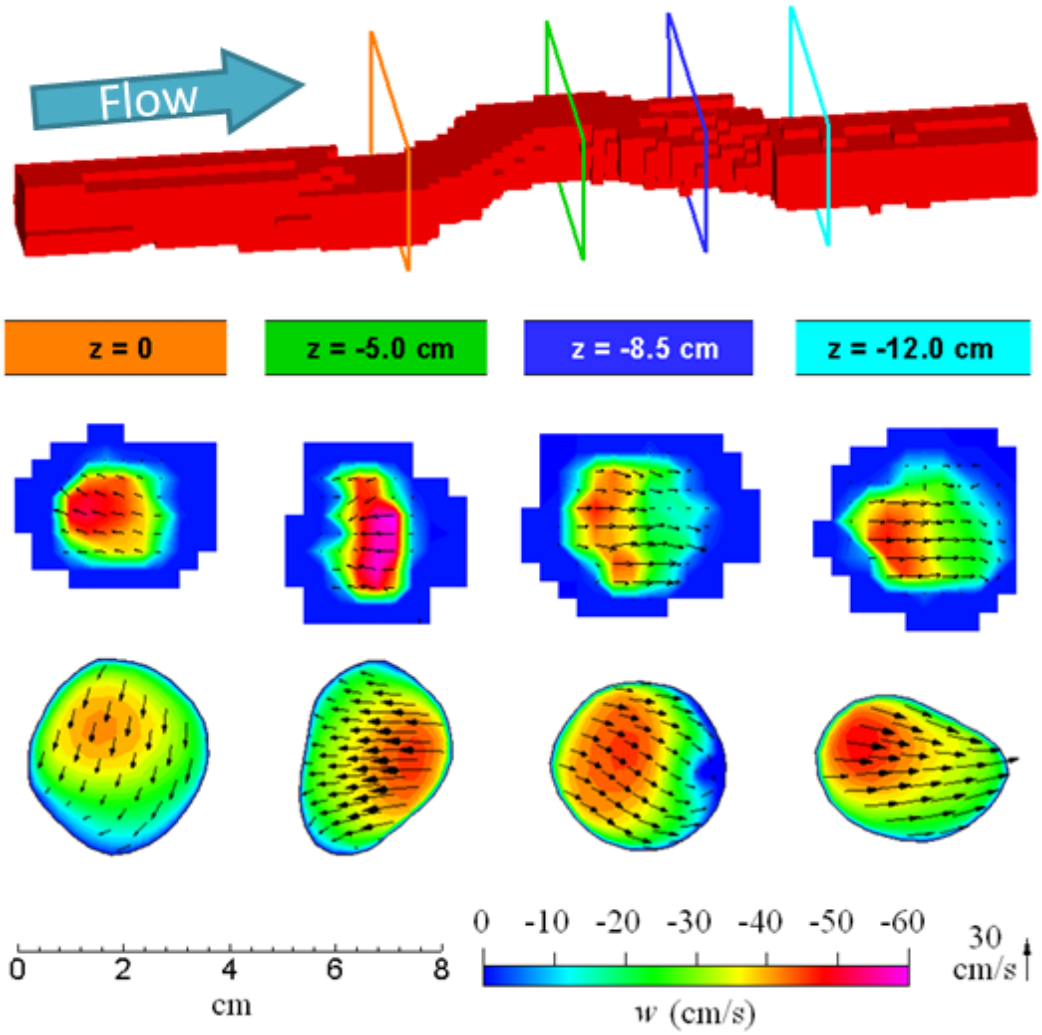

Figure 7.4 (part 2/4) 3-D velocity comparison. Comparison of experimental measurements (top row) and computational predictions (bottom row) of combined axial (colored contours) and non axial (vectors) velocities, extracted from transverse slices from phantom 3 at Re = 3000. Top: experimental measurements, bottom: computational predictions.

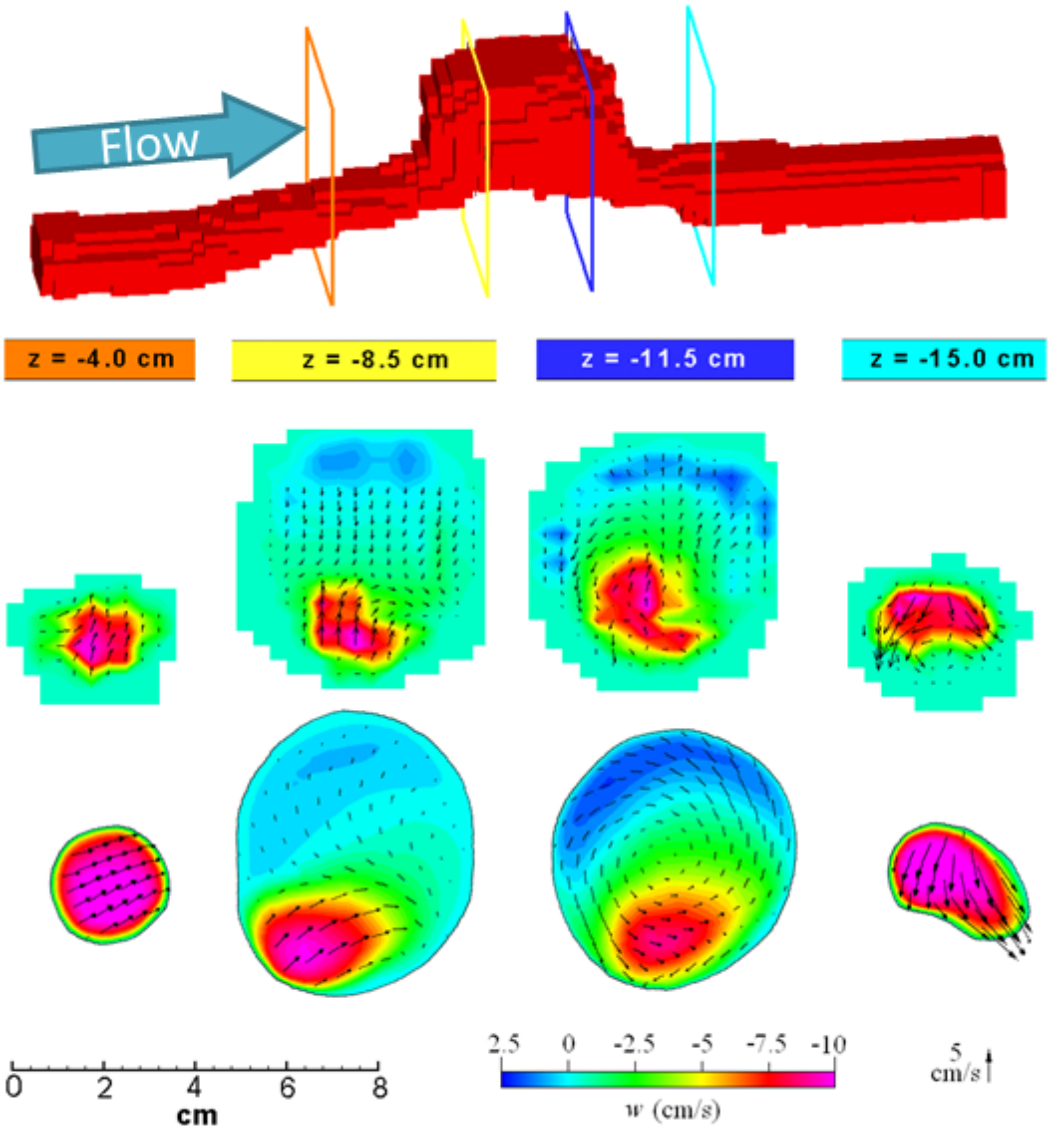

Figure 7.4 (part 3/4) 3-D velocity comparison. Comparison of experimental measurements (top row) and computational predictions (bottom row) of combined axial (colored contours) and non axial (vectors) velocities, extracted from transverse slices from phantom 4 at Re = 500. Top: experimental measurements, bottom: computational predictions.

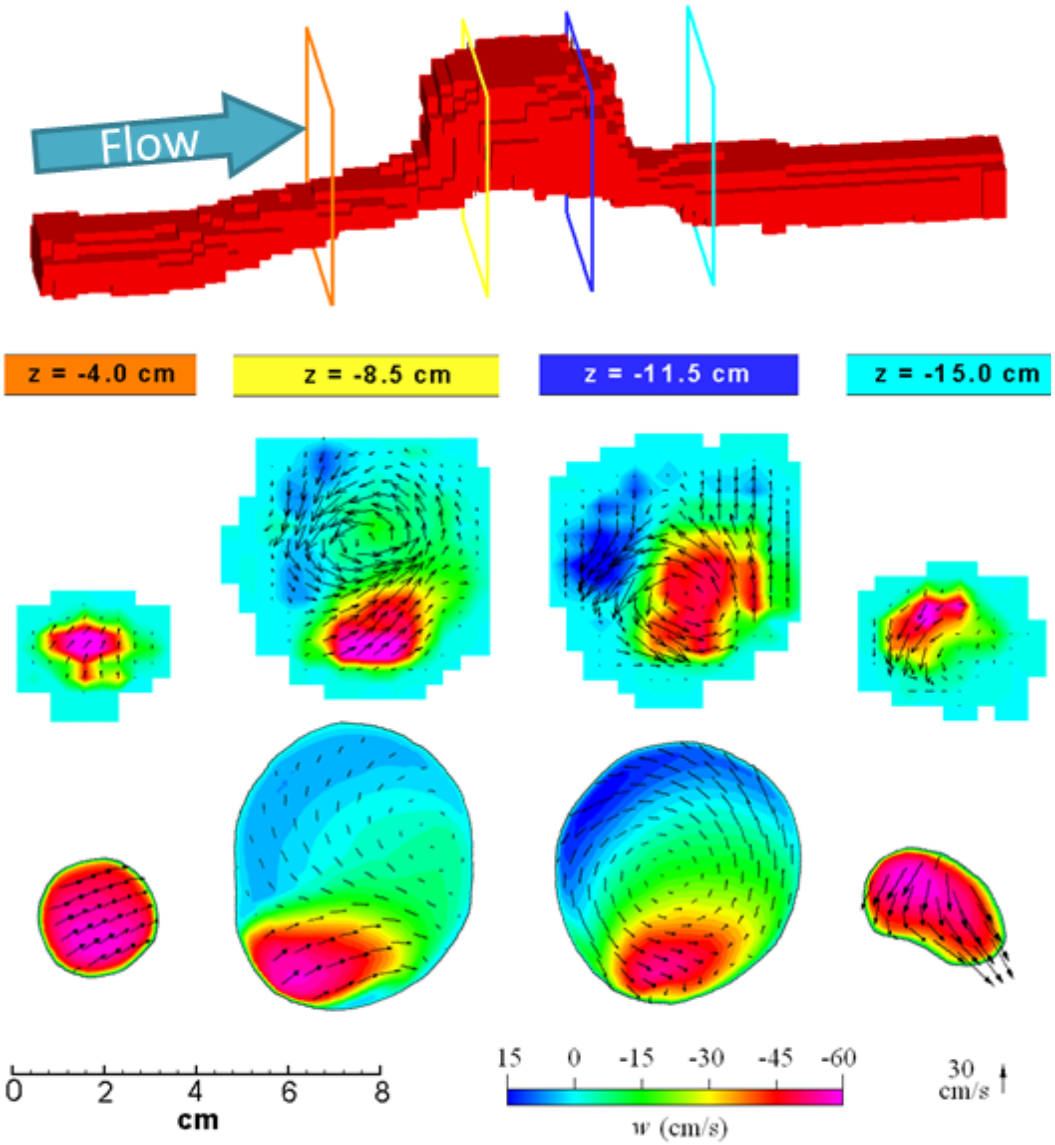

Figure 7.4 (part 4/4) 3-D velocity comparison. Comparison of experimental measurements (top row) and computational predictions (bottom row) of combined axial (colored contours) and non axial (vectors) velocities, extracted from transverse slices from phantom 4 at Re = 3000. Top: experimental measurements, bottom: computational predictions.

7.4 EXPERIMENTAL CONSIDERATIONS

Some of the PIV parameters were determined by preliminary study using a straight tube model with the results not entirely described. Turbulence and velocity measurements were well characterized in the straight tube model by both 16 × 16 and 32 × 32 pixel interrogation areas. For the wall shear stress calculations, the correlation areas were originally intended to be 16 × 16 pixels to provide better near wall resolutions. Wall shear stress from straight pipe experimentation was in good agreement with Pouiselle predictions at lower Re for both 16 × 16 resolution as well as 32 × 32. At higher Re, the 16 × 16 resolution better captured the evolved profile of the transition flows

When working with the phantoms including AAA, the image quality was sufficient to consistently correlate at 16 × 16 pixels, necessitating larger interrogations windows, 32 × 32 pixels. The 32 × 32 resolution was used throughout the 2-D measurements for constancy, and the wall shear measurements at higher Re are expected to be underevaluated.

For the 3-D analysis, the original goal was to correlate at 32 × 32. However, at low points in the phantom, where reflected light had a long distance to travel within the elastomer, image quality severely diminished. Thus, 64 × 64 resolution was required here.

The inlet profiles at Re = 125 and Re = 500 for phantom 3 unexpectededly showed *n* values of below the predicted value of 2 in Poiseuille flow. This suggests two issues. First, the velocity near the walls is underreported, and second, the wall shear stress values were underreported. Since the 32 × 32 resolution was instead of the 16 × 16 resolution, the courser interrogation area may have not well captured the shear in detail sufficient for wall shear stress calculation. Browne et al. (2000) also noted lower reported near wall velocity using PIV in comparison to LDV.

This study used 200 image sets per measurement for the 2-D analysis which included turbulence and wall shear stress calculation and 50 for the 3-D analysis for velocity only. Our preliminary study suggested that correlation of 100 image sets was optimal for wall shear or turbulence analysis, and that above 20 was adequate for velocity resolution. Westerweel et al. (1996) shows that results improve through around 100 image sets and above that, the results quality asymptotically remains constant. Likewise, fifty image sets still provides some room for improved results, but seems to be appropriate for velocity characterization, and reduces computational requirements.

Peak correlation is suggested to be achieved when a particle moves one quarter of the interrogation area between images (Raffi et al. 1998). While this was attempted to be realized in the core flows, the timing was not adjusted to accounted for the slower flow rates seen within the separated and recalculating flows. Additionally, out of plane velocity was very high for phantom 4, which may mean that

shorter time differentials would be required to capture particle motion within the light plane. Better consideration of image timing and flow velocities may improve results in these separated flows.

7.5 COMPUTATIONAL CONSIDERATIONS

Flow fields in the models were determined under the condition that the flow was fully developed at the model entrance. In laminar calculations, this was achieved by establishing a Poiseuille velocity profile within an ellipse fit to the actual entrance perimeter. However, turbulent conditions were more complex. An either flat velocity profile or uniform pressure distribution at the inlet would have led to physiologically unreasonable velocity or wall shear distributions. To avoid such artifacts, an $\left(r^*\right)^4$ velocity profile was fit to the fully developed profile of a turbulent flow field at the Reynolds number of interest and applied to the inlet ellipse as the entrance condition for computation of the model flow field. This method had the advantage of establishing a rationally based entrance condition regardless of the complexity of the entrance shape, though it had the disadvantage of producing slightly artificially high velocity at the entrance at interior positions, $r^* < 1$, with corresponding retrograde flow at $r^* > 1$. However, the $\left(r^*\right)^4$ exponent was chosen in part to minimize that effect, and initial sensitivity trials showed the bulge flow fields to be insensitive to minor changes of the inlet velocity profile.

Entrance conditions for the turbulent kinetic energy and specific dissipation rate were also obtained from this fully developed flow. The entrance conditions provide radial shaping to emulate developed flow. The distribution of dissipation over the model flow field proved to be insensitive to inlet conditions. However, the turbulent kinetic energy distribution was sensitive to its entrance distribution, reinforcing the need for the best possible approximation of turbulence at the inlet. It should be considered that the inlet turbulence values are in reasonable agreement with the experimental values. In most cases, the inlet *TI* was around 0.06 to 0.10, which is very similar to the experimental conditions. The low Re cases may have been set with arbitrary but lower values, such as *TI* = 0.01, which would have better reflected their laminar character.

Since flow instability has been observed experimentally at mean Reynolds numbers as low as 500 both *in vitro* in patient-based AAA models (Bluth et al. 1990, Hollinger et al. 1992) and *in vivo* (Feller et al. 2001), a fully developed assumption of turbulence was taken as the starting point for analysis of turbulent flow. Numerous authors have shown steady flow experiments with idealized, axi-symmetric phantoms to produce intermittent instability only at Re = 1700 or higher, but the smoothly varying curvature of such phantoms can be expected to delay the onset of instability. Even under steady conditions, the irregular, complexly curving shapes of patient lesions can be expected to elicit and amplify

perturbations of the flow field even at low Re. The Wilcox k-ω technique was used here rather than the more common k-ε approach because of its ability to provide superior results for internal flows and separated flows with adverse pressure gradients (Wilcox 1993, Ghalichi et al. 1998).

These quantitative differences indicate that stringent computational grid requirements are needed for accurate three-dimensional hemodynamic modeling. Insufficient grid density would be expected to over-damp turbulence development, restrict evolution of the flow field as Re increases and limit the accuracy of wall shear stress evaluation (Prakash and Ethier 2001). In this study, the grids were arranged with maximum density nearest the walls in the expectation that would be the region of most rapid velocity change. While the total element number in the grids used here was comparable to or greater than those of similar studies, lower interior grid density may have limited development of velocity gradients in the core, while reducing turbulence propagation and flow field evolution. In addition, time-averaged flow fields and turbulence values were calculated, without considering instantaneous fluctuating effects. More complex and computationally demanding large eddy or direct numerical simulation techniques may be required to accurately evaluate fluctuating velocities and stresses numerically. Further understanding of *in vivo* instability conditions proximal to the aneurysm would also help improve the accuracy of future turbulence calculations.

7.6 CLINICAL APPLICATION

A potential goal for this project is to contribute to the knowledge of rupture risk and the effects of aneurismal flow on the lesion walls. The strongest indicator of the type of flow appears to be the geometrical shape of the aneurysm and the presence, if any, of thrombus. The correlation between luminal shape and the presence or absence of intraluminal recirculation demonstrates that the biologic process of mural thrombus deposition has significant consequences on the physical processes of momentum transport and flow field development. Intraluminal thrombus has previously been suggested to reduce peak wall stress within AAA (Wang et al. 2002) and suppress recirculation and turbulence (Peattie et al. 2004). Here the presence of thrombus inhibited recirculation and shielded the wall from exposure to the reversed, low shear associated with bulge vortices.

The computations showed significant changes in flow field properties relative to non-dilated aortas. There was a clear, direct relationship between the presence of a bulge and vortex establishment and growth. Well-defined vortices appeared in the bulged models, which were derived from patients presenting little thrombus. In contrast, there was almost no vortex development in the isodiametric model, which was derived from a patient whose bulge was filled with deposited mural thrombus.

Interestingly, at Re = 3000 the highest aneurismal wall pressure in both the fusiform and saccular models was found on their distal surface, which has been suggested to be a prevalent site for rupture (Li and Kleinstreuer, 2006). (In the saccular model, the pressure maximum was on its anterior surface, which is not shown in figure 5.5). There was also a small, localized high pressure point in each model at the iliac bifurcation, due to fluid deceleration resulting from stagnation at that point. In general, wall positions subject to local loading maxima are at risk of high stress development. Moreover, wall stress at the bifurcation is amplified by both local wall curvature and constraints on the displacement of the iliac arteries. However, it appears that the wall is normally adequate in strength to resist the resulting stresses, since AAA rupture at the bifurcation is unlikely. As a result, stress in the lesion wall, rather than at the bifurcation, remains the physiologic variable most likely to correlate with rupture probability.

Stress and strain evaluation of the AAA wall may be used as clinical tool to assess rupture risk. Our study has shown a method to apply CFD modeling to lumen extracted from patient CT. If more sophisticated imaging tools were available that could automate the masking processes, it is conceivable that a similar CFD method in conjunction with stress analysis could be performed in clinical practice.

CHAPTER 8: CONCLUSIONS

8.1 CONCLUSIONS

This study investigated hemodynamics within patient specific AAA models by interrogating steady flow using experimental measurements and computational predictions. Methods to generate flow through phantoms and computational models of abdominal aortic aneurysms from patient CT data are described. The flow in the phantoms was interrogated using particle image velocimetry and pressure measurements, while computational fluid dynamics was used to predict the flow fields within the models. Flow was measured experimentally at flow rates ranging from Re = 125 to Re = 3000, while computational fields were generated from Re = 500 to Re = 3000 using both laminar and turbulent calculations schemes, using a k-ω approach for the turbulent fields. The following conclusions were drawn from our results:

- Complex flow patterns and separated flow was found in every model studied, but greater flow disruption and larger vortices accompanied larger lumen dilations. Forward velocities of up to 64 cm/s and retrograde velocities of up to 12 cm/s were measured at Re = 3000.

- Reversed and reduced magnitude wall shear stress accompanied retrograde flow. Wall shear decreased from 2-6 dyne/cm^2 in non-dilated sections to -1 to -2 dyne/cm^2 on the anterior wall of phantom 4 at Re = 3000.

- Computational results showed adverse pressure gradients accompanying the separated flows, but this was not confirmed by experimental measurements. The experimental results showed pressure ranges of up to 3.5 mmHg, found on one wall of phantom 5. However, these pressure differentials were nearly entirely due to wall height variation, with minimal contribution to flow.

- Both non-dilated and dilated lumens induced turbulence, which was seen at all flow rates including Re = 125. Turbulence was not well predicted by the turbulent computation scheme and was an order of magnitude less than the experimental measurements.

- The laminar and turbulent computations produced similar flow fields. The same overall flow structure was seen in all laminar and turbulent cases, but some measureable quantitative differences did exist. The differences between the laminar and turbulent flow fields were greatest within the dilations, at Re = 3000.

- Qualitatively, agreement between the experimental measurements and computational predictions of the velocity and wall shear stress were in reasonable. However quantitative differences were significant, most so at Re = 3000.

8.2 FUTURE STUDY

As with any project worth investigating, more opportunities for arise than could possibly be studied. Some suggestions for future study include:

- Application of pulsatile flow to these models.
- Further computational grid refinement and independence analysis.
- Determining a turbulence calculation scheme that better describes turbulent conditions seen experimentally.
- Determining turbulent inlet conditions from experimental measurements of AAA flow from this study.
- Determining flow field patterns and evaluating wall shear stress from a single PIV correlation to provide instantaneous data.
- Use digital pressure signal to time average pressure and fluctuation magnitude.
- Compare wall stressors and velocities statistically over the series of models.
- Identification of the locations stagnation and separation points.

BIBLIOGRAPHY

Asbury, C. L., J. W. Ruberti, E. I. Bluth, and R. A. Peattie. Experimental investigation of steady flow in rigid models of abdominal aortic aneurysms. *Ann Biomed Eng*. 23:29-39, 1995.

Aslani, E. Geometric and wall pressure characterization of patient abdominal aortic aneurysm. M.S. Thesis, Oregon State University, 2005.

Atkinson, S. J., K. J. Feller, and R. A. Peattie. Measurement of fluid flow patterns and wall shear-stresses in patient-based models of abdominal aortic aneurysms. *Advances in Bioengineering, ASME BED*. 50:753-754, 2001.

Baxter, B. T., M. C. Terrin, and R. L. Dalman. Medical management of small abdominal aortic aneurysms. *Circulation*. 117:1889-9, 2008.

Bluestein, D., L. Niu, R. T. Schoephorster, and M. K. Dewanje. Steady flow in an aneurysm model: correlation between fluid dynamics and blood platelet deposition. *J Biomech Eng*. 118:280-286, 1996.

Bluth, E. I., S. M. Murphey, L. H. Hollier, and M. A. Sullivan. Color flow doppler in the evaluation of aortic aneurysms. *Int Angiol*. 9:8-10, 1990.

Boussinesq, J. Théorie de l'Écoulement Tourbillant. *Mem Présentés par Divers Savants Acad Sci Inst Fr*. 23:46-50, 1877.

Bourne, J.L., and M.R. Gaspar. Aneurysms of the aorta: a study of 64 cases. *West J Surg Obstet Gynecol*. 66:9, 1958.

Brown L.C., and J.T. Powell. UK Small Aneurysm Trial Participants. Risk factors for aneurysm rupture in patients kept under ultrasound surveillance. *Ann Surg*. 230:289-297, 1999.

Browne, P., A. Ramuzat, R. Saxena, and A. P. Yoganathan. Experimental investigation of the steady flow downstream of the St. Jude bileaflet heart valve: a comparison between laser doppler velocimetry and particle image velocimetry techniques. *Ann Biomed Eng*. 28:39-47, 2000.

Budwig, R., D. Elger, H. Hopper, and J. Slippy. Steady flow in abdominal aortic aneurysm models. *J Biomech Eng*. 115:418-423, 1993.

Cooley, D.A. *Surgical Treatment of aortic aneurysms*. W.B. Saunders Company, Philadelphia, 1986.

Cronenwett, J. L., et al. Actuarial analysis of variables associated with rupture of small abdominal aortic aneurysms. *Surgery*. 98:472-83, 1985.

Dantec Measurement Technology A/S. *Flowmap particle image velocimetry instrumentation*. Skovlunde, Denmark, 1998.

Dubost, C., M. Allary, and N. Oeconomos. Resection of aneurysm of abdominal aorta; reestablishment of continuity by preserved human arterial graft, with result after five months. *AMA Arch Surg*. 64: 405.

Di Martino, E. S., G. Guadagni, A. Fumero, G. Ballerini, R. Spirito, P. Biglioli, and A. Redaelli. Fluid-structure interaction within realistic three-dimensional models of the aneurysmatic aorta as a guidance to assess the risk of rupture of the aneurysm. *Med Eng Phys*. 23:647-55, 2001.

Di Martino, E. S., D. A. Vorp. Effect of variation in intraluminal thrombus constitutive properties on abdominal aortic aneurysm wall stress. *Ann Bio Eng*. 31:804-809, 2003.

Dombrowski N., E. A. Foumeny, S. Ookawara and A. Riza. The effect of Reynolds number on the entry length and pressure drop for laminar pipe flow. *Can J Chem Engr*. 71:472-476, 1993.

Egelhoff, C. J., R. S. Budwig, D. F. Elger, T. A. Khraishi, and K. H. Johansen. Model studies of the flow in abdominal aortic aneurysms during resting and exercise conditions. *J Biomech Eng*. 32:1319-1329, 1999.

Ekaterinaris, J. A., C. V. Ioannou, A. N. Katsamouris. Flow dynamics in expansions characterizing abdominal aorta aneurysms. *Ann Vasc Surg*. 20:351-359, 2006.

Feller, K. J., S. J. Atkinson, and R. A. Peattie. Quantification of Flow Stability in Patient-Based Models of Abdominal Aortic Aneurysms. *Advances in Bioengineering, ASME BED*. 50:729-730, 2001.

Finol, E. A., and C. H. Amon. Blood flow in abdominal aortic aneurysms: pulsatile flow hemodynamics. *J Biomech Eng*. 123:474-484, 2001.

Finol, E. A., and C. H. Amon. Flow dynamics in anatomical models of abdominal aortic aneurysms: computational analysis of pulsatile flow. *Acta Cient Venez*. 54:43-49, 2003.

Fukushima, T., T. Matsuzawa, and T. Homma. Visualization and finite element analysis of pulsatile flow in models of the abdominal aortic aneurysm. *Biorheology*. 26:109-130, 1989.

Fung, Y.-C. *Biomechanics: Circulation.* 2nd Ed. Springer-Verlag, New York, 1997.

Ghalichi, F., X. Deng, A. De Champlain, Y. Douville, M. King, and R. Guidoin. Low Reynolds number turbulence modeling of blood flow in arterial stenoses. *Biorheology* 35:281-294, 1998.

Genevès, C., F. Wilquem, F. Treyve, G. Cloutier, G. Soulez, and K. Saïdane. Study of non stationary mode flow of an abdominal aortic aneurysm. *Journal* of *Applied Biomaterials and Biomechanics*. 3:176-183, 2005.

Greenhalgh R. M., and J. T. Powell. Endovascular repair of abdominal aortic aneurysm. *New England J Med*. 358:494-501, 2008.

Greenhalgh, R. M., and EVAR trial participants. Endovascular aneurysm repair versus open repair in patients with abdominal aortic aneurysm (EVAR trial 1): randomized controlled trial. *Lancet*. 365:2179-86, 2005.

Hollinger, L. H., L. M. Taylor, and J. Ochsner. Recommended indications for operative treatment of abdominal aortic aneurysms. *J Vasc Surg*. 15:1046-1056, 1992.

Johansson, G., and J. Swedenborg. Ruptured abdominal aortic aneurysms: A study of incidence and mortality. *Br J Surg*. 73:101-103, 1986.

Khanafer, K. M., J. L. Bull, G. R. Upchurch, and R. Berguer. Turbulence significantly increases pressure and fluid shear stress in an aortic aneurysm model under resting and exercise flow conditions. *Ann Vasc Surg*. 21:67-74, 2007.

Kolmogorov, A. N., Equations of turbulent motion of an incompressible fluid (Russian). *Izv Akad Nauk SSSR Ser Fiz*. No. 1-2, 56-58, 1942.

Jones, W. P., and B.E. Launder. The prediction of laminarization with a two-equation model of turbulence. *Int. J. Heat Mass Transfer*. 15:301-314, 1972.

Lederle F. A., G. R. Johnson, S.E. Wilson, et al. Rupture rate of large abdominal aortic aneurysms in patients refusing or unfit for elective repair. *JAMA*. 287:2968-72, 2002.

Lederle F. A., D. B. Nelson, and A. M. Joseph. Smokers' relative risk for aortic aneurysm compared with other smoking-related diseases: a systematic review. *J Vasc Surg*. 38:329-334, 2003.

Leung, J. H., A. R. Wright, N. Cheshire, J. Crane, S. A. Thom, A. D. Hughes, and Y. Xu. Fluid structure interaction of patient specific abdominal aortic aneurysms: a comparison with solid stress models. *Biomedical Engineering Online*. 5:33, 2006.

Li, Z., and C. Kleinstreuer. Effects of blood flow and vessel geometry on wall stress and rupture risk of abdominal aortic aneurysms. *J Med Eng Technol*. 30:283-297, 2006.

Liddington, M. I. and B.M. Heather. The relationship between aortic diameter and body habitus. *European Journal of Vascular Surgery*. 6:619-642, 1992.

Maslak, P. Rouleaux Formation**.** American Society of Hematology Image Bank: 101153, 2004.

Newman, A. B., A. M. Arnold, G. L. Burke, D. H. O'Leary, and T. A. Manolio. Cardiovascular Disease and Mortality in Older Adults with Small Abdominal Aortic Aneurysms Detected by Ultrasonography: The Cardiovascular Health Study. *Ann Intern Med*. 134:182-190, 2001.

O'Rourke, M. J., J. P. McCullough. A comparison of the measured and predicted flowfield in a patient-specific model of an abdominal aortic aneurysm. *Proc IMechE, Part H: Journal of Engineering in Medicine*. 222:737-750, 2008.

Parodi, J.C., J. C. Palmaz, and H. D. Barone. Transfemoral intraluminal graft implantation for abdominal aortic aneurysms. *Ann Vasc Surg*. 5:491-499, 1991.

Peattie, R. A., T. Schrader, E. I. Bluth, and C. E. Comstock. Development of turbulence in steady flow through models of abdominal aortic aneurysms. *J Ultrasound Med*. 13:467-472, 1994.

Peattie, R. A., T. J. Riehle, and E. I. Bluth. Pulsatile flow in fusiform models of abdominal aortic aneurysms: flow fields, velocity patterns and flow-induced wall stresses. *J Biomech Eng*. 126:438-446, 2004.

Peattie, R. A., C. L. Asbury, E.I. Bluth, and J.W. Ruberti. Steady flow in models of abdominal aortic aneurysms. Part I: Investigation of the velocity patterns. *J Ultrasound Med*. 15:679-688, 1996.

Peattie, R. A., C. L. Asbury, R.I. Bluth, and J.W. Ruberti. Steady flow in models of abdominal aortic aneurysms. Part II: Wall stresses and their implication for in vivo thrombosis and rupture. *J Ultrasound Med*. 15:689-696, 1996.

Pedersen, E. M., et al. Quantitative abdominal aortic flow measurements at controlled levels of ergometer exercise. *Magn Reson Imaging.* 17:489-494, 1999.

Poiseuille, J. L. M. Recherches experimentales sur le mouvement des liquides dans les tubes de tres-petits diametres. In *Memoires presentes par divers savants a l'Academie Royale des Sciences de l'Institut de France,* IX: 433-544, 1846.

Pope, S. B. *Turbulent flows*. Cambridge University Press, Cambridge, 2000.

Prakash, S., C. R. Ethier. Requirements for Mesh Resolution in 3D Computational Hemodynamics. *J Biomech Eng*. 123:134-144, 2001.

Prandtl, L. On fluid motions with very small friction. *Verhdlg 3 Intern Math Kongr*. 1904.

Raffel, M., C. Willert, J. Kompenhans. *Particle image velocometery: a practical guide*. Springer-Verlag, New York, 1998.

Raghavan, M. L., D. A.Vorp, M. P. Federle, M. S. Makaroun, and M. W. Webster. Wall stress distribution on three-dimensionally reconstructed models of human abdominal aortic aneurysm. *J Vasc Surg*. 31:760-769, 2000.

Reynolds, O. An experimental investigation of the circumstances which determine whether the motion of water shall be direct or sinuous, and of the law of resistance in parallel channels. Proceedings of the Royal Society of London, 35: 84-99, 1883.

Roberts, W.C. The aorta: its acquired diseases and their consequences as viewed from a morphologic perspective, Lindsay J Jr, Hurst JW (eds). Grune & Stratton, New York, 1979, pg 51.

Rutgers, M. A., X. L. Wu, and W. I. Goldburg. The Onset of 2-D Grid Generated Turbulence in Flowing Soap Films. *Phys Fluids* 8:S7, 1996.

Salsac, A. V., S. R. Sparks, J. M. Chomaz, and J. C. Lasheras. Evolution of the wall shear stresses during the progressive enlargement of symmetric abdominal aortic aneurysms. *J Fluid Mech*. 560:19-51, 2006.

Schoephoerster, R.T., F. Oynes, G. Nunez, M. Kapadvanjwala, and M. K. Dewanjee. Effects of local geometry and fluid dynamics on regional platelet deposition on artificial surfaces. *Arteriosclerosis, Thrombosis*, *and Vascular Biology*. 13:1806-1813, 1993.

Schrader, T., R. A. Peattie, E. I. Bluth, and C. E. Comstock. A Qualitative Investigation of Turbulence in Flow Through a Model Abdominal Aortic Aneurysm. *Invst Radiol*. 27:515-519, 1992.

Scotti, C. M., and E. A. Finol. Compliant biomechanics of abdominal aortic aneurysms: a fluid-structure interaction study. *Computers and Structures*. 85:1097-1113, 2007.

Silver, M.D. *Cardiovascular Pathology*. Churchill Livingstone, New York, 1983.

Singh, K., K. H. Bønaa, B. K. Jacobsen, L. Bjørk, and S. Solberg. Prevalence of and Risk Factors for Abdominal Aortic Aneurysms in a Population-based Study: The Tromsø Study. *Am J Epidemiol*. 154: 236-244, 2001.

Szilagyi, D.E., J.P. Elliot, and R.F. Smith. Clinical fate of the patient with asymptomatic abdominal aortic aneurysm and unfit for surgical treatment. *Arch Surg*. 104:600-6, 1972.

Taylor, C. A., C. P. Cheng, L. A. Espinosa, B. T. Tang, D. Parker, and R. J. Herfkens. In vivo quantification of blood flow and wall shear stress in the human abdominal aorta during lower limb exercise. *Ann Biomed Eng*. 30:402-408, 2002.

Van de Graaff, K. M. *Human anatomy*. 5th Ed. WBC/McGraw Hill, New York, 2002.

Viswanath, N., C. M. Rodkiewicz, and S. Zajac. On the abdominal aortic aneurysms: pulsatile state considerations. *Med Eng Phys*. 19:343-51.

Wang, D.H., M.S. Makaroun, M.W. Webster, and D.A. Vorp. Effect of intraluminal thrombus on wall stress in patient-specific models of abdominal aortic aneurysm. *J Vasc Surg*. 36:598-604, 2002.

Westerweel, J., A. A. Dradd, J. G. Th. Van der Hoeven, J. van Oord. Measurement of fully-developed turbulent pipe flow with digital particle image velocimetry. *Experiments in fluids*. 20:165-177, 1996.

Wilcox, D. C. *Turbulence Modeling for CFD*. 2nd Ed. DCW Industries, La Canada, California. 1993.

Wille, S. O. Pulsatile pressure and flow in an arterial aneurysm simulated in a mathematical model. *J Biomed Eng*. 3:153-8, 1981.

Wilmore, J. H. and D. L. Costill. *Physiology of Sport and Exercise*. 3rd Ed. Champaign, IL: Human Kinetics, 2005.

Wolters, B. J., M. C. Rutten, G. W. Schurink, U. Kose, J. de Hart, and F. N. van de Vosse. A patient-specific computational model of fluid-structure interaction in abdominal aortic aneurysms. *Med Eng Phys*. 27:871-883, 2005.

Yip, T.H., and S.C. Yu. Cyclic transition to turbulence in rigid abdominal aortic aneurysm models. *Fluid Dynamics Research*. 29:81-113, 2001.

Yu, S. C. Steady and pulsatile flow studies in abdominal aortic aneurysm models using particle image velocimetry. *Int J Heat Fluid Flow*. 21:74-83, 2000.

Zarins C. K., M. A. Heikkinen, E. S. Lee, J. M. Alsac, and F. R. Arko. Endovascular treatment of abdominal aortic aneuryms: latest results. *J Cardiovascular Surg*. 45: 321-333, 2004.

APPENDICES

Appendix A: AAA model numeration

Aslani Models	Edgar CFD Models	Phantoms
1	1	4
2	2	-
3	-	-
4	4	-
5	5	-
6	6	-
7	7	3
8	8	1
9	9	-
10	10	5 / prototype
11	3	2
12	-	-

Table A.1 AAA model numeration. The numeration of the AAA models became inconsistent. Aslani and Peng used the naming conventions in the left column. Atkinson and Feller studied phantoms 1 – 3, and limited study on the 'prototype' phantom, named phantom 5 in this study.

Appendix B: CFD results

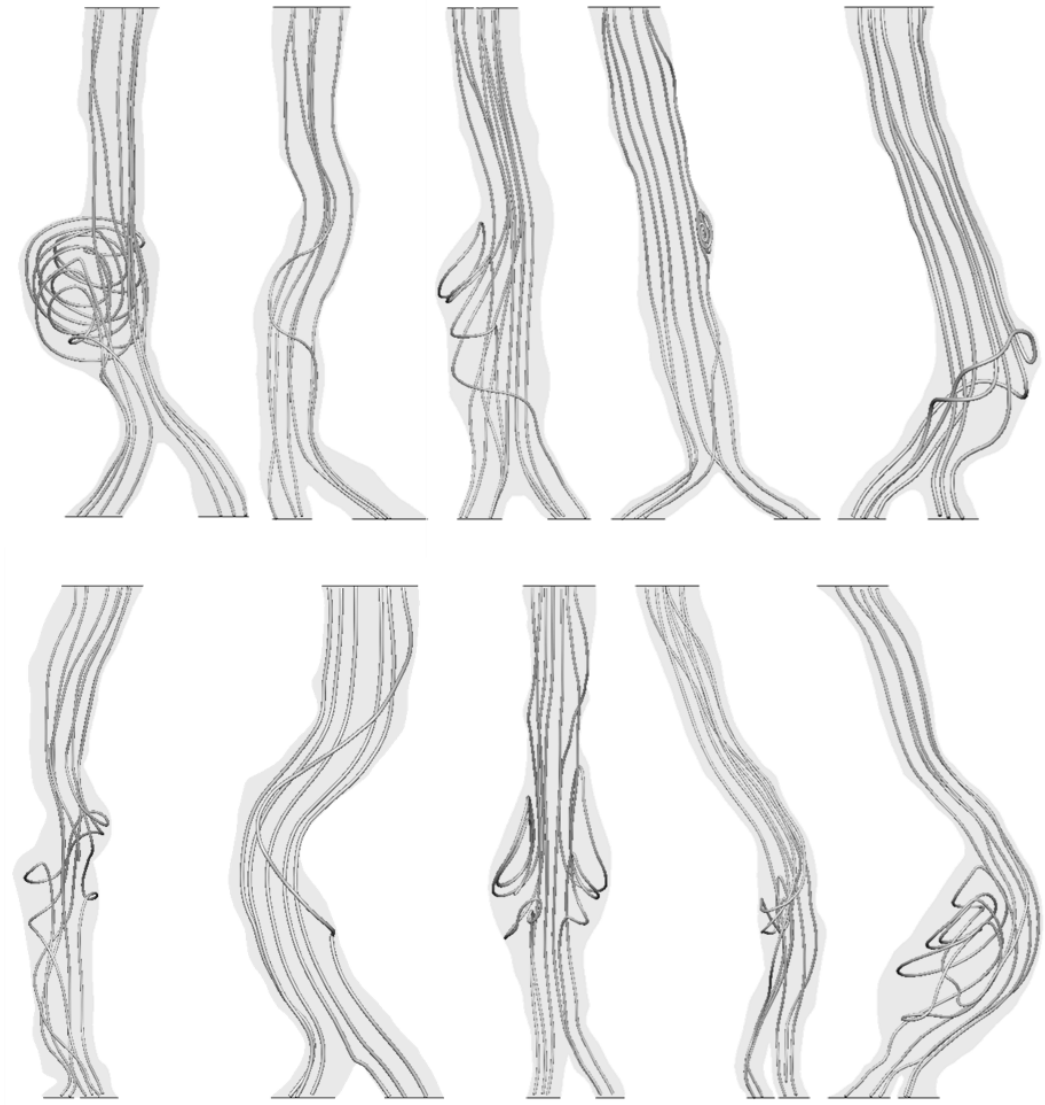

Figure B.1 Stream tubes. Stream tube traces taken from turbulent CFD simulation at Re = 3000. The point of view presented is from the posterior.

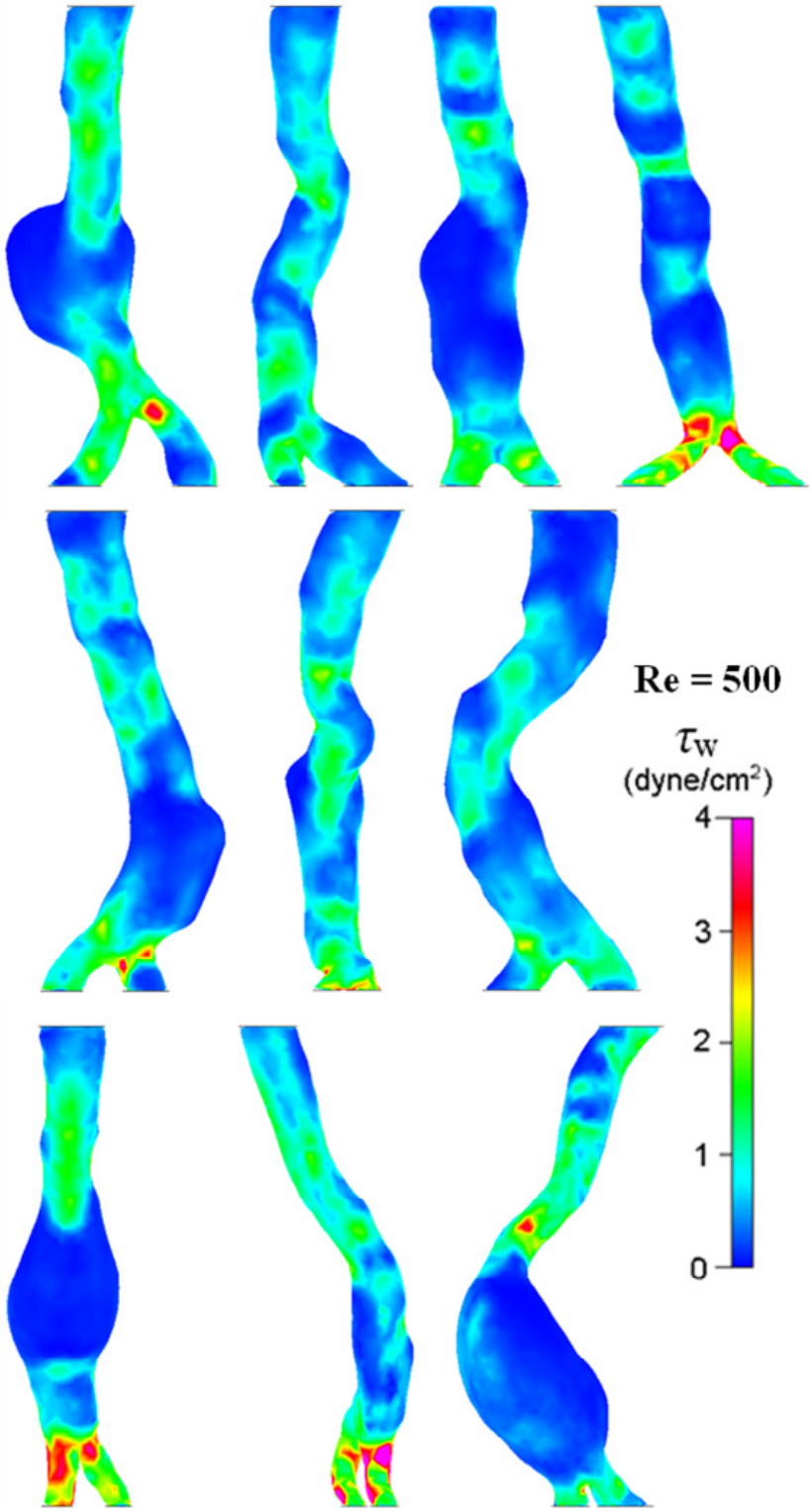

Figure B.2 Wall shear stress at Re = 500. Wall shear stress for models 1-10 at Re = 500 from laminar simulation. The point of view is from the posterior.

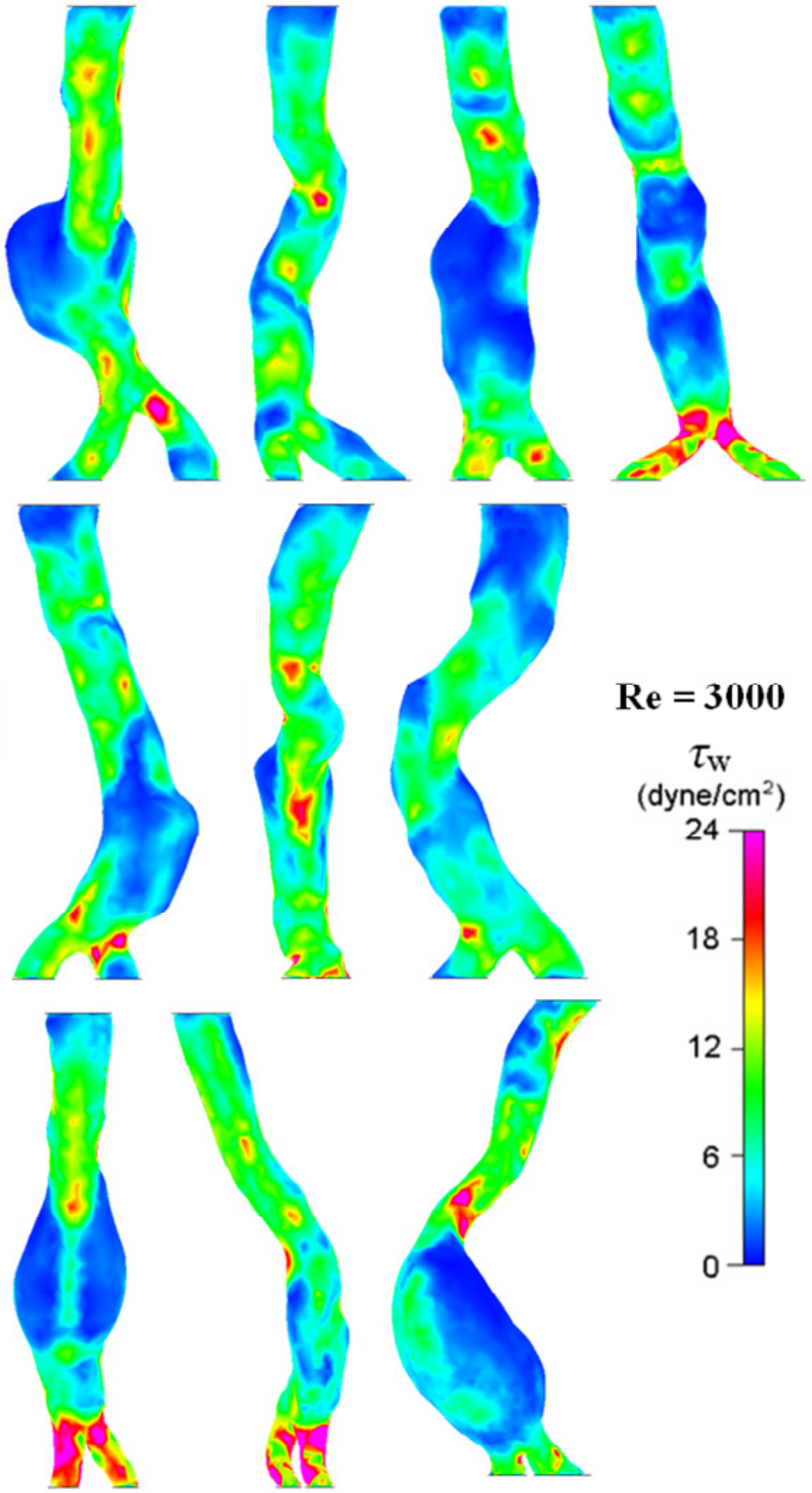

Figure B.3 Wall shear stress at Re = 3000. Wall shear stress for models 1-10 at Re = 3000 from turbulent simulation. The point of view is from the posterior.

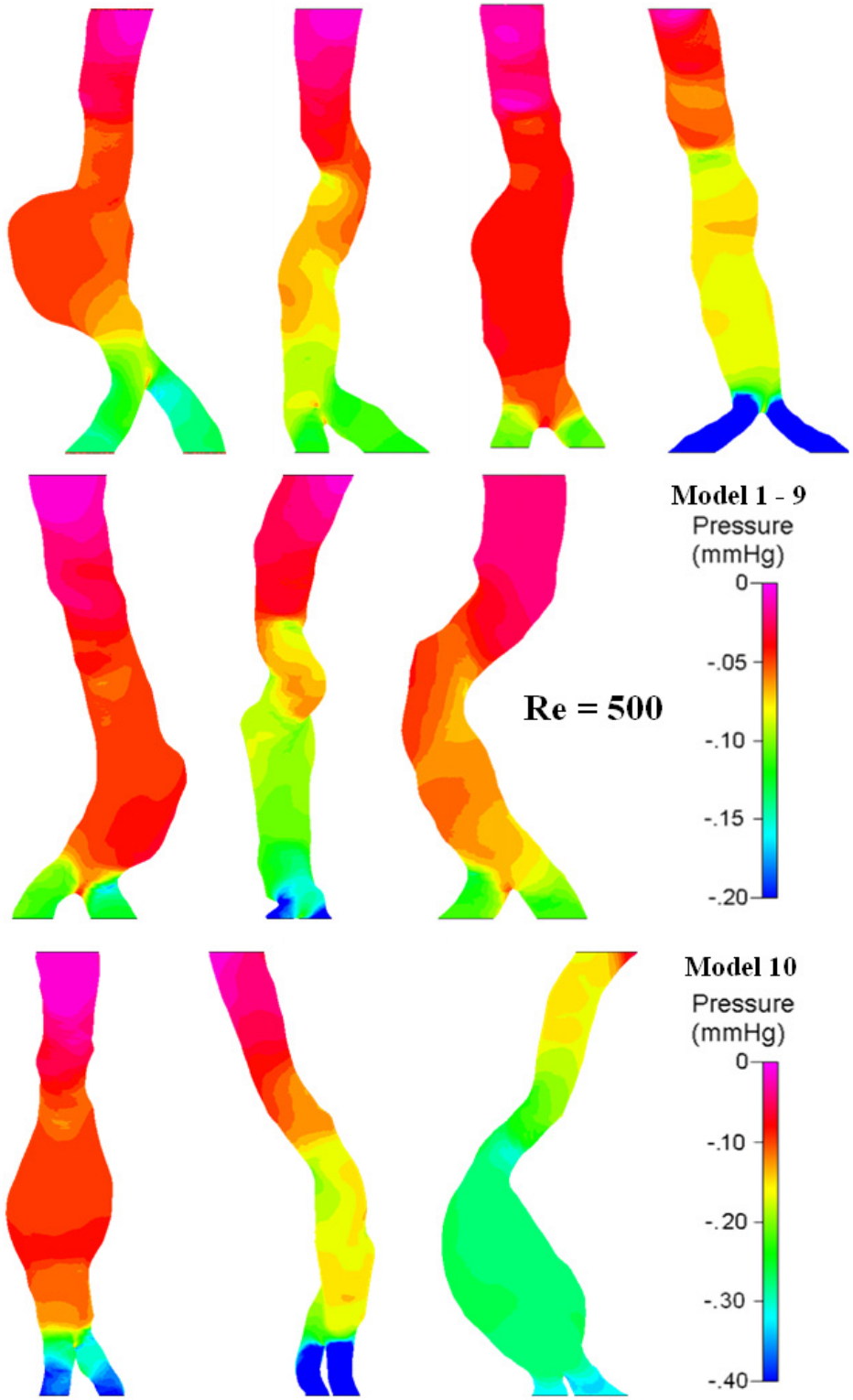

Figure B.4 Wall pressure at Re = 500. Wall pressure for models 1-10 at Re = 500 from laminar simulation. The point of view is from the posterior.

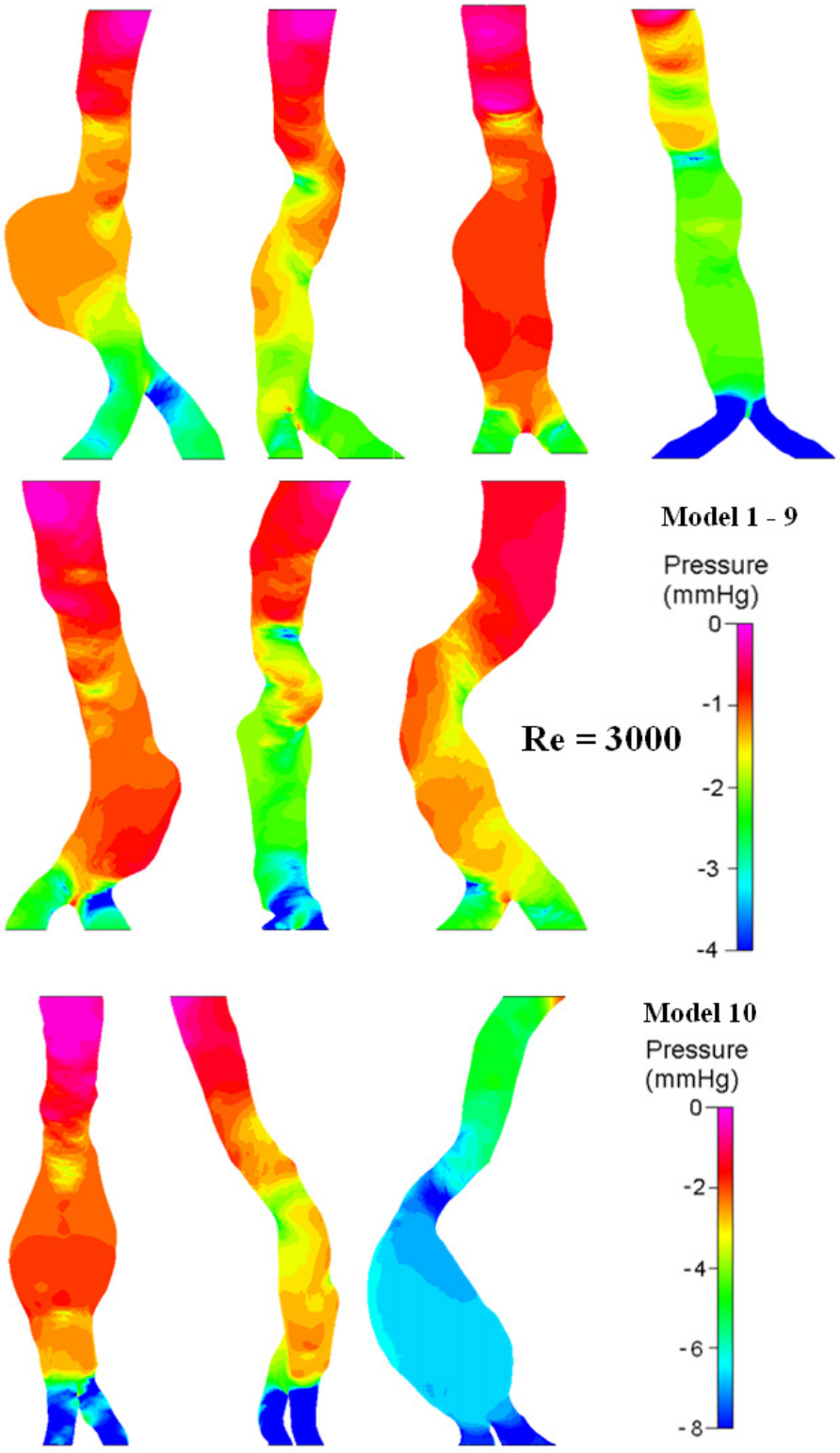

Figure B.5 Wall pressure at Re = 3000. Wall pressure for models 1-10 at Re = 3000 from turbulent simulation. The point of view is from the posterior.

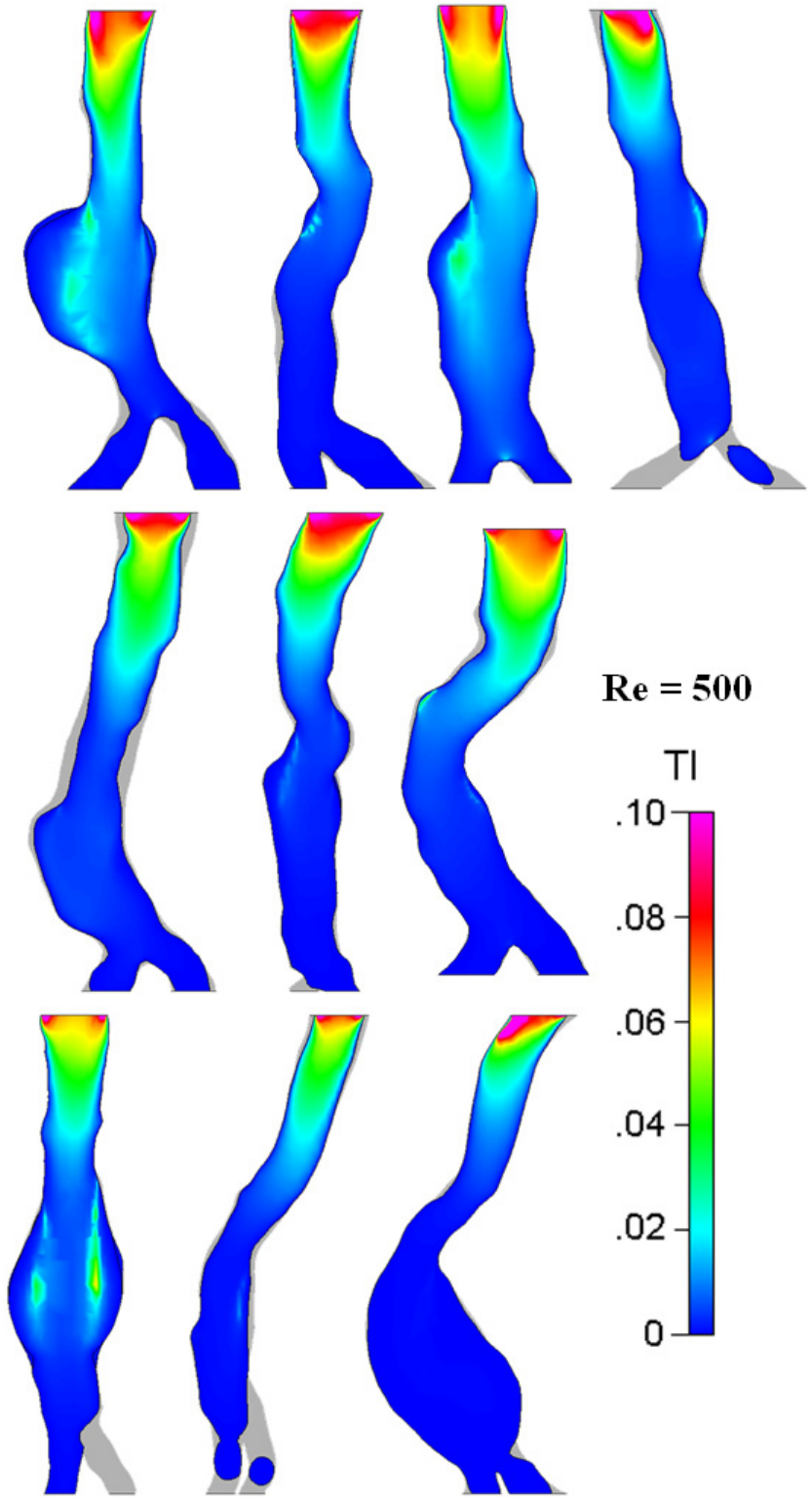

Figure B.6 Turbulence intensity at Re = 500. Turbulence intensity for models 1-10 at Re = 500 from turbulent simulation. The point of view is from the posterior.

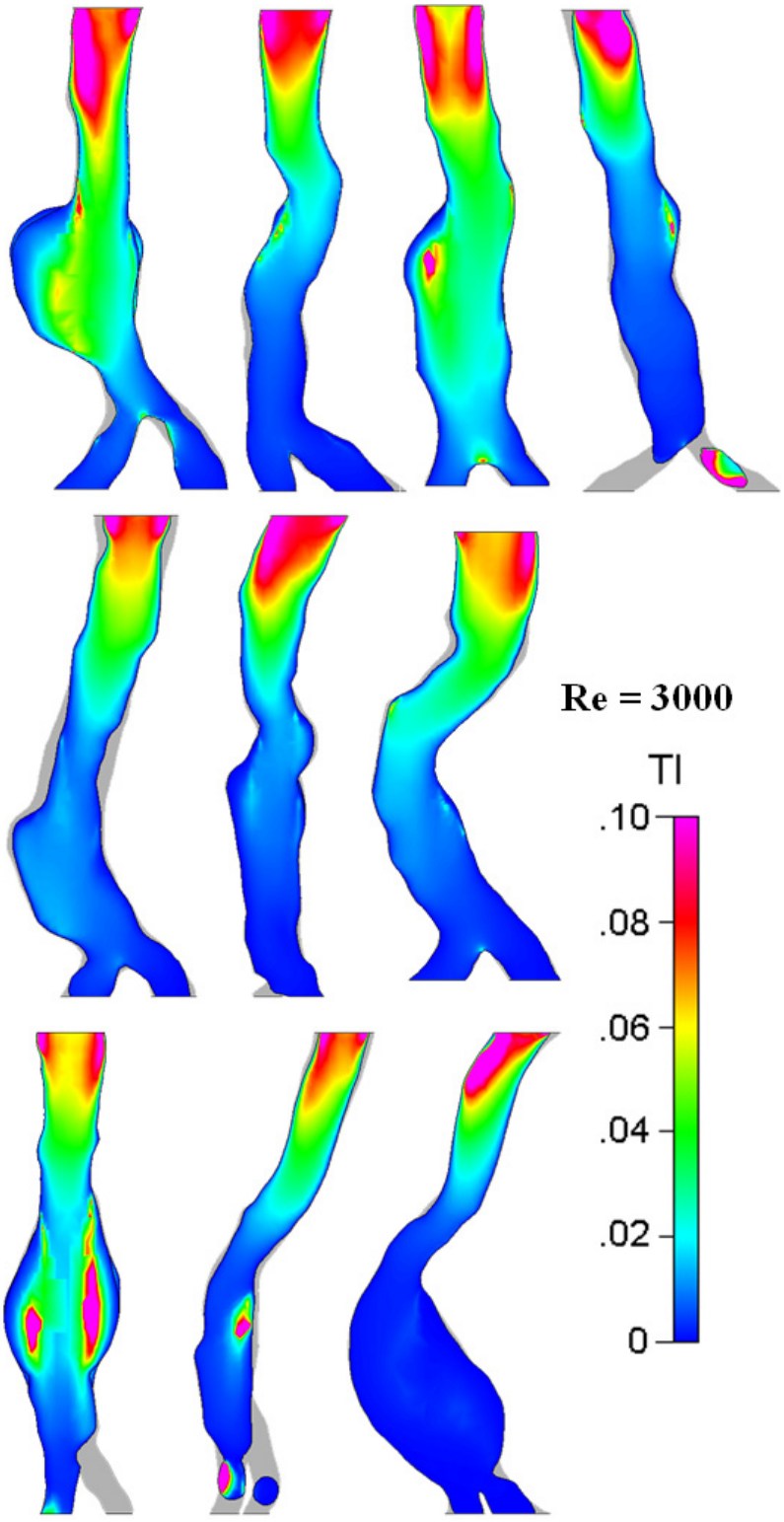

Figure B.7 Turbulence intensity at Re = 3000. Turbulence intensity for models 1-10 at Re = 3000 from turbulent simulation. The point of view is from the posterior.

d_p = 2.25 cm

Re	C_k	$C_{\omega,1}$	$C_{\omega,2}$
500	-4.3	0.1	2.1
1000	-3.7	0.2	2.1
2000	-3.1	0.3	2.2
3000	-2.8	0.5	2.3

d_p = 2.32 cm

Re	C_k	$C_{\omega,1}$	$C_{\omega,2}$
500	-4.3	0.0	2.1
1000	-3.6	0.1	2.1
2000	-3.1	0.3	2.2
3000	-2.8	0.4	2.2

d_p = 2.42 cm

Re	C_k	$C_{\omega,1}$	$C_{\omega,2}$
500	-4.3	0.0	2.1
1000	-3.7	0.1	2.1
2000	-3.1	0.3	2.1
3000	-2.9	0.4	2.1

d_p = 2.68 cm

Re	C_k	$C_{\omega,1}$	$C_{\omega,2}$
500	-4.4	-0.2	2.0
1000	-3.8	0.0	2.0
2000	-3.2	0.2	2.0
3000	-3.0	0.3	2.0

d_p = 2.92 cm

Re	C_k	$C_{\omega,1}$	$C_{\omega,2}$
500	-4.5	-0.2	1.9
1000	-3.9	-0.1	1.9
2000	-3.3	0.1	1.9
3000	-3.0	0.2	1.9

Table B.1 Inlet turbulence parameters. Compilation of inlet turbulence parameters from the preliminary fully developed turbulent pipe flow simulations

Appendix C: Wall pressure results

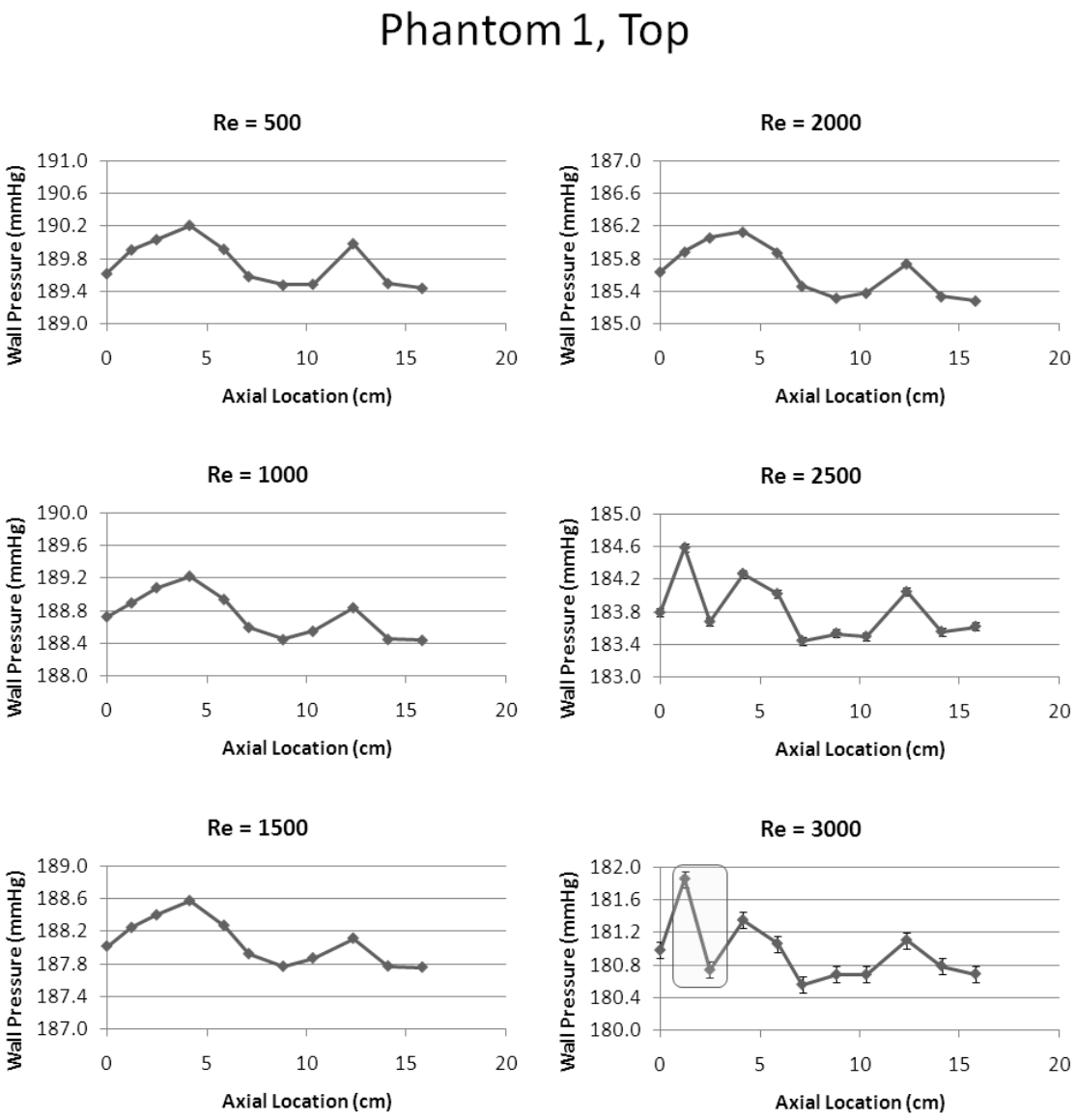

Figure C.1 Phantom 1, top. Highlighted area in Re = 3000 plot indicates questionable points.

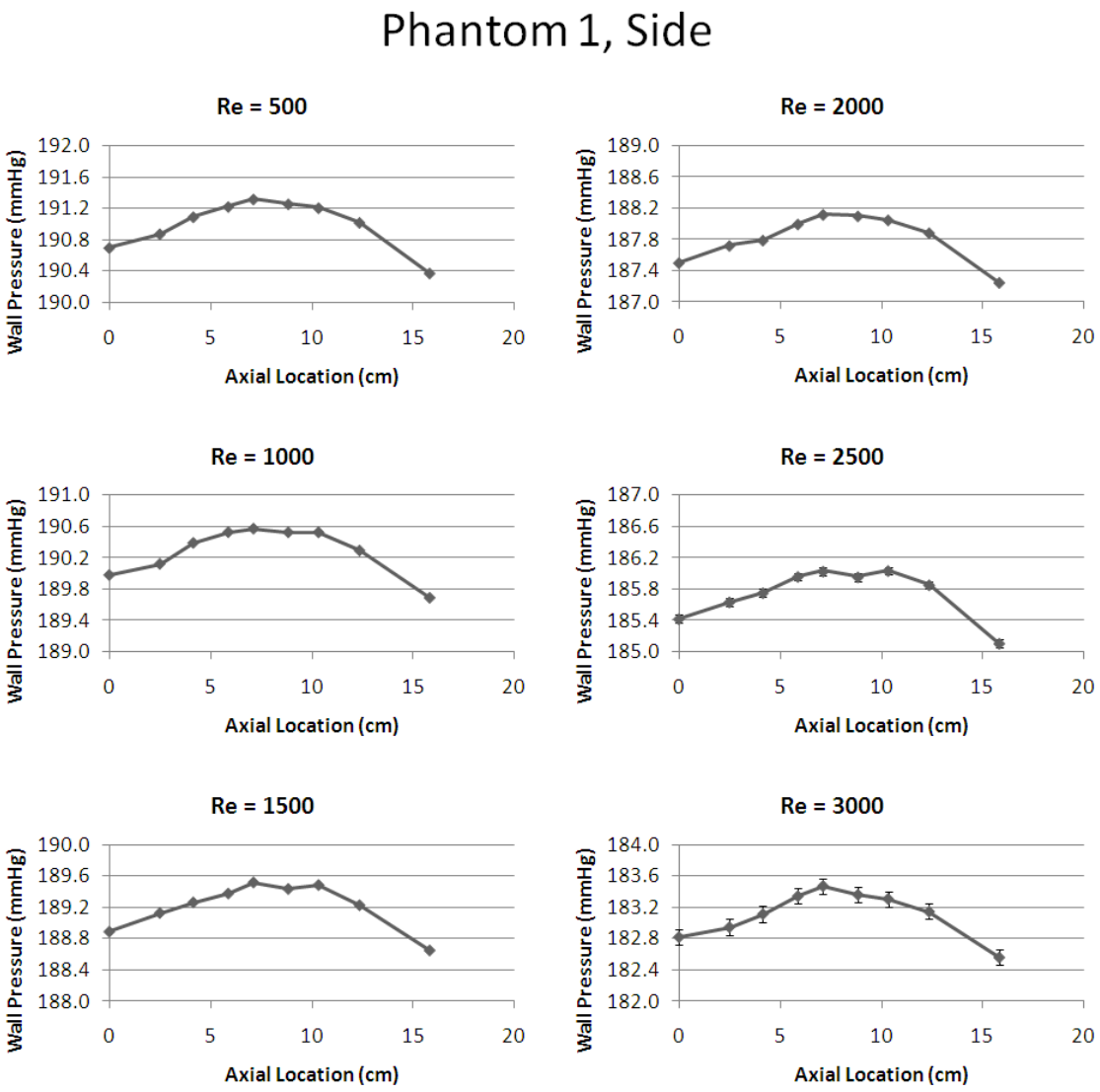

Figure C.2 Phantom 1, side.

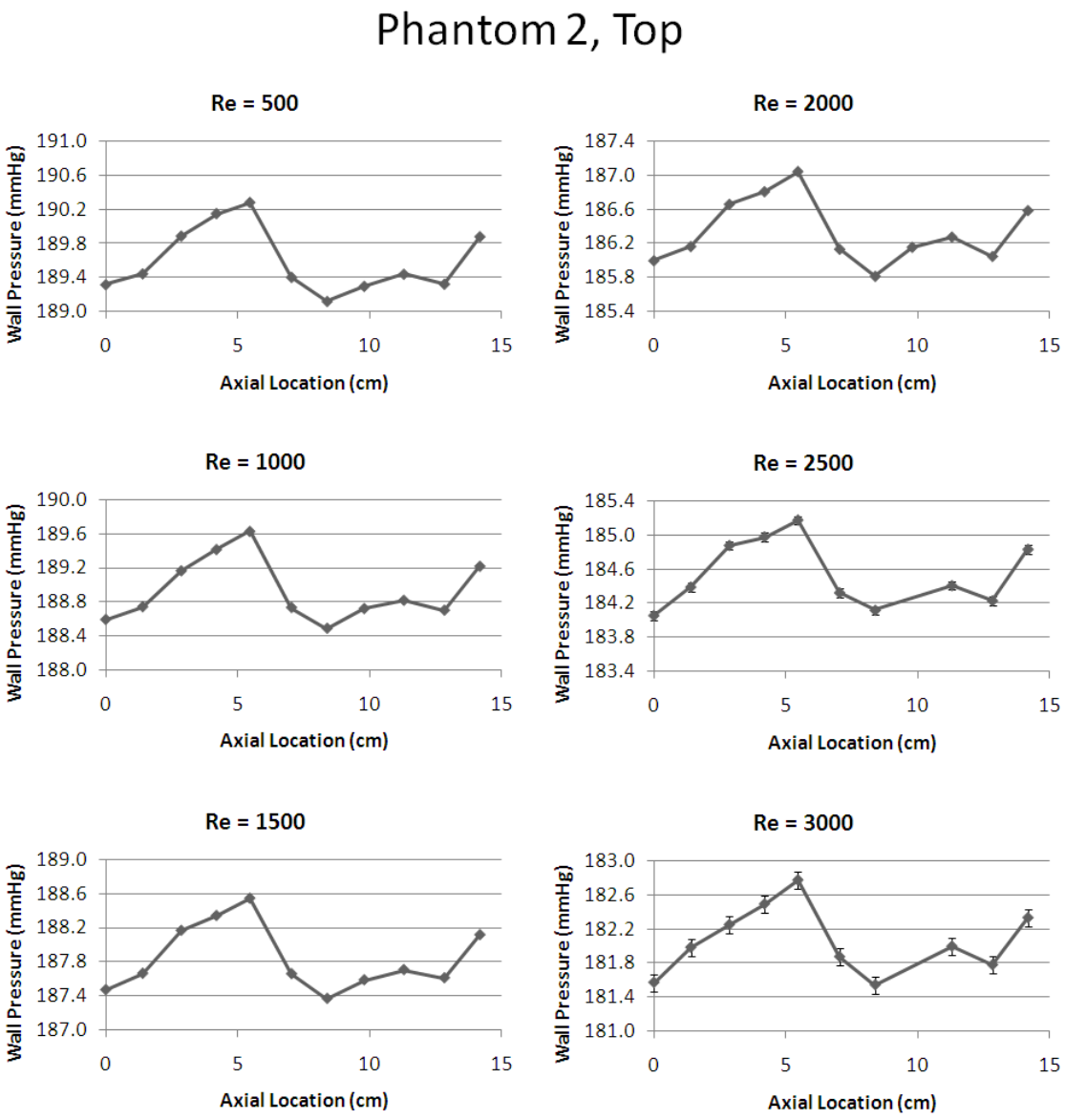

Figure C.3 Phantom 2, top.

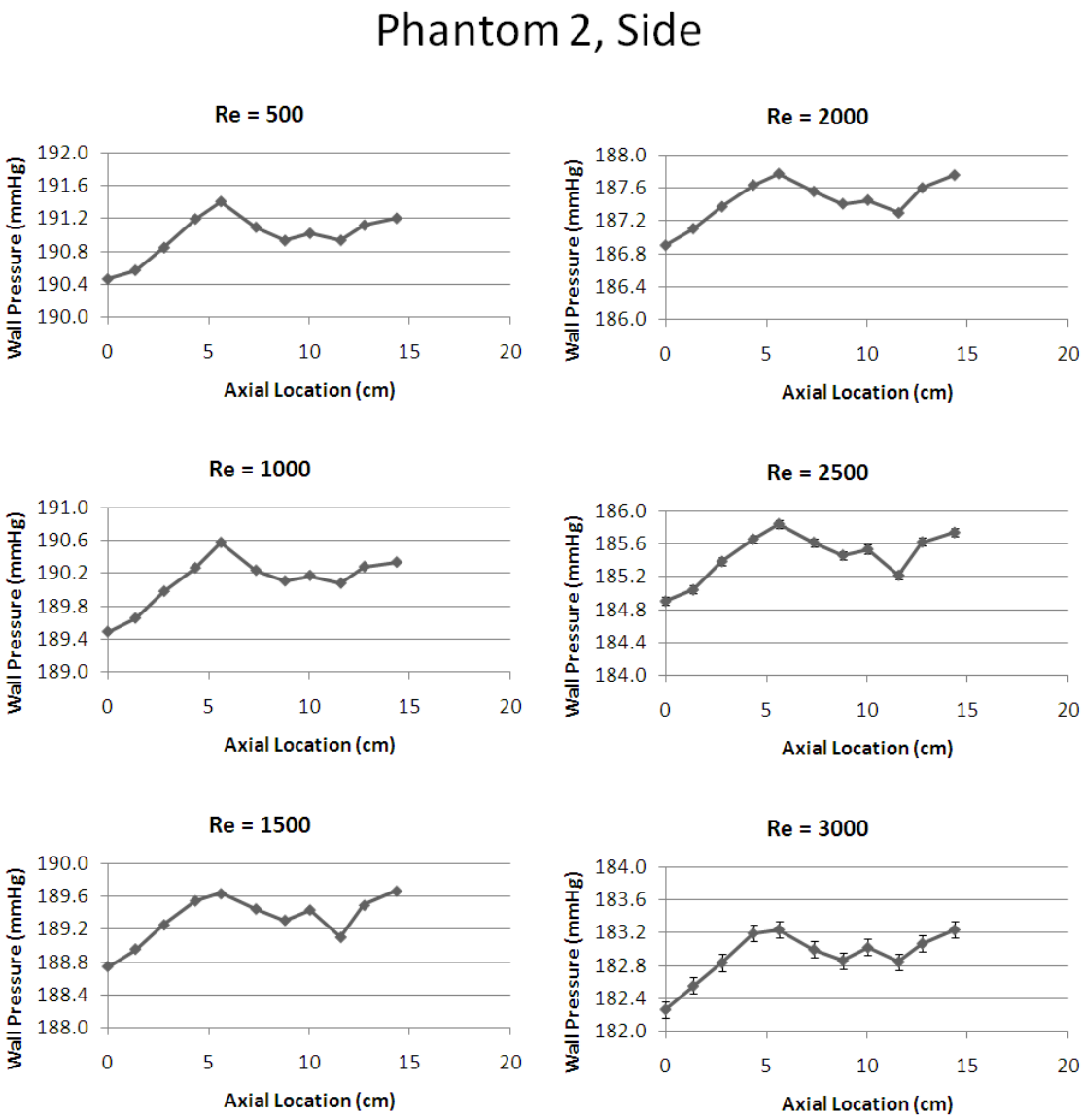

Figure C.4 Phantom 2, side.

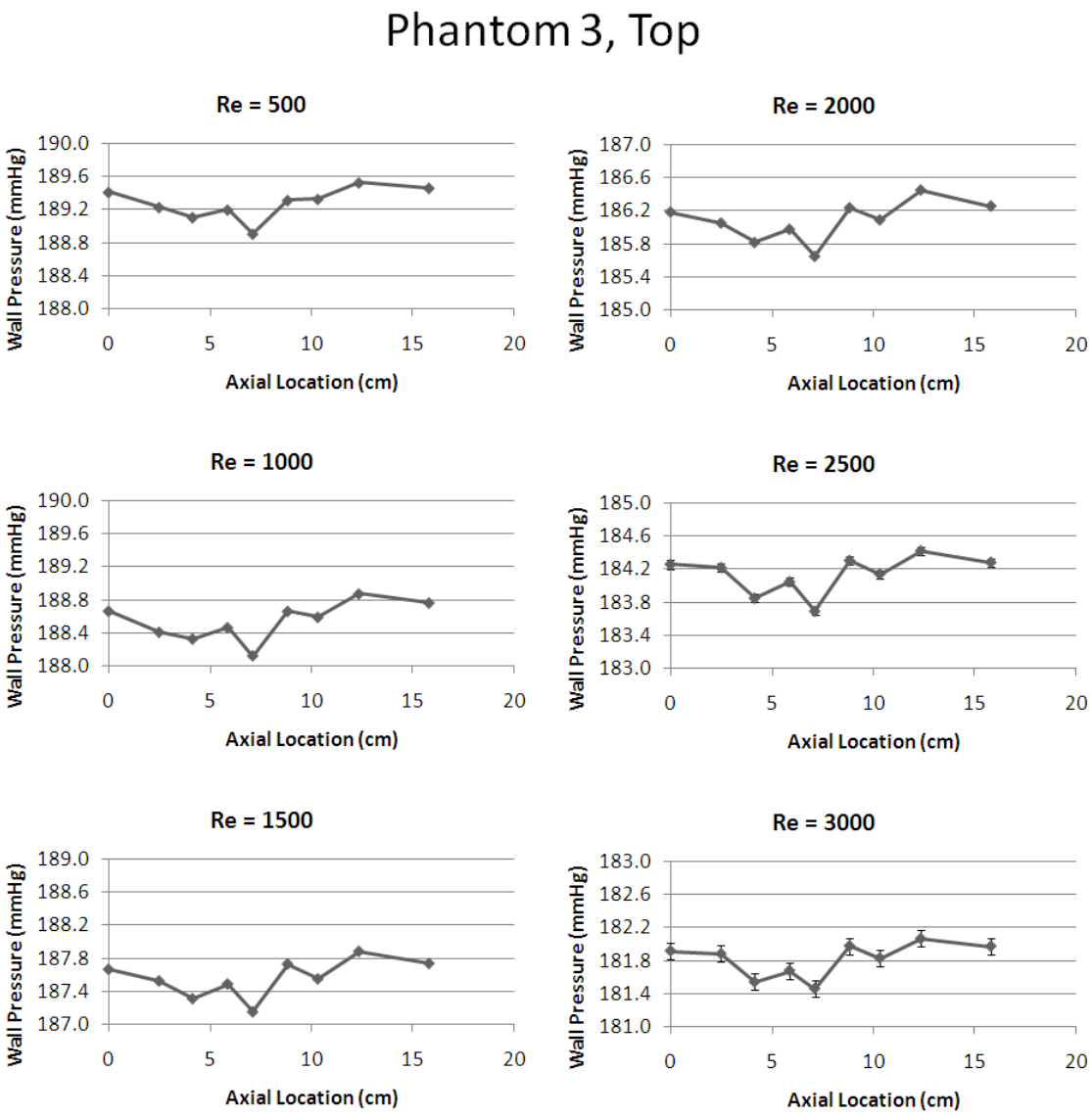

Figure C.5 Phantom 3, top.

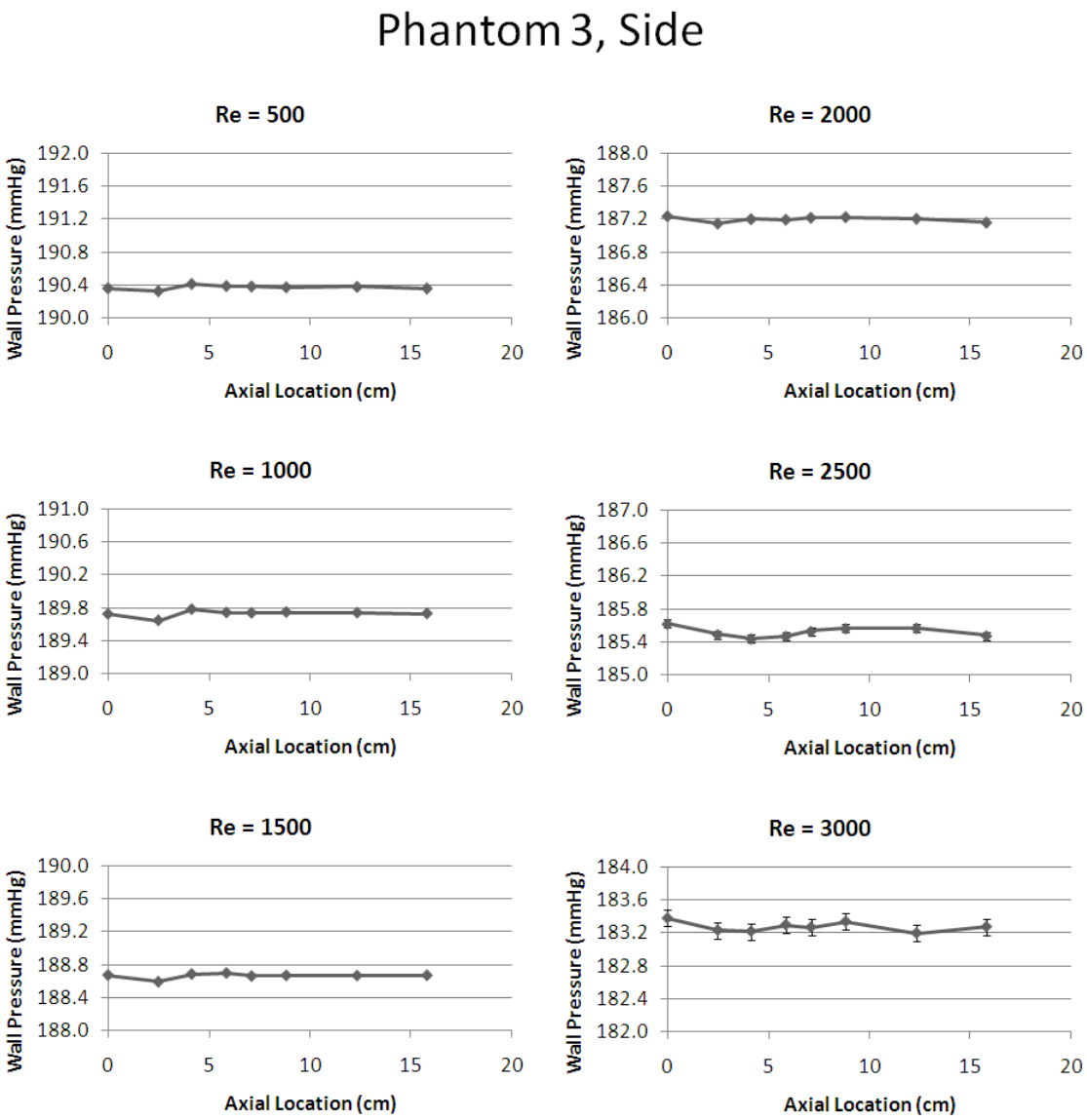

Figure C.6 Phantom 3, side.

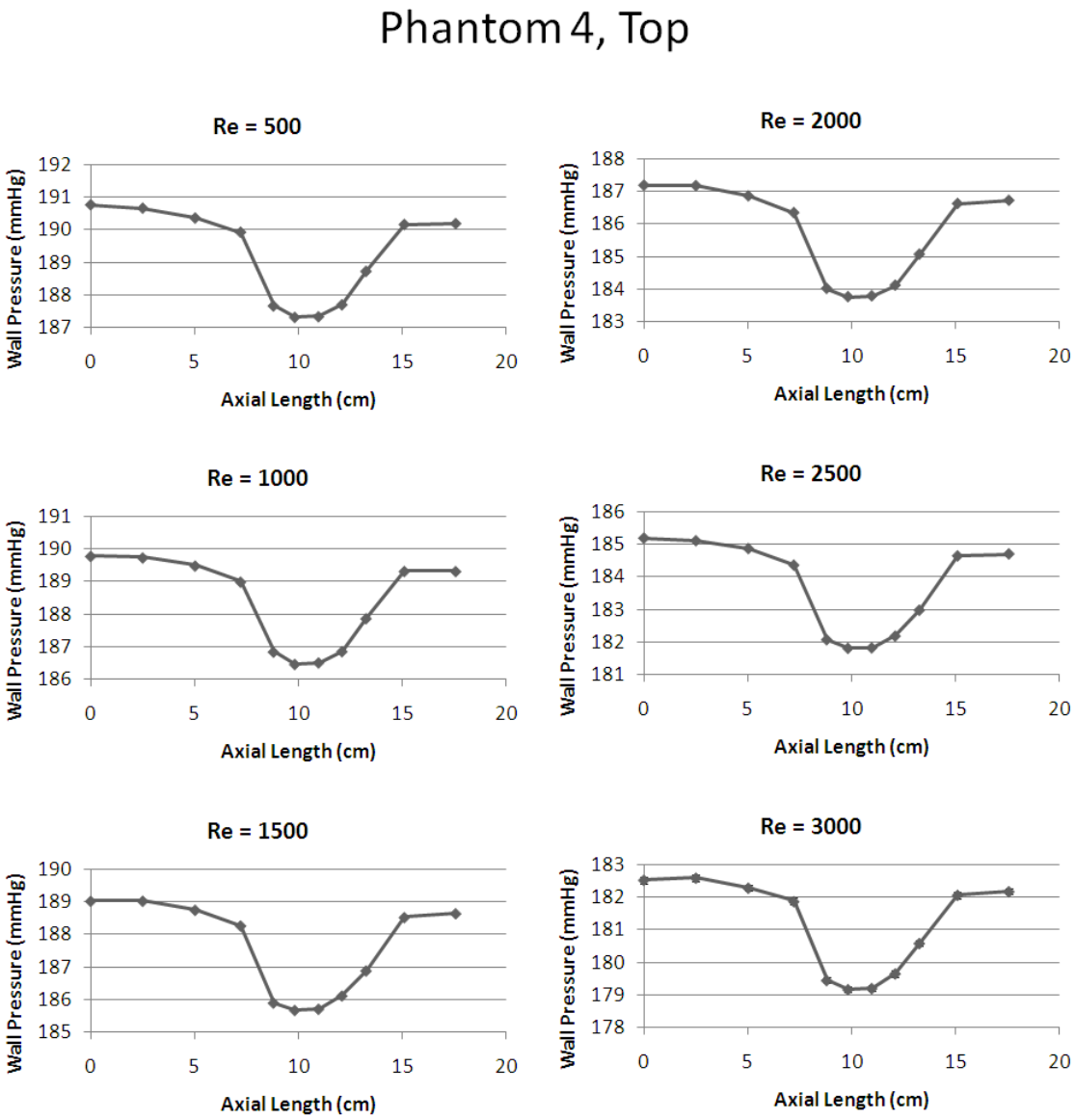

Figure C.7 Phantom 4, top.

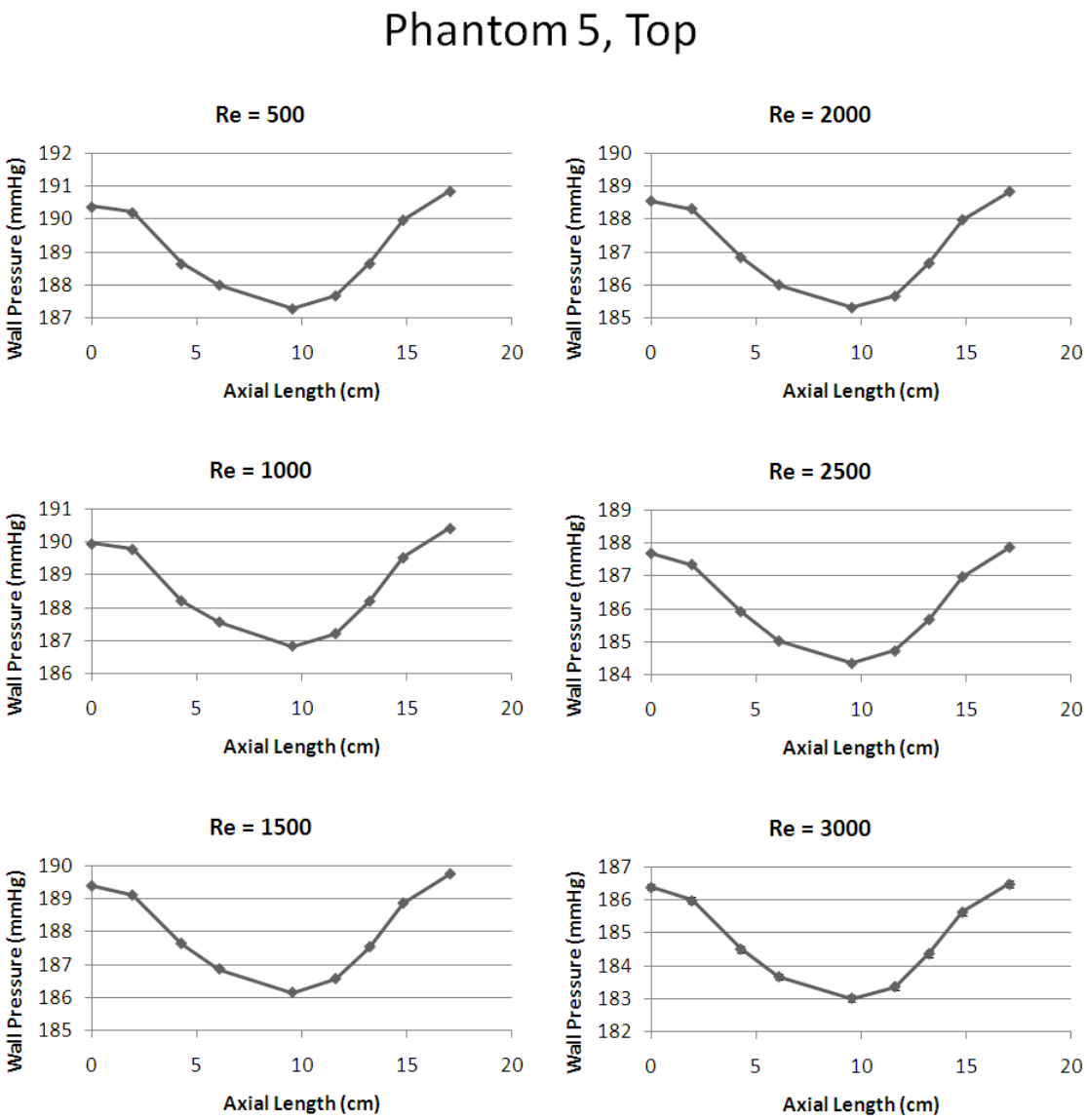

Figure C.8 Phantom 5, top.